UTS UNIVERSITY OF TECHNOLOGY SYDNEY

Fiber-Based Single Aerosol Optical Trapping and Manipulations

by Ling Zhang

Thesis submitted in fulfilment of the requirements for the degree of

Doctor of Philosophy

under the supervision of
Prof. David McGloin Prof. Fan Wang

University of Technology Sydney
Faculty Engineering and Information Technology

September 2023

CERTIFICATE OF ORIGINAL AUTHORSHIP

I, *Ling ZHANG* declare that this thesis, submitted in partial fulfillment of the requirements for the award of Doctor of Philosophy, in the *School of Electrical and Data Engineering*, *Faculty of Engineering and Information Technology* at the University of Technology Sydney, Australia, is wholly my own work unless otherwise referenced or acknowledged.

In addition, I certify that all information sources and literature used are indicated in the thesis. This document has not been submitted for qualifications at any other academic institution. This research is supported by the UTS International Research Scholarship, UTS President's Scholarship, as well as the Australian Government Research Training Program.

SIGNATURE: Production Note: Signature removed prior to publication.

[Ling ZHANG]

DATE: 3rd September, 2023

PLACE: Sydney, Australia

Abstract

Aerosols, comprising dispersed solid or liquid particles in gases, serve diverse functions with substantial economic implications. From everyday items like air fresheners and asthma inhalers to extensive emissions from industrial sources and vehicles, aerosols have far-reaching effects, causing local and global pollution, which poses health risks. Additionally, they wield a profound influence on our climate system, contributing to atmospheric processes that regulate planetary temperatures and curb unchecked warming. Studying and isolating single aerosol processes is, however, still in its infant phase. Many processes at the single aerosol level are still not yet fully understood.

This thesis endeavors to establish an advanced platform for trapping individual aerosol particles, utilizing fiber-based optical traps. Through the synergy of counter-propagating (CP) dual fiber trapping techniques and sophisticated beam shaping algorithms, this platform transcends conventional constraints in single aerosol particle trapping and manipulation. Its capabilities enable real-time analysis of single aerosol particle dynamics, presenting an adaptable, user-friendly framework for comprehensively understanding aerosol processes that drive both climate dynamics and critical industrial applications.

Initially, the thesis formulates a theoretical framework for the interaction between light and optically trapped aerosols. By evaluating the size range of trapped aerosols within the CP dual fiber trap under varying dual fiber separations, the study yields consistent, quantifiable outcomes for aerosol trapping in the CP dual fiber setup.

Subsequently, the investigation delves into the repercussions of angular deviations on the dynamics of trapped individual aerosol particles. The study quantifies trapping feasibility under different misalignment scenarios and examines how factors like beam divergence, fiber separation, fiber power, and aerosol radius influence the trapping performance and dynamic behavior of individual aerosol particles within tilted CP dual fiber traps. These findings contribute insights into the evolution of optical fiber-based traps, along with a novel strategy for controlling light-induced rotation in air.

Moreover, the thesis elucidates non-spherical particle dynamics within CP dual fiber traps across three distinct trapping schemes. By introducing a novel model, it offers

enhanced comprehension of droplet trapping dynamics within CP dual fiber traps, facilitating the exploration of challenging-to-obtain parameters for experimental validation in the future.

Furthermore, the integration of beam shaping techniques into CP dual fiber traps is advanced to enhance stability in trapping individual aerosol particles. The findings pave the way for beam shaping-assisted CP dual beam traps to improve the single aerosol trappings stability for arbitrary aerosol undergoing dynamic processes.

Dedication

To my parents, xu zhang and weiqing dou,
my wife, changqi li,
for their endless love and support.

ACKNOWLEDGMENTS

Time flies!!! After three years PhD studies, I have improved and changed significantly in terms of philosophical thinking, professional skillsets and living capabilities, which made me further clarify my pursuit and guidelines for future life and career.

Over the past three years, many historical events have occurred, and I have not only been a witness to these events, but also an experiencer. These experiences have influenced and reshaped my values and methodologies in dealing with issues in my future life. However, I always believe that the only way to explore and create greatness in life is to always have faith in truth, goodness and beauty, then you will leave something beautiful and inspiring for your family, friends and society at large. In the end, it will inspire and motivate them to explore and create their own greatness, which is what I really agree the true meaning of individual existence in the history of human beings' civilization!

First of all, I feel very fortunate and grateful to be able to pursue my PhD under the supervision from Prof. David McGloin, and Prof. Fan Wang. I would not be able to complete my PhD without their mentoring and support. David gave me the patience and freedom to take the ownership of my PhD projects, and whenever I encountered difficult problems, he would engage me in productive discussions, inspiring and helping me to overcome one problem after another. Through this training, I have come to truly appreciate the real meaning of PhD as an educational experience. As my co-supervisor, Fan's help and mentoring during my PhD was crucial. Whenever I encountered technical difficulties in optics, he was always available to give me very detailed and specific professional guidance. In addition, through my time with Fan, his enthusiasm and professionalism in doing research, and his guidance and care for students are very encouraging and heartwarming, and have inspired me to be more clear about the manner and attitude I should act in my future life.

In addition, I would like to thank Dr. Kevin Cook, senior optical technical support officer in the UTS Photonics lab, for his help during my PhD. Whether I needed technical or equipment assistance, or discussions and concerns in my research works, Kevin were always there to keep the whole lab running in an orderly and safe manner, and to provide me with the best and most immediate support. I would also like to thank my lab

mate, Miss. Anna Szmalenberg, for always sharing your experience in optical tweezers without reservation, and stopping work many times to help me with my experiments. We sometimes even joked that you could be my co-supervisor as well. I am very grateful for your help and discussions during my PhD and enjoyed working with you very much. I would also like to give a special thanks to Dr. Peter Reece from UNSW for his help and discussion on my beam shaping project. I really appreciate your patience in guiding me through the LabVIEW programming and your many times personal visiting to the UTS Techlab to provide technical support for my experiments. Moreover, I would like to thank my colleagues and friends during my time in UTS Techlab, they are Dr. Lei Ding, Dr. Baolei Liu, Dr. Chaohao Chen, Dr. Xuchen Shan, Dr. Xiaofei Wang, and Miss. Guanshu Zhao.

I would also like to thank my friends at UTS for their presence, companionship, help and support, which has made my PhD life more fulfilling and enriching. I would like to express my gratitude to Dr. Derek Hao, Dr. Idris Ibrahim, Mr. Ben Chapple, Mr. Xin Cheng, Mrs. Haixia Zhang, Dr. Chi Li, Dr. Dejiang Wang, Dr. Xiangjun Di, Dr. Peter Su, Dr. Yang Yang.

Of course, I would like to express my deepest gratitude and love to my family and my wife. I am grateful to my parents, Weiqing Dou and Xu Zhang, for their constant love and dedication to me. You both always respect my choices and give me your strongest support all the time. As your son, I feel so blessed and proud. I would also like to thank my wife, Changqi Li, for being there and for trusting me and deciding to marry me during the most difficult phase of my life while I was in Australia. I will always remember the commitment I made to you in front of God during our wedding ceremony, and I am keen to explore the world with you until the end of the world.

Finally, I would like to acknowledge UTS for providing me the International Research Scholarship and President's Scholarship to financially support my PhD studies and life in Australia, and I would also like to acknowledge Dr. Chandranath Adak for providing this LaTeX template for facilitating my PhD thesis writing and formatting. The various experiences I have had in Australia over the past three years and the diverse people I have met have been shaping the new me that I am today, and with that I will continue to explore, pursue, and create something unique and unpredictable, which I do believe it can make a positive difference for this world, even just a little bit.

Ling Zhang
February 2023

List of Publications

Journal :

1. Ling Zhang, Anna Szmalenberg, Kevin Cook, Baolei Liu, Lei Ding, Fan Wang, David McGloin. "Trapped aerosol sizes under fiber-based counterpropagation optical trapping" [J]. JOSA B, 2023. DOI:10.1364/JOSAB.46863.

2. Lei Ding, Xuchen Shan, Dejiang Wang, Baolei Liu, Ziqing Du, Xiangjun Di, Chaohao Chen, Mahnaz Maddahfar, Ling Zhang, Yuzhi Shi, Peter Reece, Benjamin Halkon, Igor Aharonovich, Xiaoxue Xu, Fan Wang "Ion resonance Rayleigh scattering from rare-earth ion doped nanoparticles" [J]. Advanced Science, 2022. DOI:10.1002/advs.202270207.

3. Ling Zhang, Anna Szmalenberg, Kevin Cook, Baolei Liu, Lei Ding, Fan Wang, David McGloin. "Fiber-based counter-propagating optical trapping aerosol with angle deviations" [J]. 2023. (To be submitted).

Conference :

4. Ling Zhang, Anna Szmalenberg, Kevin Cook, Baolei Liu, Lei Ding, Fan Wang, David McGloin. "Fiber-based single aerosol optical trapping and manipulations", The 14th Research Symposium for Chinese PhD Students and Scholars in Australia, Oral Presentation, Melbourne, Australia, 2022.

5. Ling Zhang, Kevin Cook, Anna Szmalenberg, Baolei Liu, Lei Ding, Fan Wang, David McGloin. "Dual beam optical fiber traps for aerosols with angular deviation", Conference of Complex Light and Optical Forces XVI, SPIE Photonics West, Oral Presentation, San Francisco, California, United State, 2022.

6. Ling Zhang, Kevin Cook, Anna Szmalenberg, Baolei Liu, Lei Ding, Fan Wang, David McGloin. "Trapped aerosol sizes in dual beam optical fiber-based traps",

Australian and New Zealand Conference on Optics and Photonics (ANZCOP), Poster Presentation, Sydney, Australia, 2021.

TABLE OF CONTENTS

List of Figures

Figure **Page**

List of Tables

CHAPTER 1

INTRODUCTION

1.1 Motivation

Aerosols are microscopic solid and liquid particles dispersed in air. They have a wide range of uses and economic impact, for example in air fresheners and asthma inhalers, and are also emitted on a large scale through factory chimneys and automobile exhausts, causing local and global pollution. At the same time, they make a significant contribution to our climate through atmospheric processes and play an important role in cooling the earth and protecting it from uncontrolled warming. Studying isolated single aerosol processes is, however, difficult with major outstanding uncertainties. One major reason for this is that aerosols are often fast-moving, small, and in constant interaction with their environment, and so conventional *in situ* analysis of aerosols is both challenging and, crucially destructive. As a result, we need to develop new techniques to offer insight into these critical mechanisms, to have an impact across all areas where aerosols are used, both environmental and industrial.

A plausible solution to the problem of probing single aerosol dynamics has made use of the single particle manipulation technique called optical trapping (optical tweezers), which makes use of focused lasers to hold the particles. Unlike many conventional optical trapping experiments in the liquid environment, optical trapping in air can be more challenging. One reason is the lower viscosity of the suspending medium, making the suspended aerosol more sensitive to the surrounding fluctuations. The other reason is

the higher relative refractive index of the aerosols in air, which makes it more likely to push the aerosol away from the trapping field due to the greater scattering force. Apart from that, the typical optical trapping setups remain tethered to complex microscopes, are not readily reconfigurable, and tend to require specialist operators. However, fiber-based optical trap have small footprints, is integratable, does not require expensive optics.

As a result, the aim of my PhD research is to develop an advanced single aerosol trapping platform based on fiber-based optical traps, which is through the joint work of CP dual fiber trapping techniques and advanced beam shaping algorithms to overcome the traditional limitations on the single aerosol particle trapping and manipulation, and enable the analysis of single aerosol particle dynamics in real-time, offering a flexible and user-friendly system aimed at delivering a more complete understanding of the aerosol processes that underpin our climate system and major industrial applications.

1.2 Objectives

- **Objective 1:** To develop the theoretical model of light-matter interaction of optically trapped aerosols to quantify the trapped aerosol size range

  Quantifying the size range of aerosols that can be trapped in the CP dual fiber tapping configuration is important for improving the 3D aerosol trapping efficiency and studying the manipulation of single aerosol particles. For the first objective, we are going to develop the theoretical model of the light-matter interaction of optically trapped single aerosols based on the ray optics model. Then, based on the model, we aim to quantify the trapped aerosol sizes present within the trap under different dual fiber separations. The resolved aerosol size range will provide us a guide to load different size single aerosol particles into specific CP dual fiber traps.

- **Objective 2:** To explore the impact of the angular deviations on the dynamic changes of trapped single aerosol particle

  The angular deviations of two fibers in CP dual beam traps is typically seen to be critical for good single aerosol trapping performance. For the second objective, we explore the impact of the angular deviations of the optical fibers and assess trapping viability as a function of misalignment and how particle dynamics change when interacting with displaced fibers. The results will demonstrate the maximum

fiber tilt angle threshold under configurations of the single fiber tilt and dual fibers tilt together, respectively, and offer guidance in the design of fiber-based optical traps.

- **Objective 3:** To clarify non-spherical particles dynamics in the CP dual fiber traps under three different trapping schemes

  In aerosol trapping experiments, the aerosol particles are far from just exhibiting a sphere shape. They are more like non-spherical particles, and more specifically ellipsoids in my experiments. For the third objective, we quantitatively study the trapping size range and kinetic properties of individual ellipsoidal particles under three different CP dual fiber trapping schemes based on the ray optics model, and compare the results with the case of spherical particles of the same volume. The results demonstrate a more accurate understanding of the droplet trapping dynamics in the CP dual fiber traps.

- **Objective 4:** To advance beam shaping technique into the CP dual fiber traps to improve the single aerosol trappings stability

  One very specific challenge faced when trapping liquid aerosols is that for a random sample of aerosols, the surfaces of the trapping chamber and fiber end will be coated in droplets, or possibly absorbing particles. This causes scattering of the light into the chamber and will, at best, diminish trapping efficiency and, at worst, destroy any chance of trapping anything. For the fourth objective, I optimize the trapping field required to manipulate an aerosol within a targeted trapping geometry with the help of the beam shaping technique. The results will pave the way for beam shaping-assisted CP dual beam traps to improve the single aerosol trappings stability for arbitrary aerosol undergoing dynamic processes.

1.3 Outline of the thesis

In my thesis, it consists of eight chapters and a bibliography. The contents are organized sequentially from Chapter 1 until the bibliography.

- Chapter 1: Introduction: motivation, objectives, the outline of the thesis.

- Chapter 2: Preparation: theory of optical trapping, review on aerosol optical trapping configurations, and considerations on aerosol optical trapping.

- Chapter 3: Experimental preparation: aerosol sample preparation and loading, design of aerosol trapping chamber and fiber holder, optical trapping apparatus and trapping system calibration, basic results for trapping and manipulation of a single droplet in air.
- Chapter 4: Project 1: presenting the results of the developed theoretical model of light-matter interaction of optically trapped aerosols to quantify the trapped aerosol size range within the trap under different dual fiber separations.
- Chapter 5: Project 2: presenting the results of the explored impact of the angular deviation on the dynamic changes of the trapped single aerosol particle under configurations of the single fiber tilt and dual fibers tilt together, respectively.
- Chapter 6: Project 3: presenting the results of the individual ellipsoidal particles' trapping size range and kinetic properties under three different CP dual fiber trapping schemes, and demonstrating the variations in the case of spherical particles of the same volume.
- Chapter 7: Project 4: presenting the results of beam shaping-assisted CP dual beam traps to demonstrate the capability to improve the single aerosol trappings stability for arbitrary aerosol undergoing dynamic processes.
- Chapter 8: Conclusion and future work.

CHAPTER 2

PREPARATIONS

Optical tweezers or optical trapping are used in a variety of disciplines as an important tool due to their non-contact, low damage, and high versatility. It has been developed for over 50 years since it was first introduced by Ashkin in 1970 [7] and was awarded the Nobel Prize in Physics in 2018 [56, 69]. The use of this technique to confine and manipulate the dynamics of individual aerosols and to study their physicochemical properties has been of great interest for nearly a decade. Before moving on to the main part of the thesis, in this chapter I will first introduce the theory and basics of optical trapping in Section 2.1 so that the readers can have a general understanding of how trapping forces are generated and how the dynamics of trapped aerosols vary. We then summarise the four types of aerosol trapping configurations and point out their respective characteristics, which are reviewed in Section 2.2. Finally, Section 2.3 concentrates on the aerosol trapping considerations involved in the construction of optical aerosol traps.

2.1 Theory and basics

2.1.1 Optical trapping force

In the 1860s, James Clerk Maxwell, a renowned Scottish physicist, first predicted the phenomenon of radiation pressure, which describes how electromagnetic radiation, including light, exerts pressure on an object upon striking it. Maxwell arrived at this prediction

through his groundbreaking equations that describe the behavior of electromagnetic waves [101]. These equations suggest that electromagnetic radiation carries momentum that can be transferred to an object through reflection or absorption [57]. As a result, the object experiences a force that is directly related to the momentum transferred from the electromagnetic waves [51]. Despite the fact that the effect of radiation pressure is generally small, its existence has been confirmed in various experiments involving the reflection and absorption of light by objects[10]. Radiation pressure has been extensively studied, and its practical applications span a range of fields, including space propulsion and materials science [100]. Hence, Maxwell's prediction of radiation pressure has been a crucial development in the field of electromagnetic radiation and has contributed significantly to our understanding of the interaction between light and matter. As a result, the essence of optical tweezers is to exploit the mechanical effect of momentum transfer between light and particles, resulting in the precise optical manipulation of particles in optical traps, usually for particles ranging in size from a few nanometers to several hundred micrometers. The forces exerted by the trapping laser on the particles can be divided into two main categories. One is the optical scattering force along the direction of beam propagation, which originates from the transfer of optical momentum caused by scattering and absorption of the optical field. The other one is the optical gradient force along the direction of the optical gradient, which is mainly caused by the inhomogeneous distribution of the optical field.

In fact, since the interaction between the optical trapping beam and the particles is a complex process, no universal model has been established to calculate the optical force for all different particle sizes at different trapping laser wavelengths. Currently, there are three main models for calculating the optical trapping force based on the relative ratio of the particle radius r_0 to the wavelength λ of the trapping laser, as illustrated in Fig. 2.1, namely: (a) dipole approximation model in the Rayleigh regime, (b) the electromagnetic scattering theory model in the Intermediate regime, and (c) the ray optics model in the Geometrical optics regime.

2.1.1.1 Rayleigh regime

When the particle size is much smaller than the trapping laser wavelength with $2r_0 \ll \lambda$, it can be approximated that the amplitude of the electric field is constant in the space occupied by the particle, and the particle is polarized under the action of the external electric field, so that the particle is regarded as an electric dipole, and we can calculate

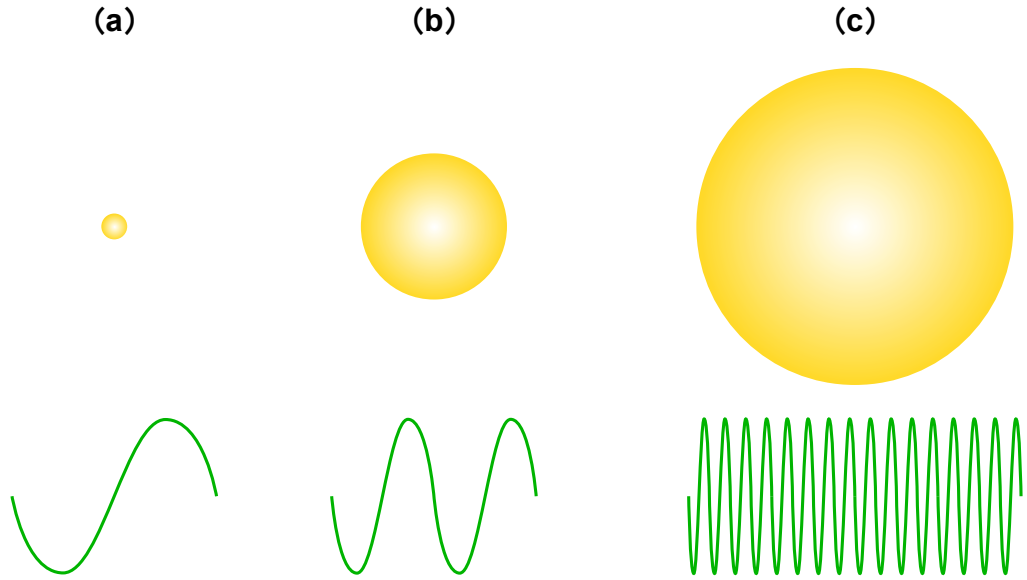

Figure 2.1: The classification of three different optical trapping regimes depends on the relationship between the value of trapping laser wavelength λ and the particle size $2r_0$. (a) Rayleigh regime, with $2r_0 \ll \lambda$. (b) Intermediate regime, with $2r_0 \simeq \lambda$. (c) Geometrical optics regime, with $2r_0 \gg \lambda$. Image adapted from [26].

the force on the particle based on the dipole approximation model [108].

As shown in Fig. 2.2, in the Rayleigh regime the particles are subjected to a gradient force in the trapped optical field due to the inhomogeneous distribution of the electric field, which is directed along the negative gradient of the electric field intensity, i.e., towards the place of maximum light intensity. The gradient force can be described in Eq. (2.1) [12]:

$$F_g = -\frac{n_m}{2}\alpha\nabla E^2 = -\frac{n_m^3 r_0^3}{2}\left(\frac{\left(\frac{n_p}{n_m}\right)^2 - 1}{\left(\frac{n_p}{n_m}\right)^2 + 2}\right)^2 \nabla E^2 \tag{2.1}$$

Where E is the electric field, α is the particle's polarizability, r_0 is the particle radius, n_m is the suspending medium's refractive index, and n_p is the particle's refractive index.

At the same time, the particle will produce scattering and re-radiation to the incident optical field, absorbing photons from the incident optical field and scattering them to the surrounding area. This process of absorption and scattering will exert a scattering force

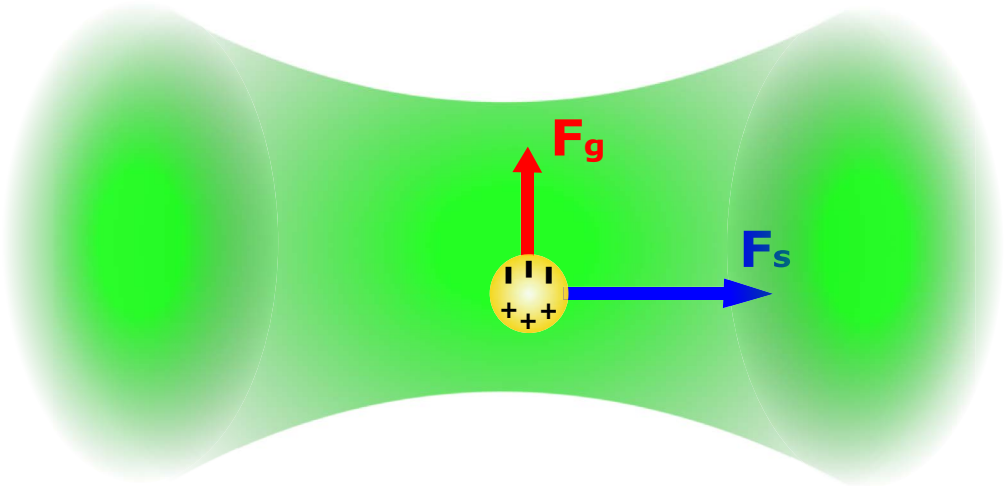

Figure 2.2: Diagram of the forces on a particle in the Rayleigh regime when it is treated as an electric dipole in the optical trapping field. Where the particle is subjected to a gradient force in the trapped optical field due to the inhomogeneous distribution of the electric field, which is directed along the negative gradient of the electric field intensity, and the scattering force exerted on the particle is along the direction of beam propagation. Image adapted from [89].

on the particle along the direction of beam propagation. The scattering force is given in Eq. (2.2) [12]:

$$F_s = \frac{I_0}{c}\frac{128\pi^5 r_0^6}{3\lambda^4}\left(\frac{\left(\frac{n_p}{n_m}\right)^2 - 1}{\left(\frac{n_p}{n_m}\right)^2 + 2}\right)^2 n_m \tag{2.2}$$

Where I_0 is the light intensity of the trapping beam, c is the speed of light in vacuum, λ is the wavelength of the trapping laser, and the remaining symbols retain the same meaning as the symbols in Eq. (2.1).

It can be seen that the scattering force is proportional to r_0^6 and the gradient force is proportional to r_0^3, i.e., as the particle radius increases, the scattering force grows faster compared to the gradient force.

2.1.1.2 Geometrical optics regime

When the size of the particle in the optical field is much larger than the wavelength of the trapping laser, i.e., with $2r_0 \gg \lambda$, the optical trapping force acting on the particle can be calculated by the ray optics model. According to the ray optics model, the incident optical field can be equated to a collection of single rays of specific intensity and direction. When a single ray is irradiated on the surface of a particle, the different refractive index between the particle and its surroundings will lead to the reflection and refraction of the incident ray on the surface of the particle. Based on these changes, we can calculate the optical force produced by a single ray on the particle, and then integrate the force produced by all the rays in the trapping optical field to calculate the total optical trapping force on the particle. In 1992, Ashkin used this model to study in detail the forces on particles in optical tweezers after transverse, axial, and arbitrary displacements [8].

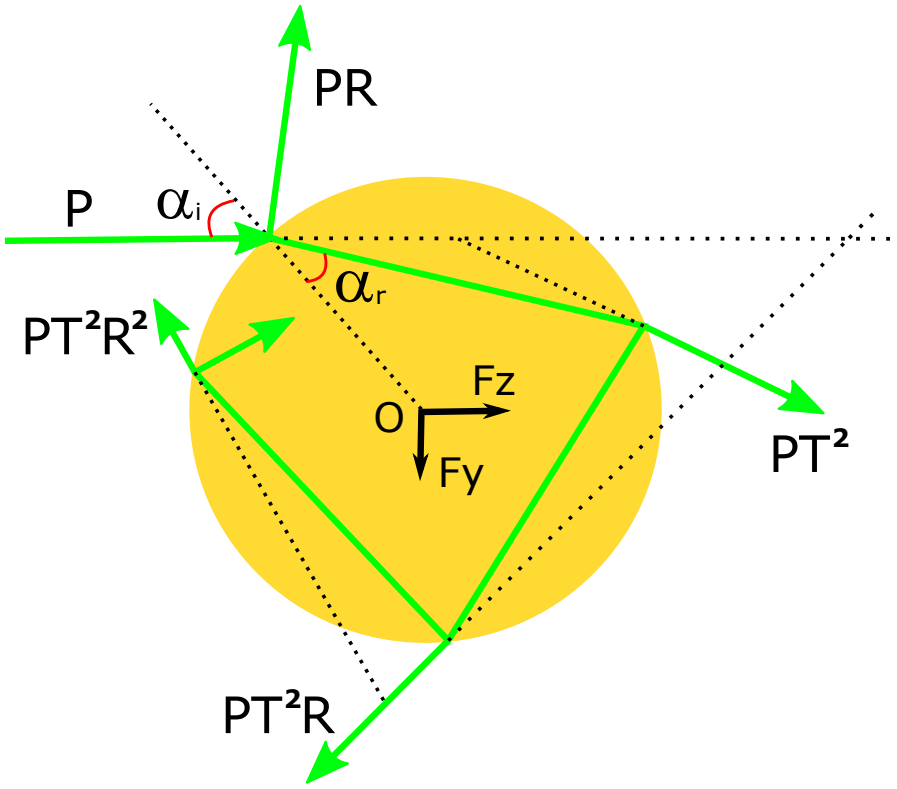

Figure 2.3: A schematic diagram of the optical force generated by the momentum transfer between light and microsphere after irradiating the microsphere with a single light ray based on the ray optics model. Image adapted from [8].

As shown in Fig. 2.3, a ray of power P incident at angle α_i strikes the surface of the microsphere, and its momentum transferred per second is $n_m P/c$, which is reflected and refracted on the surface of the microsphere according to Fresnel's law [140], where

the reflection coefficient R can be obtained according to Eq. (2.3), also the reflection coefficient R and transmission coefficient T always satisfy Eq. (2.4).

$$R = \frac{1}{2}\left[\frac{\sin^2(\alpha_i - \alpha_r)}{\sin^2(\alpha_i + \alpha_r)} + \frac{\tan^2(\alpha_i - \alpha_r)}{\tan^2(\alpha_i + \alpha_r)}\right] \tag{2.3}$$

$$R + T = 1 \tag{2.4}$$

Thereafter, depending on the number of reflections of the rays inside the microsphere, this leads to different energies carried by the outgoing rays, whose magnitudes are PR, PT^2, PT^2R, ..., PT^2R^n, ..., respectively. The optical forces generated by these beams are described as follows:

$$F_z = \frac{n_m P}{c}\left\{1 + R\cos 2\alpha_i - \frac{T^2[\cos(2\alpha_i - 2\alpha_r) + R\cos 2\alpha_i]}{1 + R^2 + 2R\cos 2\alpha_r}\right\} \tag{2.5}$$

$$F_y = \frac{n_m P}{c}\left\{R\sin 2\alpha_i - \frac{T^2[\sin(2\alpha_i - 2\alpha_r) + R\sin 2\alpha_i]}{1 + R^2 + 2R\cos 2\alpha_r}\right\} \tag{2.6}$$

The ray optics model is simple and intuitive to compute, and in 2015 Callegari et al. released an open-source MATLAB-based computational toolbox for calculating optical forces and torques of optical tweezers based on the ray optics model to facilitate teaching and researching under the Geometrical optics regime [30].

2.1.1.3 Intermediate regime

When the size of the particle in the optical field is close to the wavelength of the trapping laser, i.e., with $2r_0 \simeq \lambda$, neither the ray optics model nor the dipole approximation model can accurately describe the force on the particle in the optical field. In order to accurately quantify the optical force on the particle in the Intermediate regime, various computational models based on electromagnetic scattering theory have been developed [130, 167, 171]. The electromagnetic scattering theory model is in principle applicable to particles of all scales and mainly uses the Lorentz force acting on the particle by the electromagnetic field to study the force on the particle. The calculation process generally requires first determining the expression of the incident optical field, then solving the scattered optical field distribution of the particle on the incident optical field

from Maxwell's equations, and finally calculating the optical force on the particle from the optical field distribution around the particle, i.e., using Maxwell's stress tensor to integrate over a closed surface to calculate the optical force [77, 132, 135], which can be expressed as:

$$\langle \boldsymbol{F} \rangle = \oint_{\Omega} \langle \boldsymbol{T} \rangle \cdot \boldsymbol{n} d\Omega \tag{2.7}$$

In Eq. (2.7), $\boldsymbol{n}$ is the normal unit vector of the closed surface Ω surrounding the particle, and $\langle \boldsymbol{T} \rangle$ is the time averaged Maxwell stress tensor, which can be described as:

$$\langle \boldsymbol{T} \rangle = \frac{1}{2} \mathrm{Re} \left[\boldsymbol{D}\boldsymbol{E}^* + \boldsymbol{B}\boldsymbol{H}^* - \boldsymbol{I}_t \left(\boldsymbol{D}\boldsymbol{E}^* + \boldsymbol{B}\boldsymbol{H}^* \right) / 2 \right] \tag{2.8}$$

where $\boldsymbol{D}$ is the electric displacement vector, $\boldsymbol{E}$ is the electric field intensity, $\boldsymbol{B}$ is the magnetic induction intensity, $\boldsymbol{H}$ is the magnetic field intensity, and $\boldsymbol{I}_t$ is a unit dyadic. The electromagnetic field in Maxwell's stress tensor in Eq. (2.8) is the total electromagnetic field, including both incident and scattered fields.

For calculations based on the electromagnetic scattering theory model, several numerical computation methods have been developed, including the finite element method [166], the time-domain finite difference method [16, 60, 171], the discrete dipole approximation method [96], and the T-matrix method [103, 109, 144]. It is worth noting that it is often encountered in optical force calculations that the same particle needs to be calculated again after its position and orientation have changed. In this case, a common drawback of the first three methods mentioned above is that they require the entire calculation process to be performed again, whereas the T-matrix method depends only on the geometric configuration and electromagnetic parameters of the particle itself, independent of the position and orientation of the particle and the properties of the incident light. This means that it needs to be calculated only once and can be used multiple times to calculate the incident and scattered optical field matrices in any direction, thus reducing the computational effort significantly. In addition, the T-matrix method is applicable to particles of various shapes [110].

To facilitate the calculating optical forces and torques of particles in the Intermediate regime, Nieminen et al. open-source released the T-matrix method based Optical Tweezers Computational Toolbox (OTT) [85, 109]. Another recommended open-source optical force computational toolbox is called the Optical Tweezers Software (OTS) [77]. It covers not only the Intermediate regime, but also the Rayleigh regime and the Geometrical optics regime, and is more comprehensive and powerful with full documentation and code examples.

2.1.2 Optical trapping dynamics

The particle in the optical trapping field is not stationary. In addition to being subjected to the optical trapping force, it is subjected to Brownian motion by random collisions of molecular thermal fluctuations in the surrounding environment, and finally to form a harmonic potential trap. To understand the optical trapping dynamics, here we first introduce the Brownian motion and then model the dynamics of the trapped particle under the action of optical trapping force, gravity, environmental viscous force as well as Brownian stochastic force.

2.1.2.1 Brownian motion

Brownian motion is a common stochastic process, and particles that undergo random Brownian motion in air or liquid are called Brownian particles, first discovered by Brown in 1829 when he observed pollen particles with a microscope [23]. By the late 19th century, it was recognized that Brownian motion was related to molecular thermal motion, and then the diffusion theory of Brownian motion was explained by Einstein, Smoluchowski, and Langevin based on the equipartition of energy theorem [29, 53, 54, 84].

In a liquid environment, the number of collisions per second is about 10^{19}, and in a gas environment, the number of collisions per second reaches 10^{15}. The collision of molecules and particles is random, although the collision forces cancel each other in a long time range, however, in the transient state, the forces on the particles in each direction are variable, and the orientation and magnitude of the collision forces on the particles are random at different moments [165]. For the particle undergoing the Brownian motion, its equation of motion can be expressed by Langevin equation:

$$m\ddot{x}(t) + \gamma_0 \dot{x}(t) = \left(2k_B T_0 \gamma_0\right)^{\frac{1}{2}} \zeta(t) \tag{2.9}$$

In Eq. (2.9), m is the mass of the particle, $\gamma_0 = 6\pi\eta r_0$ is the Stokes coefficient, where η is the viscosity coefficient of the environment and r_0 is the radius of the particle. k_B is the Boltzmann constant, T_0 is the environmental temperature, and $\zeta(t)$ denotes the correlation function with Gaussian probability distribution.

2.1.2.2 Particle dynamics in harmonic potential traps

Upon entrapping the particle within an optical trap, the exerted trapping force exhibits a resemblance to a spring force, manifesting a magnitude directly tied to the particle's positional deviation. However, it's crucial to recognize that this proportionality doesn't hold uniformly across all displacements. The force-to-displacement relationship maintains its linearity solely within a specific range of distances from the equilibrium position. Hence a harmonic potential well is formed by the trapping beam, causing the particle to undergo harmonic oscillation. At this time, in addition to the optical trapping force, the trapped particles are also subject to the Brownian stochastic force generated by the thermal motion of molecules in the environment, i.e., the motion of the particles also has stochasticity, and their dynamic processes in the optical trap can be expressed through the Langevin equation as [17, 82, 164].

$$m\ddot{x}(t) + \gamma_0 \dot{x}(t) + \kappa x(t) = \left(2k_B T_0 \gamma_0\right)^{\frac{1}{2}} \zeta(t) \tag{2.10}$$

$$F = -\kappa x \tag{2.11}$$

In contrast to Eq. (2.9), Eq. (2.10) only adds the third term to the left side of the equation, i.e., the optical trapping force on the particle after it is trapped in the optical trap, which can be calculated by Eq. (2.11). where κ represents the stiffness of the optical trap (usually normally in units of pN/μm), which is an important indicator of the quality of the optical trap. The remaining symbols retain the same meaning as the symbols in Eq. (2.9).

By rearrangement of Eq. (2.10), Eq. (2.12) can be obtained as follow:

$$\ddot{x}(t) + \Gamma_0 \dot{x}(t) + \Omega_0^2 x(t) = \xi(t) \tag{2.12}$$

$$\Gamma_0 = \frac{\gamma_0}{m} \tag{2.13}$$

$$\Omega_0^2 = \frac{\kappa}{m} \tag{2.14}$$

$$\xi(t) = \frac{\left(2k_B T_0 \gamma_0\right)^{\frac{1}{2}} \zeta(t)}{m} \tag{2.15}$$

where Γ_0 denotes viscous damping of the environment, Ω_0 represents the natural angular frequency of the trapped particle, and $\xi(t)$ represents the Brownian stochastic force per unit mass [33, 129].

For a typical optical trap system, the power spectrum density (PSD) is usually used to analyze the motion of the trapped particles and thus extract the trapping stiffness κ of the optical trap. By performing the Fourier transform on Eq. (2.12), and multiplying both sides by their complex conjugates, we obtain the power spectrum of position fluctuations [149]:

$$S_x(f) = \frac{k_B T_0}{\pi \kappa} \frac{\Omega_0^2 \Gamma_0}{\left(f^2 - \Omega_0^2\right)^2 + f^2 \Gamma_0^2} \tag{2.16}$$

By rearrangement of Eq. (2.16), we can obtain Eq. (2.17) with the corner frequency f_c given by Eq. (2.18):

$$S_x(f) = \frac{k_\mathrm{B} T_0}{\pi} \frac{1}{\kappa^2} \frac{f_c^2 \gamma_0}{\left(\frac{m^2 f^4}{\gamma_0^2 - 2\kappa m}\right) + f_c^2 + f^2} \tag{2.17}$$

$$f_c = \sqrt{\frac{\kappa^2}{\gamma_0^2 - 2\kappa m}} \tag{2.18}$$

In the experiment, the corner frequency f_c can be obtained by fitting the power spectrum of the trapped particle, and then we can calculate the trap stiffness κ of the optical trap system according to Eq. (2.18).

2.2 Aerosol optical trapping configurations

Since Ashkin's successful levitation of a SiO_2 microparticle in air and vacuum by the forces of radiation pressure in 1971 [9], the stable trapping, manipulation, and characterization of individual particles in gas phase or vacuum have gradually attracted the attention of scholars around the world. Among them, Steven Chu was awarded the Nobel Prize in Physics in 1997 for his success in laser trapping and cooling atoms in a vacuum environment [39, 40, 107]. In recent years, the application of optical trapping techniques in the field of aerosol science [43, 47, 79, 127] has also been developing rapidly, and contributed quite a lot to further understanding the atmospheric chemistry [15, 48, 78, 159]. However, optical trapping and manipulation in air can be more challenging than in the more conventional liquid trapping media normally used [147]. One reason is the lower viscosity of the suspending medium, making particles more sensitive to the surrounding fluctuations. The other reason is the higher relative refractive index of the particles in air, which makes it more likely to push the particle away from the trapping field due to the greater scattering force. As a result, a reasonable optical trapping configuration is required to achieve stable particle trapping in gas phase. Since this thesis is focused on the use of optical trapping techniques for aerosol particle trapping and manipulation, in this section I will present four types of aerosol trapping configurations that are currently in common use, while the reader can also refer to more details from other excellent reviews [64, 67, 102, 163].

2.2.1 Single beam optical trapping

2.2.1.1 Optical levitation

Ashkin and Dziedzic first demonstrated the use of scattering force to achieve single beam optical trapping of a single glass sphere in air in 1971, termed the optical levitation

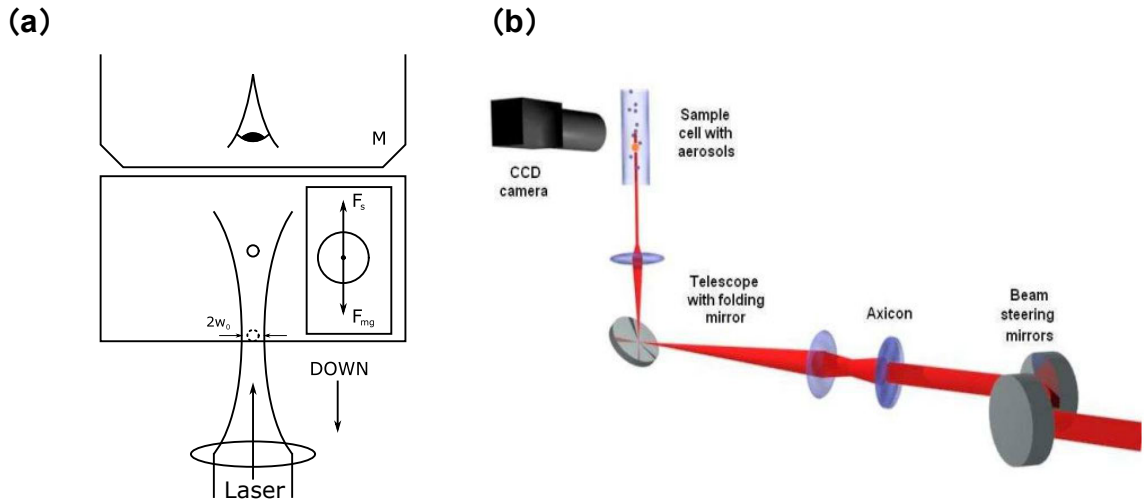

Figure 2.4: (a) The optical levitation trap developed by Ashkin and Dziedzi. A loosely focused Gaussian beam, pointing vertically upward, achieves a single glass sphere particle optically levitation by balancing the scattering force with the gravitational force acting on the particle. (b) The setup for optical levitation using a Bessel beam. Where the axicon with an opening angle of 1.5 degrees was used to shape the incoming Gaussian beam into a Bessel beam, and the telescope was used to control the beam propagation distance as well as the central core size. Images adapted from [9, 148].

trap. As shown in Fig. 2.4(a), this trap consists of a loosely focused Gaussian beam, pointing vertically upward, which achieves optical levitation of the particle by balancing the scattering force with the gravity force acting on the particle [9]. The reason for the stable force equilibrium is that in the axial direction, the scattering force decreases with increasing distance from the beam focus position until it reaches a position where the scattering force is equal and opposite to the gravitational force on the particle. While the generated gradient force provides confinement to the particle in the lateral direction. In addition, the scattering force and the intensity of the trapping laser are positively correlated, so the guiding of the particle in the axial direction can be achieved in the optical levitation trap by controlling the power of the trapping laser. Based on this principle, Summers et al, as shown in Fig. 2.4(b), demonstrated the optical levitation in air for three different droplets, including salt solution, ethanol, and dodecane, and compared the difference in guiding distances of individual droplets at different laser powers for the Gaussian and Bessel beams, respectively [102, 148]. Although the optical levitation trap is capable of achieving the suspension of individual aerosol particles in air, the delicate balance between the capture laser power and gravity, the Brownian motion of the aerosol particle, as well as the random perturbations from the external environment

can make optical levitation traps less stable and reliable. For these reasons, researchers have tried to improve the stability of optical levitation traps by using feedback control devices [11, 136].

2.2.1.2 Single beam gradient force optical trap

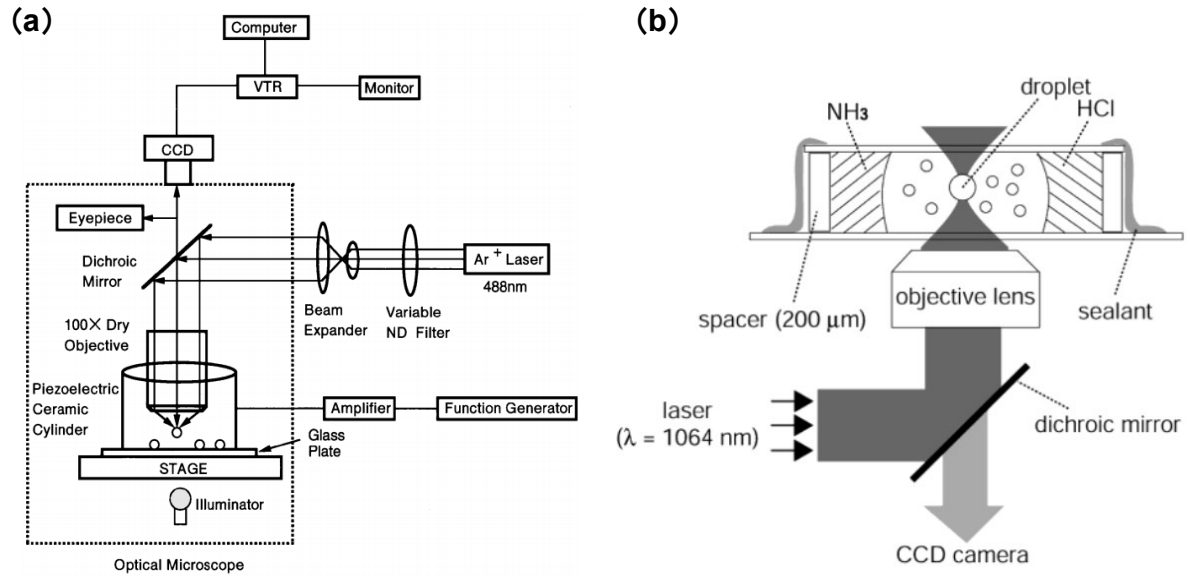

Figure 2.5: (a) Schematic diagram of the experimental setup for a single beam gradient force optical trap in air using a non-inverted trapping geometry developed by Omori et al. in 1997. Where they first used this setup to trap a solid glass particle in air. (b) An inverted single beam gradient force optical trap was developed by Magome et al. subsequently in 2003. Where they first successfully trap a water droplet in gas phase. Images adapted from [99, 112].

As we mentioned in the previous section, although optical levitation enables the suspension of individual aerosol particles in air, such traps have low stability and reliability, are susceptible to external environmental disturbances, and do not allow for stable confinement of the single aerosols in all three dimensions. It was not until 1997 that Omori et al. inspired by the optical tweezers invented by Ashkin et al. in 1986 [12], demonstrated for the first time that a tightly focused Gaussian beam using a high numerical aperture (NA) objective (NA = 0.95) with a non-inverted trapping geometry could stably trap a solid glass particle in air [112], as shown in Fig. 2.5(a). The direct reason why stable 3D trapping can be achieved is that the tightly focused laser beam by a high NA objective can produce dominant optical gradient forces that will overcome the effect of the optical scattering forces that try to push the particle away. Subsequently, Magome et al. used

an inverted trapping geometry that can use gravity to assist in balancing the optical scattering forces to successfully trap water droplets in the gas phase for the first time in 2003 [99], as shown in Fig. 2.5(b). This inverted trapping structure has been more widely used in later aerosol studies [74, 102, 104]. Compared with the Optical levitation, single beam gradient force optical trap can achieve more stable 3D trapping with higher stability and reliability, but it also faces limitations such as using a high NA objective (expensive), the short working distance (less than 1mm), and inability to trap aerosol particles in a larger size range.

2.2.2 Counter-propagating dual beam optical trapping

2.2.2.1 Counter-propagating dual beam trap

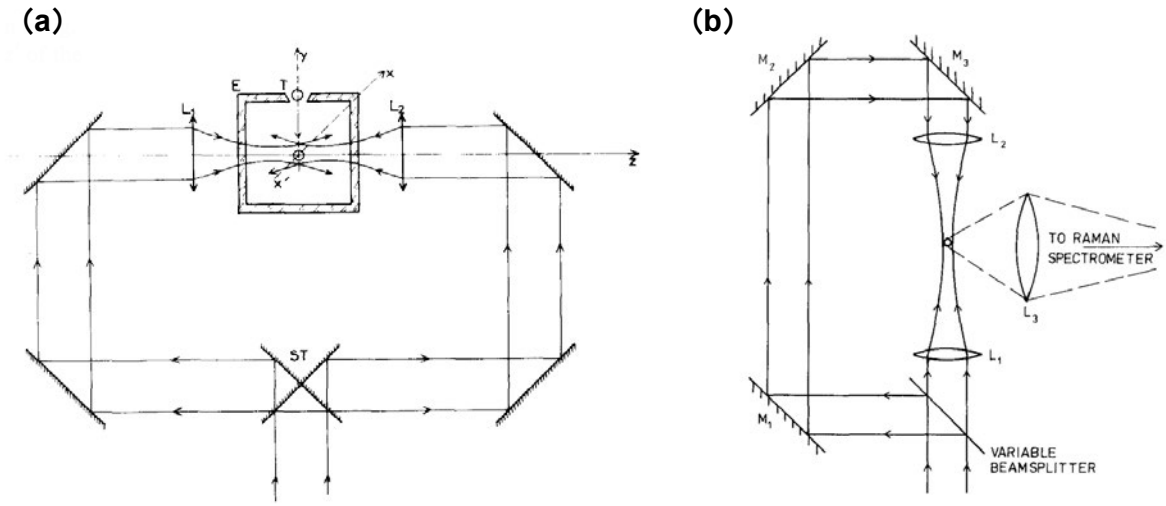

Figure 2.6: (a) A CP dual Gaussian beam trapping configuration to trap solid glass sphere in air developed by Roosen and Imbert in 1976. (b) A vertical CP dual Gaussian beam trapping geometry to facilitate the acquisition of the enhanced Raman excitation of optically trapped particles was developed by Thurn and Kiefer in 1984. Images adapted from [133, 156].

For the single beam optical trapping techniques described in Section 2.1, Optical levitation has the disadvantage of not being able to achieve stable confinement in three dimensions, while single beam gradient force optical trap has the downside of requiring the use of expensive high NA objectives, short working distance, and inability to capture aerosol particles in a large size range. To overcome the above-mentioned shortcomings,

Roosen and Imbert, inspired by Ashkin's proposal in 1970 of using two focused horizontal counter-propagating (CP) Gaussian laser beams to achieve stable trapping of glass microspheres in water [7], applied this trapping configuration to successfully confine a solid glass sphere in air six years later [133], as shown in Fig. 2.6(a). In this trapping geometry, instead of using high NA objectives to generate dominant optical gradient forces to overcome the effect of the optical scattering forces, the strong optical scattering forces are balanced in the axial direction by adding a second laser beam that can provide an equal but opposite force to counterbalance the strong optical scattering forces. At the same time, the generated optical gradient forces will equalize the weight of the aerosol particle and confine it in the lateral direction, thus forming a 3D optical potential well in the middle of the two CP laser beams. Once the aerosol particle enters this 3D optical potential well, any displacement from the center of the well will lead to a recovery force that pulls the aerosol particle back to the position where it was stably captured. Eight years later, Thurn and Kiefer in 1984 proposed the use of the vertical CP dual beam trap to capture micron-sized solid particles in air, and noted that this arrangement would facilitate the acquisition of the enhanced Raman excitation of optically trapped particles [156], as shown in Fig. 2.6(b).

In addition to using Gaussian beams to form CP dual beam optical traps to capture and manipulate aerosol particles in air [133, 156, 160], researchers have also considered using different beam profiles, such as Bessel beams [31, 32, 124], hollow beams [116, 162], vortex beams [52, 141, 142], are used in the scheme of the CP dual beam trap to confine and manipulate more different types of aerosol particles. Fig. 2.7(a) shows the schematic diagram of the experimental setup for the CP dual Bessel beam trap developed by Carruthers et al in 2012. Where an axicon with a cone angle of 177° was used to shape the incoming Gaussian beam into a Bessel beam, and then the lens relay system was used to adjust beam propagation as well as the diameter of the central core, thus enabling this trap to achieve the selection of the trapped droplet size distributions. In the same year, Pan et al. developed the experimental setup for the CP dual hollow beam trap as shown in Fig. 2.7(b). They used three axicons (cone angle of 176°) to convert the incoming Gaussian beam into the hollow beam, and then formed hollow trapping region to trap the absorbing particle in air by the generated photophoretic forces. In addition, they integrated the trapping system with Raman spectroscopy, allowing on-line quasi-real-time characterization of trapped absorbing aerosol particles. In Fig. 2.7(c), Shvedov et al used a more sophisticated vortex beam to form a CP dual beam trap, by which they

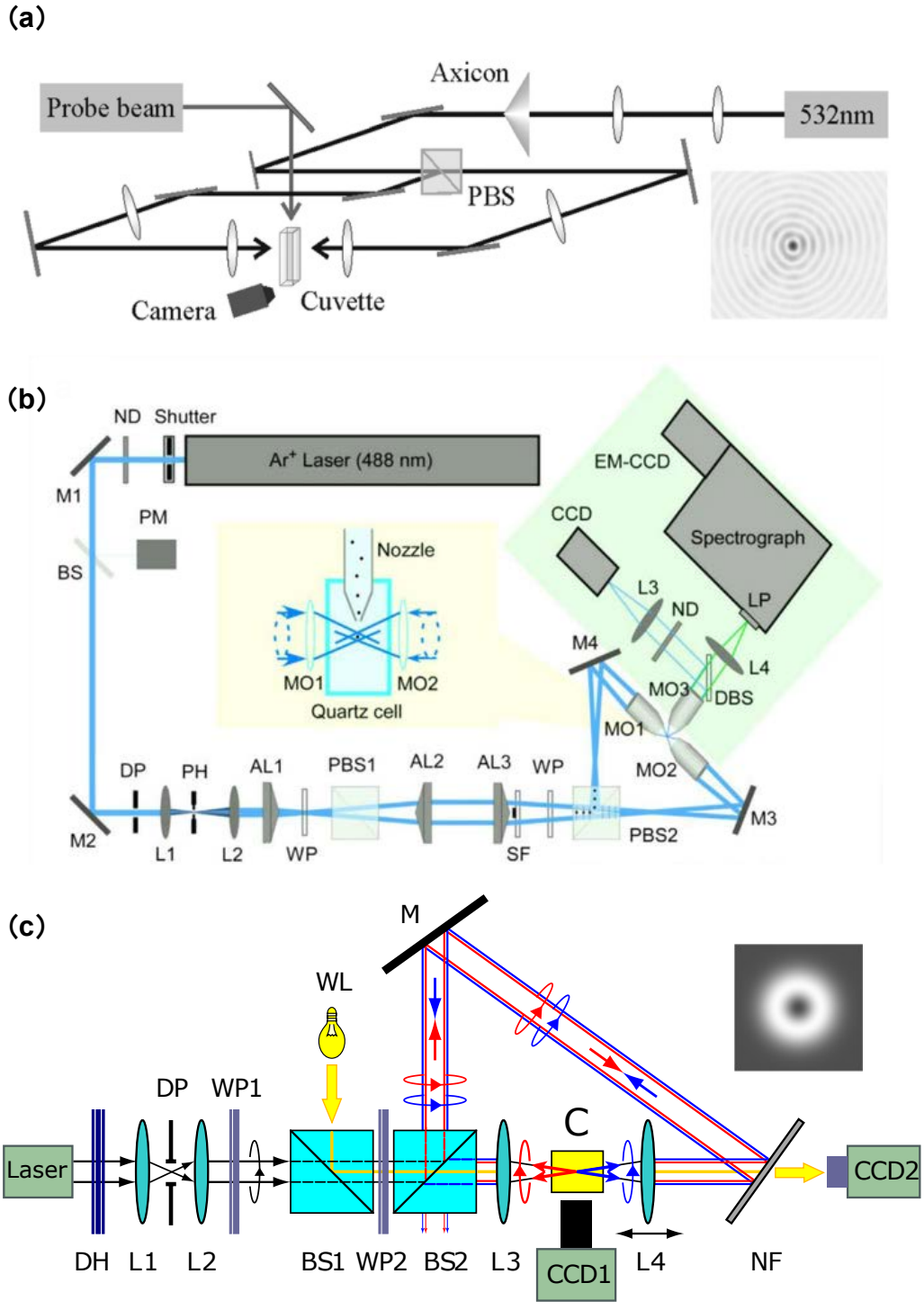

Figure 2.7: The schematic of the experimental setups for the CP dual beam trap by using (a) Bessel beam, (b) Hollow beam, and (c) Vortex beam. DP: Diaphragm; PH: Pinhole; M: Mirror; ND: Neutral Density; MO: Micro Objective; BS: Beam splitter; AL: Axicon lens; PBS: Polarizing Beamsplitter, WP: Waveplate; L: lens; C: Cuvette; NF: Notch Filter. Images adapted from [32, 116, 142, 162].

experimentally demonstrated the powerful 3D guiding of carbon particles (ranging in size from 100nm to 10μm) at distances of a few millimeters in air. The CP dual beam trap can offer high trapping stability and robustness, provide longer working distance, and enable capturing aerosol sizes in a large size range. However, the two trapping beams must be carefully aligned prior to the experiment in order to achieve stable airborne trapping, otherwise, the trapped aerosols will undergo complex dynamic variations that destabilize the trapping performance. Besides, the addition of the second trapping beam will increase the complexity of the whole trapping system and also raise the overall cost.

2.2.2.2 Confocal beam trap

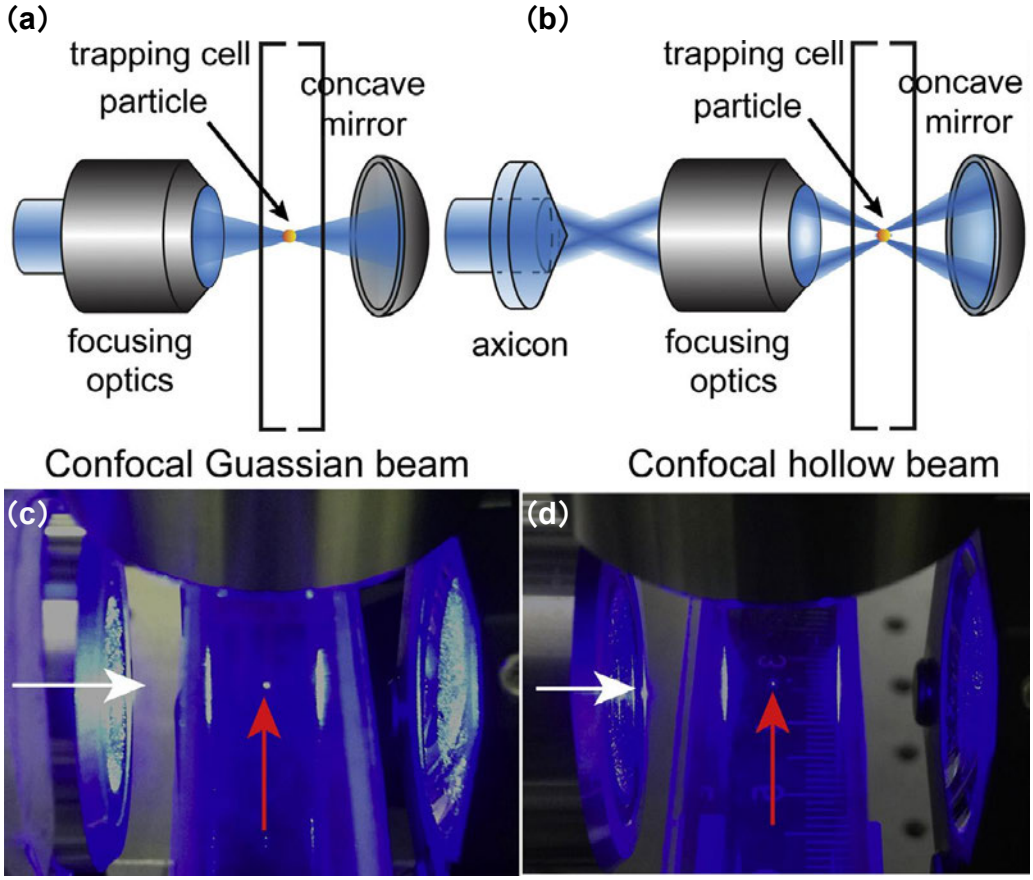

Figure 2.8: The schematic diagrams of the confocal beam trap by using (a) Gaussian beam, and (b) Hollow beam. The corresponding practical experimental trapping field image of the confocal beam trap for trapping single aerosol particles in air by using (c) Gaussian beam, and (d) Hollow beam. Images adapted from [67].

Although conventional CP dual beam traps offer several advantages, such as high

trapping stability and robustness, longer working distances, and larger trapping aerosol size distributions, the addition of a second trapping arm leads to the more complex overall trapping system, requiring additional system expenses, and placing high demands on the alignment of the dual beams. As a result, a virtual CP dual beam trap, termed confocal beam trap [67, 68, 70, 93, 161], was proposed as a substitute scheme for the 3D confinement of the airborne particles. This trapping configuration retains the advantages of the conventional CP dual beam trap, while simplifying the complexity of the overall trapping system by constructing a virtual CP trapping beam. Fig. 2.8(a) shows the schematic diagrams of the confocal beam trap by using a Gaussian beam as the trapping beam, in which a virtual CP dual beam trap is formed by using a concave mirror to reflect the collimated beam that has been focused via a convex lens or objectives at a relatively low NA, thereby forming a symmetric confocal optical field in the direction of the optical axis. In addition, by precisely adjusting the separation distance between the focusing optics and the concave mirror, the structure of the symmetric confocal optical field can be fine-tuned. Fig. 2.8(c) shows the trapped single multi-walled carbon nanotube by using this trap with high trapping stability [161]. Subsequently, Gong et al. proposed to use a Hollow beam converted by an axicon as the trapping beam in the confocal beam trap, as shown in Fig. 2.8(b) and (d), in which they experimentally demonstrated they can trap a different number of aerosols in air, as well as manipulate the number of aerosols trapped within the trapping field [68].

2.2.3 Holographic optical trapping

To enable more complex, controlled, and dynamically tunable 3D trapping and manipulation of single or multiple aerosol particles, scholars have proposed using Holographic Optical Tweezers (HOTs) [1, 25, 26]. Typically, the principle of HOTs is to modulate the phase of the incoming Gaussian trapping beam by a liquid crystal spatial light modulator (SLM), which then yields the desired complex trapping pattern, allowing for more flexible and advanced aerosols trapping and manipulations. In Fig. 2.9, Burnham et al. first demonstrated using HOTs to capture multiple water droplets in air in a matrix fashion, and also showed controlled manipulation along the x, y, and z directions, which ultimately led to the coagulation of the droplets [25]. However, Fig. 2.9(b) showed that it is hard to achieve using water droplets to fill all the trap points, mainly due to the passive waiting for randomly loaded droplets entering the trap sites. Besides, the mutual interference between loaded droplets can also lead to the crowding out of droplets

that have already entered the trap. As shown in Fig. 2.10, Alpmann et al. in 2012 used HOTs in combination with optical bottle beams generated by the convolution approach to achieve stable trapping of multiple absorbing particles in air at target locations simultaneously, and also demonstrated dynamic manipulation of absorbing particles along arbitrary paths by dynamically varying the input hologram [1].

2.2.4 Fiber-based optical trapping

In the last three sections, we have focused on several different types of lens-based or microscope objective-based aerosol optical trapping configurations, typically used in free space. However, such traps usually have complex optical structures that make the system bulky and limited to a fixed field of operation. In addition, they are not suitable for in vivo trapping and have short working distance, making them difficult to integrate with other instruments. Moreover, usually these traps use expensive optical components, making them difficult to afford. For this reason, fiber-based optical traps have been proposed to overcome the above-mentioned drawbacks. The first fiber-based trapping implementation was performed by Constable et al. in 1993, using radiation pressure trapping generated by a well-aligned CP dual fiber trapping configuration to capture dielectric spheres and live yeasts [42]. Subsequently, a single fiber-based gradient force trap was successfully proposed by Taguchi et al. in 1997 to achieve more flexible trapping and manipulation of dielectric particles and biological cells [153]. Since fiber-based optical traps are simple to fabricate, easy to integrate, flexible to adjust, and have no operational depth limitation compared to lens-based optical traps, they have been developed rapidly in the past 20 years and are widely used in biological research. Readers can find more details in these recent excellent reviews [91, 97, 128, 169, 172, 174].

Since the focus of this thesis is on aerosol particle trapping and manipulation in air using optical trapping techniques, to our knowledge, we have found only very limited literature on this topic based on the fiber-based optical traps [90, 102, 134]. As shown in Fig. 2.11(a), Rudd et al. in 2008 first demonstrated the possibility of trapping water droplets using CP dual fiber traps [102]. Fig. 2.11(b) shows the trapped single droplet marked with a red circle in the midpoint of two CP SMFs with equal output power. By changing the output power of two SMFs, the trapped droplet can move along the optical axis at a speed of up to 75μm/s. In addition to using SMFs to form CP dual beam traps, Rudd et al. have also used multimode fibers (MMFs) to replace SMFs for trapping,

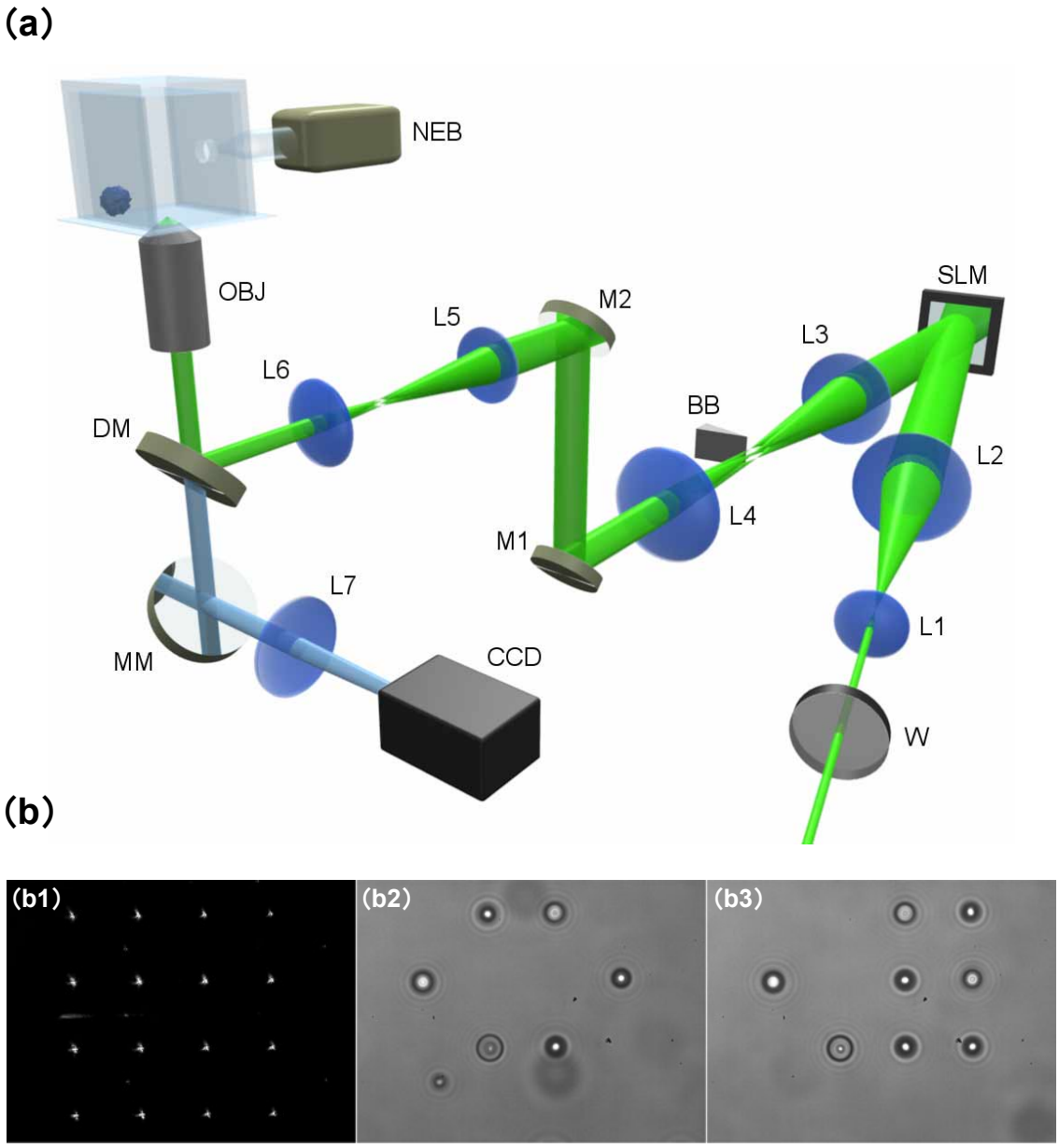

Figure 2.9: Holographic aerosol optical traps. (a) The schematic diagram of the holographic optical tweezers setup was developed by Burnham et al. in 2006. W: Half-wave plate; L: Lens; SLM: Spatial light modulator; BB: Beam block; M: Mirror; DM: Dichroic mirror; MM: Metallic mirror; OBJ: Microscope objective; NEB: Ultrasonic nebulizer for generating water droplets. (b1) The shaped matrix trapping beam by a desired holographic trapping pattern is used in the holographic aerosol optical tweezers. (b2) and (b3) show the corresponding trapped droplets within multiple trapping sites. Images adapted from [25].

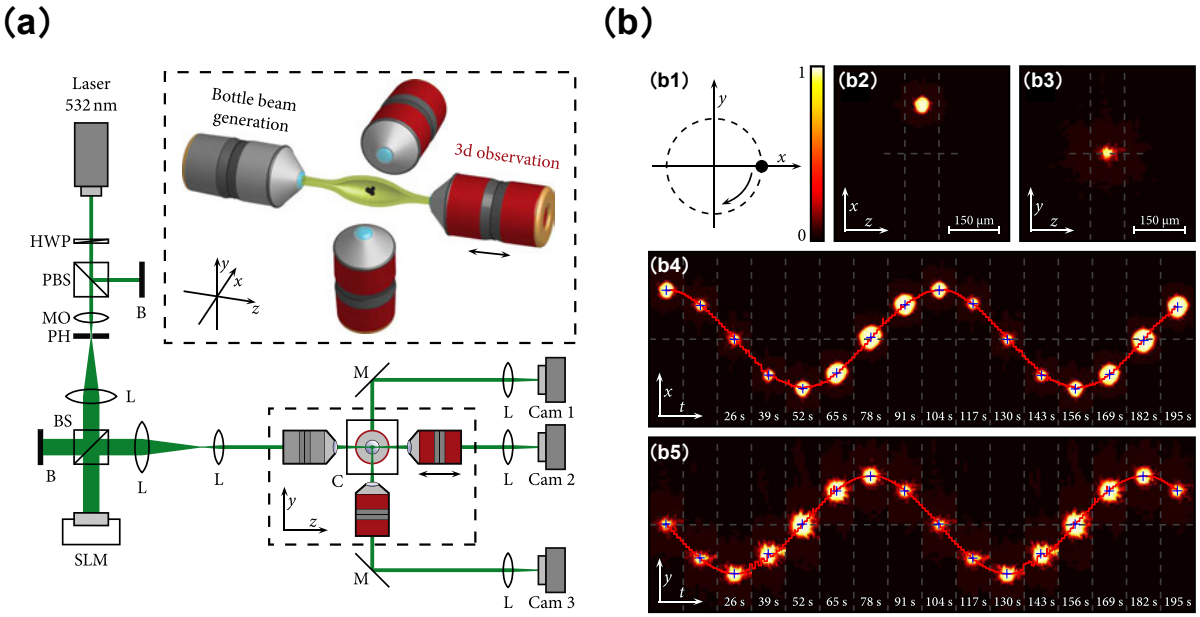

Figure 2.10: Holographic aerosol optical trapping and manipulation by using optical bottle beams. (a) The schematic diagram of the holographic optical tweezers setup was developed by Alpmann et al. in 2012. HWP: Half-wave plate; PBS: Polarrizing beam splitter; MO: Microscope objective; PH: Pinhole; L: Lens; BS: Beam splitter; B: Beam block; SLM: Spatial light modulator; C: Cuvette. (b) Trapped particle dynamics in 3D. (b1) Schematic diagram of the transverse circular motion of a trapped particle. (b2) and (b3) show the initial position of the trapped particle in xz plane and yz plane. (b4) and (b5) shown the trajectory of the particle along the x axis and y axis receptively as the function of time t. Images adapted from [1].

but the behavior of trapped droplets was more complex due to the higher laser modes carried by MMFs, making the trapping sites and a number of trapped droplets difficult to predict compared to the trapping situation with SMFs [134]. Subsequently, Li et al. successfully trapped solid particles in air using a CP dual SMFs trap in 2018, and they also verified that the trapped borosilicate spheres would change from stable trapping to exhibiting three different spatial motion trajectories when the dual fibers had different radial misalignment [90], as shown in Figure 2.11(c).

2.3 Aerosol optical trapping considerations

In this section, I will focus on the aerosol optical trapping considerations involved in the construction of optical aerosol traps, as these factors will affect the success of the optical aerosol traps and the stability of the trapping performance. Specifically, I will first introduce the methods of loading aerosol particles in different states and point out

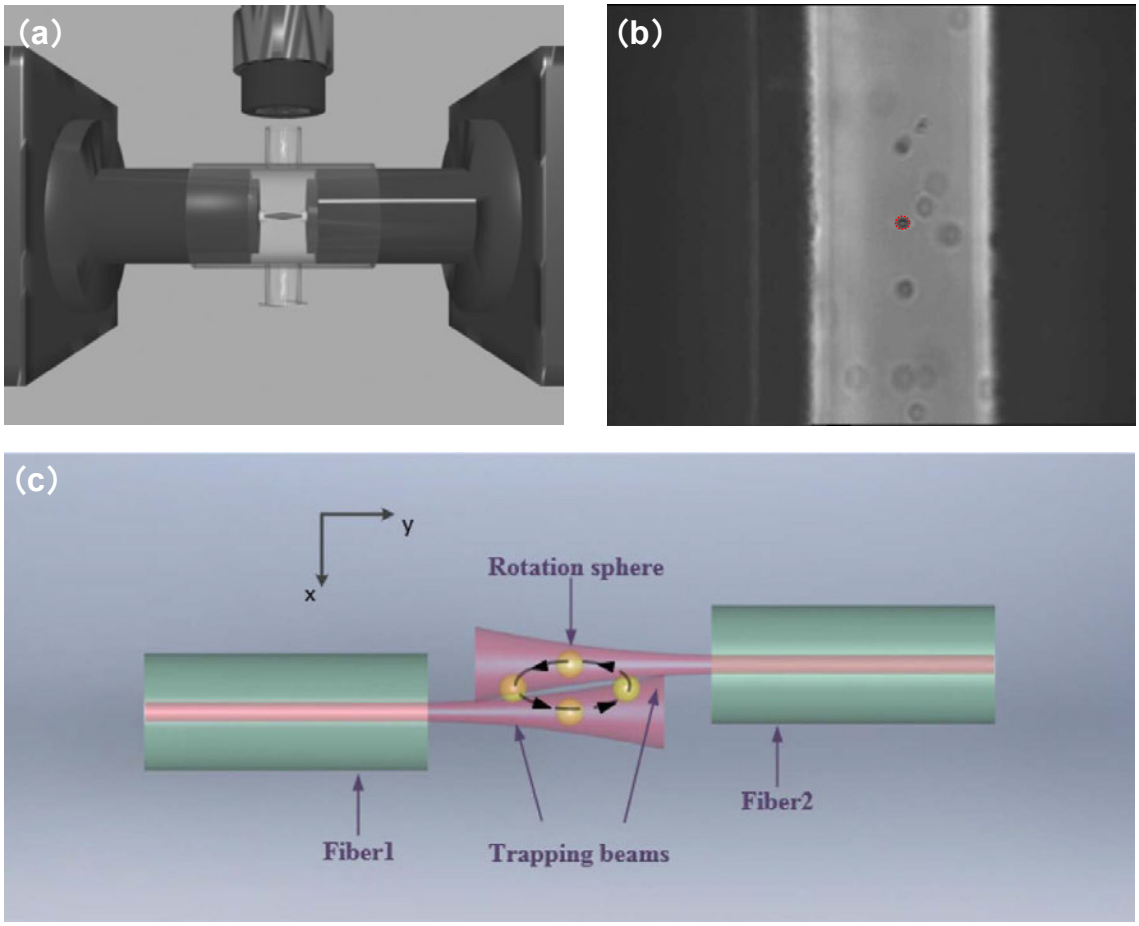

Figure 2.11: Fiber-based aerosol trapping and manipulations. (a) The schematic diagram of the CP dual fiber traps to capture aerosols in air was developed by Rudd et al in 2008. (b) Trapped single droplet marked with the red circle in the midpoint of two CP SMFs. (c) The schematic diagram of the orbit rotation of the single borosilicate microsphere under the CP dual fiber traps with radial misalignment. Images adapted from [90, 102, 134].

their respective characteristics. I will then describe several different aerosol trapping chambers and explain their design and use considerations, and finally present the methods used to image and position the trapped aerosol particles, which are important for resolving the size of the trapped aerosols and characterizing trap performance.

2.3.1 Aerosol loading method

According to section 2.1.2, we know that the ambient damping force on the particle is positively related to the environmental viscosity coefficient η, where the value for η are 1.8e-5 Pa.s in the case of air, and 8.9e-4 Pa.s for water in 25°C. Therefore, particles immersed in water will be subjected to a strongly overdamped force so that they can

be suspended in a relatively stable position and then trapped by actively moving the trapping laser. In air, however, the η is about two orders of magnitude smaller, which means that the reduced damping force cannot provide sufficient resistance to the particles, while at the same time, due to gravity, the particles fall down quickly. As a result, the development of an efficient, stable, controllable, and reproducible aerosol loading method is important for the successful capture of aerosol particles in air.

2.3.1.1 Solid aerosols

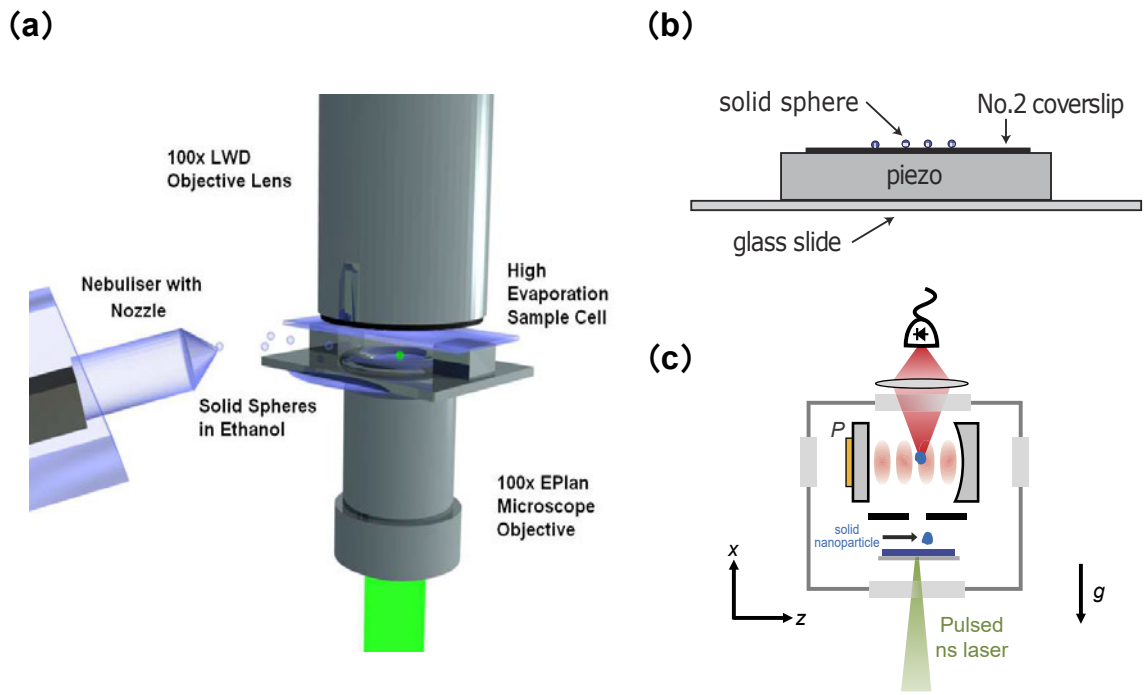

Figure 2.12: Solid aerosol loading method. (a) Nebulizer approach. Summer et al. used a commercial medical nebulizer to spray ethanol solution suspended with solid silica spheres into the trapping chamber to achieve an optical trap in air. (b) Piezo approach. By controlling the vibrations frequency of the piezo to achieve the launching of the solid aerosol particles. (c) Pulsed laser approach. Asenbaum et al. used a frequency-doubled pulse 532nm laser to launch the solid silicon nanoparticles into the trapping field by pulsed laser approach. Images adapted from [6, 87, 149].

As we mentioned before, loading aerosol particles into an optical trap is a key first step in airborne trapping. For loading the solid aerosol particles, there are three main loading methods, namely, the nebulizer approach [62, 147, 149], the piezo approach [9, 87, 88, 126, 168], and the pulsed laser approach [58, 59, 61], as shown in Fig. 2.12. Nebulizer approach is widely used for airborne particle loading because it is simple, effec-

tive, easy to handle, and can load small-size solid aerosols (less than 2μm). As illustrated in Fig. 2.12(a), Summer et al. used a commercial medical nebulizer to spray ethanol solution suspended with a certain concentration of solid silica spheres into the trapping chamber. After evaporation of the ethanol solution, the solid silica spheres falling into the optical trap will be successfully captured in air [147]. In addition, Gieseler et al. also used this approach for loading the solid nanoparticles, resulting in the capture of solid silica beads with a diameter of 147nm [62]. However, when using this method, loading is a random spray-in process, so trapping is less efficient and less controllable. In addition, the size of solid airborne particles that can be loaded is limited by the space between the piezoelectric body and the mesh, so the launching of larger solid particles is not easily achieved.

Another commonly used method for loading solid aerosol particles is the piezo approach, as shown in Fig. 2.12(b), which uses controlled high-frequency vibrations of the piezo to cause the solid particles attached to the substrate surface to gain sufficient acceleration to overcome van der Waals forces, gravity, and surface forces and to be launched into the trapping field, thereby achieving stable optical capture in air. In contrast to the nebulizer approach, the piezo approach allows for actively controlled repetitive loading of solid aerosol particles of the same size, which has been well demonstrated for the micron-size solid particles, due to the ability to select the upper size limit of the emitted solid particles by controlling the vibration frequency of the piezo [9, 87, 118, 168]. However, for solid nanoparticles, the pizeo approach is not very effective and is usually loaded using the nebulizer approach. This is mainly due to the fact that for the maximum acceleration that a piezo can provide, there is a minimum solid particle size that can be jittered off. The smallest particle diameter that can currently be launched by piezo approach is 300nm [13].

To overcome the limitations of the piezo approach in loading solid nanoparticles, the pulsed laser approach has been proposed to generate an additional transient shock wave on the substrate, so that the solid particles can be released from the substrate with sufficient transient acceleration to be launched into the trapping field. In 2013, Asenbaum et al. applied this approach and achieved the launching of silicon nanoparticles by using a 532nm Nd:YAG laser with a 5ns pulse of 3mJ at a frequency-doubled pulse [6], as shown in Fig. 2.12(c). Subsequently, Fu et al. also gave the optimized pulsed laser parameters (pulse duration, pulse beam waist size, vertical distribution of the beam

waist), as well as the suggested initial positions of the particles by numerical analysis for better application of the pulsed laser approach to the actual launching of the particles under the CP dual fiber trap in air [58].

2.3.1.2 Liquid aerosols

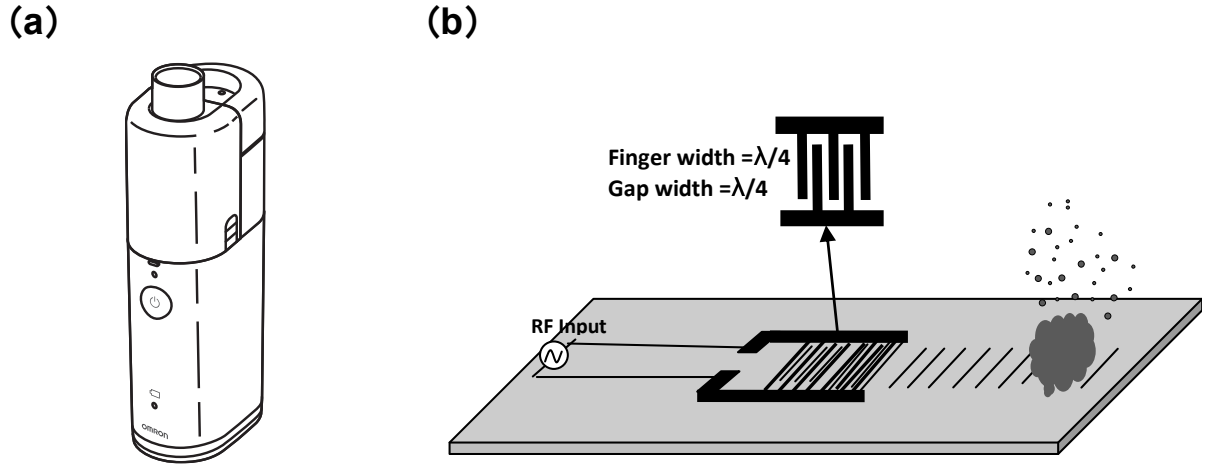

Figure 2.13: Liquid aerosol loading method. (a) Commercial medical nebulizer. (b) Surface acoustic wave nebulization. Images adapted from [2, 3, 149].

When loading liquid aerosol particles, as opposed to their solid counterparts which offer more diverse approaches, the predominant technique employed is the nebulizer method, as extensively referenced [2, 3, 25, 26, 45, 49, 50, 74, 134, 148, 149]. The core concept underlying this approach revolves around transforming solid particles into a dissolved state within a readily volatile solvent, such as alcohol. Subsequently, the dissolved solid particles undergo ultrasonication in a solution, effectively dispersing the particles within the liquid medium. This ultrasonicated solution is then introduced into the nebulizer's solution chamber. The final step entails injecting the sonicated solvent into the nebulizer's solution chamber, culminating in the comprehensive pre-injection preparation. As shown in Fig. 2.13(a), the simplest loading method is to use a commercial medical nebulizer to launch droplets directly into the trapping field. However, such commercial medical nebulizers typically produce only a small size range of liquid aerosol particles (usually between 2μm and 10μm in diameter with a mass median aerodynamic diameter of 4.5μm) and the size of the liquid aerosol falling into the trapping field is random [113]. When we try to capture larger size liquid aerosol particles, we can continuously inject atomized liquid aerosols into the trapping field to increase the ambient humidity so that the trapped small size droplet can grow to the target large size.

However, since the continuous spraying process generates a large amount of atomized liquid aerosols, it will distort the optical trapping field and also contaminate the trapping chamber and optics, thus leading to the failure of the experiment. Subsequently, Anand et al. proposed a device called surface acoustic wave nebulization (SAWN), as shown in Fig. 2.13(b), which enables the selection of the generated droplet size by tuning the RF frequency. By using SAWN, it not only allows the loading of liquid aerosols with a more controlled selection of droplet size, but it also makes the loading compact and versatile for more types of chemicals [2, 3]. This approach shows good advantages for loading very small sized liquid aerosols, but is not so effective for producing and launching large size droplets.

To this end, one can achieve large size droplet capture by growing droplets [99], but it involves designing and engineering a suitable aerosol trapping chamber to control environmental conditions such as temperature, humidity and atmospheric pressure. In the next section, I will introduce the efforts of researchers in developing aerosol trapping chambers.

2.3.2 Aerosol trapping chamber

As we mentioned in the last section, another critical step for the successful optical trapping of airborne particles is the employment of a suitable trapping chamber. Due to the different types of aerosol particles, the consideration of the trapping accuracy and efficiency, and the integration of other measurements, all of these place specific requirements on the arrangement of the mechanical structure and volume of the trapping chamber, as well as on the control of the environmental conditions (including temperature, humidity, and atmospheric pressure) inside the chamber from a design and engineering perspective [25, 26, 46, 48, 49, 55, 127, 147, 149].

In 2006, Burnham et al. proposed the use of a sealed glass cube above a glass cover slip as the aerosol trapping chamber to facilitate water droplet trapping experiments. By connecting the commercial medical nebulizer with a custom-designed glassware, the generated water droplets can be delivered into the trapping chamber accurately. Although this trapping chamber is simple in structure and can meet the demand for trapping water droplets in air, the lack of precise control of ambient factors in the chamber, especially humidity control, limits the success and trapping efficiency of capturing liquid aerosol particles, for which Burnham et al. placed a distilled water-soaked tissue to

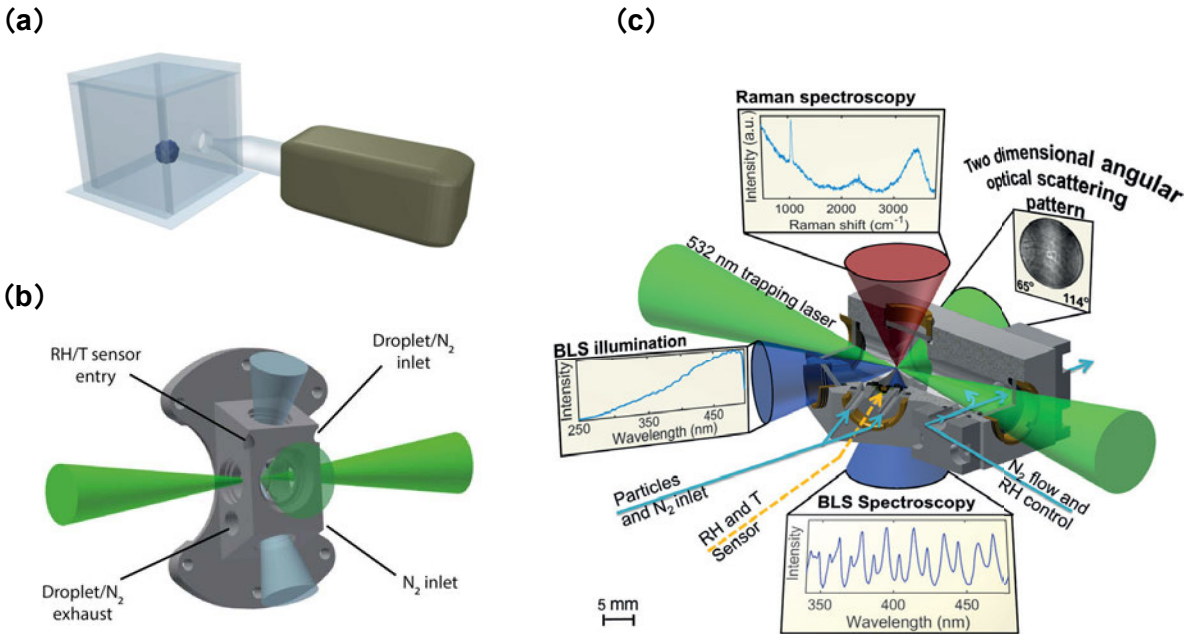

Figure 2.14: Aerosol trapping chambers. (a) A sealed glass cube was used as an aerosol trapping chamber by Burnham et al. in 2006, which had no humidity control and instead used distilled water-soaked tissue to roughly maintain a moist environment. (b) A humidity well-controlled aerosol trapping chamber developed by Reich et al.(c) A more versatile and compact aerosol trapping chamber developed by Esat et al. with precise humidity control and three integrated measurement techniques. T: Temperature; RH: Relative Humidity. Images adapted from [26, 55, 127].

roughly maintain a moist environment, allowing limited improvement of this deficiency [25]. Subsequently, the Aerosol and Nanoscience Group from ETH Zurich, led by Prof. Ruth Signorell, proposed and engineered more sophisticated and precisely controlled aerosol trapping chambers to facilitate their research on aerosols [46, 48, 49, 55, 127]. As illustrated in Fig. 2.14(b), Reich et al. used an elaborate trapping chamber to facilitate the trapping of picogram aerosol droplets. The humidity can be well controlled by mixing dry and wet nitrogen gas separately through independent air inlets. In addition, the well-designed structure allows the chamber to have suitable apertures to deliver the trapping laser and to collect scattered light and broadband light scattering for localization and measurement, respectively [127]. Moreover, Esat et al. designed a more sophisticated aerosol trapping chamber, as shown in Fig. 2.14(c), that not only maintains the functionality of the trapping chamber proposed by Reich et al. by providing a controlled trapping environment, but in addition, it integrates a 2D angular optical scattering and Raman spectroscopy that allows for a richer characterization of the

trapped aerosol particles [55].

2.3.3 Aerosol displacement measurement

Another key consideration for aerosol trapping is about accurate positioning and displacement measurement of trapped aerosol particles, as this will quantitatively characterize the trapping performance of the aerosol trap by calculating the trapping stiffness κ, and also help to resolve the trapping force exerted on the captured aerosol particles. After years of development, the two most commonly used methods for localization and displacement measurement of captured particles in optical traps are video based approach [22, 44, 71, 115] and the position detector based approach [20, 63, 76, 158, 170]. In this section, I will describe how each of them works and point out the advantages and disadvantages of their respective use.

2.3.3.1 Video based approach

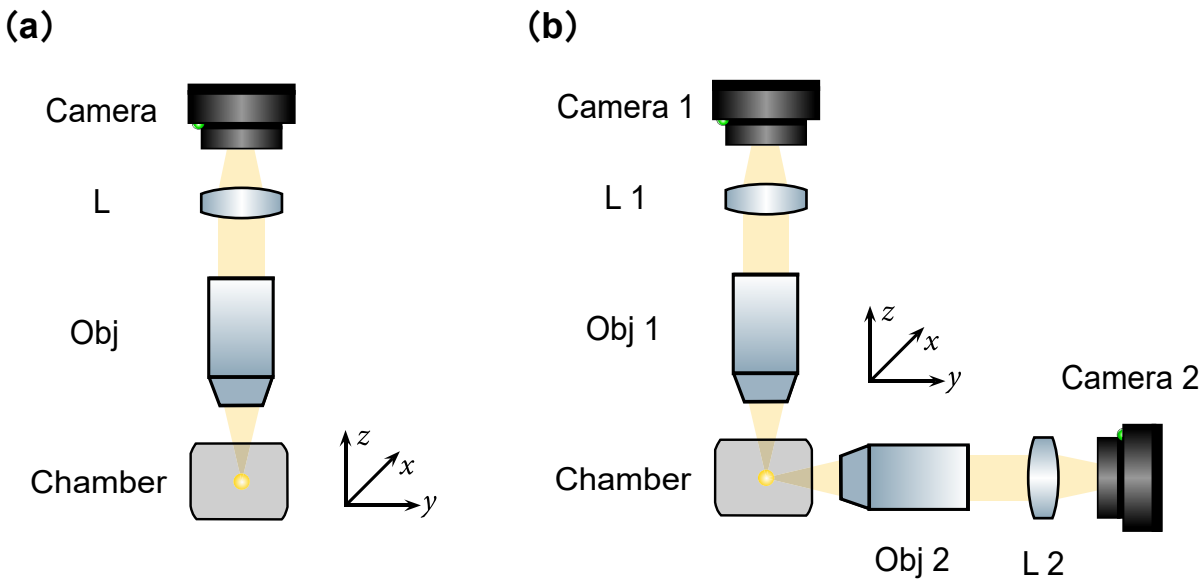

Figure 2.15: Video based approach. (a) The schematic of optical microscope imaging setup for 2D observing and tracking the trapped particle in xy plane. L: lens; Obj: Objectives. (b) 3D tracking of the trapped particle by adding a second path of optical microscope imaging setup to resolve the trapped particle's position along the z axis.

The video based approach to locate and measure the displacement of trapped particles is easy and convenient to operate, which makes most trapping systems usually employ microscopic imaging systems to monitor the trapping process. As shown in Fig.

2.15(a), it is a typical schematic of an optical microscope imaging setup for observing and tracking the trapped particle. The scattered light from the captured aerosol particles is collected by the microscope objective, and then imaged onto the camera after convergence through a tube lens to achieve real-time monitoring of the captured particles, where the filter is used to filter out the trapping laser light. Then, by calibrating the mapping relationships between the actual physical distances represented by the pixels of the video image and combining them with image processing algorithms such as center-of-mass analysis [35], it will enable the real-time tracking of particles captured in the field of view and calculate their displacement magnitudes with nanometer-level precision [114, 115]. In addition, there are also many open-source algorithms and software for video based particle tracking that can be used directly. Of particular note, with the rapid development of artificial intelligence in recent years, the DeepTrack open-source software developed by Prof. Giovanni Volpe's group has made video based particle tracking even easier and more versatile, including single particle tracking and sizing, multi-particle tracking, and 3D tracking [73, 120].

However, the video based approach has two major drawbacks. One is that observing the trapped particle based on a single microscope imaging system, as illustrated in Fig. 2.15(a), can only implement 2D particle positioning and tracking. If one wants to realize 3D tracking of the trapped particle, one option is to add an additional path in the optical microscope imaging setup to resolve the trapped particle's position along the z axis [1], as shown in Fig. 2.15(b). While this will increase the complexity and cost of the whole trapping system and cannot be implemented for those cases only with limited trapping space. An alternative option to estimate the trapped particle's position variation along the z axis is based on the image processing algorithms [21, 73, 120, 173]. The principle of this method is that the difference in axial depth will cause the captured particle image to be out of focus and therefore the brightness of the image will be different, and then based on this difference, the change in the displacement of the particle in the z axis can be estimated. However, this method cannot be as reliable as the first one and suffers from errors caused by the trade-off between the temporal and spatial resolution of the camera, which is also the source of the second major drawback of the video based approach. Specifically, because higher accuracy displacement measurements can only be obtained if a high spatial resolution is realized, this places higher demands on the acquisition frame rate of the camera. But this leads to a reduction in the required exposure time for imaging, which leads to a degradation of the imaging quality due to the

loss of high-frequency information and the introduction of noise. Therefore, for scenarios that require higher accuracy and reliability of displacement measurements, we need to consider the use of alternative measurement methods. One good option is the position detector based approach, which I will introduce in the next section.

2.3.3.2 Position detector based approach

A more popular, highly accurate, and robust method to measure the displacement of trapped particles is the position detector based approach [76, 131, 158]. As the name implies, this method uses a position detector at its core, as it provides subnanometer spatial resolution and kilohertz temporal resolution with higher measurement accuracy and stability.

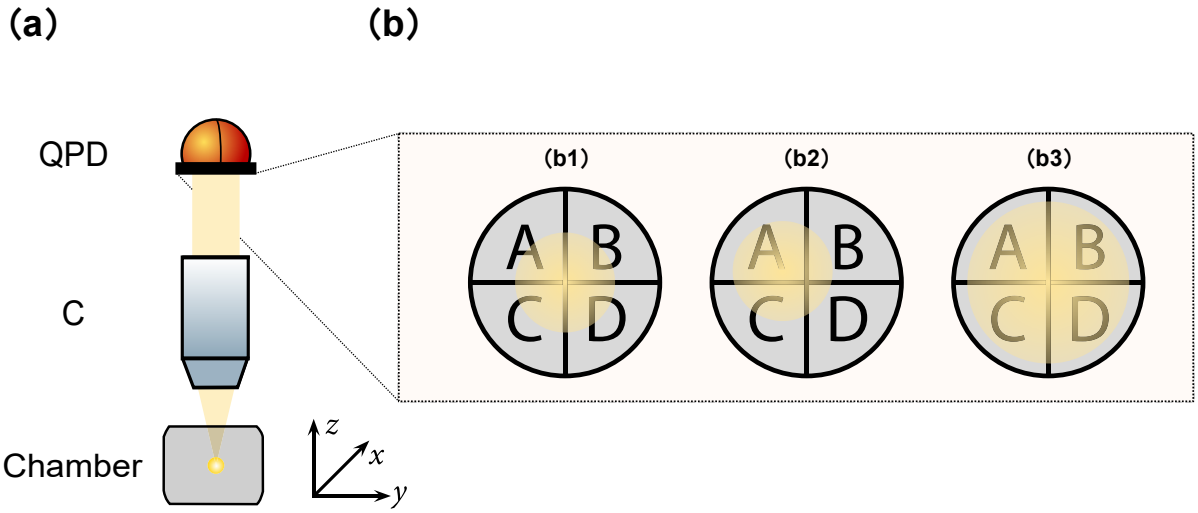

Figure 2.16: Position detector based approach. (a) The schematic of the optical setup for detecting the position shift of the trapped particle by using a QPD. QPD: quadrant photodetector; C: condenser. (b) The zoom-in figures of the three different illuminated QPD surface corresponding to the trapped particle's position shifts. The position information can be resolved by measuring the light intensity difference in four quadrants.

$$V_x = [(V_A + V_C) - (V_B + V_D)]/V_z \tag{2.19}$$

$$V_y = [(V_A + V_B) - (V_C + V_D)]/V_z \tag{2.20}$$

$$V_z = V_A + V_B + V_C + V_D \tag{2.21}$$

Fig. 2.16(a) shows the typical schematic of the optical setup for detecting the position shift of trapped particle by using a quadrant photodetector (QPD), where the scattered light from the captured particle is collected by a condenser and then imaged onto the QPD. As the captured particle moves, the light intensity projected onto the four separate quadrants of the QPD surface changes, as illustrated in Fig. 2.16(b). From Fig. 2.16(b1) to (b2), we can find that the trapped particle moves laterally from the center to the left without axial motion, which is because the entire illuminated area of the QPD surface only moves laterally without any change in the size of the illuminated area. While in Figure 2.16(b1) to (b3), we can know that the trapped particle undergoes axial displacement due to the enlargement of the illumination area of the whole QPD surface, i.e., the particle has changed its position in the z axis direction. Based on this principle, the QPD converts the light intensities collected in the four quadrants into the voltage signals, and then the positions of the trapped particle in the x, y and z directions can be represented by the voltages calculated by Eq. (2.19) to Eq. (2.22). Ultimately, the displacement of the captured particle in 3D space can be known by monitoring the change of the voltage values of V_x, V_y and V_z [158]. Position detector based methods exhibit significant advantages over video based methods in terms of measurement accuracy and reliability, but all of this presupposes careful alignment of the detector and precise calibration to determine the relationship between detector voltage and particle displacement. Therefore, in practice, you only need to choose the displacement measurement approach that meets your experimental needs.

CHAPTER 3

AEROSOL TRAPPING AND MANIPULATION IN AIR

The purpose of this chapter is to describe the methods, development, and implementation related to fiber-based aerosol trapping and manipulation in air. We know that optical trapping and manipulation in air are more challenging than in traditional liquid trapping media. One reason is that the lower viscosity of the suspension medium makes the particles more sensitive to surrounding fluctuations. Another reason is the higher relative refractive index of aerosols in air, resulting in aerosols being (more likely) pushed out of the trapping field due to greater scattering forces [157]. For these reasons, careful consideration and development of aerosol trapping systems is essential for the successful trapping and manipulation of individual aerosols under the CP dual fiber trap. To this end, this chapter will cover some of the key techniques and developments associated with the implementation of aerosol trapping. Specifically, I will first describe how I prepared and generated the aerosol samples for trapping, and then indicate how I designed, engineered, built, and calibrated the trapping system to achieve successful and robust trapping, which I believe is noteworthy and will benefit the readers for future implementation. In addition, I present the results and discoveries during the experiments.

3.1 Generating aerosols for trapping

As we have mentioned in Section 2.3.1, a variety of approaches for different types of aerosol particle loading are provided there. In this thesis, however, we are looking at

liquid aerosol particles. Therefore, in this section, I will detail how we prepared and loaded the liquid aerosol particles for trapping use and indicate how we managed the evaporation of the liquid aerosol particles to facilitate the trapping experiments.

3.1.1 Loading aerosols

To load the liquid aerosol into the trapping chamber, we used a commercial medical nebulizer (OMRON NE-U100-E) with a custom nozzle attached to feed the droplets into the trapping field. Fig. 3.1 shows the schematic diagram of loading aerosols, where the nebulizer uses a vibrating element oscillating at a high frequency to cause the liquid sample to be pushed through the mesh, producing a consistent, constant droplet flow with a median mass aerodynamic diameter of approximately 4.5μm [113]. There are two benefits to using a custom nozzle here. One is the targeted delivery of atomized aerosol particles to the trapping field more precisely, increasing the success rate of capture. The other is that by controlling the nozzle length and outlet aperture design, the airflow velocity delivered to the trapping chamber can be effectively controlled and the droplet size can also be roughly varied, thus increasing the likelihood of capturing large aerosol particles. The nozzles used in the experiment were printed by a 3D printer with custom-designed lengths and diameters.

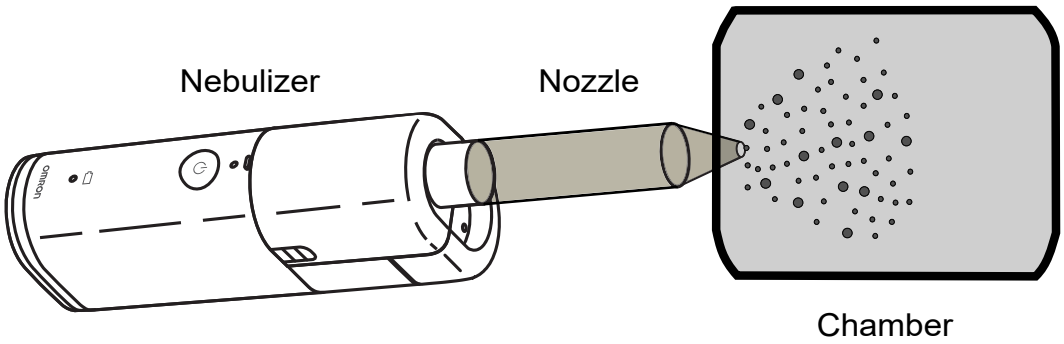

Figure 3.1: Schematic diagram of loading liquid aerosols into the trapping chamber. The commercial medical nebulizer uses a vibrating element oscillating at a high frequency to cause the liquid sample to be pushed through the mesh, producing a consistent, constant droplet flow delivered through a custom-designed 3D-printed nozzle.

3.1.2 Management of liquid aerosols evaporation

Another important issue that we need to consider carefully when generating liquid aerosols for trapping is the management of evaporation of the atomized liquid aerosol particles. One of the key factors determining the evaporation of liquid aerosols is the relative humidity (RH) of the surrounding environment at a certain temperature, which is described in Eq. (3.1) [105].

$$RH = \frac{P_{\text{vapour}}}{P^*_{\text{vapour}}} \times 100\% \tag{3.1}$$

Where P_{vapour} denotes the actual vapor pressure of the liquid, and P^*_{vapour} represents the saturation vapour pressure of the liquid.

According to the Kohler theory [137], for pure water, droplets can only reach equilibrium size at 100% RH or above. This means that to capture pure water droplets, the trapping environment needs to be tightly controlled in terms of RH and temperature to ensure that the trapping field is always supersaturated. However, in our experiments, the homemade trapping chamber does not have precise temperature and humidity control and is not perfectly sealed, so we compensate for this by managing the liquid aerosol evaporation from two aspects. On the one hand, we designed and engineered the trapping chamber to reduce the volume of the trapping chamber as much as possible (the design and working details of the trapping chamber are described in the next section), and to minimize the number and size of exits required for connection to the outside, and to seal these exits well during experiments. In addition, a completely wetted tissue is added to the trapping chamber to coarsely compensate for the vapour lost due to the imperfect sealing, thereby reducing the evaporation rate of the droplets.

On the other hand, we also consider the addition of an inorganic substance to pure water, which reduces the requirement for vapor pressure, i.e., the droplets can remain in equilibrium with the atmosphere for a longer period of time, even in a subsaturated environment. The variation of sea salt particles and pure sodium chloride (NaCl) particles with RH is represented in Fig. 3.2. We can find that as RH decreases from 100%, both sea salt droplets and NaCl droplets gradually lose their mass due to water evaporation, but still maintain stable solutions until RH decreases to 41% and 43%, respectively [154]. Therefore, in our experiments, based on this property of sea salt, we added 50g/L

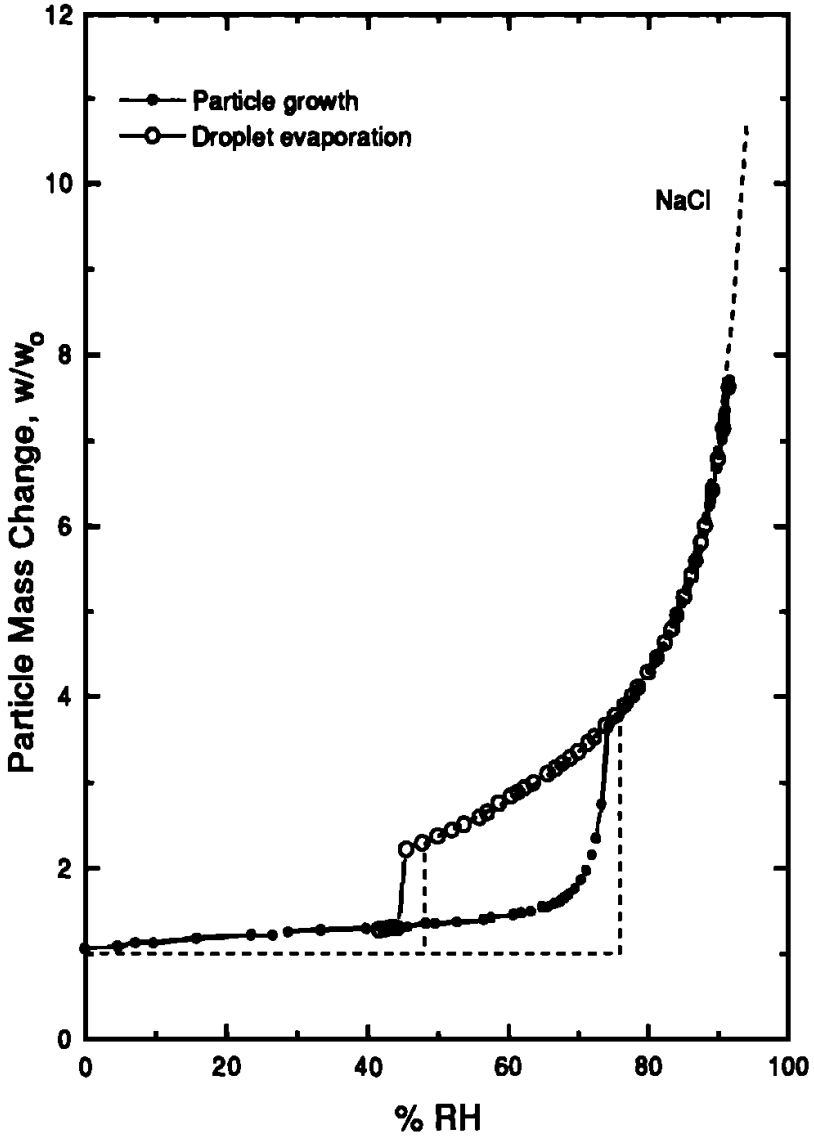

Figure 3.2: The variation of sea salt particles and pure sodium chloride (NaCl) particles with RH. As RH decreases from 100%, both sea salt droplets and NaCl droplets will gradually lose their mass due to evaporation, but remain stable solutions until RH reduces to 41% and 43%, respectively. Image from [154].

of salt to pure water to ensure that the brine droplets could be trapped continuously and stably in a subsaturated trapping environment.

3.2 Aerosols optical trapping system

In this section, I will present the liquid aerosol optical trapping system we developed to trap and manipulate individual liquid aerosol particles. I will first detail how we designed the trapping chamber for capturing aerosol particles and the fiber holder for clamping the fibers, and indicate how they work in the experiment. Then, I will introduce the CP dual fiber trapping optical system built for capturing individual aerosol particles in the experiment. Finally, I will detail the considerations for the calibration of the aerosol trapping system prior to the experiment.

3.2.1 Trapping chamber and fiber holder

As we already mentioned in Section 3.1.2, a well-designed trapping chamber is essential for the successful and stable trapping of individual aerosol particles. This means that we must not only consider the long-term preservation of the atomized aerosol particles in the trapping chamber (i.e., high RH and low airflow disturbance), but also ensure that the normal trapping functions are well implemented (e.g., easy fiber mounting and alignment, accessible image and observation of trapped droplets). Based on these considerations, we customized the trapping chamber for the trapping experiments, as shown in Fig. 3.3. In particular, Fig. 3.3(a) shows a standard three-view of the trapping chamber with design parameters, which corresponds to the 3D view of the designed trapping chamber illustrated in Fig. 3.3(b). We can find that the trapping chamber is a square structure with a side length of 50mm, and circular through-holes with different diameters are designed on each side of the square to facilitate different functions. The ∅40mm circular through-hole shown in Fig. 3.3(a1) has two functions. One is to fit the extra long working distance objective lens used in the experiment from the upper end, thus enabling observation of the captured aerosol particles, while the lower end provides access for illumination. The sides shown in Fig. 3.3(a2) are designed with four ∅6.6mm and one ∅20.2mm circular through-holes respectively. These four circular through-holes are used with the cage assembly rod (∅6mm) so that the trapping chamber can be mounted and aligned with the cage system. The ∅20.2mm circular through-hole is designed to be used with the fiber holder to facilitate the installation and alignment of the dual fibers. In

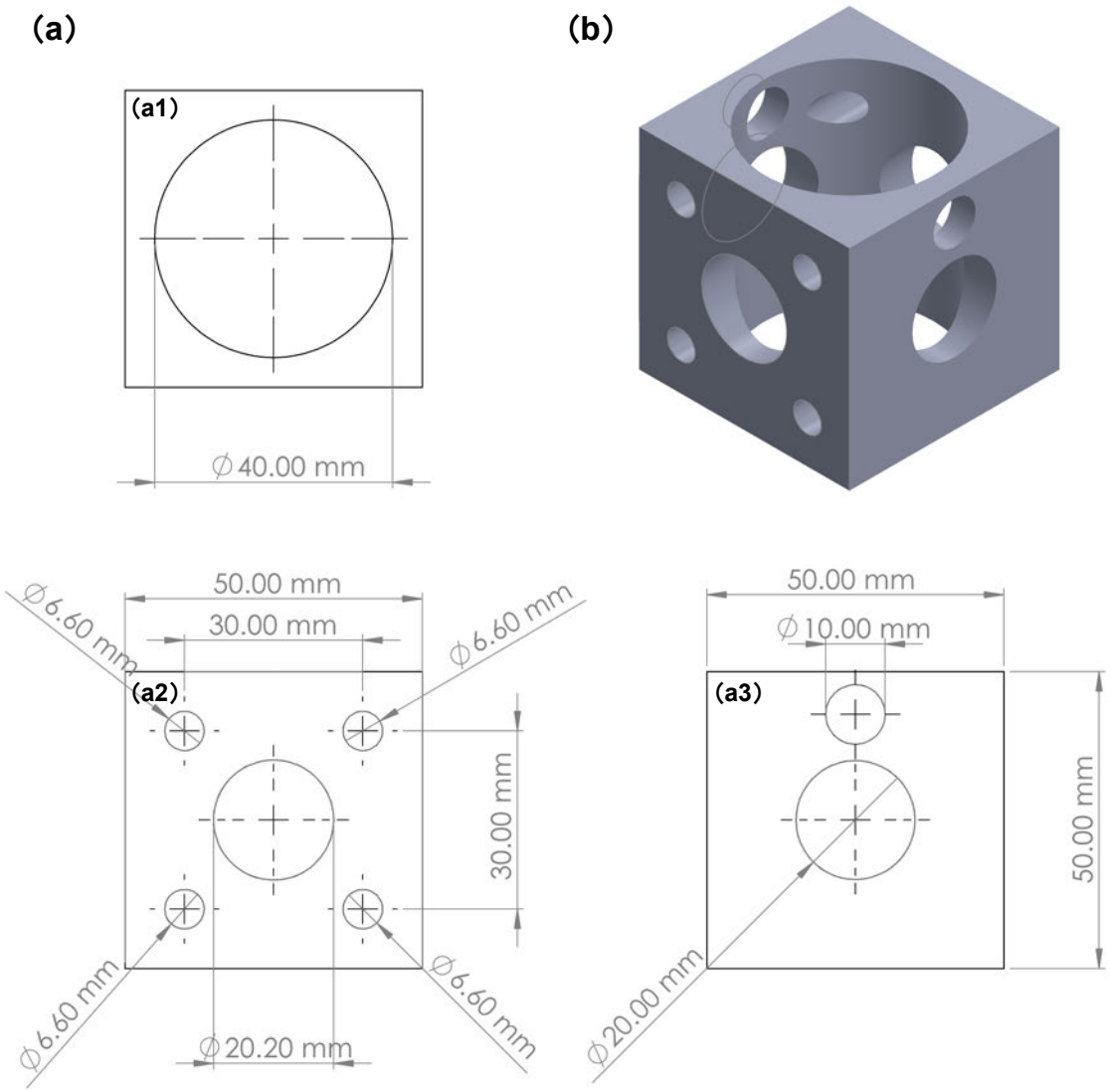

Figure 3.3: Home-made trapping chamber used for capturing single aerosol particle. (a) Standard three-view of the trapping chamber with specific design parameters. (b) 3D view of the designed trapping chamber.

Fig. 3.3(a3), the ∅10mm circular through-hole is connected to the nozzle that feeds the atomized droplets into the chamber. And the ∅20mm circular through-hole below is for directly observing the alignment of the dual fibers during the coarse alignment phase, and will be sealed when the experiment begins.

Since we use the SMF patch cable (Thorlabs P1-460AR-2) to form the CP dual beam traps, we need to engineer a suitable and robust fiber holder to clamp the SMF, so that it can facilitate the installation and alignment of the dual fibers. Fig. 3.4 shows the custom-

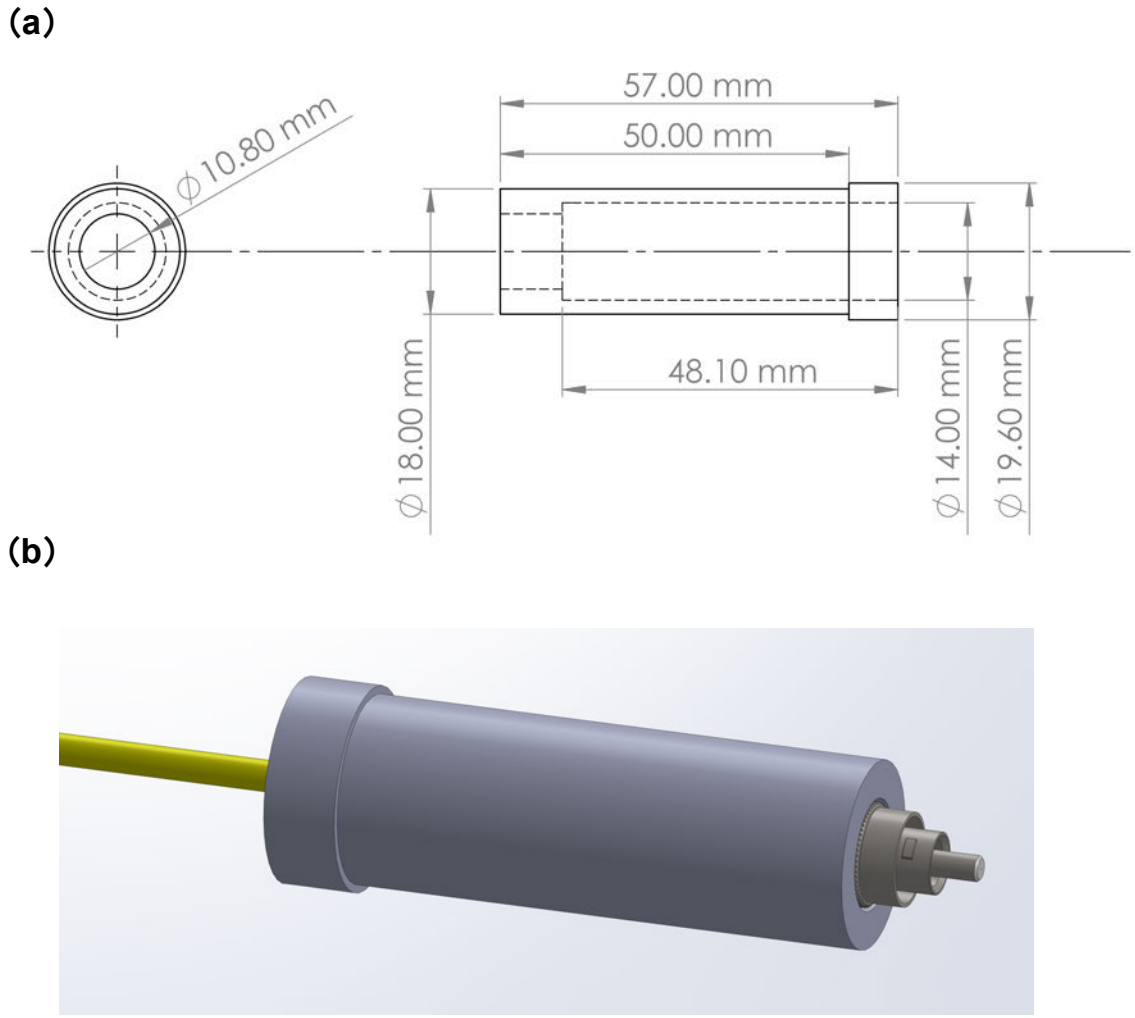

Figure 3.4: The custom-designed fiber holder for clamping the fiber. (a) Diagram of the design parameters of the fiber holder. (b) 3D view of the designed fiber holder clamping the SMF.

designed fiber holder we used for our experiments. Among them, Fig. 3.4(a) shows the specific design parameters of the fiber holder. Notably, the distal end of the fiber holder will be connected to the 3D stage by increasing the size of the fiber holder from ∅18mm to ∅19.6mm to facilitate high precision fiber displacement and dual fiber alignment. At the proximal end of the fiber holder, the bore size is reduced from ∅14mm to ∅10.8mm, so that the SMF can be clamped stably in the fiber holder with an interference fit. In addition, the length of 57mm can compensate for the influence of fiber drift. Fig. 3.4(b) shows the 3D view of the designed fiber holder clamped to the SMF.

3.2.2 Counter-propagating dual fiber trapping setup

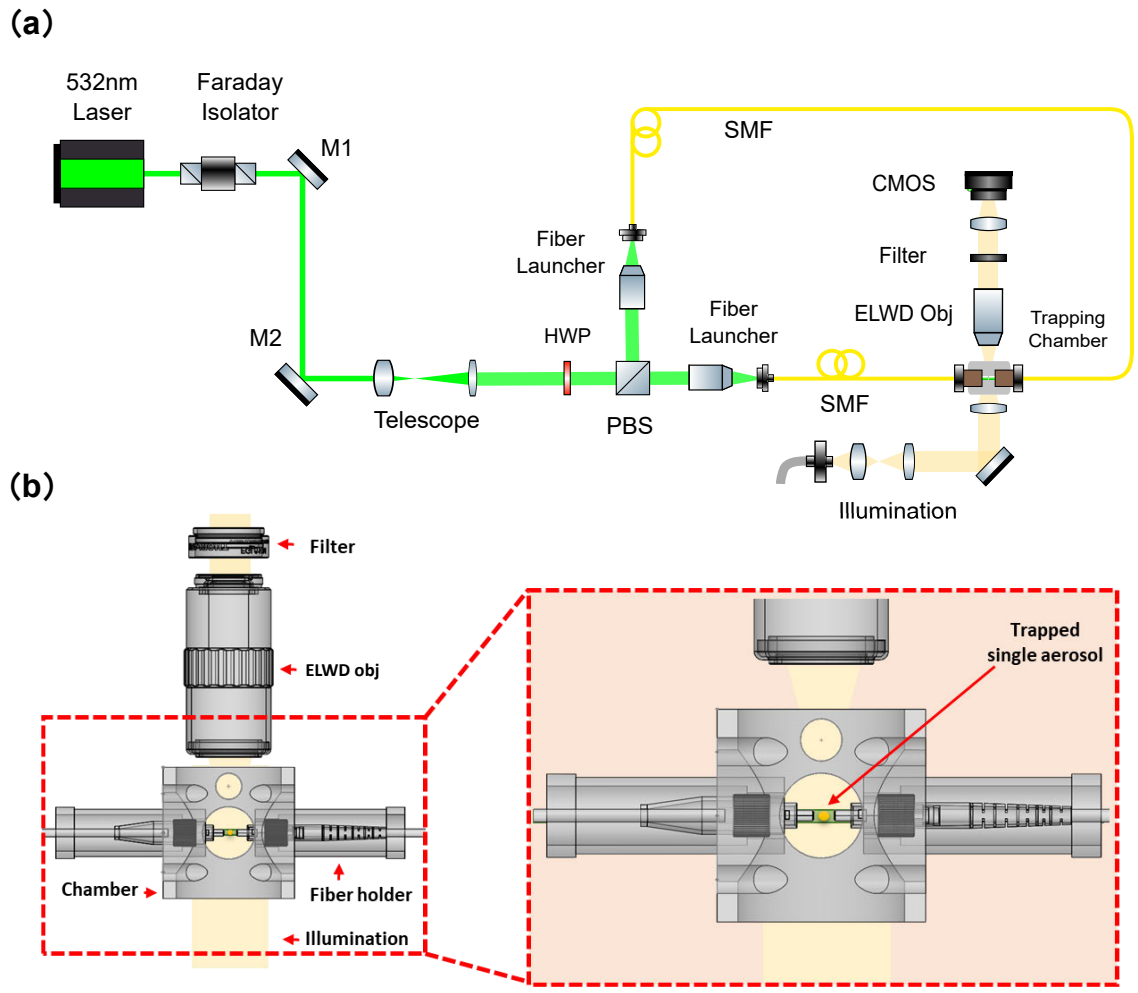

Figure 3.5: (a) Schematic diagram of CP dual fiber aerosol trapping setup. M: mirror; HWP: half-wave plate; PBS: polarizing beam splitter; SMF: single mode fiber; ELWD: extra long working distance. (b) 3D setup of the aerosol trapping area and the zoom-in trapping field.

Our CP dual fiber trapping experimental setup is shown in Fig. 3.5(a). A 532nm laser (Torus, Laser Quantum 891mW) was used for all the experiments. After the laser beam passed through an isolator (Thorlabs IO-3-532-LP), the beam was expanded by a 6X telescope, and then split into two beams by a half waveplate (HWP) and a polarizing beamsplitting (PBS) cube. By rotating the HWP, we can control the distribution of the two beams power. Subsequently, the two beams were launched into SMFs (Thorlabs P1-460AR-2) using two 10X objectives; the fibers had a mode field diameter from 2.8μm to 4.1μm @ 488nm and both were used with straight tip (ST) connectors. Because of

the SMFs small core plus the mechanical drift during the launch phase, the optimized maximum transmission power through the SMFs is around 50%. Finally, two fibers went directly into a custom-designed 3D printed trapping chamber, as shown in Fig. 3.5(b), where a 20X extra long working distance objective lens (Motic ELWD 20X) and a CMOS camera (Basler acA2040-120μm) are used to observe and record the trapped single aerosol particle. Kohler illumination was used to illuminate the captured aerosol particles, and custom-written MATLAB algorithms were used to analyze the acquired videos, and resolve captured particles' size.

3.2.3 System calibration

To achieve the CP dual fiber aerosol trapping, there are several critical aspects before starting the experiment that directly determines the success of the trapping and the stability of the trapped aerosol particles. For this reason, in the following sections, I will introduce how I prepared for the experiment, how I calibrated the system, how I successfully stabilized the trapping of individual aerosol particles, and what I did after completing the experiment.

3.2.3.1 Step 1: Laser coupling and fiber cleaning

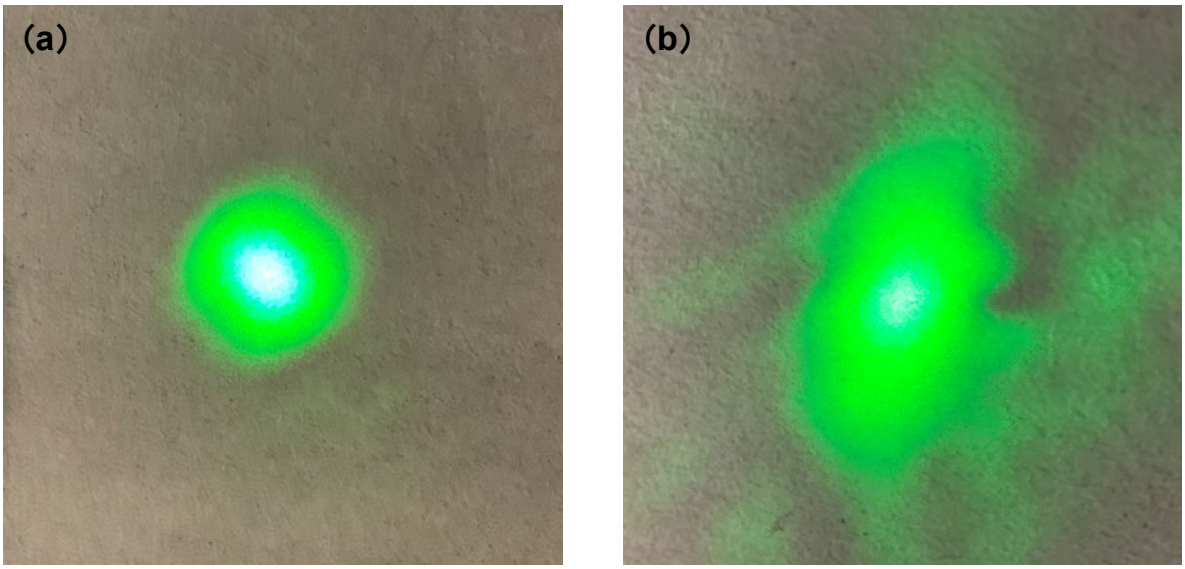

Figure 3.6: (a) Ideal Gaussian beam from the cleaned fiber facet. (b) The distorted beam from the uncleaned fiber facet contaminated by aerosols from previous experiments.

In order to ensure that a single droplet can be stably trapped in the midpoint of the dual fibers, we first need to guarantee that the power output from the dual fibers used in the experiment is the same and stable, which is a necessary condition for a successful experiment. To this end, for our experimental system, as a first step, we let the lasers emit 1mW of power to check whether the transmission efficiency of each fiber is optimal, including ensuring that the laser transmission efficiency of the isolator generally exceeds 85% and that the coupling efficiency of both SMFs reaches about 50%. Then taking into account the laser power transmission losses in other free spaces, the final combined transmission efficiency of the laser power of an SMF is between 17% and 18%. After completing the first step, in the second step, we first thoroughly cleaned the fiber ends of both SMFs to exclude contamination due to aerosols or dust adhering to the fiber ends from previous experiments, which can eliminate distortions in the final outgoing laser beam as shown in Fig. 3.6(b), and thus lead to instability or failure of the trapping. Fig. 3.6(a) shows the ideal Gaussian beam from a cleaned SMF.

After finishing the cleaning, we match the output power of the two SMFs by rotating the HWP and use a power meter to measure and observe that the power does not change significantly within 3 minutes before starting the experiment. It is worth noting that after each experiment, we need to clean the fiber end thoroughly and re-align the fibers. After completing the above steps, we can ensure that the output laser power from the dual fibers we use for trapping is the same and stable, and that the two outgoing beam profiles are ideal as a Gaussian beam.

3.2.3.2 Step 2: Alignment of two SMFs

After the coupling of the laser and the cleaning of the fiber ends, the next critical aspect is the precise alignment of the dual fibers, which directly determines whether the CP dual fiber traps can be successfully constructed to achieve stable trapping of single aerosol particles. In the first step, we first clamped the two SMFs into the specially designed and 3D printed fiber holder, and then mounted the fiber holder onto a high-precision 3D stage to perform a coarse alignment of the dual fibers by manual mechanical adjustment as shown in Fig. 3.7(a). It is worth noting that the dual fibers clamped by the fiber holder can effectively overcome the angular misalignment of the dual fibers, so we only need to reduce the positional misalignment of the dual fibers during the actual dual fiber alignment. Subsequently, the projection image of the dual fiber on CMOS is observed by the ultra-long working distance microscope imaging system to ensure that the top of the

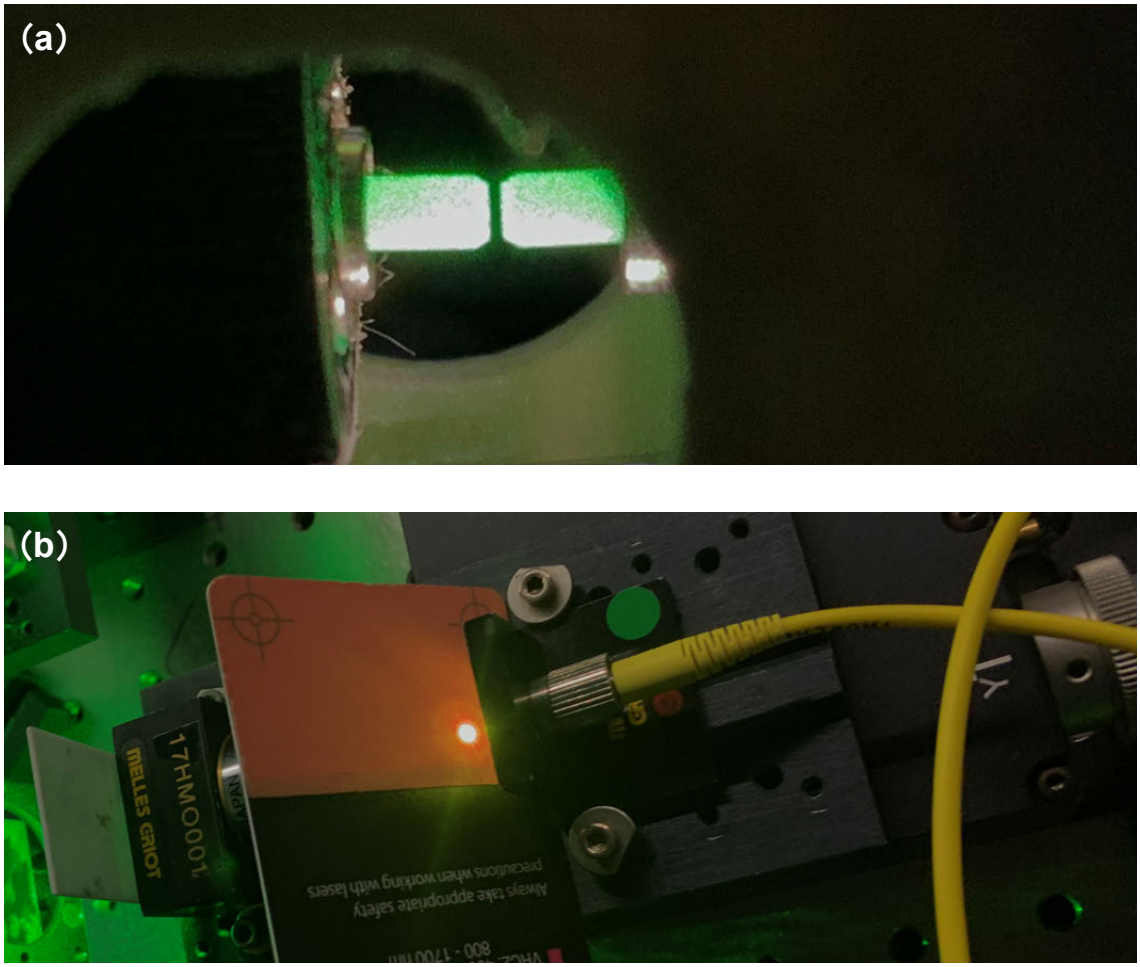

Figure 3.7: (a) Coarse alignment of the two fibers held in the fiber holder by manual mechanical adjustment. (b) Precise alignment of the two fibers by adjusting the 3D stage carrying one of the SMFs and using the intensity of the light emitted from the other end of the SMF as a criterion for the best two fiber alignment.

focused dual fiber can be seen within the imaging field of view, and the spacing of the dual fiber is controlled by adjusting the 3D stage to prepare for the next step of precise alignment.

After the first step of coarse alignment, the second step of precise alignment of the dual fibers is performed by adjusting one of the 3D stages carrying one of the SMF. The intensity of the light emitted from the other end of the SMF is used as a criterion to determine the best dual fiber precision alignment. As shown in Fig. 3.7(b), when the x and y directions of the 3D stage are adjusted to obtain the maximum light intensity at the other end of the SMF at a determined dual fiber spacing, the two fibers can be

considered to be well-aligned. While it is worth noting that when the spacing of the two fibers changes, we have to execute precise alignment again.

3.2.3.3 Step 3: Find core position and trap single droplet

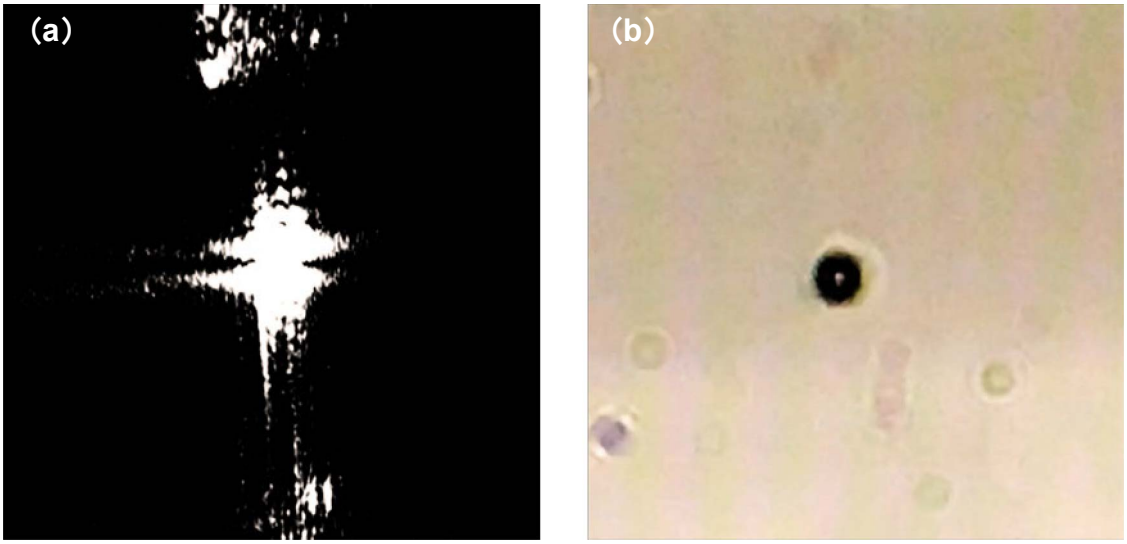

Figure 3.8: (a) Scattered image of a trapped single droplet after system calibration. (b) The focused individual droplet particle after filtering the trapping green laser.

After completing the above two steps, we can start to prepare for the single droplet trapping experiment. First, we adjust the laser output power to 20mW for both fibers, and then we use a 50g/L salt solution to prevent rapid droplet evaporation in our custom-designed trapping chamber, which lacks precise RH control [154]. Then we use the ultrasonic nebulizer (OMRON NE-U100-E) connected to the home-made nozzle to deliver droplets into the trapping chamber, which is designed to reduce airflow interference within the trap, maintain relatively high RH during trapping, provide robust delivery of droplet samples, and easy fiber installation and alignment, as well as accessible image and observation of trapped droplet. In addition, to facilitate our finding of the location of the trapped droplet, we removed the filter in the imaging system at the beginning of the experiment to observe the scattered light image of the droplet so that we could quickly find the location of the trapped droplet. Subsequently, by adjusting the 3D stage of the imaging system, we move the position of the trapped droplet to the center of the imaging field of view, as shown in Fig. 3.8(a). Furthermore, by remounting the filter onto the imaging system, we can see the out-of-focus image of the trapped droplet, and then by adjusting the z-direction of the 3D stage of the imaging system, we can see the focused

stable trapped single droplet as shown in Fig. 3.8(b). In addition, by turning the HWP that controls the power of the dual fiber outgoing light, we can achieve displacement control of the trapped single droplet in the optical axis direction, which will be discussed in detail in Section 3.3.3.

3.3 Results and discussions

In this section, I will present the quantitative results and discoveries I found by using the developed CP dual fiber trapping system. Specifically, I will first experimentally quantify the variation in the diameter of the captured droplets at an output power of 20mW for both fibers, while their spacing is 90μm and 180μm, respectively. I then increase dual fiber output power from 20mW to 100mW in steps of 10mW to see how the droplet diameter variations with this change. Finally, I achieved manipulation of a single droplet along the optical axis by varying the output power of the dual fiber.

3.3.1 Trapped single aerosol under different separation

Fig. 3.9 shows the diameters of maximum and minimum droplets that can be captured when the separation distance between the two fibers is 90μm and 180μm, respectively, and the output power of both fibers is always set to 20mW. We can find that the maximum diameter of a single droplet that can be captured increases from 11.0μm to 16.6μm, while the minimum diameter of a single droplet that can be captured changes only slightly from 4.4μm to 5.0μm when other conditions remain the same but the distance between the two fibers increases from 90μm to 180μm. Through this simple experiment, we can find that by changing the spacing of the dual optical fibers, there will be a variation in the size range of the droplets that can be captured. The quantitative study of the effect of the change of the dual fiber spacing on the size range of the captured droplets will help us to determine the appropriate experimental parameters for CP dual fiber traps, which will help us to efficiently and selectively trap individual droplets of the target diameter. The quantitative study will be presented in Chapter 4.

3.3.2 Trapped single aerosol under different trapping power

In addition to varying the separation of the dual fibers, we also wanted to know the effect of varying the trapping power emitted from the dual fibers on the size range of the droplets that could be captured, while holding other conditions constant. For this reason,

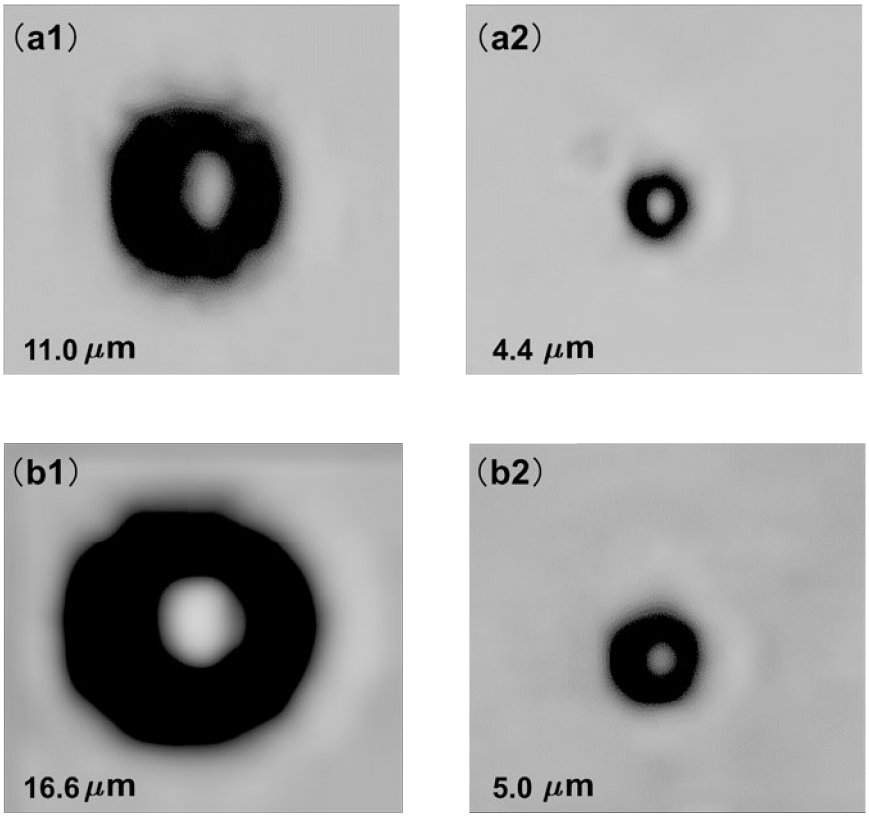

Figure 3.9: Real images of a trapped droplet under CP dual fiber traps with dual fibers' separation of 90μm, and 180μm respectively. The maximum trapped droplet diameter at a separation of 90μm is (a1) of 11.0μm, and the minimum trapped droplet diameter is (a2) of 4.4μm. When only increasing the separation to 180μm, the maximum trapped droplet diameter is (b1) of 16.6μm, and the minimum trapped droplet diameter is (b2) of 5.0μm. Trapping power is 20mW, and saltwater concentration is 50g/L.

we increase dual fiber output power from 20mW to 100mW in steps of 10mW to see how the droplet diameter varies at dual fibers' separation of 90μm and 180μm respectively.

As shown in Fig. 3.10, with increasing the trapping power, the diameters of the smallest droplets that can be trapped at the dual fiber separation of 90μm and 180μm both fluctuate slightly around 5.0μm, and do not increase or decrease significantly with increasing dual fibers' emitting power. While for the maximum trapped droplet, the diameter of the maximum captured droplet fluctuates around 11.0μm when the dual fiber spacing is set to 90μm. However, when the dual fiber spacing is increased to 180μm,

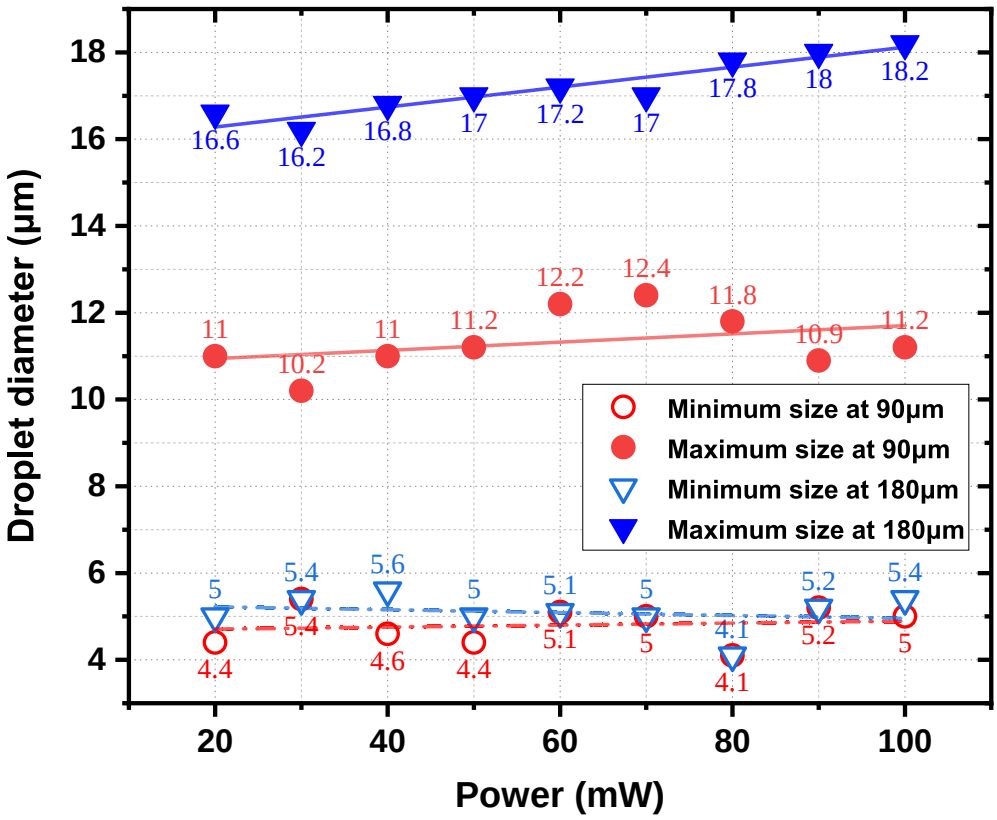

Figure 3.10: Plot of the maximum and minimum diameters of captured droplets with the trapping power increasing from 20mW to 100mW at dual fibers' separation of 90μm and 180μm respectively. Saltwater concentration is 50g/L. The solid and dashed lines are linear fits of the discrete data for the diameters of the maximum and minimum droplets that can be trapped for the corresponding trapping power and different dual fiber separations, respectively. The smallest trapped droplet diameter varies slightly around 5.0μm as the trapping power increases. For the maximum captured droplet diameter, it fluctuates around 11.0μm when the dual fiber spacing is 90μm. However, when increasing the dual fiber separation to 180μm, larger droplet diameters can be trapped, and the maximum trapped droplet diameter increases with increasing trapping power.

larger diameter droplets can be trapped and the size range of the trapped droplets increases with increasing trapping power. The above analysis implies that increasing the output power of the dual fiber does not have a significant effect on the minimum value of the trapped droplet diameter, while the maximum value of the captured droplet diameter is also related to the dual fibers' separation. At a smaller separation distance, the maximum diameter of the trapped droplet does not change significantly with increasing trapping power, while at larger dual fiber spacing, the maximum diameter of the trapped droplet will increase gradually with increasing dual fibers' output power. Therefore, to quantitatively quantify the size range of droplets that can be captured in the CP dual fiber traps, we need to collaboratively consider the relative relationship between the output power and the separation distance of dual optical fibers so that we can efficiently and selectively capture individual droplets of the target size with optimized experimental parameters. Detailed findings and results will be further discussed in Chapter 4 as well.

3.3.3 Single aerosol manipulation along the optical axis

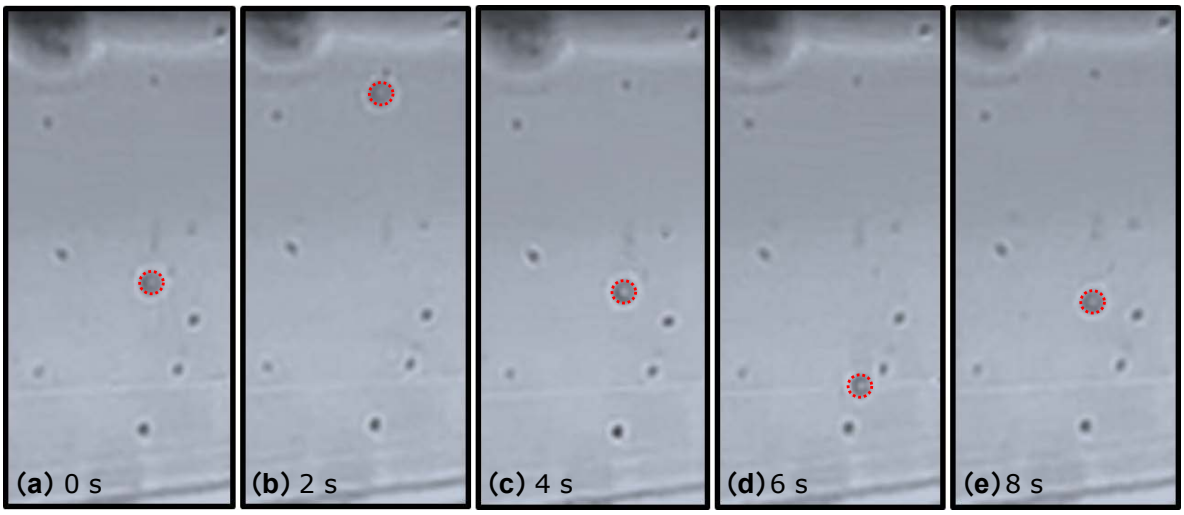

Figure 3.11: Trapped single droplet with a diameter of 10μm moves along the trapping beam axis by tuning the output power of the two fibers. The separation of dual fiber is 180μm, and saltwater concentration is 50g/L.

In addition to achieving stable trapping of single droplets, we also achieve controlled manipulation of an individual droplet along the optical axis by varying the outgoing power of the dual optical fibers. As shown in Fig. 3.11(a), a single droplet with a diameter

of 10μm is stably confined at the midpoint of the dual optical fibers at the separation of 180μm and the emitting power of 50mW for both fibers. By rotating the HWP, we can control the power distribution of the two trapping arms, so that the captured single droplet will leave the initial equilibrium position (midpoint of the dual optical fibers) and move along the optical axis of the trapping beam, which is well demonstrated from the Fig. 3.11(b) to Fig. 3.11(e). Furthermore, we note that the captured individual droplet does not escape the traps due to the change in the output power of the two trapping arms. Instead, the trapped droplet moves predictably as new equilibrium positions are formed, and the moving speeding can reach up to 40μm/s under such trapping conditions.

3.4 Conclusion

In this chapter, we systematically describe the strategies, development, and implementation related to the successful trapping and manipulation of individual aerosol particles based on the CP dual fiber traps. The loading method of the liquid aerosol sample we used in the experiment and the strategy to manage its evaporation was first described, and a salt solution with a concentration of 50g/L was finally chosen as the sample to be used. Next, the key technical details of the CP dual fiber trapping system used to capture and manipulate individual aerosol particles are pointed out by detailing the design, construction, and calibration of the experimental system. Finally, quantitative results of the trapped droplet diameters at different dual fibers' separation distances and trapping powers are shown. In addition, we also demonstrated the manipulation of a single droplet along the optical axis by varying the output power of the dual fibers.

CHAPTER 4

TRAPPED AEROSOL SIZES WITHIN THE TRAPPING FIELD

Quantifying the size range of aerosols that can be trapped in the CP dual fiber tapping configuration is essential to improve the 3D aerosol trapping efficiency and study the manipulation and characterization of single aerosol particles in such traps. Here, we present simulations and experiments describing the trapped aerosol size range variations in the midpoint of two fibers under different fiber separations, particle sizes, fiber powers, and radial offset. By doing so, we build the size area plot for stable aerosol trapping through a parameter analysis that allows the tolerance of such trap to trapping fluctuations to be understood.

4.1 Introduction

Since Arthur Ashkin's pioneering work using lasers to exhibit the optical trapping and manipulation of microscopic particles [7], this method has been applied to various fields within the scientific community, including single-molecule biophysics [18, 27], cell biology [36, 111], laser cooling [4, 41], nanostructures [98, 138] and aerosol science [47, 79, 127]. Optical trapping lends itself well to precision single particle studies across disciplinary areas and the analysis of airborne particles has developed significantly in recent years [64–66, 119, 125, 127]. Aerosols, microscopic solid and liquid particles dispersed in gas as illustrated in Fig. 4.1 showing some of the scanning electron microscopes (SEM) images of common aerosol particles, play a significant role in a range of areas of topical interest, such as atmospheric chemistry and human health, but many processes at the single

aerosol level are still not yet fully understood.

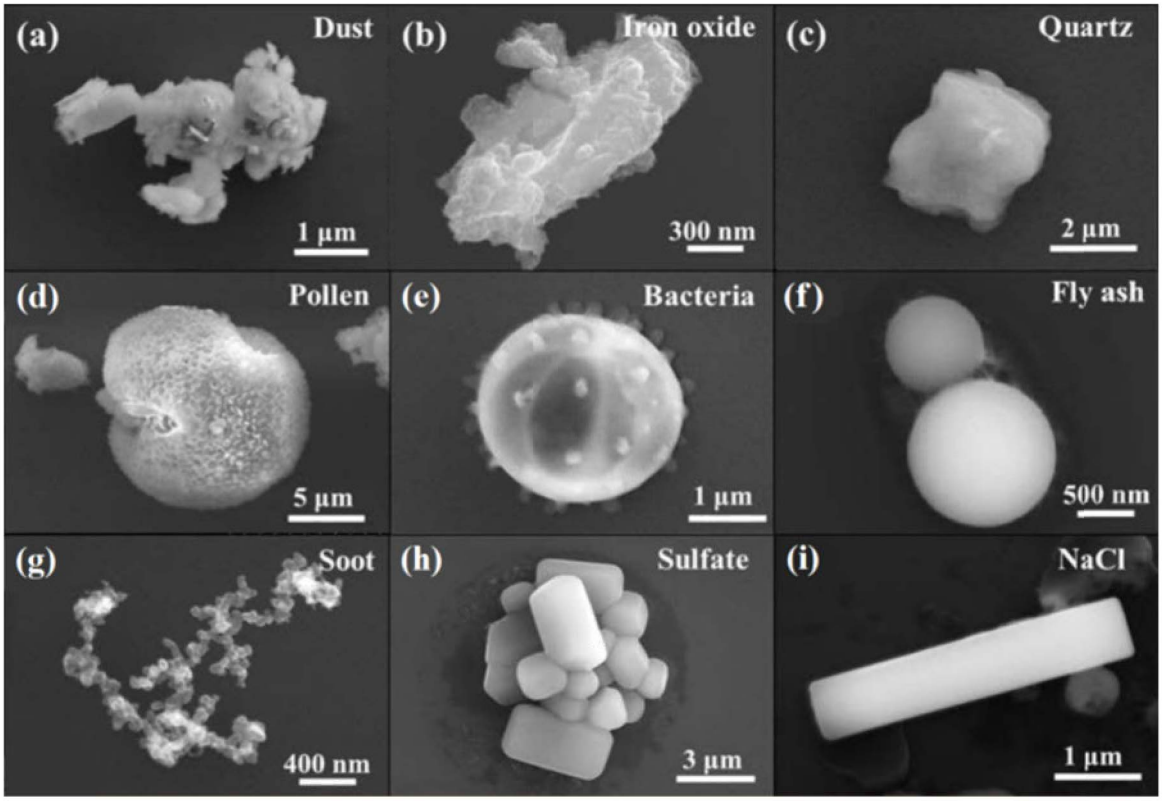

Figure 4.1: Collage of SEM images of common aerosol particles with (a) dust, (b) iron oxide, (c) quartz, (d) pollen, (e) bacteria, (f) fly ash, (g) soot, (h) sulfate, and (i) NaCl. Image adapted from [86].

Performing optical trapping and manipulation in air can be tougher compared to conventional liquid trapping media due to two reasons. First, the suspending medium in air has a lower viscosity, making particles more susceptible to surrounding fluctuations. Second, the aerosols in air have a higher relative refractive index, making it more likely for them to be pushed away from the trapping field due to a greater scattering force [157]. To accomplish stable 3D aerosol trapping, it is necessary to balance the scattering and gradient components generated by the light-matter interaction. One method is to use a high NA objective lens to strongly focus the incident beam: optical tweezers [25]. A second method is to use diverging beams, but in a counter-propagating geometry: a counter-propagating dual beam trap [92]. In this case, the trapped aerosol is usually suspended in the middle area of the two beams. A further option makes use of a confocal beam trap, which forms a stable virtual CP beam trap by using a single spherical concave mirror after the single beam trap, thereby reducing the complexity of the second config-

uration [67, 68, 161]. However, the above three types of configuration to achieve a 3D aerosol trap involve relatively complicated optical path design and many conventional optical elements, which can make the whole system cumbersome. In contrast, optical fiber has the advantage of lower complexity, but more powerfully allows greater system integration. In the initial work in this area, researchers have shown the dual fiber configuration could trap a broader range of aerosol particle sizes at the trap center by providing large forces while allowing more flexible optical access to the trapping area [102, 134]. Additionally, they also demonstrated that such systems can be straightforwardly integrated with spectroscopic tools and microfluidic analysis systems to achieve more functional single aerosol particle characterization and analysis [24, 59, 75, 163]. However, while most recent works focus on the manipulation and characterization of single aerosol particles, there has yet to be a quantitative theoretical and experimental analysis that accurately quantifies the trapped aerosol sizes present within the trap under different dual fiber separations and fiber orientations.

In this chapter, a CP dual fiber trap is used to trap and manipulate aerosol particles. We calculate and verify the trapped aerosol size range under different fiber separations and fiber output powers under the condition of well-aligned fibers. Then we demonstrate the variations of the trapped aerosol size range when the dual fibers have a radial offset. We also examine the situation where the particle is not trapped in the middle of the gap between the two fibers, but can be trapped near the fiber facets.

4.2 Model

4.2.1 Dual beam trap for spherical aerosols

In this chapter, the relative ratio of the aerosol size to the wavelength of the trapping light is typically greater than ten. Following [143], we adopt the ray optics model to build up our mathematical model, as illustrated in Fig. 4.2(a), we only draw one ray SB to demonstrate how the ray interacts with the single aerosol particle. Specifically, the ray SB strikes the aerosol surface B, thus generating the force, which can be divided into two components, the scattering force F_s and the gradient force F_g. F_s is parallel to the incoming ray, and F_g is perpendicular to the incoming light. Fig. 4.2(b) shows a single aerosol particle trapped at the midpoint between two fibers, representing the system being modeled. The reason why the single aerosol can be trapped stably

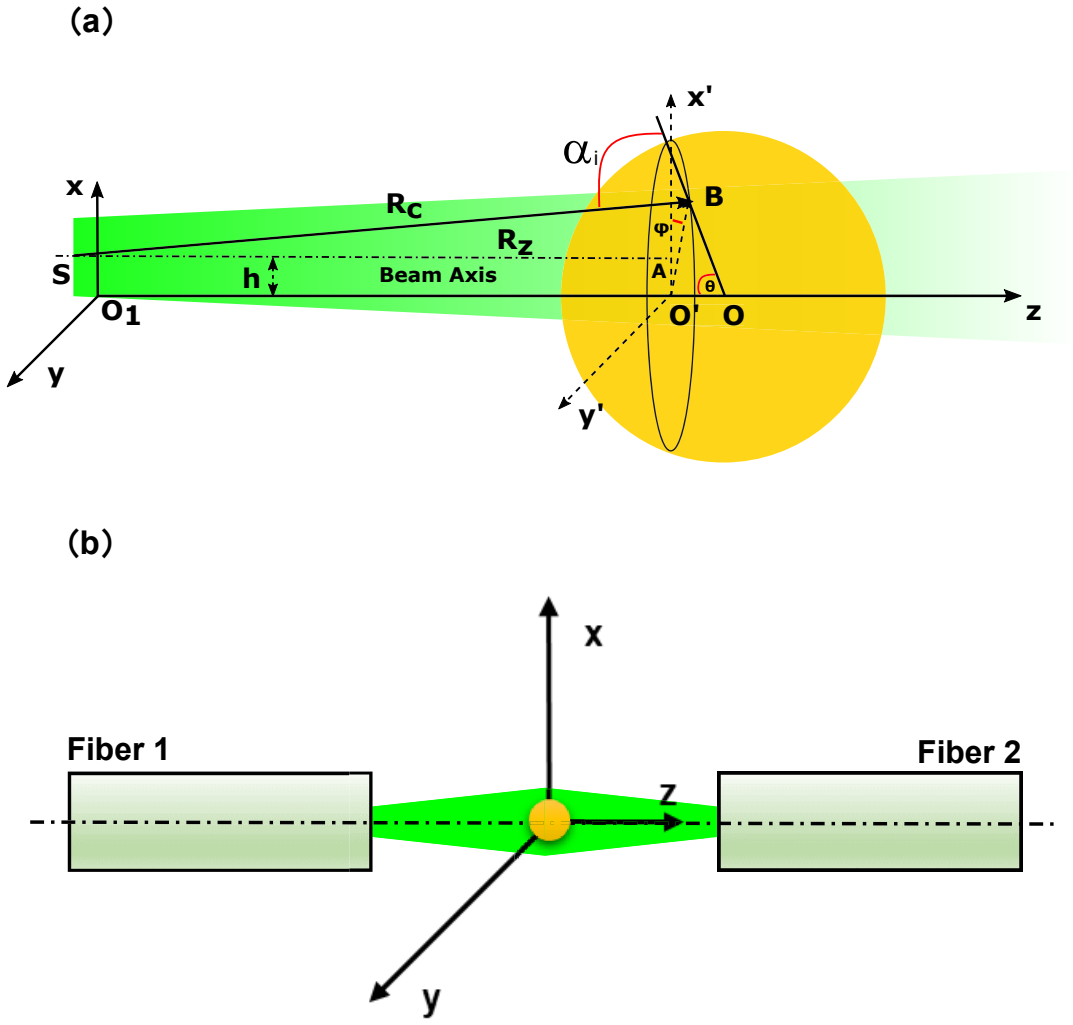

Figure 4.2: The basic theory and principle of the optical fiber based aerosol trap. (a) a Gaussian beam impinges on a single aerosol particle. θ denotes the angle between the normal of the differential area and the beam axis; h is the distance between the beam axis and the optical axis; R_c denotes the radius of curvature of the beam; R_z is the projection distance of R_c on the z axis. (b) Schematic diagram of the CP dual fiber trap.

in this position along the z axis is because of the balance of the forces from the two beams.

To better understand and predict the behavior of aerosols in our trap, we base our model on that used in [143]. The trapping efficiency of a single beam in the axial and radial direction is:

$$Q_z = \frac{2r_0^2}{\pi}\int_0^{\pi} d\varphi \int_0^{\theta_{\max}} d\theta \sin 2\theta \frac{\exp\left(-2r^2/w^2\right)}{w^2 R_c} \times \left\{ q_s R_z + \frac{q_g}{\tan\gamma}\left[R_z - \frac{R_c\left(R_z + r_0\cos\theta\right)}{a\cos\gamma}\right]\right\} \tag{4.1}$$

$$Q_x = \frac{2r_0^2}{\pi}\int_0^{\pi} d\varphi \int_0^{\theta_{\max}} d\theta \sin 2\theta \frac{\exp\left(-2r^2/w^2\right)}{w^2 R_c} \times \left\{ q_s\left(r_0\sin\theta\cos\varphi - h\right) + \frac{q_g}{\tan\gamma} \times \left[r_0\sin\theta\cos\varphi - h\left(1 - \frac{R_c}{a\cos\gamma}\right)\right]\right\} \tag{4.2}$$

Here, r_0 denotes the aerosol particle radius, θ denotes the angle between the normal of the differential area and the beam axis, r denotes the distance from the incident surface to the beam axis, h is the distance between the beam axis and the optical axis, ω denotes the beam waist at point B, γ denotes the half apex angle of the incoming beam, and a denotes the separation between aerosol center and the source of the incoming ray. R_c denotes the radius of curvature of the beam, and R_z is the projection distance of R_c on the z axis. q_s and q_g represent the momentum components in the parallel and perpendicular directions of the incident light.

The trapping forces due to a single beam in the axial and radial directions are:

$$F_{x,z} = \frac{n_1 P}{c} Q_{x,z} \tag{4.3}$$

Here, n_1 denotes the refractive index of air, P is beam power, c denotes the speed of light in the vacuum.

For CP beams, the forces from each beam are added together, as shown in Eq. (4.4) and Eq. (4.5). Along the z axis, the two forces cancel each other out at the midpoint between the fibers. In contrast, the generated forces add along the x axis:

$$F_{z,\,\mathrm{tot}} = \frac{n_1\left(P_{+z} + P_{-z}\right)}{c}\left(\frac{P_{+z}Q_{+z}}{P_{+z}+P_{-z}} - \frac{P_{-z}Q_{-z}}{P_{+z}+P_{-z}}\right) \tag{4.4}$$

$$F_{x,\,\mathrm{tot}} = \frac{n_1\left(P_{+z} + P_{-z}\right)}{c}\left(\frac{P_{+z}Q_{+z}}{P_{+z}+P_{-z}} + \frac{P_{-z}Q_{-z}}{P_{+z}+P_{-z}}\right) \tag{4.5}$$

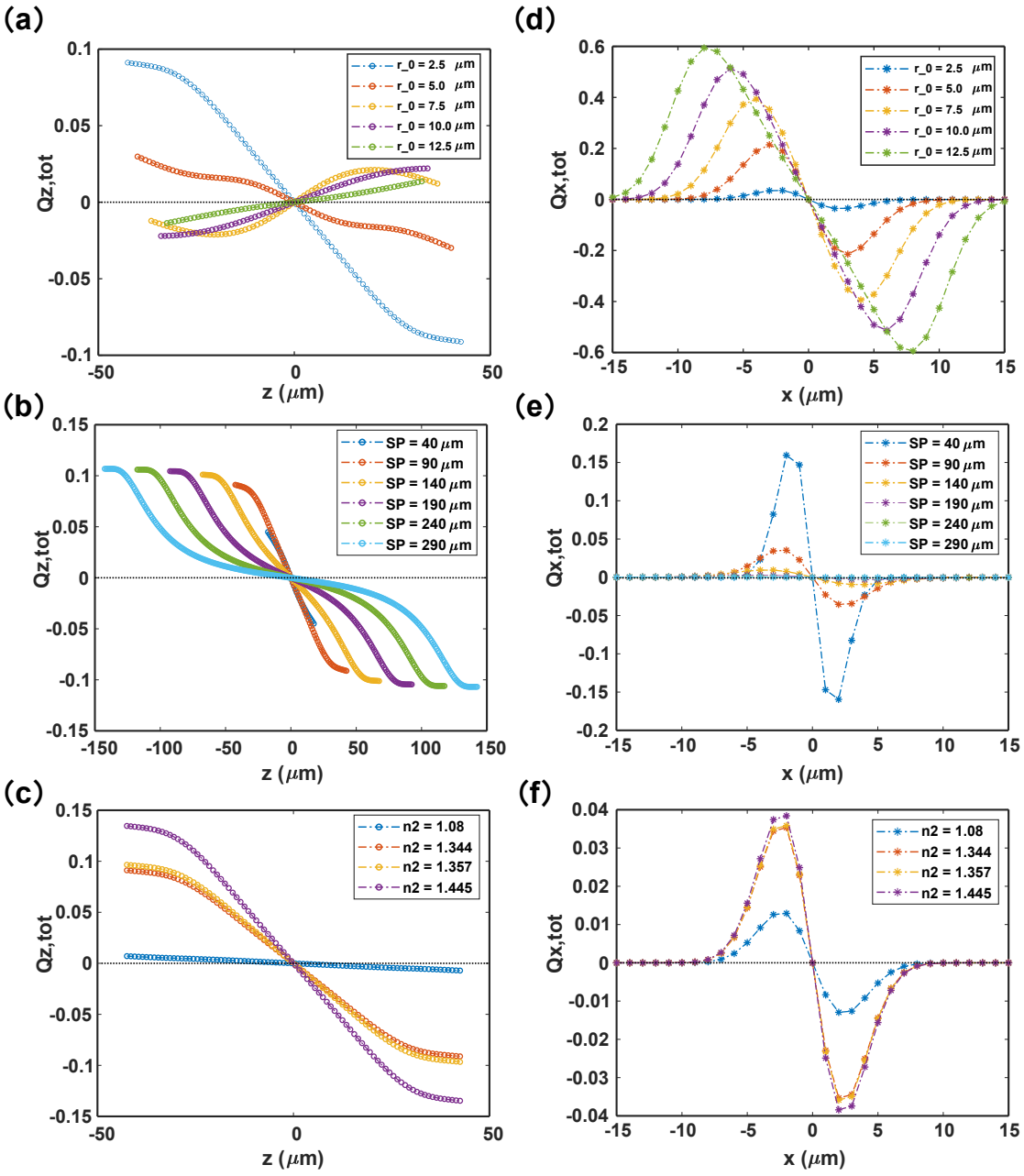

Figure 4.3: Variation of $Q_{z,tot}$ as a function of z with (a) the aerosol sphere radius r_0, and (b) two fiber end separation distance (SP), and (c) the refractive index of the aerosol particle n_2. Variation of the $Q_{x,tot}$ as a function of the x with (d) the aerosol sphere radius r_0, and (e) two fiber separation distance SP, and (f) the refractive index of the aerosol particle n_2. Parameters that are fixed where appropriate are r_0 = 2.5μm, SP = 90μm, and $n2$ = 1.344.

By setting different aerosol particle radii, fiber separations, and aerosol particle refractive indexes, we plot the $Q_{x,tot}$ and $Q_{z,tot}$ curves in Fig. 4.3, where the $Q_{x,tot}$ and $Q_{z,tot}$ are define for two beams. These will act as a guide in understanding where the potential stable and unstable trapping positions are in the z axis direction. For example, the radius of the aerosol particle has a direct effect on the magnitude of the trapping efficiency it experiences in the trapping field as presented in Fig. 4.3 (a) and (d), which will ultimately affect whether a stable trap can be formed at the midpoint. In addition, in Fig. 4.3(a), as the particle size increases from a 5.0μm radius to 7.5μm, there is a significant slope change at z=0. This shift from negative to positive slope is crucial, signaling the inability to create a stable optical trap at this position under the given circumstances. From Fig. 4.3 (b) and (e), we can see that the larger fibers separation will contribute to the smaller trapping efficiency, which means that we need higher laser power to generate greater optical force to balance gravity to ensure the aerosol trapping stability at the midpoint. From Fig. 4.3 (c) and (f), the higher refractive index of the aerosol particle will ensure the optical trap is more stable at the midpoint of the fibers.

4.2.2 3D aerosol trap at the midpoint

It should be noted that due to symmetry, a single aerosol particle on the z axis will not receive a force in the x axis direction. Similarly, assuming that the power of each fiber is equal, the particle located at the midpoint of the two fibers will not receive a force along the z axis. That means if we hope to know the trapped aerosol sizes at the midpoint of two fibers under different aerosol particle radius, fiber separation, we should first understand the conditions of how to achieve a stable 3D aerosol trap at the midpoint of two fibers.

Based on the above model, we have to maintain two conditions simultaneously to achieve a stable 3D aerosol trap at the midpoint between the two fibers. The first one is to maintain a two-dimensional (2D) trap along the z axis by using the optical scattering forces to balance each other. Its numerical expression is as shown in Eq. (4.6) and Eq. (4.7). It is necessary to simultaneously satisfy that the axial trapping efficiency at z = 0 is zero, and the slope of the axial trapping efficiency at z = 0 needs to be less than zero.

$$Q_{z,tot\ (z=0)} = 0 \tag{4.6}$$

$$\nabla Q_{z,tot\ (z=0)} < 0 \tag{4.7}$$

After achieving a 2D trap, the next step is to use the gradient force to balance the weight of the trapped particle and its viscosity resistance in air to maintain a 3D trap. Its numerical expression is shown in Eq. (4.8).

$$F_{x,tot} - mg - F_v \geq 0 \tag{4.8}$$

$$F_v = 6\pi\eta\, r_0 v \tag{4.9}$$

Here, m denotes the mass of the aerosol particle. F_v represents the viscosity resistance of the aerosol particles in air, and its specific calculation expression is shown in Eq. (4.9). Where v denotes the velocity of the aerosol particle, η denotes the viscosity coefficient in air.

If we satisfy these two conditions simultaneously, we are able to systematically research and understand the trapped aerosol sizes at the midpoint of two fibers under different aerosol particle radii and fiber separations.

4.3 Results and discussions

4.3.1 Trap at the midpoint without radial misalignment

To understand the trapped aerosol size range at the midpoint, we first studied the case of no radial misalignment between the two fibers. Fig. 4.4(a) shows the simulation results of how we use the theoretical model to define the stable trapped aerosol size area with the variation of the two fibers' separations. The refractive index of the aerosol particle is 1.344 (50g/L NaCl), and the laser output power from both fibers is 20mW. Fig. 4.4(a1) presents the size range of droplets to achieve a stable axial trap (a 2D trap) with the separations between the two fibers from 30μm to 300μm. The colors within the plot reflect the different slopes of Q_z with Q_z = 0. A negative value means a stable 2D axial

trap, and the larger the absolute value, the higher the relative stability. Similarly, as shown in Fig. 4.4(a2), the gradient force F_g balances other radial forces to maintain radial force balance. Thus the positive value region within the plot reflects that the droplet can be suspended radially in the midpoint trapping area. When the conditions of Fig. 4.4(a1) and (a2) for achieving a stable trap are met at the same time, the size range of the droplets that achieve 3D stable trapping at the midpoint of two fibers under different separations is obtained, as shown in Fig. 4.4(a3). Within the plot, a negative value means a stable 3D trap can be achieved.

The above simulations provide a direct way to display the size range of the trapped single droplet at the midpoint with different fiber separations under the CP dual fiber trapping setup. To further understand the trapped aerosol size range, we conducted experiments under three different fiber powers, results shown in Fig. 4.4(b1) 20mW, Fig. 4.4(b2) 50mW, and Fig. 4.4(b3) 100mW, to verify the simulation results, and analyze how the fiber power will influence the variation of the trapped aerosol size range. The red dots and the pink five-pointed stars represent the largest and smallest trapped droplet sizes in the experiment, respectively. For the smallest trapped droplet, considering the applicability of the ray optics model and the physical limitation of the mesh size of the nebulizer we used, this determines that the lower limit of the aerosol size that can be experimentally verified is about 4.5μm. Therefore, when an aerosol size of about 4.5μm is captured experimentally, we consider that the smallest aerosol is captured at this time under the current setup. To determine the largest trapped droplet, we first trapped a small droplet, and then by continuing to continuously inject aerosols into the trap field, we could find that the originally trapped droplet would grow due to the increase in humidity within the trapping chamber and droplets coagulating. When the size of the droplet increases to a certain point, this droplet leaves the optical trap and we take the size of the droplet before it leaves as the largest size that can be trapped under the current trapping setup. We performed three iterations for each configuration, with prior meticulous cleaning of the fiber end and comprehensive dual fiber calibration before every trial. Following the three trials, we chose the highest and lowest recorded experimental sizes as the conclusive dataset.

By comparison, as the fiber power increases, the simulation results show that droplets with a larger size range can achieve the stable trap within a more extensive range of fiber separation. This is mainly due to the increase of gradient force F_g, balancing the radial

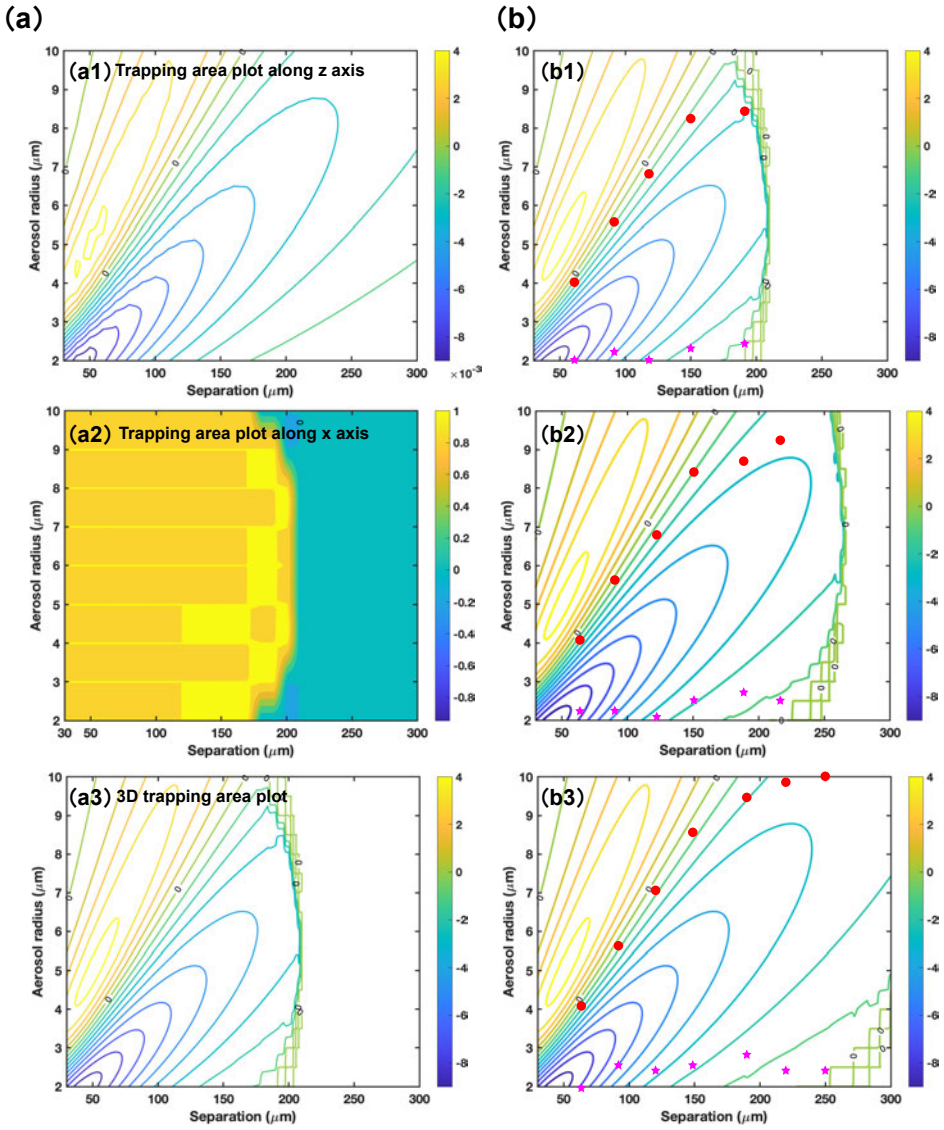

Figure 4.4: (a) Area plot describing the expected trapped aerosol size range at the midpoint under different fiber separations. (a1) The simulation area plot of the size range of 2D aerosol trapping at the midpoint under conditions satisfying Eq. (4.6) and Eq. (4.7). (a2) The simulation area plot showing the size range of aerosols suspended radially in the midpoint trapping area under the condition of satisfying Eq. (4.8). (a3) The simulation area plot of the size range of 3D aerosol trapping at the midpoint combining all three conditions within (a1) and (a2), hence showing stable 3D trapping points. In all plots $n2$ = 1.344 (Refractive index of 50g/L NaCl solution), Power = 20mW from each fiber. (b) Simulation overlaid with experimental results of the area plots describing the expected 3D trapped aerosol size range at the midpoint under different fiber powers with (b1) 20mW, (b2) 50mW, and (b3) 100mW. Markers give experimental data. The red dots represent the largest size aerosol that can be trapped, and the pink five-pointed stars represent the smallest aerosol that can be trapped. Label of 0 indicates instances where the value is zero, reflecting an unstable position and uncertainty in the target aerosol trapping state.

forces of the larger droplet in the radial direction. It is worth noting that the balance condition in the axial direction is independent of the variation of fiber power. That is to say, even with more considerable fiber power, the maximum droplet size that can be trapped in 3D at the midpoint is not larger than the maximum droplet size trapped in 2D along the axis simulated under the same conditions, which can be demonstrated by comparison of Fig. 4.4(a1) and (b1). Besides, in Fig. 4.4(b), we find that the maximum 3D trapped droplet size in the experiment is generally smaller than the maximum 3D trapped size obtained by simulation. However, as the fiber power increases, the 3D trapped droplet size increases in the experiment, but it doesn't exceed the maximum size obtained by simulation. The potential reasons are the interference from the airflow, the humidity within the chamber, and aerosol contamination on the fiber end, which will ultimately lead to limits in the experimental observations. Although the mass median aerodynamic diameter of the droplet size produced by the nebulizer we used here is around 4.5μm [113], the addition of salt to the water, as well as the effects of ambient conditions, particularly humidity, resulted in the minimum radius of the droplet trapped in the experiment is around 2.5μm. In addition, as our simulations are based on the ray optics model, the size of the aerosol particle should be greater than 10 times the wavelength of the trapping light to be more in line with the actual results, which means that the simulation results for aerosols with a radius of 2.5μm or larger are relatively more accurate and reliable. For aerosol particles with a diameter of less than 5μm, this is not included in the scope of this thesis. If one wants to quantify the range of sizes that can be captured for particle diameters less than 5μm, one needs to make predictions by using other appropriate models and verify the predicted results by adopting the aerosol loading method that can produce smaller sizes. The experimental size data on the largest and smallest trapped aerosols under three different trapping power of 20mW, 50mW, and 100mW, illustrated in Table 4.1, is consistent with the numerical modeling, where the term S is an abbreviation for simulation and the term E is an abbreviation for the experiment.

Table 4.1: Trapped aerosol sizes range data without radial misalignment

All Unit:		Fiber power = 20mW				Fiber power = 50mW				Fiber power = 100mW			
μm		S_r_0 max	S_r_0 min	E_r_0 max	E_r_0 min	S_r_0 max	S_r_0 min	E_r_0 max	E_r_0 min	S_r_0 max	S_r_0 min	E_r_0 max	E_r_0 min
	60	4.2	1.0	4.0	2.0	4.2	1.0	4.1	2.2	4.2	1.0	4.1	1.9
	90	5.7	1.0	5.5	2.2	5.7	1.0	5.6	2.2	5.7	1.0	5.6	2.5
	120	7.4	1.0	6.8	2.0	7.4	1.0	6.9	2.1	7.4	1.0	7.1	2.3
SP	150	9.0	1.0	8.2	2.3	9.0	1.0	8.3	2.5	9.0	1.0	8.4	2.5
	190	8.9	2.5	8.3	2.5	10.0	1.5	8.6	2.7	10.0	1.5	9.4	2.7
	220	no	no	no	10.0	10.0	2.0	9.2	2.5	10.0	2.0	9.9	2.3
	250	no	no	no	no	no	no	no	no	10.0	2.5	10.0	2.3

4.3.2 Trap at the midpoint with radial misalignment

We know that using SMFs coupling and alignment is essential when we hope to trap a single aerosol at the midpoint. However, in practice, the alignment of two fibers experiences varying degrees of deviation, especially for the radial misalignment, as shown in Fig. 4.5(a). It is because of human alignment errors or fiber mechanical drift, which will cause the trapped single aerosol to leave the stable trapping position and undergo different dynamic changes [90, 176]. Therefore, to understand the variations of the trapped aerosol size range at the midpoint with the radial misalignment between the two fibers, we conducted the following simulations and experiments.

Fig. 4.5(b) presents the simulation and experimental results of the area plots describing the expected 3D trapped aerosol size range at the midpoint under three different radial misalignments of two fibers with (b1) d = 1μm, (b2) d = 4μm, and (b3) d = 8μm, when the power of two fibers is equal to 20mW. By comparing with Fig. 4.4(b1), we found that with the radial misalignment of 1μm, there is little effect on changing the trapped aerosol size range at the midpoint position. However, as the radial misalignment increases to 4μm, the range of trapped aerosol size and two fiber separations that can achieve 3D trapping at the midpoint both are reduced significantly. Specifically, in the experiment, the maximum trapped aerosol radius is reduced from 8.3μm to 7.3μm, and the maximum fiber separation distance that can achieve trapping is decreased from 200μm to 150μm. When the radial misalignment is expanded to 8μm, setting any two fiber separations, there are no aerosols trapped at the midpoint position. Besides, the experiment size data on trapped largest and smallest aerosols illustrated in Table 4.2 is

consistent with the simulated data.

To further understand how the fiber power will influence the variation of the trapped aerosol size range with the radial misalignment, we only increase the fiber power from 20mW to 100mW and keep other conditions the same. In Fig. 4.5(c), it demonstrated the results of the 3D trapped aerosol size range at the midpoint under three different radial misalignments of two fibers with (c1) d = 1μm, (c2) d = 4μm, and (c3) d = 8μm, when the output power from the two fibers is equal to 100mW. By comparing with Fig. 4.5(b), we found that with the same radial misalignment, using a larger fiber power can achieve a larger size droplet trapping at the midpoint within wider fiber separations. Especially when the radial misalignment is equal to 8μm, we can clearly see that a droplet with a radius from 7.0μm to 10.0μm can still achieve 3D trapping in the middle position when the fiber separation is in the range of 60μm to 150μm. However, there are no aerosols trapped at the midpoint position under any fiber separations when the fiber power is equal to 20mW. In Table 4.3, we record the largest and smallest trapped droplet sizes, which agree with the simulation result.

4.3.3 Trap at two fiber ends with short fiber separations

Through the analysis of the above two sections, we have clarified the relationship of the midpoint-trapped aerosol size range with fiber separation, power, and radial misalignment. It provides a straightforward guide for understanding the aerosol size range that can achieve 3D trapping at the midpoint between two fibers under different CP dual fiber tapping settings. However, we might also ask if stable trapping can be achieved in other locations between the fibers?

When assuming there is no radial misalignment, we simulated axial trapping efficiency $Q_{z,tot}$ as a function of the z axis offset for a droplet with a radius of 3.0μm, the refractive index of 1.344, and three different fiber separations, namely, 20μm, 28μm and 38μm. We find that when SP is equal to 38μm, the dual fiber trapping setup forms a stable trapping position in the midpoint between the fibers. When SP is decreased to 28μm, stable trapping is no longer possible at the center position, but new stable positions appear close to the fiber ends (two positions are at z = -10μm and z = 10μm, as shown in Fig. 4.6(b)). When SP is further decreased to 20μm, the droplet cannot be trapped at any position. Fig. 4.6(a) is a schematic diagram showing how the trapping

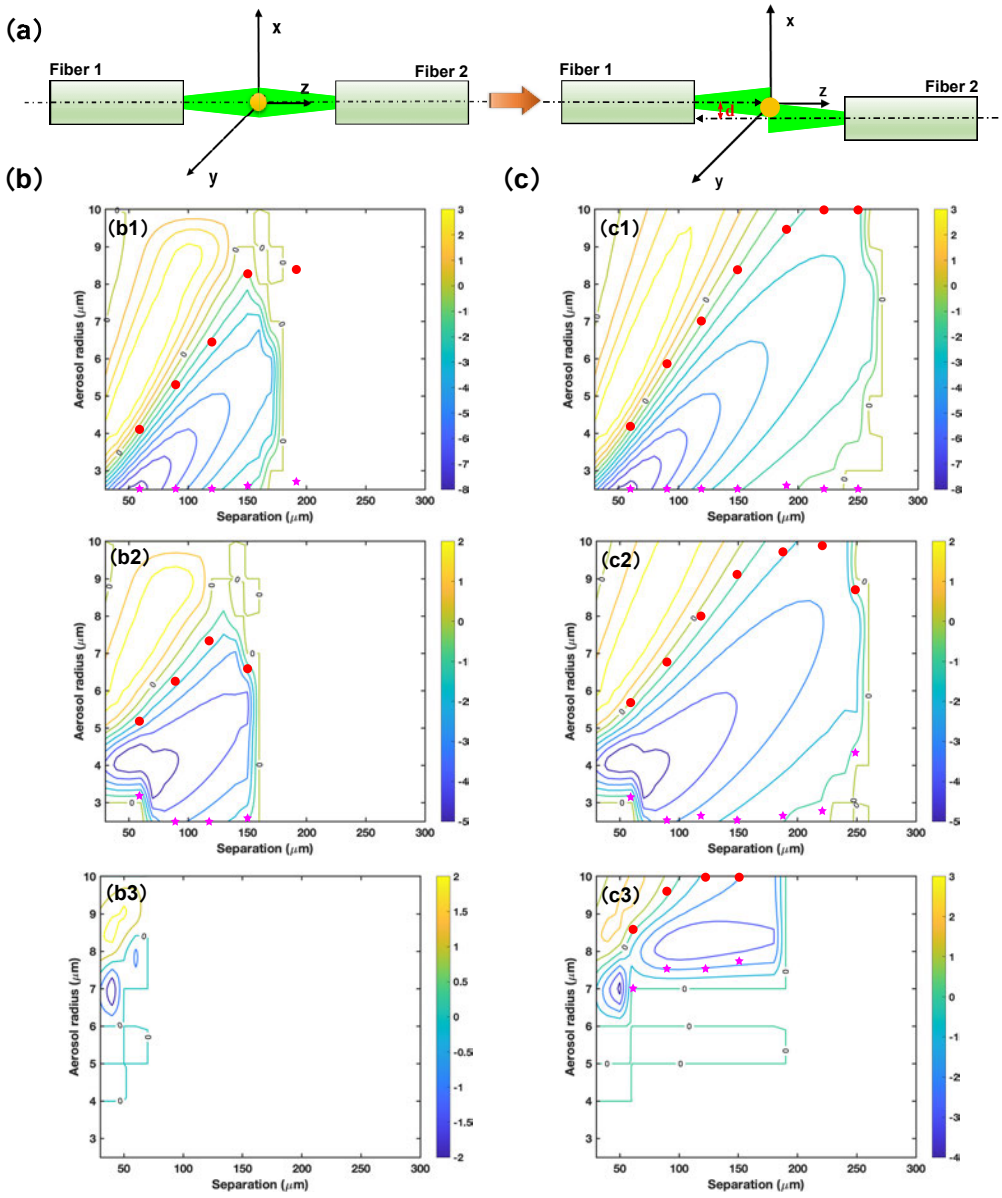

Figure 4.5: (a) A schematic diagram showing the principle of aerosol trapping at the midpoint under the radial misaligned CP dual fiber trapping setup (d denotes the radial misalignment of two fibers). (b) Simulation and experimental results of the area plots describing the expected 3D trapped aerosol size range at the midpoint under different radial misalignment of two fibers with (b1) d = 1μm, (b2) d = 4μm, and (b3) d = 8μm, when the power of the two fibers is equal to 20mW. (c) when the power of the two fibers is equal to 100mW, simulation and experimental results of the area plots describing the expected 3D trapped aerosol size range at the midpoint under different radial misalignment of two fibers with (c1) d = 1μm, (c2) d = 4μm, and (c3) d = 8μm. Markers give experimental data. The red dot represents the largest aerosol that can be trapped, and the pink five-pointed star represents the smallest aerosol that can be trapped. label of 0 indicates instances where the value is zero, reflecting an unstable position and uncertainty in the target aerosol trapping state. Parameters not shown in the plots are $n2$ = 1.344.

Table 4.2: Trapped aerosol sizes of the simulation and experimental data with fiber power of 20mW

All Unit: μm		Radial offset = 0				Radial offset = 1				Radial offset = 4				Radial offset = 8			
		S_r_0 max	S_r_0 min	E_r_0 max	E_r_0 min	S_r_0 max	S_r_0 min	E_r_0 max	E_r_0 min	S_r_0 max	S_r_0 min	E_r_0 max	E_r_0 min	S_r_0 max	S_r_0 min	E_r_0 max	E_r_0 min
	60	4.2	1.0	4.0	2.0	4.3	2.5	4.1	2.5	5.8	3.0	5.2	3.2	no	no	no	no
	90	5.7	1.0	5.5	2.2	5.8	2.5	5.3	2.5	7.0	2.5	6.3	3.5	no	no	no	no
	120	7.4	1.0	6.8	2.0	7.4	2.5	6.5	2.5	9.1	2.5	7.3	2.5	no	no	no	no
SP	150	9.0	1.0	8.2	2.3	9.1	2.5	8.2	2.6	7.0	2.5	6.6	2.6	no	no	no	no
	190	8.9	2.5	8.3	2.5	9.1	2.5	8.3	2.7	no	no	no	no	no	no	no	no
	220	no	no	no	no	no	no	no	no	no	no	no	no	no	no	no	no
	250	no	no	no	no	no	no	no	no	no	no	no	no	no	no	no	no

Table 4.3: Trapped aerosol sizes of the simulation and experimental data with fiber power of 100mW

All Unit: μm		Radial offset = 0				Radial offset = 1				Radial offset = 4				Radial offset = 8			
		S_r_0 max	S_r_0 min	E_r_0 max	E_r_0 min	S_r_0 max	S_r_0 min	E_r_0 max	E_r_0 min	S_r_0 max	S_r_0 min	E_r_0 max	E_r_0 min	S_r_0 max	S_r_0 min	E_r_0 max	E_r_0 min
	60	4.2	1.0	4.1	1.9	4.3	2.5	4.2	2.5	5.8	3.0	5.7	3.1	8.5	7.0	8.6	7.0
	90	5.7	1.0	5.6	2.5	5.8	2.5	5.9	2.5	7.0	2.5	6.8	2.5	9.5	7.5	9.6	7.5
	120	7.4	1.0	7.1	2.3	7.4	2.5	7.0	2.5	8.4	2.5	8.0	2.6	10.0	7.5	10.0	7.5
SP	150	9.0	1.0	8.4	2.5	9.1	2.5	8.4	2.5	9.8	2.5	9.1	2.5	10.0	7.5	10.0	7.7
	190	10.0	1.5	9.4	2.7	10.0	2.5	9.5	2.6	10.0	2.5	9.7	2.6	no	no	no	no
	220	10.0	2.0	9.9	2.3	10.0	2.5	10.0	2.5	10.0	2.5	9.9	2.7	no	no	no	no
	250	10.0	2.5	10.0	2.3	10.0	2.5	10.0	2.5	9.0	4.0	8.7	4.3	no	no	no	no

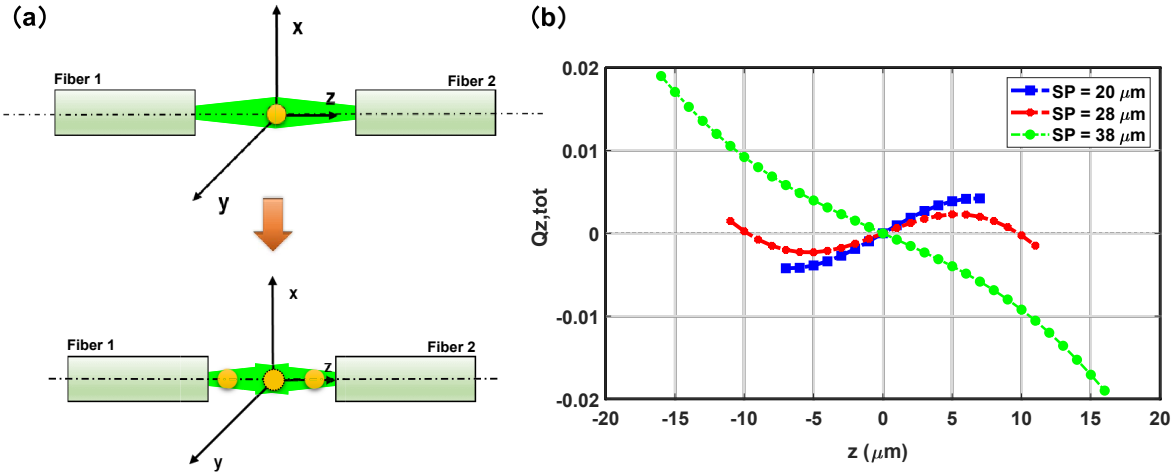

Figure 4.6: Trapped aerosol at two fiber ends under CP fiber trap in air with short fiber separation. (a) Schematic diagram of aerosol particles being trapped from the midpoint to the two fiber ends. (b) Under three different separations, variation of the axial trapping efficiency $Q_{z,tot}$ as a function of the z axis offset. When SP is equal to 38μm, CP dual fiber trapping setup forms a stable trapping position at the midpoint of two fibers; When SP is 28μm, CP dual fiber trapping setup cannot form stable trapping at the center position, but it can form the trapping position closing to the two fiber ends. When SP is equal to 20μm, no droplet can be trapped at any position in air. Parameters not shown in the legends are aerosol size r_0 = 3.0μm, and aerosol refractive index $n2$ = 1.344.

points shift from the center to positions close to the fiber facets with the reduction of fiber separation. Apart from simulations, we also conducted experiments to verify this phenomenon.

At the initial stage, we are trying to observe the scatting image of the trapped droplet at two fiber ends under CP dual fiber trap in air with short fiber separation, since the size range of the droplet that can be trapped under short fiber separation is relatively small and difficult to be observed. Fig. 4.7(a) shows the scattering image of the trapped single droplet in air between the two fiber ends with short fiber separation with Fig. 4.7(a1) trapped in the midpoint, Fig. 4.7(a2) trapped in the one fiber end, and Fig. 4.7(a3) trapped in the other fiber end under dual fiber output power both of 50mW. By adding the filter, in Fig. 4.7(b), we can find the single droplet was trapped between the two fibers and it was focused in the focal plane. From Fig. 4.7(b1), we can calculate the radius of the trapped droplet is equal to 3.1μm, and the fiber separation is 38.5μm. We then gradually shortened the distance between the two fibers to observe the change in the position of the trapped single droplet. Fig. 4.7(b2) and Fig. 4.7(b3) show the single droplet was

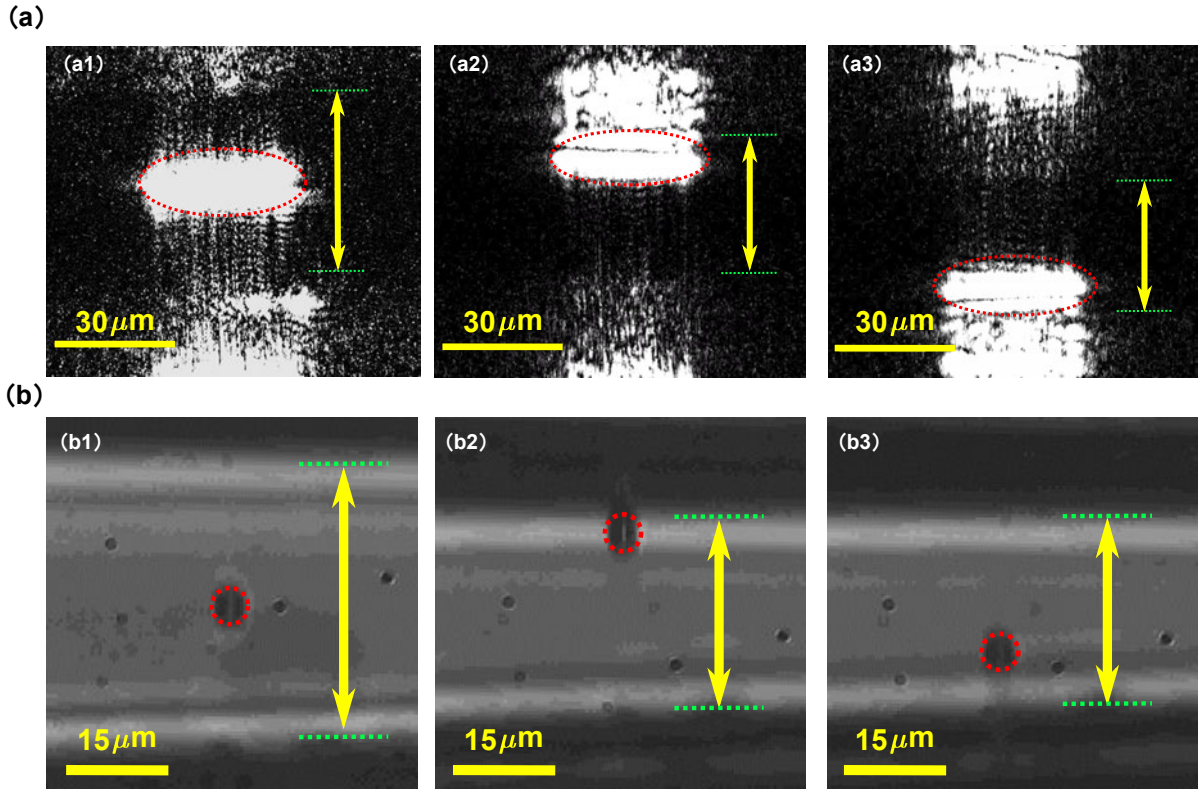

Figure 4.7: Scattering images and real images of trapped aerosol at two fiber ends under CP fiber trap in air with short fiber separation. (a) The scattering image of the trapped single droplet in air between the two fiber ends with short fiber separation with (a1) trapped in the midpoint, (a2) trapped in the one fiber end, and (a3) trapped in the other fiber end. (b) Single droplet is trapped in air between the two fibers with a radius of 3.1μm and fiber output power of 50mW. (b1) It shows the focused single droplet trapped in the midpoint of two fibers with SP = 38.5μm. (b2) Single droplet is trapped in air at one fiber end with SP = 27.7μm, and (b3) trapped at the other fiber end with SP = 28.1μm. The aerosol shown in (a) and (b) is the same particle with filter-out/filter-in, respectively.

trapped at the two fiber ends with the SP of 27.7μm and 28.1μm in air, respectively. The results are in good agreement with the simulations. In addition, the individual droplet trapped at the fiber end can still return to the central position of the two fibers and achieve stable trapping when we increase the spacing of the two fibers. However, in our experiment, we did not observe the simultaneous trapping of the droplets at the two fiber ends. The potential reason may be because when we trapped one droplet at one fiber end, the presence of this droplet will distort the optical field on the other potential trapping position at the other fiber end. If we can find a way like beam shaping or adaptive optics to compensate for the optical field distortion, maybe we can observe this interesting phenomenon of trapping two droplets at two fiber ends simultaneously. Additionally, it's important to highlight that the experimental outcomes exhibit repeatability, even though they may not consistently align precisely with the positions documented in the thesis. Fig 4.7's illustration is merely a representation of one validation outcome, aimed at showcasing the strong concurrence between our experimental and simulated results. Furthermore, as previously mentioned, the introduction of aerosol is unpredictable and stochastic, leading to a degree of contamination on the fiber facet. Consequently, the quality of the output beam profile deteriorates. This variability also extends to the trapping experiments, where the trapped position isn't guaranteed to be identical in every instance.

4.4 Conclusion

We have quantified the size range of the aerosols that can be trapped in the CP dual fiber trapping setup under the variation of fiber separations, particle sizes, fiber powers, and radial offset. When we trap the single aerosol at the midpoint without the radial offset, we find that the increased fiber power will contribute to a large size aerosol being trapped, but the maximum aerosol size that can be trapped in 3D at the midpoint is not larger than the maximum aerosol size trapped in 2D along the axis simulated under the same conditions. In addition, the maximum size of aerosol trapped in the experiment is usually smaller than the simulation result, which is mainly caused by the influence of airflow, humidity, and pollution on the fiber end. When we trap the single aerosol at the midpoint with the radial offset, we find that when the radial offset is within 4μm, the range of aerosol size that can be captured stably is not significantly affected, and the main affected range is in the case of large fiber separations. When the radial offset

is further increased, the size range of aerosol that can be trapped at the midpoint will be drastically reduced until it disappears completely. However, it is worth noting that under the same radial offset, increasing the fiber power can improve the shrinkage of the trapped aerosol size range caused by the radial offset to a certain extent. Finally, we also examined the situation where aerosol is not trapped in the midpoint of two fibers, but can be trapped at the ends of the two fibers. Doing so will contribute to the repeatable quantitative results of aerosol trapping under the CP dual fiber trapping setup and pave the way to further research on the manipulation and characterization of single aerosol particles.

In addition, it is important to address that the radial alignment of the two fibers introduces more intricate motions for individual particles within the CP dual fiber traps. While Chapter 4 primarily centers on quantifying the influence of radial misalignment on variations in trapped aerosol size range, we acknowledge that the heightened radial misalignment can lead to more complex particle movements. Despite this, we didn't conduct comprehensive experimental trials to validate this phenomenon directly. Instead, we employed numerical analysis to comprehend this behavior, aiding our understanding of the degree of radial misalignment at which single aerosol particles can still be captured within our traps. It's noteworthy that previous work by Chen et al. [37, 38]. and Li et al. [90] delved into systematic analyses and experimental verification of changes in particle dynamics, both in liquid environments and in air, respectively. Given this existing body of research, we refrain from duplicating experiments in this thesis to validate these aspects once more.

CHAPTER 5

TRAPPING VARIATIONS WITH ANGULAR DEVIATIONS

Dual beam fiber traps are potentially useful for integrated trapping devices aimed at studying aerosols, and offer opportunities for cavity-enhanced traps. The alignment of such traps is typically seen to be critical. Here we explore the impact of the angular deviation of the optical fibers, and assess trapping viability as a function of misalignment and how particle dynamics change when interacting with displaced fibers. We find good trapping capability for dual fibers tilted at the same angle, while more complex aerosol dynamics become apparent at higher single fiber tilt angles. Besides, the four main factors (including beam divergence, fiber separation distance, fiber output power, and aerosol radius) will also influence the single aerosol particle trapping performance and introduce dynamic changes in the tilted CP dual fiber traps. We present simulation and experimental results.

5.1 Introduction

The ability of light to interact with microscopic objects to generate forces that allow for precise non-contact methods for trapping bodies is enclosed in a technique called optical trapping or optical tweezers [7, 12]. Over the last 50 years, this technique has been extended into various areas across physical, chemical, and biological sciences and aerosol science [4, 18, 27, 36, 41, 47, 79, 98, 111, 127, 138]. Of particular note is that optical trapping lends itself well to precision single aerosol studies that have developed significantly in recent years [3, 25, 28, 64–66, 119, 125, 127, 134, 147, 148]. Although

aerosols are of particular interest to atmospheric chemistry and human health, many processes at the single aerosol level still need to be fully explored.

Optical trapping and manipulation in air present greater challenges than in liquid environments, with two key difficulties being the lower viscosity of the suspending medium and the higher relative refractive index of the aerosol, which increases the likelihood of the aerosol being pushed out of the trapping field due to greater scattering forces [157]. To overcome these limitations and study the dynamics of single airborne particles interacting with the light field, various schemes have been proposed in recent years. One such configuration involves using a strongly focused laser from a high NA objective to converge onto the aerosol, allowing for optical momentum and transportation to the beam focus [25]. However, the limitations of this approach include the need for a high numerical aperture objective lens, difficulty in trapping larger aerosols, and a relatively short working distance, which limits the use of single-beam optical tweezers [177]. As an alternative, counter-propagating dual beam optical tweezers can effectively overcome these limitations [102, 155], but this comes at the cost of increased complexity and difficulty in aligning the dual beams.

To achieve miniaturization of optical trapping devices and facilitate easier alignment, optical fibers can be utilized in the CP dual beam optical trapping setup for the delivery of optical transmission. This has been demonstrated by researchers who have shown that the CP dual fiber setup can trap and manipulate a wider range of aerosol particle sizes while providing greater flexibility in terms of optical accessibility to the trapping field [102, 134]. Moreover, studies have revealed that the CP dual fiber aerosol trapping device can be readily integrated with spectroscopic and microfluidic systems, enabling more versatile characterization and analysis of single aerosol particles [24, 59, 75, 163]. By incorporating optical fibers into the CP dual beam optical trapping system, researchers are able to expand the range of potential applications and enhance the overall functionality of this device. However, it is worth noting that the alignment of two fibers of such traps is typically seen to be critical for good trap performance. Constable et al. pointed out that CP dual fiber trap usually experiences two types of misalignment, as shown in Fig. 5.1, namely radial misalignment (transverse offset) and rotational misalignment (angular deviations), and both types of misalignment may occur at the same time [42]. In this thesis, I provide an additional clarification to highlight a specific concept: "Counter-propagating with angular deviations." This concept pertains to an

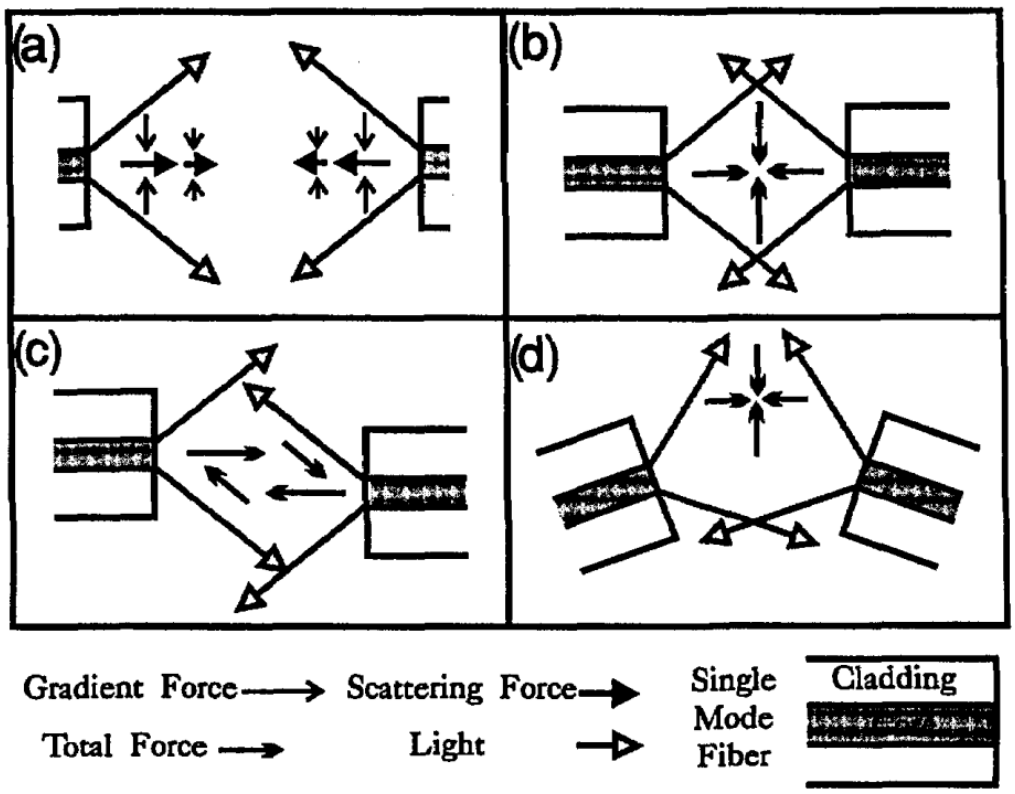

Figure 5.1: Illustration of dual fiber-based traps with different alignment conditions. (a) Schematic diagram of the gradient and scattering forces of the two fibers forming the traps. (b)-(d) Total force direction when the fibers are (b) perfectly aligned, (c) positional misalignment (transverse offset), and (d) rotational misalignment (angular deviations). Figure adapted from [42].

innovative state wherein the trapping dynamics of aligned CP dual beam traps undergo modifications due to the introduction of angular deviations. To precisely depict these newly recognized trapping configurations, I have coined the term "CP dual fiber trap with angular deviation." This term aptly captures the essence of the altered trapping setups. Up to date, CP dual fiber trap with transverse offset has been conducting a systemic study in terms of the quantitative tolerance range of the transverse offset to achieve stable trapping, the relationship between the dynamics of the trapped particles and transverse offset, and the trapping characteristics in different trapping environments (liquid, air) [36–38, 90]. However, to the best of our knowledge, we noticed CP dual fiber trap with angular deviations has only been employed for some specific applications, and all these works were conducted in the liquid environments [19, 94, 95, 151, 152]. Moreover, there has yet to be a quantitative analysis that accurately explains how the

airborne particle dynamics change when interacting with displaced fibers.

In this chapter, we investigate the effect of optical fiber angular alignment on trapping viability and how particle dynamics change while interacting with displaced fibers. First, we computed the optical forces and simulated the behavior of a single aerosol particle in single and dual fiber tilt configurations. We show that reliable single aerosol trapping can still be obtained at the highest tilt angle threshold using two alternative trapping strategies. Then, with angle deviations greater than the highest stable trapping point, we express all the aerosol particle dynamical types under CP dual fiber traps. At greater single fiber tilt angles, three independent sets of movements appear, revealing more complicated aerosol dynamics. When the dual fibers are tilted beyond their maximum trapping threshold and into a configuration that surpasses the limits of complex dynamics, individual aerosol particles will simply escape directly. Finally, we investigate the impact of four major factors (fiber beam divergence, two fiber separation distance, two fiber output power, and aerosol radius) on the trapping characteristics and dynamics of individual aerosol particles in two tilted CP dual fiber traps. The findings provide insight into the development of fiber-based optical traps as well as a novel approach to managing light-induced rotation in air.

5.2 Model

Here, the relative ratio of the aerosol size to the wavelength of the trapping light is typically greater than ten. Following [8, 143], we adopt the ray optics method and approximate the beam into a set of rays impinging on the particle. As shown in Fig. 5.2(a) and (b), it illustrates how a single ray strikes an aerosol particle contributing to the scattering force and the gradient force, along with the model of how a Gaussian beam is composed of multiple rays impinges an aerosol particle. When a single ray is reflected and refracted on the surface of the aerosol, the momentum change transferred to the aerosol causes the particle to receive the trapping force. The trapping force exerted on the aerosol particle by the Gaussian beam is the sum of the contributions of all rays. In Eq. (5.1) and Eq. (5.2), it shows the optical forces generated by the case of a single ray impinging an aerosol particle, where the $d\boldsymbol{F}_s$ and the $d\boldsymbol{F}_g$ denote the scattering force and the gradient force respectively.

$$d\boldsymbol{F}_s = \frac{n_1 q_s}{c} \boldsymbol{s} dP \tag{5.1}$$

(5.2) $$d\boldsymbol{F}_g = \frac{n_1 q_g}{c}\boldsymbol{g}dP$$

Where n_1 denotes the refractive index of air, c is the speed of light in a vacuum, $\boldsymbol{s}$ and $\boldsymbol{g}$ are the unit vectors in the directions of $d\boldsymbol{F}_s$ and the $d\boldsymbol{F}_g$, respectively. dP represents the differential power of the ray, q_s and q_g are represent the momentum components in the parallel and perpendicular directions of the incident light.

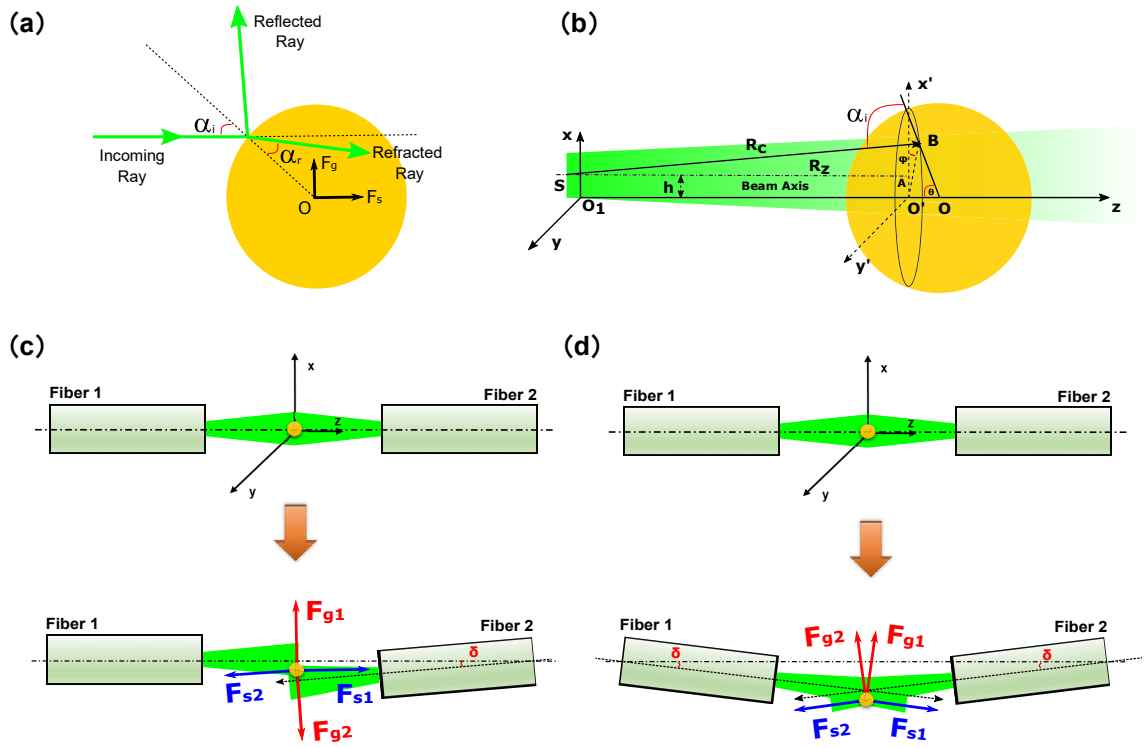

Figure 5.2: (a) A ray strikes an aerosol particle contributing to the scattering force and the gradient force. (b) a Gaussian beam impinges on a single aerosol particle. This figure has also been used in Fig. 4.2(a) to help explain the model used in Chapter 4. (c) Schematic of CP fiber-based aerosol trapping with single fiber tilt. (d) Schematic of CP fiber-based aerosol trapping with two fibers tilted at the same angle together.

Among them, the dP, q_s and q_g are given as follows:

(5.3) $$dP = I\cos\theta dS = \frac{2P_0}{\pi\omega_o^2}\exp\left(\frac{-2r^2}{\omega^2}\right)\cos\theta dS$$

(5.4) $$dS = r_0^2\sin\theta d\theta d\varphi$$

$$q_s = 1 + R\cos 2\alpha_i - T^2 \frac{\cos(2\alpha_i - 2\alpha_r) + R\cos 2\alpha_i}{1 + R^2 + 2R\cos 2\alpha_r} \tag{5.5}$$

$$q_g = -R\sin 2\alpha_i + T^2 \frac{\sin(2\alpha_i - 2\alpha_r) + R\sin 2\alpha_i}{1 + R^2 + 2R\cos 2\alpha_r} \tag{5.6}$$

Where I is the light intensity, P_0 denotes the power of the Gaussian beam, ω_o represents the beam waist, ω is the beam waist at point B as indicated in Fig. 5.2(b), dS denotes the differential area of the aerosol particle, r_0 denotes the aerosol particle radius, r represents the distance between point B and the optical axis, θ denotes the angle between the normal of the differential area and the beam axis, α_i and α_r are the incident angle and refraction angle of the ray, R and T represent the reflectance and transmittance at the surface of the aerosol particle.

To calculate the total optical trapping force of the entire Gaussian beam to the aerosol particle, the optical trapping force of all rays needs to be summed as follows:

$$\boldsymbol{F}_{sum} = \int \left(F_s \boldsymbol{s} + F_g \boldsymbol{g}\right) dS = \frac{n_1 P_0}{c} \frac{4r_0^2}{\pi} \int_0^{\pi} d\varphi \int_0^{\theta_{\max}} \sin\theta\cos\theta \left(\boldsymbol{s} q_s + \boldsymbol{g} q_g\right) \frac{\exp\left(-2r^2/\omega^2\right)}{\omega_o^2} d\theta \tag{5.7}$$

For CP dual fiber traps with angle deviations, as shown in Fig. 5.2 (c) and (d), the optical forces from each fiber are added together:

$$\boldsymbol{F}_{tot} = \boldsymbol{F}_{sum,\ \text{fiber 1}} + \boldsymbol{F}_{sum,\ \text{fiber 2}} \tag{5.8}$$

When loading the aerosol into the trapping field, the particle is also subjected to gravitational force $\boldsymbol{F}_{gravity}$, viscous force $\boldsymbol{F}_v$ and Brownian stochastic force $\boldsymbol{F}_{Brownian}$ in the air. They are given as follows:

$$\boldsymbol{F}_{\text{gravity}} = m\boldsymbol{g} \tag{5.9}$$

$$\boldsymbol{F}_v = 6\pi\eta r_0 \boldsymbol{v} \tag{5.10}$$

(5.11) $$\boldsymbol{F}_{\text{Brownian}} = m\boldsymbol{\xi}(t)$$

Here, m denotes the mass of the aerosol particle and $\mathbf{g}$ is the acceleration due to gravity. $\boldsymbol{v}$ denotes the velocity of the aerosol particle, η denotes the viscosity coefficient in air, and $\boldsymbol{\xi}(t)$ represents the Brownian stochastic force per unit mass.

To understand the dynamics of the aerosol particle within the trapping field, the single aerosol dynamical performance can be modeled by Newton's second law:

(5.12) $$m\ddot{r}(t) = \boldsymbol{F}_{\text{gravity}} + \boldsymbol{F}_{\text{tot}} + \boldsymbol{F}_{v} + \boldsymbol{F}_{\text{Brownian}}$$

Here $\boldsymbol{r}$ denotes the aerosol particle's position changing with time t. Based on Eq. (5.12) and OTS toolbox [30], we can simulate the aerosol particle trajectory and forces under CP dual fiber tilted configurations. Importantly, akin to the models discussed in Chapter 4, our approach in this context is rooted in the Ray optics model outlined in Chapter 5. Nonetheless, a distinction arises in the methodology: within this chapter, we employ the vector tracing method, whereas in Chapter 4, computations rely on scalar calculations.

5.3 Experimental preparation

5.3.1 Optical setup

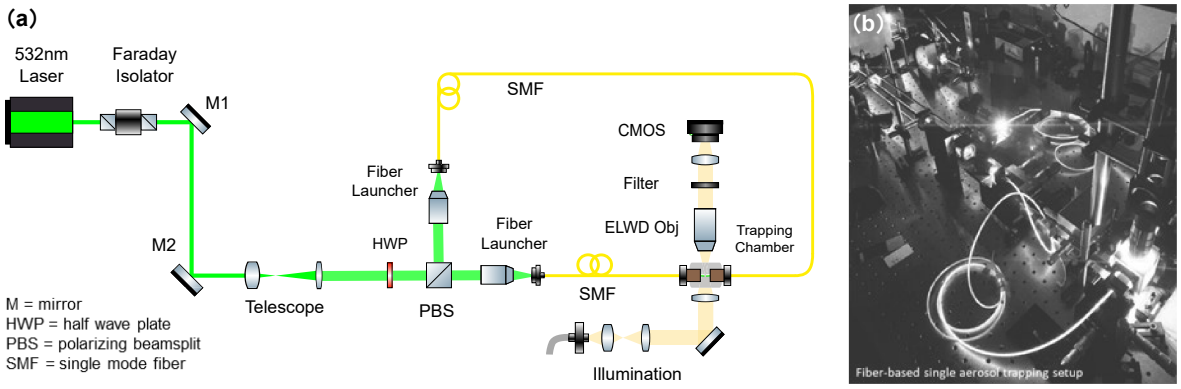

Figure 5.3: (a) Schematic of CP tilted fiber-based aerosol trapping. (b) Actual tilted fiber-based CP single aerosol trapping setup.

The optical setup is the same as in the previous chapter but the trapping chamber and fiber-holder are different. Specially, Fig. 5.3(a) depicts the schematic of the aerosol trapping setup using CP tilted fibers. The experiments employed a continuous-wave (CW) laser at 532nm (Laser Quantum Torus, 891mW). The laser beam passed through an isolator (Thorlabs part IO-3-532-LP), underwent expansion through a 6X telescope, and then underwent splitting via a half-wave plate (HWP) and a polarizing beam splitter (PBS). Manipulating the HWP's rotation allowed control over the power splitting ratio achieved by the PBS. These divided beams were directed into single-mode fibers (SMFs) (Thorlabs part P1-460AR-2) via two 10X objectives. The fibers possessed mode field diameters ranging from 2.8μm to 4.1μm at 488nm and were both equipped with ST connectors. Due to the SMFs' small core and potential mechanical drift during launching, the optimized maximum transmission power through the SMFs settled at around 16% to 18%. Concluding the optical path, the two fibers were affixed to a custom-designed angled fiber holder and introduced into a 3D-printed chamber. Within this chamber, observations and recordings of trapped single aerosol particles were enabled using a 20X long working distance objective lens (Motic ELWD 20X) and a CMOS camera (Basler acA2040-120μm, 120fps). Analyzing the acquired videos and determining the captured particle sizes were accomplished through custom MATLAB algorithms. Notably, the actual tilted fiber-based CP single aerosol trapping configuration is represented in Fig. 5.3(b).

5.3.2 Trapping consideration

For the aerosol generation and delivery process, a 50g/L NaCl solution was employed to prevent rapid droplet evaporation within our custom-designed trapping chamber, which lacks precise humidity control [154]. Subsequently, an ultrasonic nebulizer (OMRON NE-U100-E), depicted in Fig. 5.4(a), was utilized, coupled with a custom nozzle for effective aerosol delivery into the trapping chamber. The trapping chambers themselves were purposefully crafted to accommodate two distinct tilted fiber based CP aerosol trapping setups. These include the single fiber tilt aerosol trapping configuration shown in Fig. 5.4(c), as well as the dual fiber tilt simultaneous aerosol trapping setup illustrated in Fig. 5.4(d). These specially designed chambers serve to mitigate airflow disturbances within the trap, uphold high humidity levels during trapping, ensure reliable aerosol sample delivery, and provide ease of fiber installation and alignment. In order to achieve the desired tilted fiber trapping, fibers can be securely held using a 3D-printed fiber holder with precise angular deviations, as outlined in Fig. 5.4(b). This setup enables accurate

quantitative angular tilting of the fibers. It's imperative to optimize the coupling of each fiber with the laser for precise fiber alignment. Additionally, the output power of both fibers is balanced through the manipulation of the HWP's rotation, while a power meter is employed to monitor power stability over a 3-minute period prior to commencing the experiment. An essential post-experiment procedure involves a thorough cleaning of the fiber ends and realignment of the fibers for subsequent trials.

5.4 Results and discussions

To precisely anticipate and comprehend the impact of angular alignment of optical fibers in CP dual fiber traps on the stability and dynamics of aerosol trapping, we examine scenarios involving both single fiber tilt and simultaneous tilt of dual fibers. The simulation parameters are matched with those utilized in the actual experiments. Here, we consider a typical 50g/L NaCl aerosol (diameter $2r_0$ = 5μm, the refractive index n_2 = 1.344) as the trapped airborne particle, and the air (the viscosity coefficient η = 1.8e-5 Pa.s, and the refractive index n_1 = 1.000) as the surrounding media. The wavelength of the laser λ = 532nm, and the beam profile emitted from each fiber is the Gaussian beam. Besides, two fiber separation distance SP = 90μm, and each fiber's output power is equal to 20mW. The polarization directions of the lasers emitted from the two fibers are orthogonal.

5.4.1 Fiber tilted threshold for single aerosol stable trapping

Here, we first studied the effect of a single fiber tilt on the stable trapping of a single aerosol particle. In Fig. 5.5(a), it illustrates the simulated moving trajectory of the single droplet under dual fiber trapping scheme with one fiber tilted at 5°. The green arrow lines indicate the incoming laser rays, the red ball denotes the trapped droplet, and the blue curve represents the trajectory of the droplet calculated according to Eq. (5.12). For two crosses, the black one represents the intersection of the optical axis of the non-tilted left fiber and line of z = 0, and the pink one denotes the intersection of the optical axis of the right inclined fiber and line of z = 0. From the trajectory, we see that the final trapped position of the droplet is in the middle to the left of the two crosses. To better understand that, the forces distributions applied on this droplet in the xz plane are shown in Fig. 5.5(b). The length and direction of the arrow line indicate the magnitude and direction of the force applied to the droplet. The blue rhombus indicates the intersection of the optical

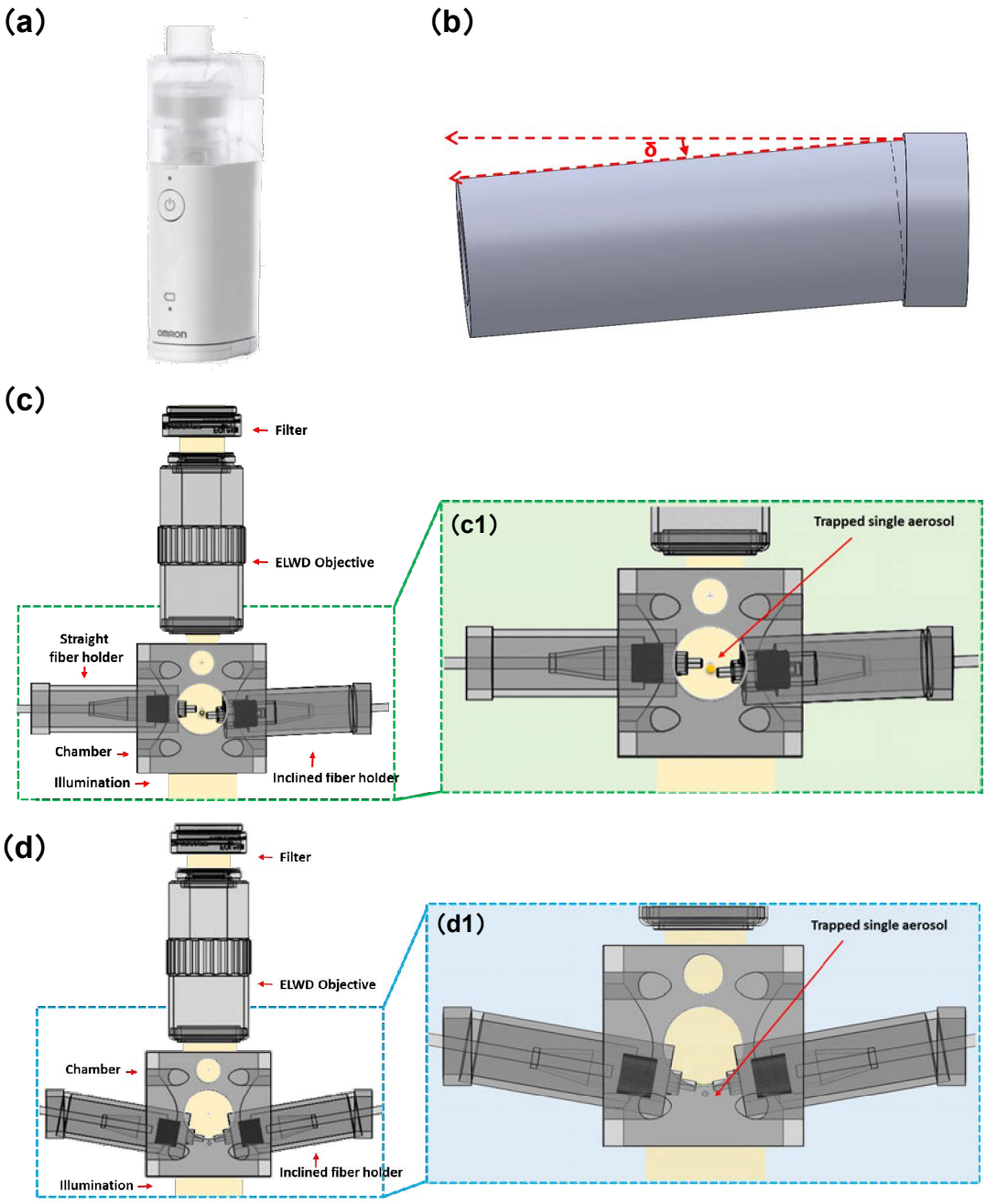

Figure 5.4: (a) Ultrasonic nebulizer for generating aerosol particles. (b) Custom-designed fiber holder with a specific angular deviation. (c) 3D setup of the aerosol trapping area and the (c1) zoom-in trapping chamber with one fiber tilted. (d) 3D setup of the aerosol trapping area and the (d1) zoom-in trapping chamber with two fibers tilted together.

axis of the right-inclined fiber and the line of z = 0. As the force field depends on the fiber's tilted angle, the droplet is finally stably trapped at the red dot position under the action of the force field. By doing so, we can quantify all possible trapped positions with the change of the tilt angle of one fiber, thus knowing the single fiber tilted threshold for single aerosol particle stable trapping. In Fig. 5.5(c) and (d), it demonstrates the droplet trapping positions on z axis and x axis as the increase of the one fiber tilted angle. The error bars represent data from calculating the average position and standard deviation of the trajectory data along one axis. We found that all achievable trapping positions are on the left side of the middle area of the two optical fibers' optical axis, and the maximum single fiber tilt angle that can achieve stable single droplet trapping does not exceed 8°.

After knowing the single fiber tilted threshold for single aerosol particle stable trapping, we are also interested in the case where dual fibers tilt together. In Fig. 5.6(a), it shows the simulated moving trajectory of the single droplet under the dual fiber trapping scheme with two fibers tilted of 10°. Also, Fig. 5.6(b) indicates the forces distributions applied to this aerosol particle in the xz plane under Fig. 5.6(a)'s trapping scheme. By analyzing these two figures, we found that the single droplet will finally be trapped in the position directly below the intersection of the optical axis of the two tilted fibers. Besides, we also found that dual fibers tilted trapping configuration shows better-trapping capability in terms of angular deviations. To quantify the maximum fiber tilted angle threshold for the dual fiber tilt configuration, in Fig. 5.6(c) and (d), the plots demonstrate the droplet trapped positions on the z-axis and x-axis as the increase of fiber tilted angle in the dual fibers tilt traps. We found that the maximum tilt angle that can achieve stable trapping is 13° for the dual fiber tilt configuration, which is more than 1.6 times compared with the one fiber tilted scheme. Besides, we also noticed that all the trapped positions are around the midpoint of the two optical fibers in the z-axis direction. However, in the x-axis direction, its position is directly below the intersection of the optical axes of the two optical fibers. Unlike the case of dual fiber tilted traps, the single droplet trapped positions are distributed on the left side of the middle area of the two fibers' optical axis in the one fiber tilted traps.

To verify the simulation results about the fiber tilted threshold for single aerosol particle stable trapping under two different trapping configurations, we designed and 3D printed the fiber holders with tilt angles of 5° and 10°, as shown in Fig. 5.7(a1) and (d1), to carry out the experiments of CP dual fiber trapping a single aerosol particle under

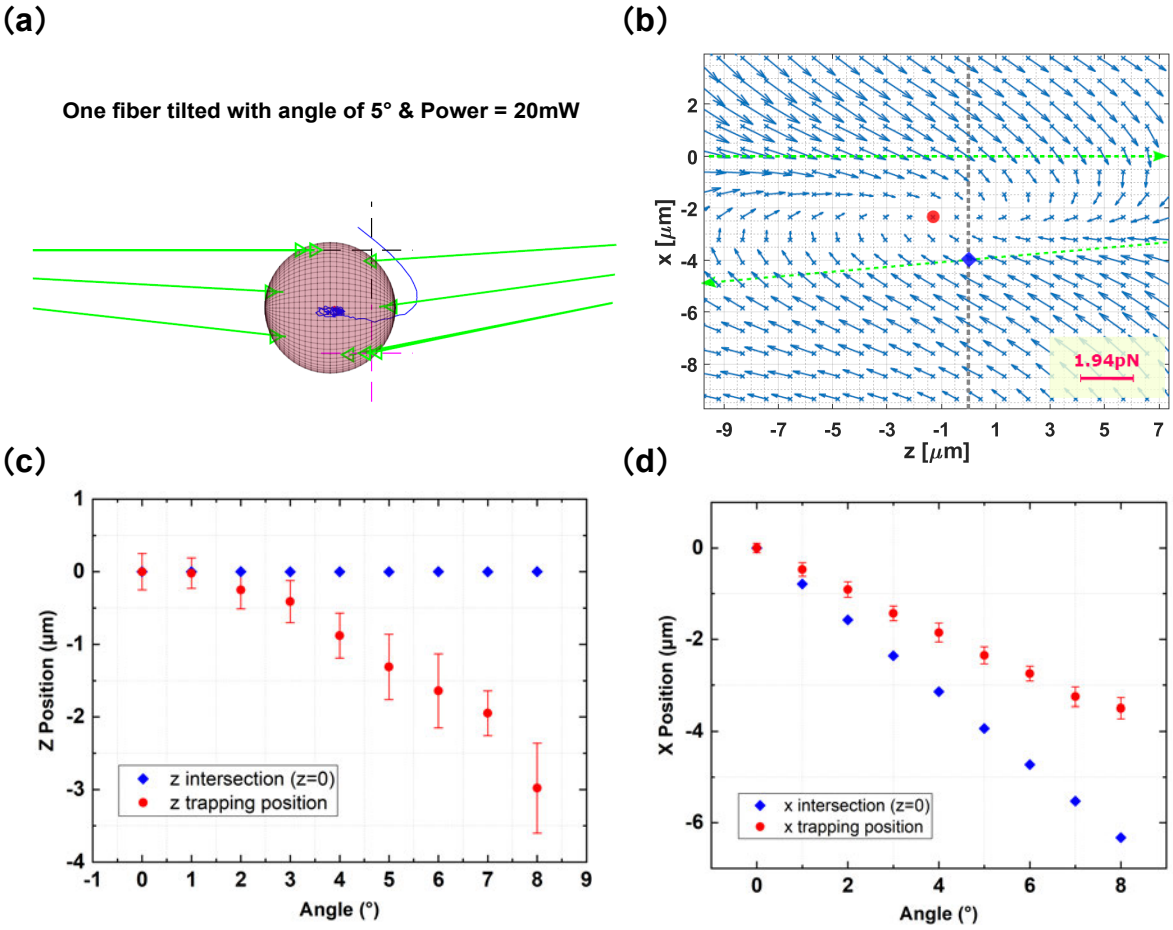

Figure 5.5: (a) Simulated moving trajectory of an aerosol under dual fiber trapping scheme with one fiber tilted at 5°. Each arrow represents each ray of light incident on the particle, since the display is a 2D plane view, multiple rays of light projected spatially will be superimposed on top of each other. (b) Forces distributions are applied to this aerosol particle in the xz plane under (a)'s trapping scheme, and the green dash lines indicate the optical axes of the two fibers. The blue rhombus indicates the intersection of the optical axis of the right-inclined fiber and the line of z = 0. The red dot position indicates the finally stably trapped position. (c) Variations of z-axis trapping positions as the increase of the one fiber tilted angle. (d) Variations of x-axis trapping positions as the increase of the one fiber tilted angle.

fiber tilted settings. As illustrated in Fig. 5.7(a2) and (d2), they showed the assembly models of the CP dual fiber trapping region in two trapping settings. By using these setups, we trapped the single salt droplet with a diameter of about 5μm, as shown in Fig. 5.7(b) and (e), respectively. To analyze the trapped droplet performance, we resolved the trapped droplets' trajectories along the x-axis and z-axis, as illustrated in Fig. 5.7(c) and (f), respectively, based on a custom-developed video-based single aerosol sub-pixel

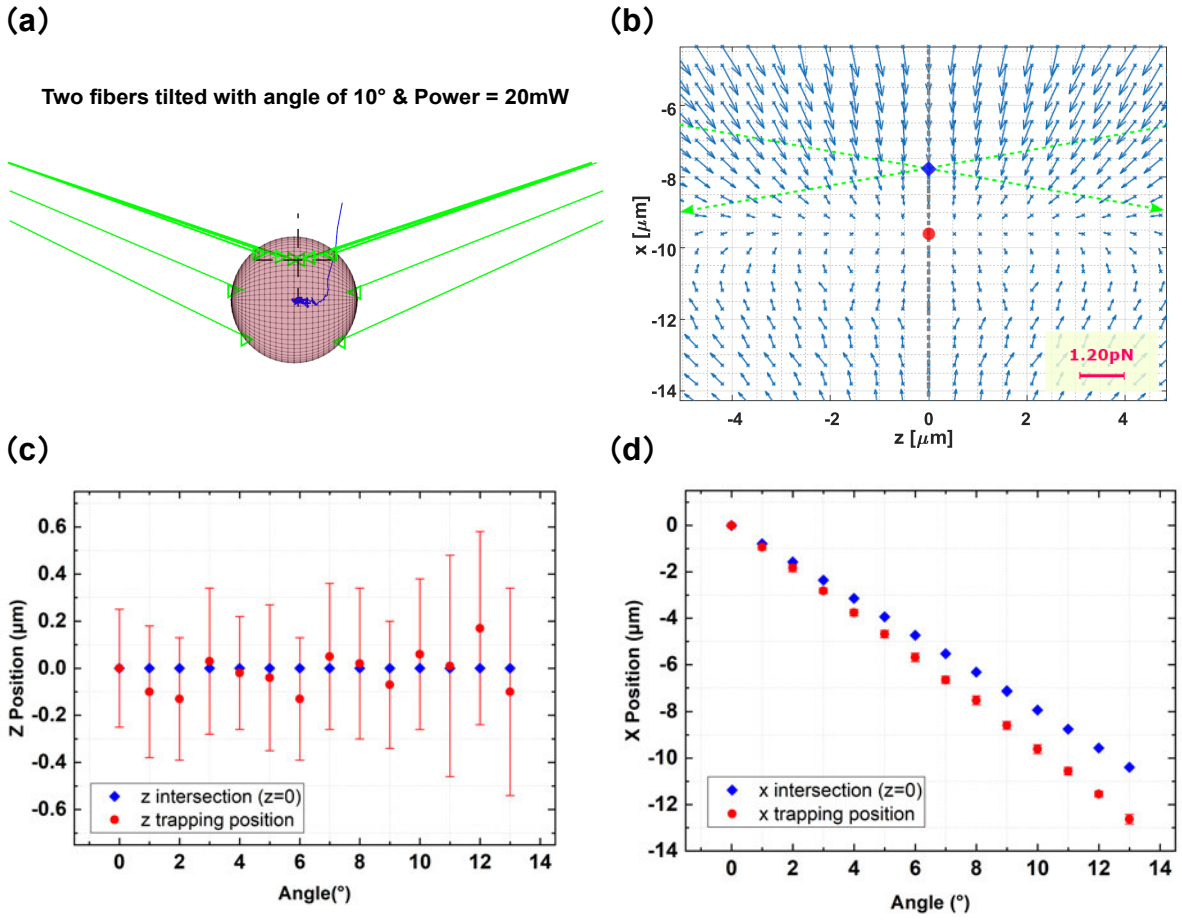

Figure 5.6: (a) Simulated moving trajectory of an aerosol under dual fiber trapping scheme with two fibers tilted of 10°. (b) Forces distributions are applied to this aerosol particle in the xz plane under (a)'s trapping scheme, and the green dash lines indicate the optical axes of the two fibers. The blue rhombus indicates the intersection of the optical axis of the two inclined fibers. The red dot position indicates the finally stably trapped position. (c) Variations of z-axis trapping positions as the increase of the two fibers' tilted angle. (d) Variations of x-axis trapping positions as the increase of the two fibers' tilted angle.

precision tracking algorithm. From the trajectories, we know that the single droplets trapped under the two tilted trapping settings all perform Brownian motion at the trapping position. The amplitude on the x-axis is smaller than the motion amplitude on the z for both droplets. It is worth noting that the amplitude of the single particle captured in the traps with a dual fiber tilt of 10° on the x-axis and z-axis is higher than the case of the single droplet captured in the traps with a single fiber tilt of 5°. The trapping stability in CP dual fiber traps with one fiber tilt of 5° is better than the case of CP dual fiber traps with two fiber tilts together of 10°. The above experimental results

demonstrate the consistency of the fiber tilt threshold for stable trapping of a single aerosol particle obtained by simulation.

5.4.2 Dynamics change with tilt angle over trapping threshold

After understanding the fiber-tilted threshold for single aerosol particle stable trapping under configurations of the single fiber tilt and dual fibers tilt together, we hope to explore the dynamic changes of the single droplet when the fiber angular deviation is more than the fiber tilt threshold for achieving stable trapping under these two trapping schemes.

Fig. 5.8(a) showed the simulated escaping motion trajectory of the single droplet in the dual fibers tilted traps with both fibers' angular deviations of 14°. The forces distributions plot shown in Fig. 5.8(b) well explains that when the tilt angle of the dual fiber is larger than 13°, the force field distribution applied on the single droplet cannot form a stable trapping position, and the distorted force field will make the droplet finally escape. Unlike the case of the large tilted angles of dual-fiber traps, more complex aerosol dynamics become apparent at higher single fiber tilt angles. In Fig. 5.9, it demonstrated three different types of droplet motions as the tilt angle moves beyond the stable trapping point. When the single fiber tilted angle ranges from 8.1° to 8.6°, the droplet will spiral inward in the area between the two fibers' optical axis until they arrive at the stable trapping position. Fig. 5.9(a) shows a single droplet's simulated spiral motion trajectory with a fiber tilt of 8.4°. In Fig. 5.9(b), the red dot indicates the finally trapped position after the spiral motion.

Table 5.1: Data of the orbit motion trajectory

Tilt angle / °	Orbit motion		Perimeters / μm	Frequency / Hz
	z axis (long axis) / μm	x axis (short axis) / μm		
8.7	1.96	0.54	4.52	56.8
8.8	2.28	0.62	5.25	87.7
8.9	2.93	0.69	6.69	92.6
9.0	2.96	0.71	6.76	99.0
9.1	3.06	0.82	7.04	100.0
9.2	3.16	1.04	7.39	103.1

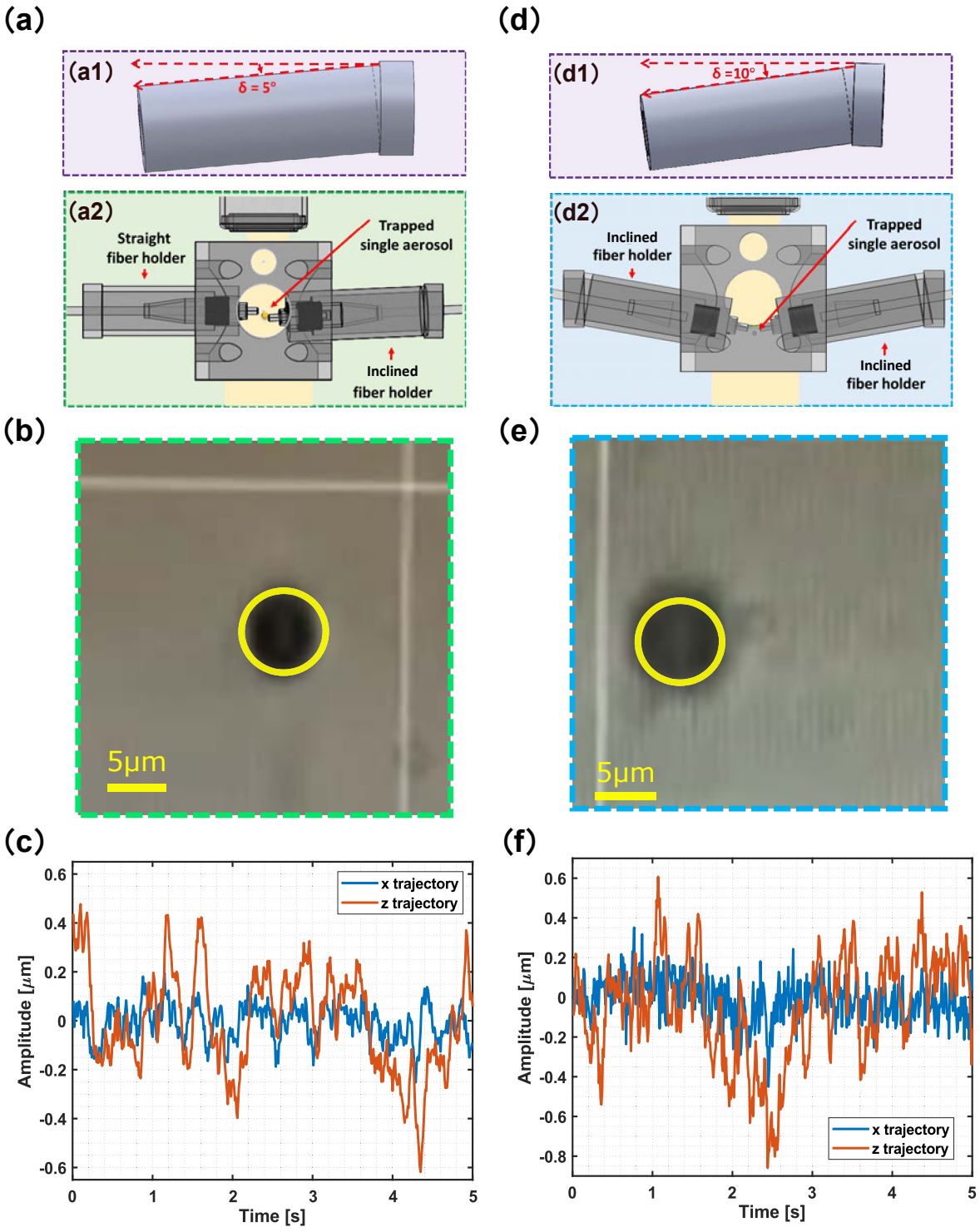

Figure 5.7: (a1) 3D printed tilted fiber holder with 5°. (a2) Model of the CP dual fiber trapping region with one fiber tilt. (b) Trapped droplet under (a)'s setting. (c) The trajectory of (b)'s trapped single droplet on the x-axis and z-axis. (d1) 3D printed tilted fiber holder with 10°. (d2) Model of the CP dual fiber trapping region with two fibers tilted together. (e) Trapped droplet under (d)'s setting. (f) The trajectory of (e)'s trapped single droplet on the x-axis and z-axis.

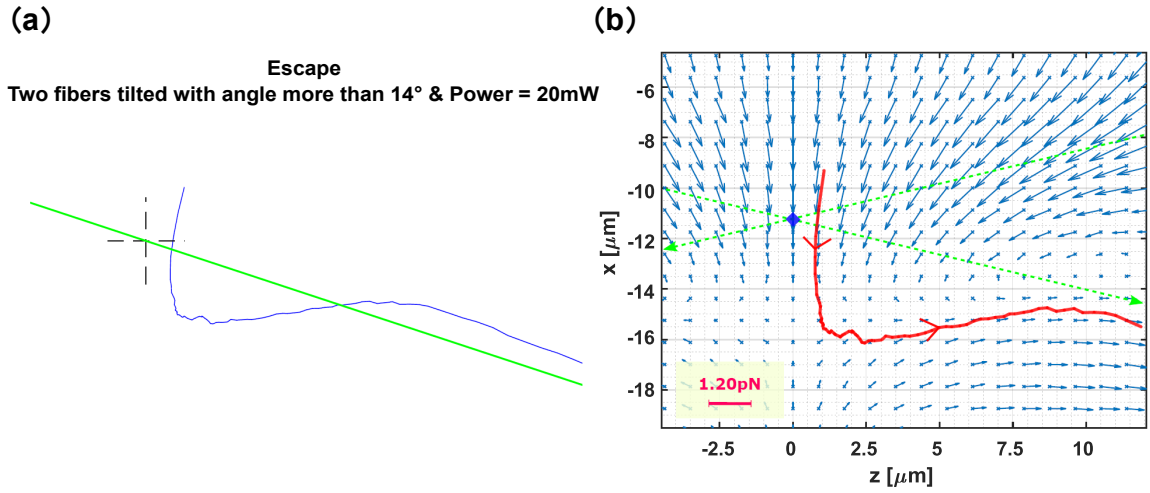

Figure 5.8: (a) The escaping motion trajectory of an aerosol under the dual fiber trapping scheme with two fibers tilted of 14°. (b) Forces distributions are applied to this aerosol particle in the xz plane under (a)'s trapping scheme. The green dash lines indicate the optical axes of the two fibers, and the solid red curve denotes the aerosol's trajectory.

When we further increased the single fiber tilted angle to the range of 8.7° to 9.2°, we found that the single droplet makes an approximately elliptical orbital motion in the middle region of the optical axis of the two fibers. As an example of this kind of motion type, Fig. 5.9(c) shows a single droplet's approximately elliptical orbit motion trajectory under a dual fiber capture scheme with a single fiber tilt of 9.0°. The droplet cannot finally reach a trapped position. Instead, it can only make the approximately elliptical orbit motion, which is mainly due to the effect of the vortex force field on the droplet at this time, as illustrated in Fig. 5.9(d). Moreover, according to Table 5.1, we also found that the perimeter and the frequency of the approximately elliptical orbit motion increase with the increase of the tilt angle of the single fiber. Finally, when the single fiber titled angle is more than 9.3°, Fig. 5.9(e) and (f) demonstrate that the single droplet will finally push away from the trapping field under the action of the distorted force field. It's important to highlight that with a consistent fiber output power, the emitted beam is divided into a uniform set of rays. This division serves to simulate the spatial impact of light force on individual aerosol particles. However, the varying tilt angles of the fiber introduce changes in the distribution of these rays. As the fiber's tilt angle increases, the spatial spread of rays expands. Initially, all rays have the potential to interact with the particles, but gradually, they lose this capability. Consequently, a

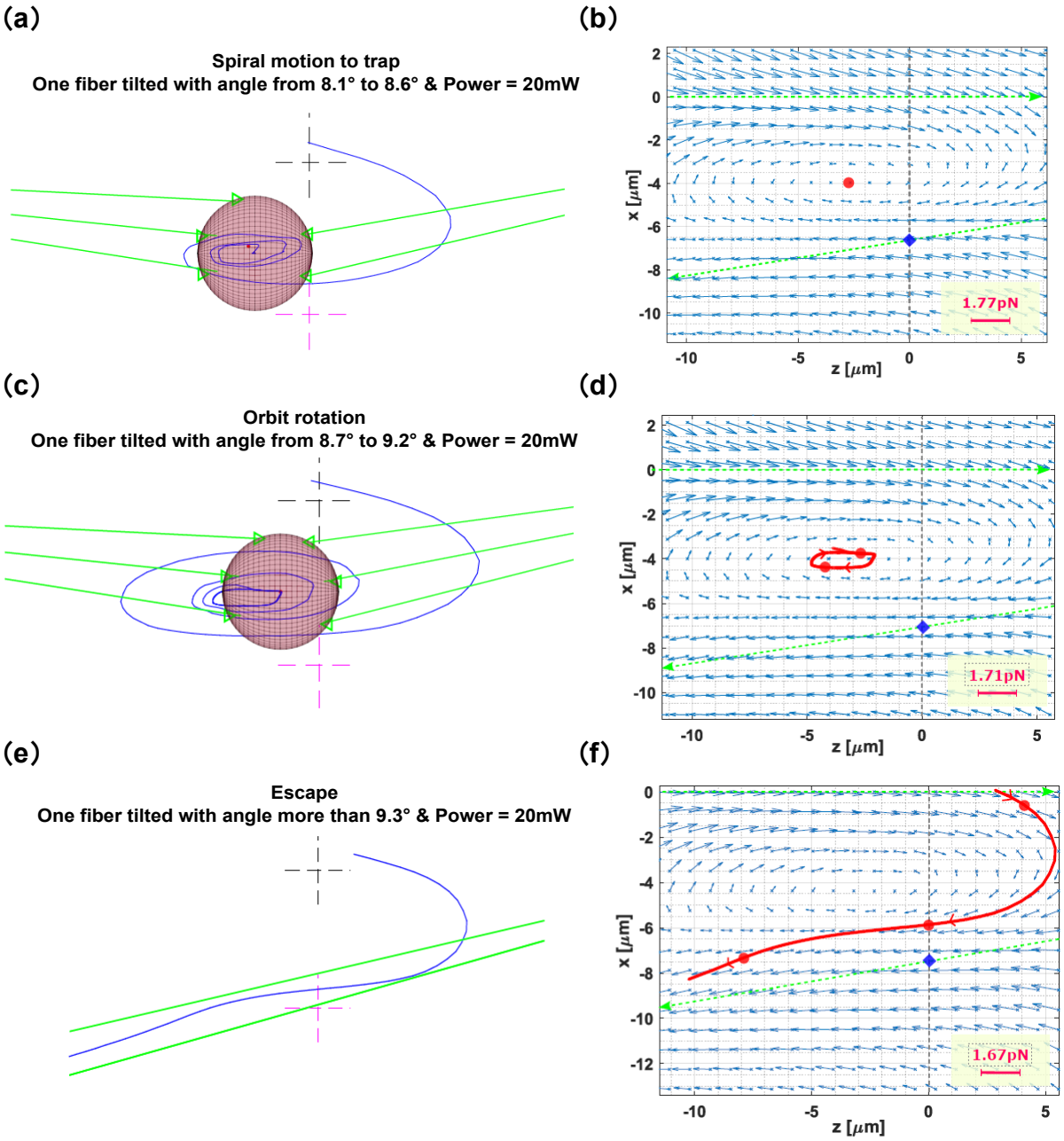

Figure 5.9: (a) The spiral motion trajectory of a single aerosol is simulated under a dual fiber trapping scheme with a fiber tilt of 8.4°. (b) Forces distributions are applied to this aerosol particle in the xz plane under (a)'s trapping scheme. (c) The orbit motion trajectory of a single aerosol is simulated under a dual fiber trapping scheme with a fiber tilt of 9.0°. (d) Forces distributions are applied to this aerosol particle in the xz plane under (c)'s trapping scheme. (e) The escaping motion trajectory of a single aerosol is simulated under a dual fiber trapping scheme with a fiber tilt of 9.3°. (f) Forces distributions are applied to this aerosol particle in the xz plane under (e)'s trapping scheme. The green dash lines indicate the optical axes of the two fibers in (b), (d) and (f), and the solid red curve denotes the aerosol's trajectory in (d) and (f). The green dash lines indicate the optical axes of the two fibers, and the solid red curve denotes the aerosol particle's trajectory.

noticeable discrepancy emerges in the count of rays influencing the particles' left and right sides. This phenomenon is clearly depicted in Fig. 5.9(a).

5.4.3 Trapping performance changes with four main factors

In this section, we seek to understand how four main factors (including beam divergence, fiber separation, fiber power, and aerosol radius) will affect the trapping performance of the tilted CP dual fiber traps. We can then find the selected quantitative four main parameters in the tilted CP dual fiber traps corresponding to the four main factors, providing us with a controlled way to improve the stable trapping performance as well as to manipulate the dynamics of the single aerosol. In anticipation of subsequent sections, I have introduced two specific terms: "maximum trap tilt angle" and "minimum escape tilt angle." I have provided these explanations preemptively to enhance reader comprehension of the upcoming content. To elaborate, the term "maximum trap tilt angle" denotes the utmost angle attainable within the established tilt trap arrangement. This angle ensures the maintenance of a stable trapping state. Conversely, the notion of the "minimum escape tilt angle" pertains to the smallest angle permissible in the defined tilt trap configuration. This angle induces a shift from either stable particle trapping or complex dynamics to a state of particle escape. In addition, it is important to highlight that in the scenario involving dual fiber tilt trapping, the kinetics of aerosol trapping exhibit a binary behavior, characterized by two states: trapping and escape. As a result, the intricate kinetics observed in the single fiber tilt trapping process are absent. Consequently, we focus solely on establishing the uppermost angle at which trapping occurs. It is worth noting that this maximum trap tilt angle is also a critical value for the corresponding minimum angle at which escape occurs.

5.4.3.1 Output beam divergence

As shown in Fig. 5.10(a), for the one fiber tilted CP dual fiber traps, as the SMF beam divergence increases (NA increases from 0.10 to 0.40 in steps of 0.05, i.e., the Beam divergence angle increases from 5.73° to 22.92°), the maximum trap tilt angle in one fiber tilted CP dual fiber traps that can achieve single aerosol stable trapping is increasing first and then decreasing. When the NA of the SMF is equal to 0.30 (beam divergence of 17.19°), the maximum trap tilt angle that can achieve single aerosol stable trapping in CP dual fiber traps with single fiber tilt is 12.2°. Similarly, as the SMF beam divergence increases, the minimum escape tilt angle in one fiber tilted CP dual fiber trap that

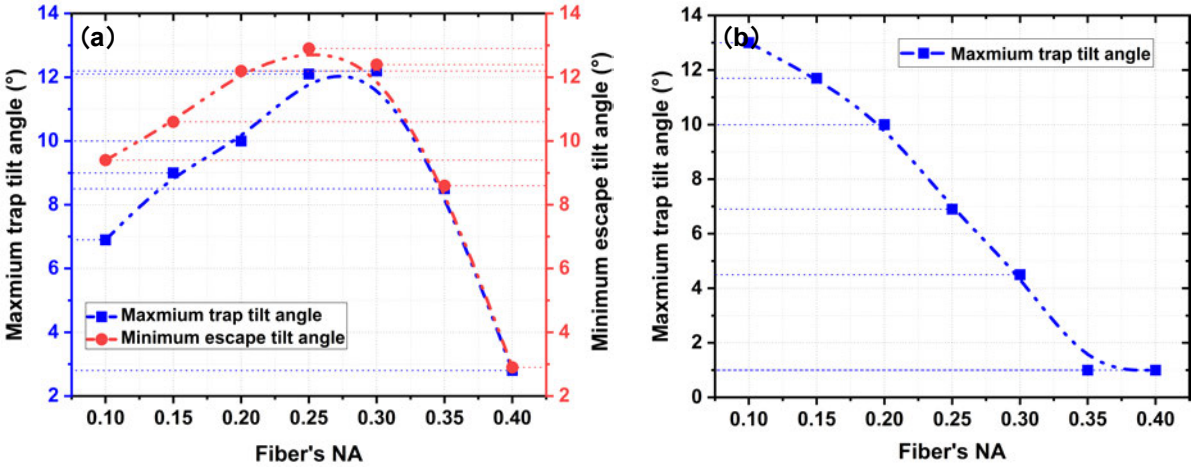

Figure 5.10: Variation of the maximum trap tilt angle and minimum escape tilt angle with different fiber output beam divergence (Fiber's NA increases from 0.10 to 0.40 in steps of 0.05) under (a) one fiber tilt CP dual fiber traps, and (b) two fiber tilt CP dual fiber traps.

can result in individual aerosol escaping also increases first and then decreases. When the NA of the SMF equals 0.25 (beam divergence of 14.32°), the minimum escape tilt angle that causes single aerosol escaping in CP dual fiber traps with single fiber tilt is 12.9°. Furthermore, in the CP dual fiber traps with single fiber tilt, all the minimum escape tilt angles that cause single aerosol escaping are larger than the maximum trap tilt angle that can achieve single aerosol stable trapping at the corresponding NA (or beam divergence). Finally, in the NA range from 0.10 to 0.25, when the single fiber tilt angle is between the maximum trap tilt angle for single aerosol stable trapping and the minimum escape tilt angle for single aerosol escaping, the dynamics of the individual aerosol changes in a complex and diverse manner (including spiral motion, orbit rotation) as the single fiber tilt angle varies. However, when NA is in the range of 0.30 to 0.40, the dynamics of the single aerosol are only trapped and escape as the single fiber tilt angle changes, with no other complex dynamic processes.

For the two fiber tilted CP dual fiber traps shown in Fig. 5.10(b), as the SMF beam divergence increases (NA increases from 0.10 to 0.40 in steps of 0.05, i.e., the beam divergence angle increases from 5.73° to 22.92°), the maximum trap tilt angle in two fiber tilted CP dual fiber traps that can achieve single aerosol stable trapping shows an approximately linear decrease with a reduction of 82.3% or 12° from 13° to 1°. When the two fibers' tilt angle is greater than the maximum trap tilt angle that can achieve single aerosol stable trapping in two fiber tilted CP dual fiber traps under the corresponding

SMF beam divergence, the individual aerosol will no longer be trapped and will escape directly.

5.4.3.2 Fiber separation distance

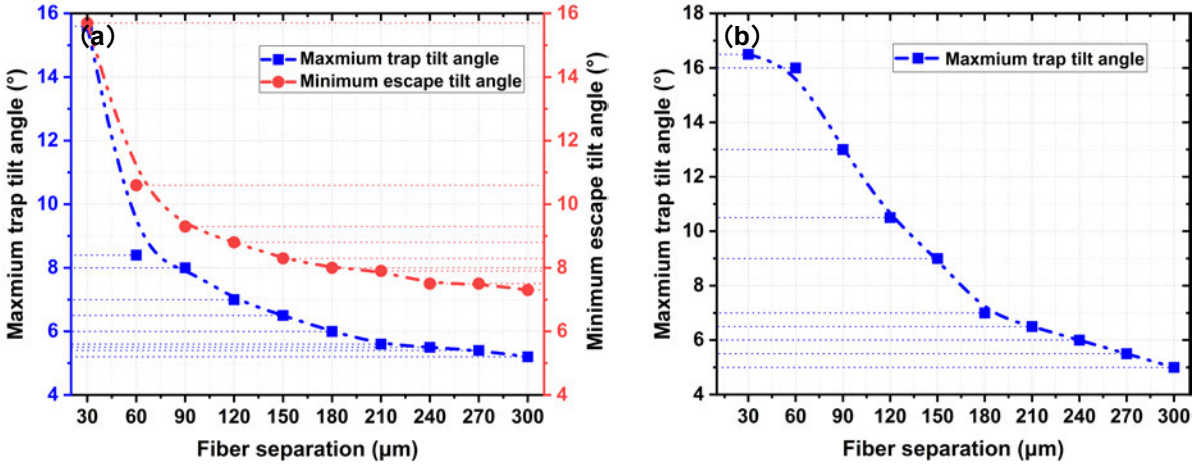

Figure 5.11: Variation of the maximum trap tilt angle and minimum escape tilt angle with different fiber separation distance increasing from 30μm to 300μm in steps of 30μm under (a) one fiber tilt CP dual fiber traps, and (b) two fiber tilt CP dual fiber traps.

In Fig. 5.11((a), as the separation of two fibers increases (Fiber separation increases from 30μm to 300μm in steps of 30μm), the maximum trap tilt angle in one fiber tilted CP dual fiber traps that can achieve single aerosol stable trapping decreases gradually. When the separation is between 30μm and 90μm, the maximum trap tilt angle is reduced more rapidly by 7.6° from 15.6° to 8.0° with a reduction of 48.7%. When separation is between 120μm and 300μm, single fiber tilt CP dual fiber traps can achieve a slower reduction in the maximum trap tilt angle, with the maximum trap tilt angle decreasing from 7.0° to 5.2°, a decrease of 1.8°, or 25.7%. Similarly, as the two fiber separation increases, the minimum escaping tilt angle in one fiber-tilted CP dual fiber trap that can result in individual aerosol escaping also decreases gradually. When the separation is between 30μm and 90μm, the minimum escaping tilt angle is reduced by 6.4° from 15.7° to 9.3°, a reduction of 40.8%. When separation is between 120μm and 300μm, single fiber tilt CP dual fiber traps can achieve a slower reduction in the minimum escaping tilt angle, with the minimum escape tilt angle decreasing from 8.8° to 7.3°, a decrease of 1.5°, or 17.0%. Furthermore, in the CP dual fiber traps with single fiber tilt, all the minimum escape tilt angles that cause single aerosol escaping are larger than the maximum trap tilt angle that can achieve single aerosol stable trapping at

the corresponding fiber separation. Finally, in the range of fiber separation from 30μm to 300μm, except in the case of fiber separation of 30μm, the dynamics of the single aerosol are only trapped and escape as the single fiber tilt angle changes. While in the fiber separation range of 60μm to 300μm, the dynamics of the individual aerosol change in a complex and diverse manner (including spiral motion, and orbit rotation) as the single fiber tilt angle changes, when the single fiber tilt angle is between the maximum trap tilt angle for single aerosol stable trapping and the minimum escape tilt angle for single aerosol escaping. In addition, this interval of single fiber tilt angles, in which the dynamics of single aerosol exhibit complex and diverse processes, also increases slowly with increasing fiber separation, by 76.9%.

The present investigation examines the performance of two fiber-tilted CP dual fiber traps, as depicted in Fig. 5.11(b), as a function of the distance between the fibers. Specifically, the maximum tilt angle required for achieving single aerosol stable trapping was determined for various fiber separations, ranging from 30μm to 300μm at intervals of 30μm. The results demonstrate a gradual reduction in the maximum trap tilt angle as the distance between the fibers increases, declining by 69.7% or 11.5° from 16.5° to 5°. Notably, when the tilt angle of the two fibers exceeds the maximum trap tilt angle for achieving single aerosol stable trapping at the corresponding fiber separation distance, the individual aerosol will no longer be confined and will escape directly.

5.4.3.3 Fiber output power

In Fig. 5.12(a), as the two fiber output power increases (fiber output power increases from 20mW to 200mW in steps of 20mW), the maximum trap tilt angle in one fiber tilted CP dual fiber traps that can achieve single aerosol stable trapping decreases gradually by 3° from 8.0° to 5.0° with a reduction of 37.5%. Similarly, as the two fiber output power increases, the minimum escaping tilt angle in one fiber tilted CP dual fiber traps that can result in individual aerosol escaping also decreases gradually by 1° from 9.3° to 8.3° with a reduction of 10.8%. Furthermore, in the CP dual fiber traps with single fiber tilt, all the minimum escape tilt angles that cause single aerosol escaping are more significant than the maximum trap tilt angle that can achieve single aerosol stable trapping at the corresponding fiber output power. Finally, in the range of fiber output power from 20mW to 200mW, when the single fiber tilt angle is between the maximum trap tilt angle for single aerosol stable trapping and the minimum escape tilt angle for single aerosol escaping, the dynamics of the single aerosol changes in a complex and diverse manner

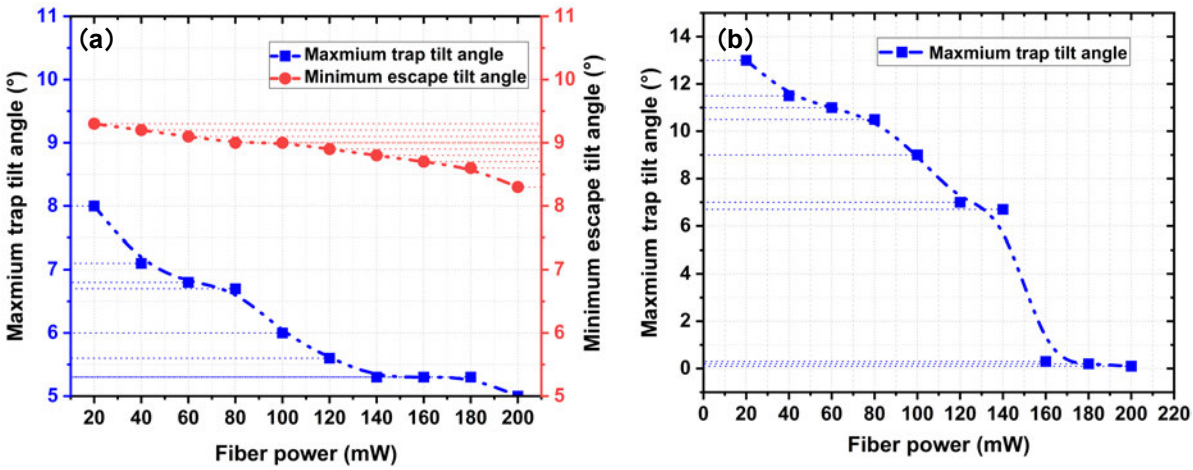

Figure 5.12: Variation of the maximum trap tilt angle and minimum escape tilt angle with different fiber output power increasing from 20mW to 200mW in steps of 20mW under (a) one fiber tilt CP dual fiber traps, and (b) two fiber tilt CP dual fiber traps.

(including spiral motion, orbit rotation) as the single fiber tilt angle varies. In addition, this interval of single fiber tilt angles, in which the dynamics of single aerosol exhibit complex and diverse processes, also increases intensively with increasing fiber output power, by around 153%.

The study explores the efficacy of two fiber tilted CP dual fiber traps, as shown in Fig. 5.12(b), concerning the output power of the fibers. The study measured the maximum tilt angle necessary to achieve single aerosol stable trapping for various fiber output powers ranging from 20mW to 200mW in increments of 20mW. The findings reveal a gradual decline in the maximum trap tilt angle as the output power of the fibers increases, with a reduction of 99.2% or 12.9° from 13° to 0.1°. Notably, at an output power of 160mW, the maximum trap tilt angle decreases dramatically from 6.7° to 0.3°, with a reduction of 6.4° or 95.5%. Exceeding the maximum trap tilt angle for achieving single aerosol stable trapping in two fiber tilted CP dual fiber traps at the corresponding fiber output power by the tilt angle of the two fibers results in the direct escape of the individual aerosol, as it is no longer confined.

5.4.3.4 Aerosol radius

The results presented in Fig. 5.13(a) indicate that, as the radius of an aerosol particle increases incrementally from 0.5μm to 10.5μm, the maximum tilt angle required for stable trapping of a single aerosol in one fiber tilted CP dual fiber trap increases gradually,

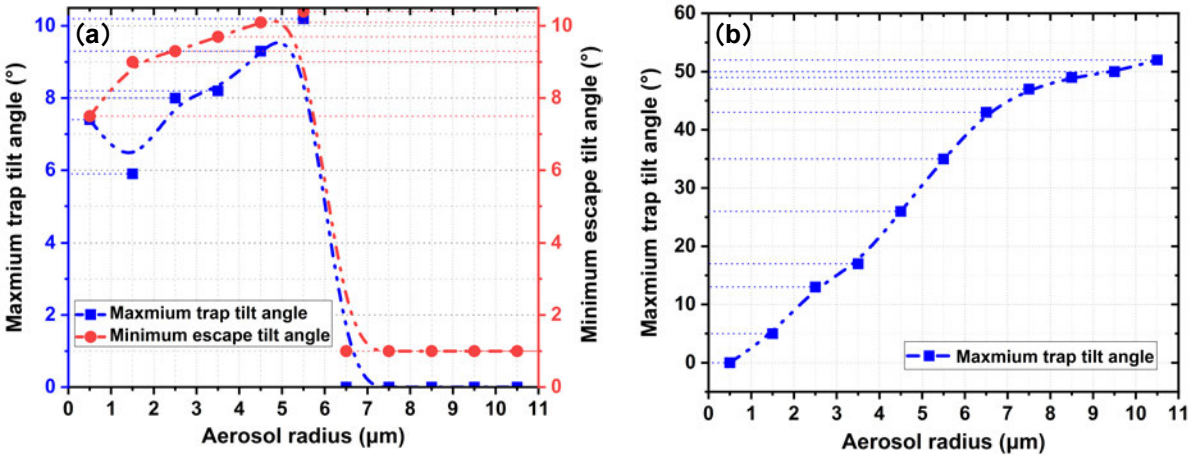

Figure 5.13: Variation of the maximum trap tilt angle and minimum escape tilt angle with different aerosol radius increasing from 0.5μm to 10.5μm in steps of 1.0μm under (a) one fiber tilt CP dual fiber traps, and (b) two fiber tilt CP dual fiber traps.

reaches a peak of 10.2° when the aerosol radius is 5.5μm, and then abruptly decreases to 0° beyond 6.5μm. Similarly, the minimum tilt angle required for a single aerosol to escape the trap increases gradually before reaching a maximum value of 10.4° at an aerosol radius of 5.5μm, and then drops sharply to 1° for larger radii. Furthermore, the minimum escape tilt angles in one fiber tilted CP dual fiber traps are found to be greater than the maximum trap tilt angles required for stable trapping of a single aerosol at corresponding radii. The dynamics of a single aerosol in this type of trap change in a complex manner when the tilt angle is between the maximum trap tilt angle and the minimum escape tilt angle, with various behaviors such as spiral motion and orbit rotation observed for aerosols with radii in the range of 1.5μm to 5.5μm. However, this complex behavior interval decreases with increasing aerosol radius by 93.5%. For larger aerosol radii (6.5μm to 10.5μm), the dynamics of a single aerosol are limited to trapping and escape as the single fiber tilt angle changes, with no other complex processes observed. The results in Fig. 5.13(b) demonstrate that in two fiber tilted CP dual fiber traps, the maximum trap tilt angle required for stable trapping of a single aerosol increases gradually with increasing aerosol radius, reaching a peak of 52° at a radius of 10.5μm, and that the individual aerosol will escape directly when the two fiber tilt angle exceeds the maximum trap tilt angle at corresponding radii. It should be noted that the results for an aerosol radius of 0.5μm are unreliable due to the limitations of the ray optics model used in this study.

5.5 Conclusion

Dual beam fiber traps are potentially useful for integrated trapping devices aimed at studying aerosols, and offer opportunities for cavity-enhanced traps. The alignment of such traps is typically seen to be critical. Here we explore the impact of the angular alignment of the optical fibers, and assess trapping viability as a function of misalignment and how particle dynamics change when interacting with displaced fibers. We calculated the optical forces and simulated dynamics of the single aerosol particle under configurations of the single fiber tilt and two fibers tilt together, respectively, based on the ray optics model and OTS toolbox. We consider a typical aerosol (diameter of aerosol: 5μm, the refractive index of aerosol: 1.344, two fiber separation distance: 90μm, fiber output power: 20mW), and find that in the situation where one of the fibers is tilted, stable aerosol trapping with a maximum tilt angle of 8° is possible. For the dual-fiber tilt configuration, the maximum tilt angle that can achieve stable trapping is 13°. In the case of single fiber tilt configuration, we find three different sets of dynamics as the tilt angle moves beyond the stable trapping point: spiral motion (tilt angle is from 8.1° to 8.6°), orbital rotation (tilt angle is from 8.7° to 9.2°), and escape (tilt angle is more than 9.3°). While in the case of the dual fibers tilt configuration with the tilted angle more than 13°, an aerosol will escape. Furthermore, we also investigate how the four main factors (including beam divergence, fiber separation distance, fiber output power, and aerosol radius) will influence the single aerosol particle trapping performance and dynamic changes in the tilted CP dual fiber traps. The carefully selected quantitative four main parameters corresponding to four main factors in the one fiber tilted CP dual fiber traps is to provide a controllable way to manipulate the single aerosol complex dynamics (including spiral motion, and orbit rotation). The findings provide insight into the development of fiber-based optical traps as well as a novel approach to managing light-induced rotation in air.

While it is important to highlight that our analysis in this chapter has been confined to the examination of four primary factors. These factors have been instrumental as inputs for quantitatively investigating the efficacy of trapping individual aerosol particles across three distinct trapping configurations. However, it is crucial to acknowledge the existence of a multitude of additional variables that warrant comprehensive consideration within the framework of a systematic inquiry. Notably, these variables encompass factors such as the aerosol species, and consequently entail parameters like refractive index and

scattering efficiencies, as well as the kinetic behavior of aerosol evaporation when exposed to light irradiation. Incorporating these nuanced variables into our analytical framework holds the promise of refining our understanding and enhancing our modeling pursuits, ultimately yielding a more precise comprehension of the intricate capacity and variability inherent in aerosol particle trapping characteristics.

CHAPTER 6

NON-SPHERICAL AEROSOL TRAPPING DYNAMICS

In previous studies, we treated aerosol particles as a sphere to investigate the size range of trapped particles, as well as their dynamics under the CP dual fiber traps. However, many aerosols are non-spherical and often approximately ellipsoids. As such, in this chapter, we quantitatively study the trapping size range and kinetic properties of individual ellipsoidal particles under three different CP dual fiber trapping schemes based on the ray optics model, and compare the results with the case of spherical particles of the same volume, which provides a more accurate understanding of the droplet trapping dynamics in the CP dual fiber traps.

6.1 Introduction

Aerosols are small solid or liquid particles found in the air that have various uses and economic impacts. They are present in many products, from air fresheners to car exhausts, and they can have negative effects on the environment and human health [14, 34]. At the same time, aerosols play an important role in our climate by cooling the planet and protecting it from excessive warming [145]. One possible solution to studying individual aerosol dynamics and properties is to use optical trapping [64], a technique that uses focused lasers to confine the particles [12]. Researchers have developed different types of aerosol optical trapping configurations in recent years, each with its own advantages and benefits. For example, optical levitation can be used to achieve 2D trapping and guiding in air [9, 148], while optical tweezers allow for more stable 3D trapping [99, 112].

CP dual beam traps make it possible to capture aerosol particles in a larger size range and provide longer working distances [133, 156], and confocal beam traps retain these benefits while being easier to set up [67]. Holographic tweezers modulate the trapping beam to enable controlled and dynamically tunable 3D trapping and manipulations [1, 25]. Optical fiber-based traps, on the other hand, offer more flexibility and unique advantages in trapping and manipulating individual aerosol particles [90, 102, 134], including simple fabrication, easy integration, flexible arrangement, no operational depth limitation, and low-cost. The focus of this thesis is on using CP dual fiber traps to study the trapping and manipulation of single aerosol particles. It is noteworthy that all previous studies on the trapping performance of liquid aerosol particles by the CP dual fiber traps have treated them as standard spheres [134]. However, from an experimental point of view, the real liquid aerosol particle is far from exhibiting this simple shape. It is because the actual shape of liquid aerosol particles, like a water droplet in my previous trapping experiment, can be influenced by various factors such as air resistance, gravity, and surface impurities, which result in their shape being more like an ellipsoid. As a result, it is necessary to develop a new particle model that takes these factors into account and utilizes numerical calculations of the optical forces in the CP dual fiber trap. This will provide a more accurate representation of the physical reality and allow researchers to explore certain parameters that may be difficult or impossible to obtain through experimentation in the short term. By doing so, valuable insights can be gained for future experiments.

In this chapter, we will first develop a new model for liquid ellipsoidal particles and show how we calculate the optical force and optical torque, as well as model the dynamics of liquid ellipsoidal particles in the CP dual fiber traps. Then we will quantitatively investigate the trapping size range and kinetic properties of individual ellipsoidal particles under three different CP dual fiber trapping schemes and compare the results with the case of spherical particles of the same volume.

6.2 Model

In this section, I will calculate the optical forces and torques of a micron-sized ellipsoid trapped in the CP dual fiber trap based on vector ray tracing and rotational coordinate transformation [140, 175], thus numerically simulating its dynamics in the optical trap to provide a computational model for quantitatively describing the range of trapping sizes

and dynamics of individual ellipsoid particles in three different CP dual fiber trapping schemes.

6.2.1 Single ray

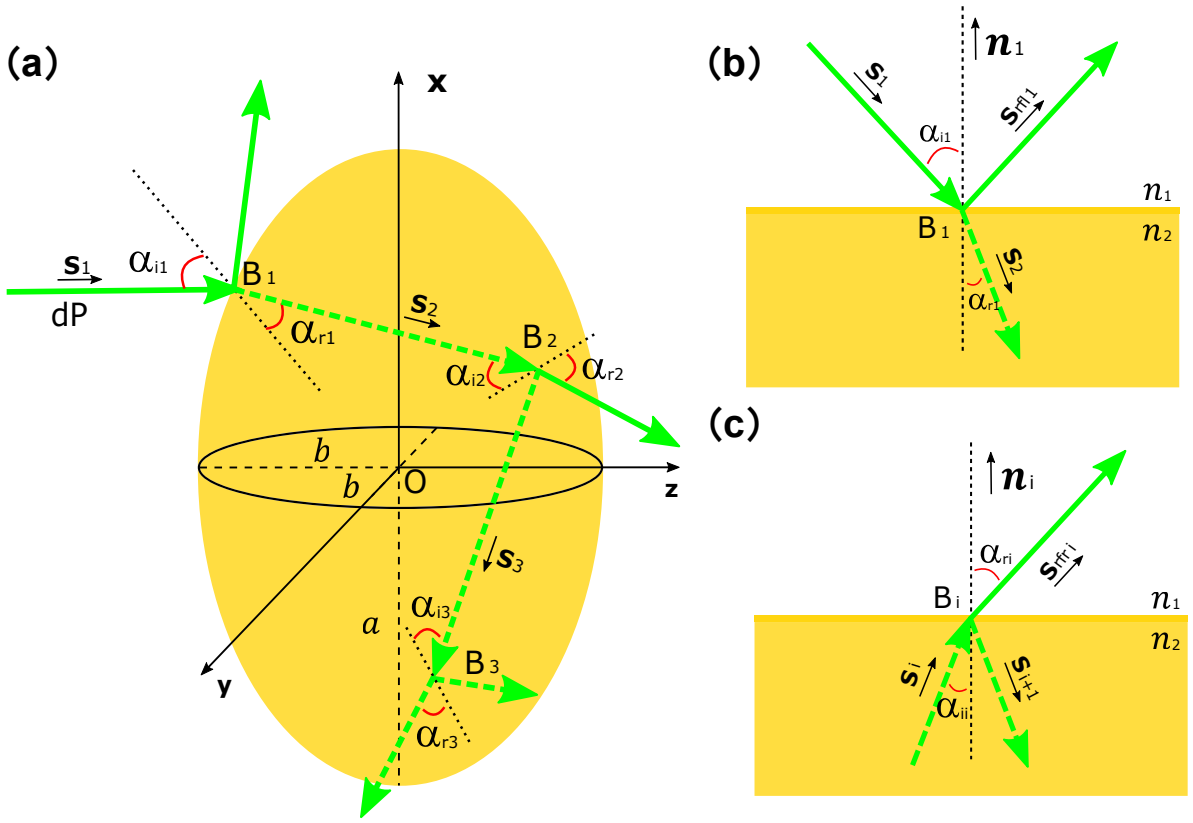

Figure 6.1: (a) Schematic diagram of the ray model of the effect of momentum transfer between light and micro-sized ellipsoidal particle after irradiating the ellipsoid with a single ray. (b) Schematic diagram of the reflection and refraction occurring when a single ray first hits the surface of an ellipsoid. (c) Schematic diagram of the reflection and refraction of a single ray of light when it makes its i^{th} transmission from the ellipsoid to air.

As shown in Fig. 6.1(a), a ray of power dP incident at an angle of α_{i1} hits the surface of the micro-sized ellipsoidal particle with a transferred momentum of $n_1 dP/c$ per second, which is reflected and refracted at point B_1 on the ellipsoidal surface. According to Fresnel's law [140], the reflection coefficient R_1 can be obtained according to Eq. (6.1), also the transmission coefficient T_1 follows Eq. (6.2). To simplify the calculation, we assume that two axes of the ellipsoid are equal in length and less than the third axis,

letting the long axis be $2a$ and the short axis be $2b$. In addition, we establish a Cartesian coordinate system S with the long axis of the ellipsoid as the x-axis, the two short axes as the y-axis and z-axis, and the center of the ellipsoid O as the origin. The points on the surface of the ellipsoid satisfy Eq. (6.3).

$$R_i = \frac{1}{2}\left[\frac{\sin^2(\alpha_{ii}-\alpha_{ri})}{\sin^2(\alpha_{ii}+\alpha_{ri})}+\frac{\tan^2(\alpha_{ii}-\alpha_{ri})}{\tan^2(\alpha_{ii}+\alpha_{ri})}\right] \tag{6.1}$$

$$R_i + T_i = 1 \tag{6.2}$$

$$\frac{x^2}{a^2}+\frac{y^2}{b^2}+\frac{z^2}{b^2} = 1 \tag{6.3}$$

Thereafter, depending on the number of reflections of the rays inside the ellipsoid, this leads to different energies carried by the outgoing rays, whose magnitudes are dPR_1, dPT_1T_2, $dPT_1R_2T_3$,...., $dPT_1R_2\cdots R_{i-1}T_i$, ... respectively. Based on these changes, we can calculate the optical forces and torques produced by a single ray on the ellipsoid. However, unlike the spherical particle, the angle of each reflection and refraction of a single ray inside the ellipsoid is different, so the optical trapping forces and torques generated by each reflection and refraction need to be calculated separately and finally integrated. Since we are simulating the trapping performance of ellipsoidal droplets in air, for the first reflection and refraction, the incident light is incident from a low refractive index medium to a high refractive index medium, while the subsequent reflection and refraction are the opposite, incident from a high refractive index medium to a low refractive index medium. Therefore, the calculation of optical forces and torques is different for these two cases, and we will discuss them separately.

Fig. 6.1(b) is a schematic diagram of the reflection and refraction occurring when a single ray first hits the surface B_1 of the ellipsoid, where n_1 denotes the ambient refractive index, n_2 denotes the refractive index of the ellipsoid, and $\boldsymbol{n}_1$ represents the unit vector in the normal direction. Here, we assume that the azimuth of point B_1 is (θ,φ), then its coordinates can be expressed as:

$$\mathbf{r}_1 = (x_1, y_1, z_1) = \mathrm{r}_1(\sin\theta\cos\varphi, \sin\theta\sin\varphi, \cos\theta) \tag{6.4}$$

By substituting B_1 into Eq. (6.2), r_1 can be expressed as:

$$\mathrm{r}_1 = \sqrt{\frac{a^2 b^2}{b^2\sin^2\theta\cos^2\varphi + a^2\sin^2\theta\sin^2\varphi + a^2\cos^2\theta}} \tag{6.5}$$

Assuming that the coordinates of the light source of the single ray are (x_0, y_0, z_0), the unit vector $\mathbf{s}_1$ of the incident ray can be expressed as:

$$\mathbf{s}_1 = \frac{1}{\sqrt{(x_1 - x_0)^2 + (y_1 - y_0)^2 + (z_1 - z_0)^2}}(x_1 - x_0, y_1 - y_0, z_1 - z_0) \tag{6.6}$$

By deriving Eq. (6.2), the unit vector $\boldsymbol{n}_1$ corresponding to the normal direction at B_1 can be obtained as:

$$\boldsymbol{n}_1 = \sqrt{\frac{x_1^2}{a^4} + \frac{y_1^2}{b^4} + \frac{z_1^2}{b^4}} \cdot \left(\frac{x_1}{a^2}, \frac{y_1}{b^2}, \frac{z_1}{b^2}\right) \tag{6.7}$$

The optical force $\boldsymbol{F}_1$ resulting from the first reflection and refraction can be expressed as:

$$\begin{aligned} \boldsymbol{F}_1 = \frac{\Delta \boldsymbol{P}}{\Delta t} &= \frac{n_1 dP}{c}\mathbf{s}_1 - \frac{n_1 dP R_1}{c}\mathbf{s}_{rfl1} - \frac{n_2 dP T_1}{c}\mathbf{s}_2 \\ &= \frac{dP}{c}[n_1(1 + R_1)\cos\alpha_{i1} - n_2 T_1 \cos\alpha_{r1}]\boldsymbol{n}_1 \end{aligned} \tag{6.8}$$

Where the incidence angle α_{i1} and refraction angle α_{r1} can be calculated through Eq. (6.9) and Eq. (6.10).

$$\cos\alpha_{i1} = -\mathbf{s}_1 \cdot \boldsymbol{n}_1 \tag{6.9}$$

$$\sin\alpha_{r1} = \frac{n_1}{n_2}\sin\alpha_{i1} \tag{6.10}$$

Next, I will calculate the optical forces due to subsequent reflections and refractions of a single ray of light as it is transmitted from the ellipsoid to air. To facilitate the calculation, we define the new Cartesian coordinate system S_i' with the $\boldsymbol{n}_i$ direction as the z-axis direction. In the original coordinate system S, assuming spatial azimuth of $\boldsymbol{n}_i$ is (θ_i, φ_i), then this azimuth is the angle of spatial change from the coordinate system S to the coordinate system S_i', and the corresponding rotation matrices are defined as follow:

$$\mathrm{Rot}_{zi} = \begin{bmatrix} \cos\varphi_i & \sin\varphi_i & 0 \\ -\sin\varphi_i & \cos\varphi_i & 0 \\ 0 & 0 & 1 \end{bmatrix} \tag{6.11}$$

$$\mathrm{Rot}_{yi} = \begin{bmatrix} \cos\theta_i & 0 & -\sin\theta_i \\ 0 & 1 & 0 \\ \sin\theta_i & 0 & \cos\theta_i \end{bmatrix} \tag{6.12}$$

Then the coordinates of $\mathbf{s}_i$ in S_{i-1}' can be obtained through Eq. (6.13), where "T" denotes the transpose operation. Meanwhile, the spatial azimuth $(\theta_{si}', \varphi_{si}')$ of $\mathbf{s}_i'$ with respect to the coordinate system S_{i-1}' can also be calculated through Eq. (6.13).

$$\mathbf{s}_i'^{\mathrm{T}} = \mathrm{Rot}_{yi} \cdot \mathrm{Rot}_{zi} \cdot \mathbf{s}_i^{\mathrm{T}} \tag{6.13}$$

According to Fig. 6.1(b), $\mathbf{s}_2$ is the unit vector of the refracted ray when the reflection and refraction occur for the first time. Based on the spatial geometric relationship, the spatial azimuth of $\mathbf{s}_2'$ in the coordinate system S_1' can be expressed as $(\pi - \alpha_{r1}, \varphi_{s1}')$, then its coordinates can be expressed as:

$$\mathbf{s}_2' = \left(\sin\alpha_{r1}\cos\varphi_{s1}', \sin\alpha_{r1}\sin\varphi_{s1}', -\cos\alpha_{r1}\right) \tag{6.14}$$

According to Fig. 6.1(c), when the single ray undergoes the i^{th} reflection and refraction ($i \geqslant 2$), $\mathbf{s}_{i+1}$ is the unit vector of the reflected ray at the i^{th} reflection and refraction. Based on the spatial geometric relationship, the spatial azimuth of $\mathbf{s}_{i+1}'$ in the coordinate system S_i' can be expressed as $(\pi - \theta_{si}', \varphi_{si}')$, then its coordinates can be expressed as:

$$\mathbf{s}_{i+1}' = \left(\sin\theta_{si}'\cos\varphi_{si}', \sin\theta_{si}'\sin\varphi_{si}', -\cos\theta_{si}'\right), i \geq 2 \tag{6.15}$$

By bringing $\mathbf{s}'_{i+1}$ into Eq. (6.13) and doing the inverse operation as shown in Eq. (6.16), $\mathbf{s}_{i+1}$ can be obtained.

$$\mathbf{s}_{i+1}^{\mathrm{T}} = \mathrm{Rot}_{zi}^{-1} \cdot \mathrm{Rot}_{yi}^{-1} \cdot \mathbf{s}_{i+1}'^{\mathrm{T}}, i \geq 1 \tag{6.16}$$

When the coordinates of $B_{i-1}(x_{i-1}, y_{i-1}, z_{i-1})$ and $\mathbf{s}_i$ are known, we can build the equations shown in Eq. (6.17), so as to solve for the increment Δ and finally for the coordinates of $B_i(x_i, y_i, z_i)$.

$$\begin{gathered} \frac{x_i^2}{a^2} + \frac{y_i^2}{b^2} + \frac{z_i^2}{b^2} = 1 \\ \frac{x_{i-1}^2}{a^2} + \frac{y_{i-1}^2}{b^2} + \frac{z_{i-1}^2}{b^2} = 1 \\ \frac{x_i - x_{i-1}}{\mathrm{s}_{ix}} = \frac{x_i - y_{i-1}}{\mathrm{s}_{iy}} = \frac{x_i - z_{i-1}}{\mathrm{s}_{iz}} = \Delta \end{gathered} \tag{6.17}$$

$$\Delta = -2 \frac{b^2\, \mathrm{s}_{ix} x_{i-1} + a^2\, \mathrm{s}_{iy} y_{i-1} + a^2\, \mathrm{s}_{iz} z_{i-1}}{b^2\, \mathrm{s}_{ix}^2 + a^2\, \mathrm{s}_{iy}^2 + a^2\, \mathrm{s}_{iz}^2} \tag{6.18}$$

$$\begin{aligned} x_i &= x_{i-1} + \Delta\, \mathrm{s}_{ix} \\ y_i &= y_{i-1} + \Delta\, \mathrm{s}_{iy} \\ z_i &= z_{i-1} + \Delta\, \mathrm{s}_{iz} \end{aligned} \tag{6.19}$$

By deriving Eq. (6.2), the unit vector $\boldsymbol{n}_i$ corresponding to the normal direction at B_i can be obtained as:

$$\boldsymbol{n}_i = \sqrt{\frac{x_i^2}{a^4} + \frac{y_i^2}{b^4} + \frac{z_i^2}{b^4}}^{-1} \cdot \left(\frac{x_i}{a^2}, \frac{y_i}{b^2}, \frac{z_i}{b^2} \right) \tag{6.20}$$

The incidence angle α_{ii} and refraction angle α_{ri} for the i^{th} reflection and refraction can be calculated through Eq. (6.21) and Eq. (6.22).

$$\cos \alpha_{ii} = -\mathbf{s}_i \cdot \boldsymbol{n}_i \tag{6.21}$$

$$\sin \alpha_{ri} = \frac{n_2}{n_1} \sin \alpha_{ii} \tag{6.22}$$

The optical force $\boldsymbol{F}_i$ resulting from the i^{th} reflection and refraction can be expressed as:

$$\begin{aligned}\boldsymbol{F}_i = \frac{\Delta \boldsymbol{P}}{\Delta t} &= \frac{n_2 P_i}{c}\mathbf{s}_i - \frac{n_2 P_i R_i}{c}\mathbf{s}_{i+1} - \frac{n_1 P_i T_i}{c}\mathbf{s}_{rfr1} \\ &= \frac{P_i}{c}[n_2(1+R_i)\cos\alpha_{ii} - n_1 T_i \cos\alpha_{ri}]\boldsymbol{n}_i\end{aligned} \tag{6.23}$$

Where $\mathbf{s}_{rfr1}$ is the unit vector of the refracted light when making the i^{th} reflection and refraction, and P_i denotes the power of i^{th} incident light ray, calculated through Eq. (6.24):

$$P_i = \begin{cases} dPT_1, & i = 2 \\ dPT_1R_2, & i = 3 \\ dPT_1R_2\cdots R_{i-1}, & i > 3 \end{cases} \tag{6.24}$$

Finally, the total optical force $\boldsymbol{F}(\theta,\varphi)$ generated by a single ray is obtained by adding up all the optical force $\boldsymbol{F}_i$. In addition, the ellipsoidal particle is subjected to the optical torque, which makes the particle rotate. The total optical torque $\boldsymbol{T}(\theta,\varphi)$ is given in Eq. (6.26).

$$\boldsymbol{F}(\theta,\varphi) = \sum \boldsymbol{F}_i \tag{6.25}$$

$$\boldsymbol{T}(\theta,\varphi) = \sum (\mathbf{r}_i \times \boldsymbol{F}_i) \tag{6.26}$$

6.2.2 Gaussian beam

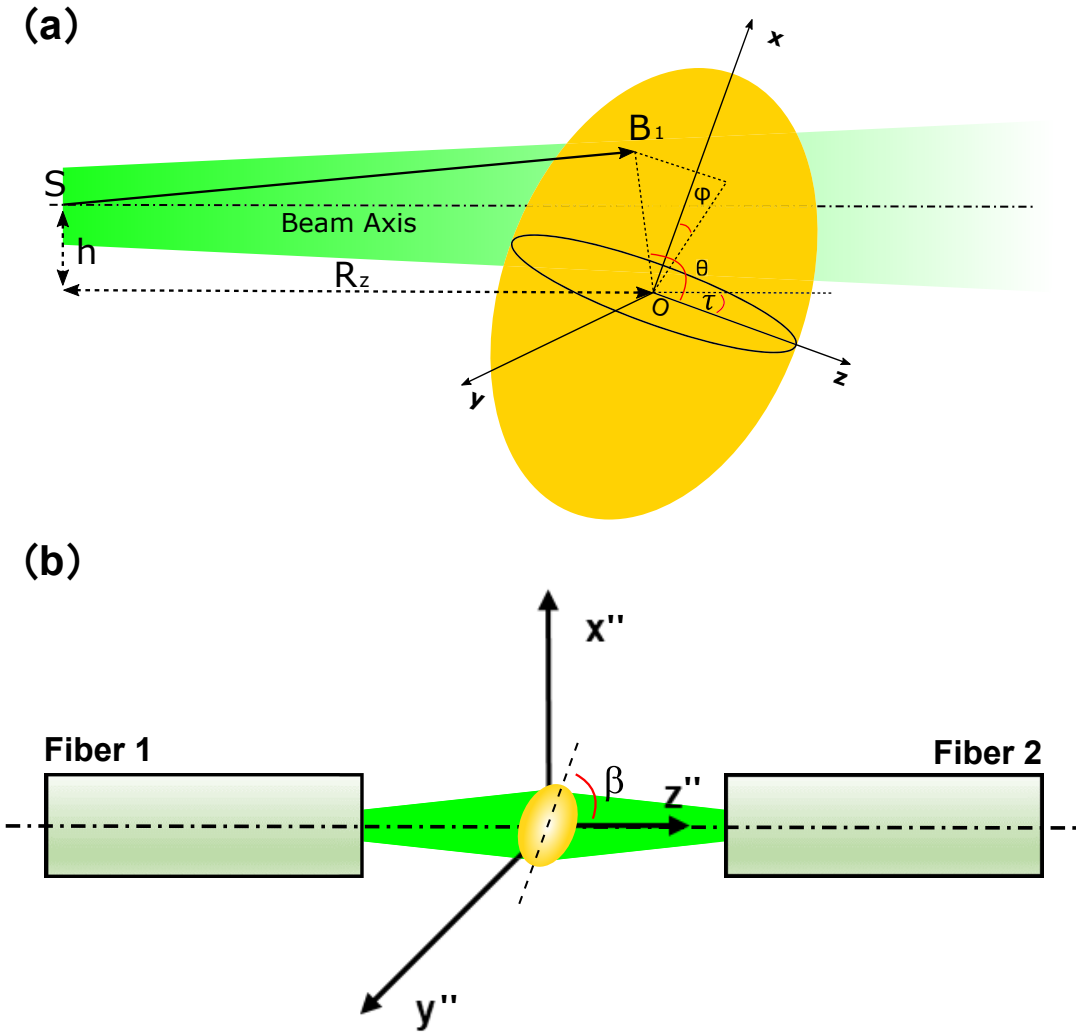

Figure 6.2: (a) A Gaussian beam composed of multiple rays acts on a micro-sized ellipsoidal particle. (b) Schematic diagram of the CP dual fiber traps for capturing a micro-sized ellipsoidal particle in air.

In section 6.2.1, we have modeled in detail how the change in momentum transferred to a micro-sized ellipsoidal particle subjects the particle to optical force and optical torque when a single ray is reflected and refracted on the ellipsoidal surface. Fig. 6.2(a) illustrates a Gaussian beam acting on a micro-sized ellipsoidal particle, where the optical force and torque exerted on the particle is the sum of the contributions of all the rays. Therefore, to calculate the optical force and torque generated by a Gaussian beam, first of all, let us consider a single ray SB_1 in the Gaussian beam directed to point B_1 on the surface of the particle, then the incident power of this single ray can be expressed as:

$$dP = I\cos\alpha_{i1}dS = \frac{2P_0}{\pi\omega_o^2}\exp\left(\frac{-2r^2}{\omega^2}\right)\cos\alpha_{i1}dS \tag{6.27}$$

Where I is the light intensity, P_0 is the power of the Gaussian beam, α_{i1} denotes the incident angle, ω_o denotes the Gaussian beam waist, r represents the distance between B_1 and the optical axis, ω denotes the beam waist at B_1, dS denotes the differential area of the particle. These quantities are given as follows:

$$r = \left|\mathrm{r}_1\sin\theta\cos\varphi\sin\tau - \mathrm{r}_1\cos\theta\cos\tau - h\right| \tag{6.28}$$

$$\omega = \omega_o\sqrt{1+\left(\frac{z\lambda}{\pi n_1\omega_o^2}\right)^2} \tag{6.29}$$

$$z = \mathrm{r}_1\sin\theta\cos\varphi\cos\tau + \mathrm{r}_1\cos\theta\sin\tau + R_z \tag{6.30}$$

$$\mathrm{d}S = \mathrm{r}_1^2\sin\theta d\theta d\varphi \tag{6.31}$$

To calculate the total optical force $\boldsymbol{F}_{sum}$ and torque $\boldsymbol{T}_{sum}$ of the Gaussian beam to the ellipsoidal particle, the optical force and torque of all rays need to be summed as follows:

$$\boldsymbol{F}_{sum} = \int \boldsymbol{F}(\theta,\varphi)\mathrm{dS} = \int_{\varphi_{\min}}^{\pi}\int_{\theta_{\min}}^{\pi} 2\boldsymbol{F}(\theta,\varphi)\mathrm{r}_1^2(\theta,\varphi)\sin\theta d\theta d\varphi \tag{6.32}$$

$$\boldsymbol{T}_{sum} = \int \boldsymbol{T}(\theta,\varphi)\mathrm{dS} = \int_{\varphi_{\min}}^{\pi}\int_{\theta_{\min}}^{\pi} 2\boldsymbol{T}(\theta,\varphi)\mathrm{r}_1^2(\theta,\varphi)\sin\theta d\theta d\varphi \tag{6.33}$$

Where the range of θ and φ can be determined by Eq. (6.34):

$$\mathbf{s}_1\cdot\boldsymbol{n}_1 \le 0 \tag{6.34}$$

For CP dual fiber trap, the optical force and torque from each fiber are added together:

$$\boldsymbol{F}_{tot} = \boldsymbol{F}_{sum,\text{ fiber 1}} + \boldsymbol{F}_{sum,\text{ fiber 2}} \tag{6.35}$$

$$\boldsymbol{T}_{tot} = \boldsymbol{T}_{sum,\text{ fiber 1}} + \boldsymbol{T}_{sum,\text{ fiber 2}} \tag{6.36}$$

As illustrated in Fig. 6.2(b), we establish a new Cartesian coordinate system S$''$ at the midpoint of the dual fibers as the origin, which can be transformed with respect to the original coordinate system S by defining the rotation matrix Rot'_y:

$$\text{Rot}'_y = \begin{bmatrix} \cos\beta & 0 & -\sin\beta \\ 0 & 1 & 0 \\ \sin\beta & 0 & \cos\beta \end{bmatrix} \tag{6.37}$$

In the subsequent modeling, we will use the coordinate system S$''$ as a unifying reference to define the dynamics of the ellipsoidal particle in the CP dual fiber trap. At this point, the optical force and torque applied to the ellipsoid will be transformed as:

$$\boldsymbol{F}''_{tot} = \text{Rot}'_y \boldsymbol{F}_{tot} \tag{6.38}$$

$$\boldsymbol{T}''_{tot} = \text{Rot}'_y \boldsymbol{T}_{tot} \tag{6.39}$$

When simulating the dynamics of ellipsoidal particles in the optical trap, the particles are not only subject to optical force $\boldsymbol{F}''_{tot}$ and torque $\boldsymbol{T}''_{tot}$, they are also subjected to gravitational force $\boldsymbol{F}_{\text{gravity}}$, viscous force $\boldsymbol{F}_v$ and Brownian stochastic force $\boldsymbol{F}_{\text{Brownian}}$ in air. They are given as follows:

$$\boldsymbol{F}_{\text{gravity}} = m\mathbf{g} = \frac{4}{3}\pi\rho a b^2 \mathbf{g} \tag{6.40}$$

$$\boldsymbol{F}_v = \frac{16\pi\eta}{A + a^2 A_x}\boldsymbol{v}_x + \frac{16\pi\eta}{A + b^2 A_y}\boldsymbol{v}_y + \frac{16\pi\eta}{A + b^2 A_z}\boldsymbol{v}_z \tag{6.41}$$

$$A = \int_0^\infty \frac{ds}{\sqrt{(s+a^2)(s+b^2)(s+b^2)}} \tag{6.42}$$

$$\begin{aligned} A_x &= \int_0^\infty \frac{dx}{(x+a^2)\sqrt{(x+a^2)(x+b^2)(x+b^2)}} \\ A_y &= \int_0^\infty \frac{dy}{(y+b^2)\sqrt{(y+a^2)(y+b^2)(y+b^2)}} \\ A_z &= \int_0^\infty \frac{dz}{(z+b^2)\sqrt{(z+a^2)(z+b^2)(z+b^2)}} \end{aligned} \tag{6.43}$$

$$\boldsymbol{F}_{\text{Brownian}} = m\boldsymbol{\xi}(t) \tag{6.44}$$

Here, ρ denotes the density of the particle and $\mathbf{g}$ is the acceleration due to gravity. $\boldsymbol{v}_x$, $\boldsymbol{v}_y$, and $\boldsymbol{v}_z$ represent the velocity in x, y, z directions at the coordinate system S$''$, respectively. η denotes the viscosity coefficient in air [5], and A, A_x, A_y, A_z represent the characteristic constant of the ellipsoidal particle [139]. $\boldsymbol{\xi}(t)$ represents the Brownian stochastic force per unit mass. Finally, based on the OTS toolbox [30], we can simulate the micro-sized ellipsoidal particle's dynamics under the CP dual fiber traps.

6.3 Results and discussions

In this section, I will quantitatively investigate the trapping size range and kinetic properties of individual ellipsoidal particles under three different CP dual fiber trapping schemes and compare the results with the case of spherical particles of the same volume. To accurately predict and understand how the ellipsoidal particles dynamics change within the trapping field, we consider the ellipsoidal droplets with 50g/L NaCl concentration (long axis $2a > 5\mu$m, short axis $2b = 5\mu$m, the refractive index $n_2 = 1.344$) as the trapped airborne particles, and the air as the trapping environment (the refractive index $n_1 = 1.000$). For the trapping setup, the wavelength of the laser $\lambda = 532$nm, and the beam profile emitted from each fiber is the Gaussian beam. In addition, the two fibers' output power is equal to 20mW. The polarization directions of the lasers emitted from the two fibers are orthogonal.

6.3.1 Trapping performance under well-aligned condition

First of all, we investigated the ellipsoidal particle's trapping size range under well-aligned CP dual fiber traps. Fig. 6.3 shows the maximum and minimum size of ellipsoidal particles that can be captured under the well-aligned CP dual fiber traps when the SP is 90μm and 180μm, respectively. We can find that the maximum trapped ellipsoid's long axis increases from 12μm to 17μm, while the minimum trapped ellipsoid's long axis keeps 5μm constant when other trapping conditions remain the same but only the SP increases from 90μm to 180μm. The trend in captured size for ellipsoids matches my experimental results demonstrated in Section 3.3.1, which means that for ellipsoidal particles, the confinement of larger size ellipsoidal particles can also be achieved by varying the spacing of the dual optical fibers.

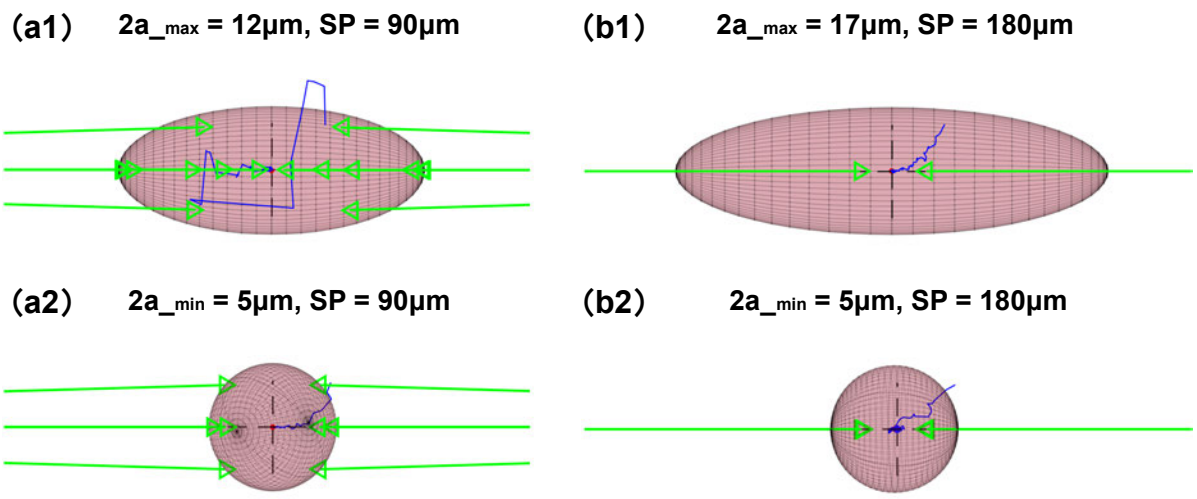

Figure 6.3: The maximum and minimum size of ellipsoidal particles that can be trapped under the well-aligned CP dual fiber traps with dual fibers' separation SP of 90μm and 180μm respectively. The maximum trapped ellipsoid's long axis at SP of 90μm is (a1) of 12μm, and the minimum trapped ellipsoid's long axis is (a2) of 5μm. When only increasing the SP to 180μm, the maximum trapped ellipsoid's long axis is (b1) of 17μm, and the minimum trapped ellipsoid's long axis is (b2) of 5μm. The green arrow lines indicate the incoming laser rays, and the blue curves represent the trajectories of the particle.

In addition, we noted that in Fig. 6.3, the ellipsoid's long axis is all oriented along the optical axis after being stably trapped in the optical trap. Since we previously defined the initial orientation of the particles β as 0° (i.e., the angle between the long axis of the ellipsoid and the optical axis of fibers, which is illustrated in Fig. 6.2(b)), in order

to verify whether the orientation of the ellipsoid after being stably captured in the CP dual fiber traps is related to its initial orientation, we selected the ellipsoid with long axis $2a$ = 7μm and short axis $2b$ = 5μm, and performed the simulation by changing the initial orientation varied from 0° to 180° in the steps of 30°, while ensuring the other parameters remain the same. The simulation results, as illustrated in Fig. 6.4, demonstrated that the ellipsoids will finally be stably captured with the orientation of 0° and their long axis remains along the optical axis of the optical fiber regardless of their initial orientation.

6.3.2 Quantifying the effect of radial misalignment

In the previous section, we have clarified the size range of ellipsoids that can be stably captured in well-aligned CP dual fiber traps, as well as knowing that the initial orientation does not have an impact on the final trapped orientation. However, during the actual trapping process, as we already mentioned in Chapter 5, CP dual fiber traps usually experience two types of misalignment, namely radial misalignment (transverse offset) and rotational misalignment (angular deviations) [42]. Therefore, in the following sections, I will quantify the effects of radial misalignment and angular deviation in CP dual fiber traps on the capture of ellipsoids and compare the results with the case of spherical particles of the same volume.

For all the simulations, we defined the ellipsoidal particle with a long axis $2a$ = 3.5μm and set its initial orientation β as of 0°. Also, we set the trap with the SP of 90μm. After that, by quantitatively varying the radial misalignment d, as illustrated in Fig. 6.5(a), we can find how the trapping dynamic and orientation changes of the ellipsoidal particle in the CP dual fiber traps with the radial misalignment. First, in Fig. 6.5(b), we simulated the moving trajectory of the defined ellipsoidal particle in the trap with the radial misalignment d of 5.5μm, where the green arrow lines indicate the incoming laser rays, the red ellipsoid denotes the defined particle, the blue curve represents the trajectory, and the dark dashed cross indicates the location of the coordinate system S$''$. We found that the ellipsoidal particle can still end up being captured at the midpoint of the two fibers, but unlike the case without radial misalignment, the long axis of the ellipsoidal particle will no longer be parallel to the optical axis (β = 0°), but at an angle (β $\neq$ 0°). In addition, Fig. 6.5(c) demonstrated snapshots of the ellipsoidal particle dynamics during the trapping process, where Fig. 6.5(c1) to Fig. 6.5(c4) correspond to the different positions labeled in Fig. 6.5(b), respectively. We found that the spatial orientation of

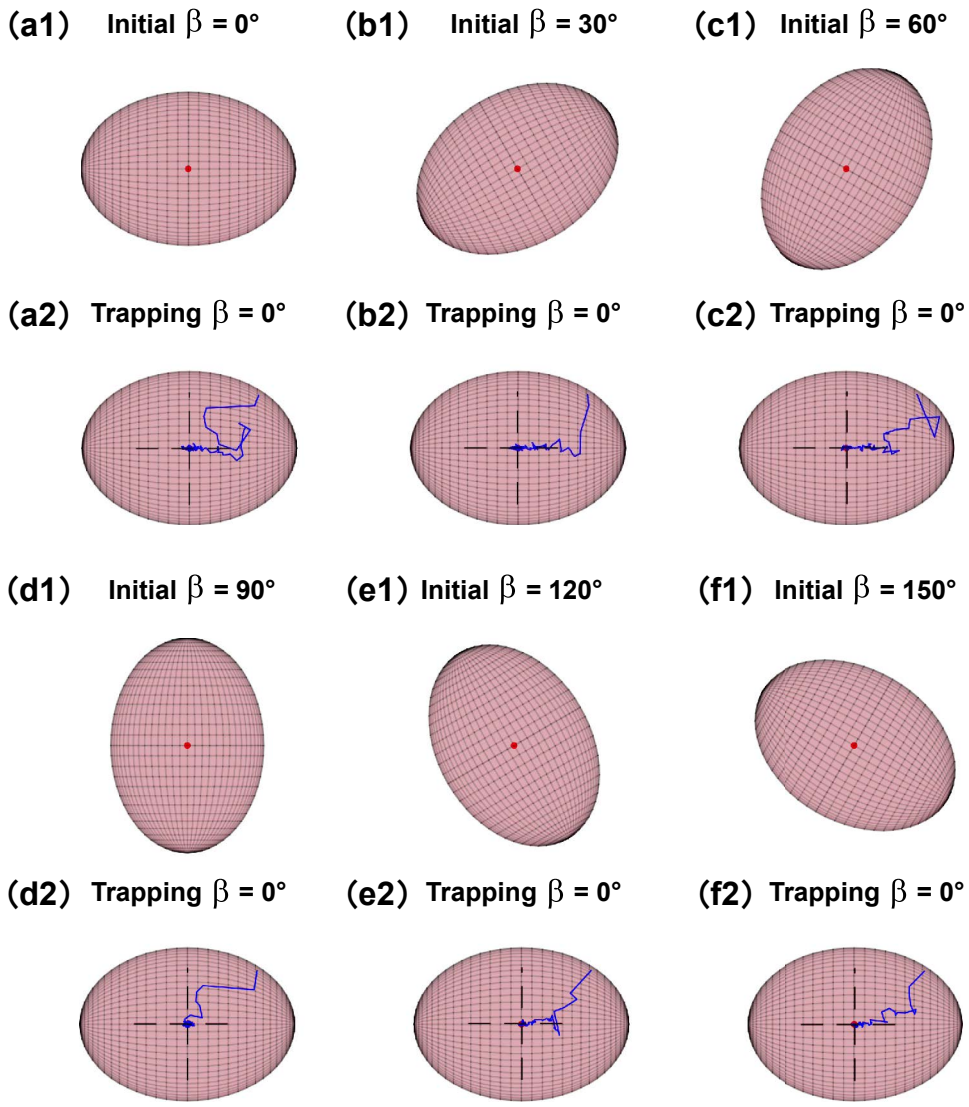

Figure 6.4: Orientation variations of the stably trapped ellipsoidal particles in the well-aligned CP dual fiber traps with different initial orientations of (a1) 0°, (b1) 30°, (c1) 60°, (d1) 90°, (e1) 120°, and (f1) 150°, respectively. (a2) to (f2) demonstrate that the ellipsoids will be trapped with the orientation of 0° and their long axis remains along the optical axis of the optical fiber regardless of their initial orientation.

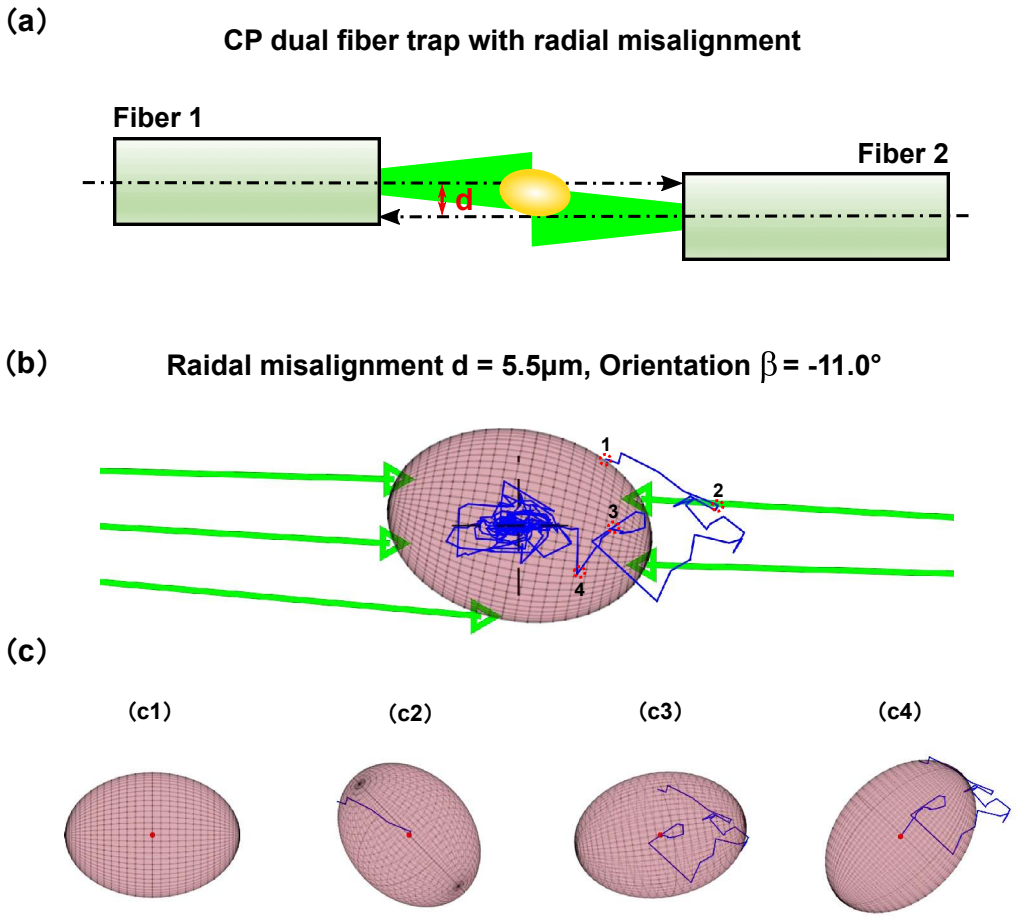

Figure 6.5: (a) Schematic diagram of CP dual fiber trapping micro-sized ellipsoidal particle with radial misalignment d of the two fibers. (b) Simulated moving trajectories of the ellipsoidal particle in the CP dual fiber trap with the maximum radial misalignment d of 5.5μm. (c) Dynamic snapshots of the ellipsoidal particle during the trapping process, where (c1) to (c4) correspond to the different positions labeled in (b), respectively. The green arrow lines indicate the incoming laser rays, and the blue curves represent the trajectories of the particle.

the particle varies randomly and continuously in 3D, unlike the case of trapping an ellipsoidal particle in liquids, where the particle is accompanied by periodic rotation [36]. Furthermore, in Fig. 6.6, we present orientation variations of the stably trapped ellipsoidal particles in the CP dual fiber traps as the increase of the radial misalignment of the two fibers. We found that the magnitude of trapping orientation $|\beta|$ is increasing with the increment of radial misalignment d, and the fitted curve satisfies the law of linear variation.

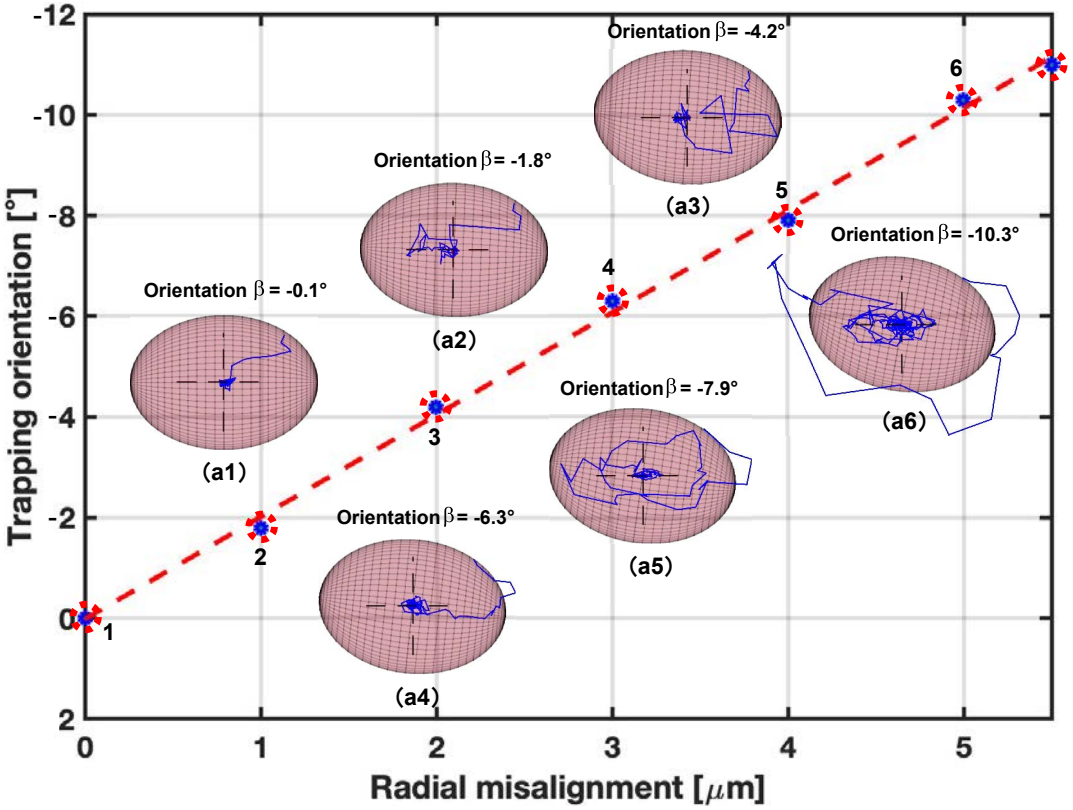

Figure 6.6: Orientation variations of the stably trapped ellipsoidal particles in the CP dual fiber traps as the increase of the radial misalignment of the two fibers. (a1) to (a6) present the spatial orientation of the stably trapped ellipsoidal particles corresponding to radial misalignment d from 0 to 5μm in increments of 1μm, respectively.

Finally, we also want to quantify how the dynamics of the ellipsoidal particle will change as the radial misalignment continues to increase (d > 5.5μm). As shown in Fig. 6.7, it shows the simulated results of dynamics of an ellipsoidal particle and spherical particle with the same volume as the increase of radial misalignment of two fibers in the CP dual fiber traps. For the ellipsoidal particle, when the radial misalignment d is increased to the range of 5.6μm to 6.9μm, the ellipsoidal particles are in a subtrap state in the optical trap. At this point, the spatial orientation of the ellipsoidal particle will not be finally trapped at the midpoint of two fibers and form a stable orientation angle as when the radial misalignment d is less than 5.5μm. If we further increase the radial misalignment to more than 7.0μm, the ellipsoidal particle will directly escape from the trapping field. As for a spherical particle of the same volume, we found that when the radial misalignment is greater than its stable trapping threshold (0 to 5.2μm) and does not increase above

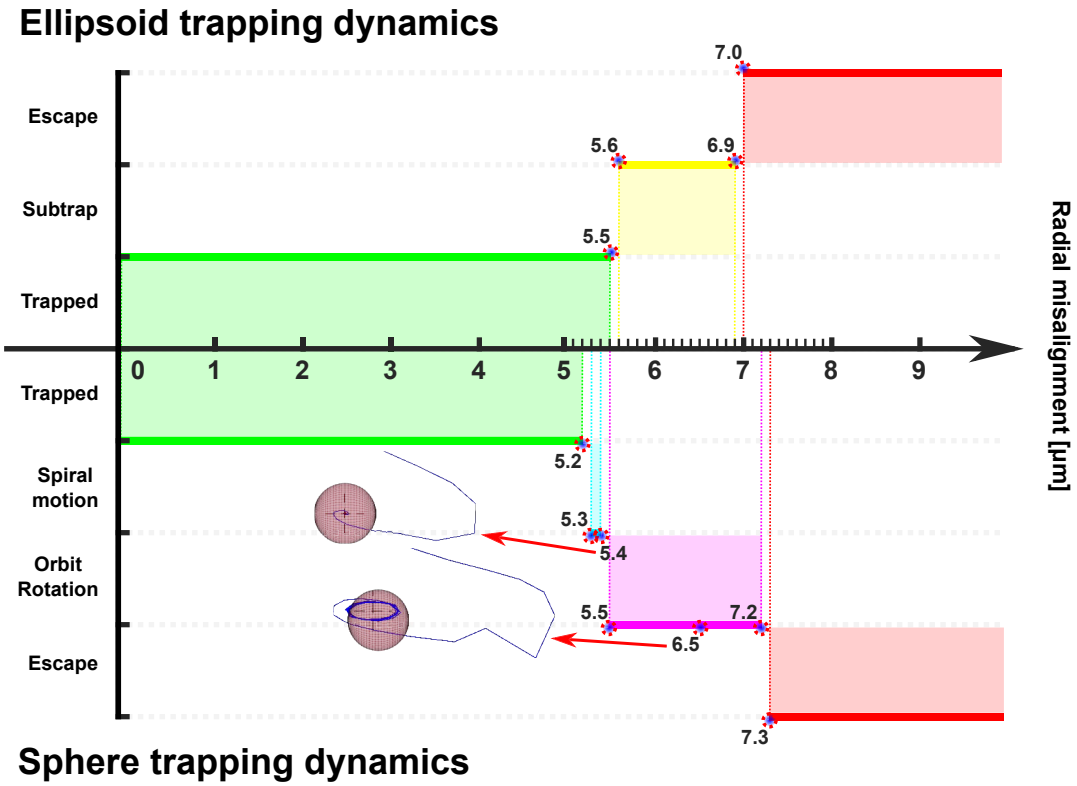

Figure 6.7: Comparison of the variation of dynamics of an ellipsoidal particle and spherical particle with the same volume ($65.45\mu m^3$) as the increase of radial misalignment of two fibers in the CP dual fiber traps.

7.3μm, the particle presents two other trapping dynamics in the trapping field, while they fail to form for the same volume of the elliptical particle. Specifically, when the radial misalignment is in the range of 5.3μm to 5.4μm, the spherical particle made spiral motion in the trapping field, while continuing to increase the radial misalignment in the range of 5.5μm to 7.3μm, the spherical particle would make the orbital rotation. It is worth noting that the range of radial misalignment at this point basically corresponds to the range of radial misalignment when the ellipsoid is in the subtrap state.

6.3.3 Quantifying the effect of angular deviations

6.3.3.1 One optical fiber tilt

After quantifying the effect of the radial misalignment of two fibers when capturing the single ellipsoidal particle in the CP dual fiber traps, I will proceed to investigate the effect of another misalignment factor, namely angular deviation, on trapping dynamic

and orientation changes in the optical trapping field. First of all, as shown in Fig. 6.8(a), we studied the case where only one fiber is tilted in the CP dual fiber traps. Fig. 6.8(b) illustrates the simulated moving trajectory of the ellipsoidal particle in the trap with the one fiber tilted with angle δ of 7.0°, in which we defined two dashed crosses (black one represents the intersection of the optical axis of the non-tilted left fiber and line of z = 0, and the pink one denotes the intersection of the optical axis of the right inclined fiber and line of z = 0) as references to locate the position of the trapped particle. We found that the particle was eventually captured at the position to the right of the middle of the two dashed crosses, which is similar to the trapping position of the spherical particle investigated in Chapter 5 under the same trapping conditions. For the trapping orientation β, like the result when trapping with radial misalignment, it is not equal to zero as well. In addition, as shown in Fig. 6.8(c), snapshots of the ellipsoidal particle dynamics during the trapping process demonstrated that the spatial orientation of the particle kept changing randomly in 3D until it reached the stable trapping position.

Furthermore, in Fig. 6.9, we present orientation variations of the stably trapped ellipsoidal particles in the CP dual fiber traps as the increase of the one fiber tilted angle δ. We found that the magnitude of trapping orientation $|\beta|$ is increasing with the increment of one fiber tilted angle δ, and the fitted curve also satisfies the linear variation law, which is the same as the case of trapping with radial misalignment. However, it is worth noting that the maximum magnitude of trapping orientation $|\beta|$ is of 13.9° when trapping with one fiber tilted angle δ of 7.0°, while in the trapping with radial misalignment, the maximum magnitude of trapping orientation $|\beta|$ can only reach 11.0° when the radial misalignment d is of 5.5μm.

Also, we further explored the trapping dynamics of a single ellipsoidal particle corresponding to the increase of one fiber tilt angle δ in the CP dual fiber traps. According to Fig. 6.10, we found that for ellipsoidal particles, when the single fiber tilt angle δ increases to the range of 7.1° to 8.4°, the ellipsoidal particles are in the subtrap state as well, which is same as the trapping dynamics when trapping with radially misalignment d in the range from 5.6μm to 6.9μm. When we further increased the one fiber tilt angle δ to more than 8.5°, the ellipsoidal particles will directly escape from the trapping field. For the same volume of spherical particles, we found that when the one fiber tilt angle δ is between 7.7° and 7.9°, the spherical particles did spiral motion in the optical trapping field, while continuing to increase the one fiber tilt angle δ between 8.0° and 9.3°, the

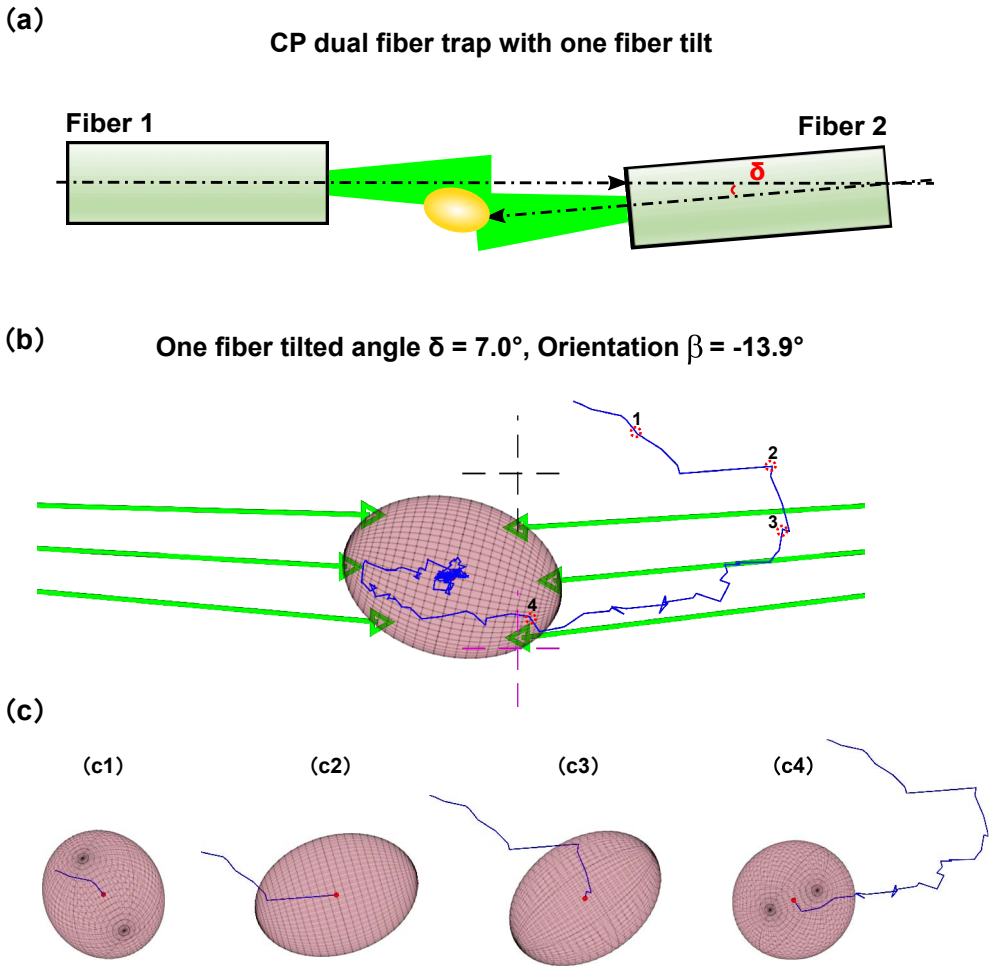

Figure 6.8: (a) Schematic diagram of CP dual fiber trapping micro-sized ellipsoidal particle with one fiber tilt. (b) Simulated moving trajectory of the ellipsoidal particle in the CP dual fiber trap with the maximum one fiber tilted angle δ of 7.0°. (c) Dynamic snapshots of the ellipsoidal particle during the trapping process, where (c1) to (c4) correspond to the different positions labeled in (b), respectively. The green arrow lines indicate the incoming laser rays, and the blue curves represent the trajectories of the particle.

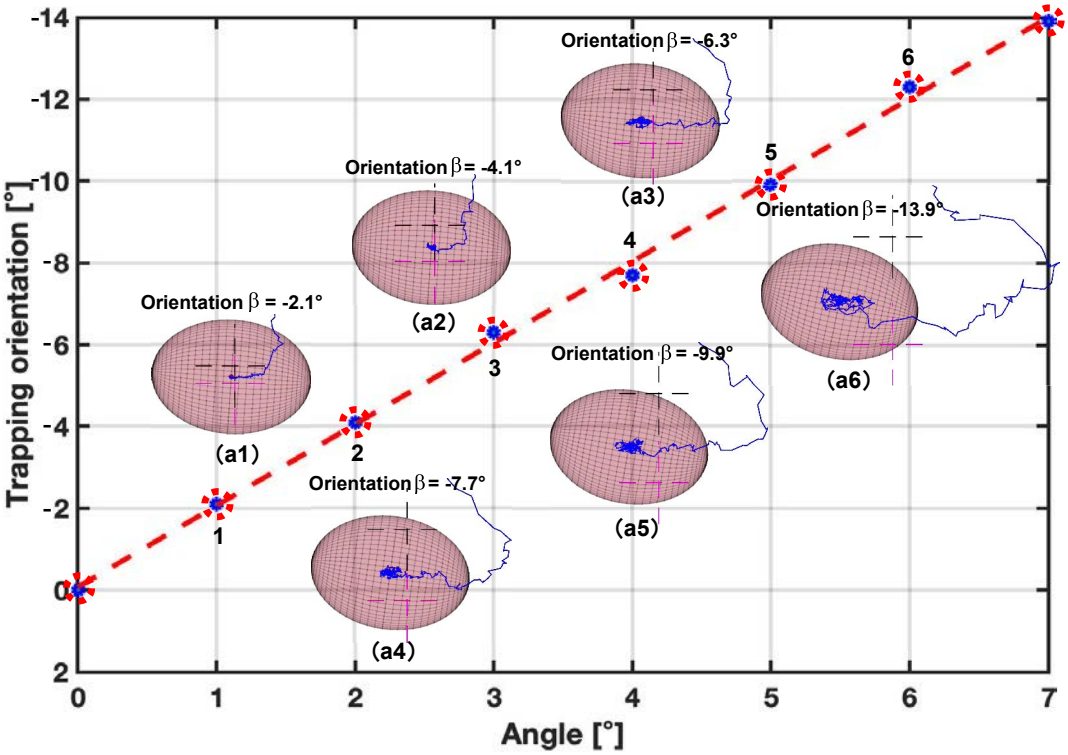

Figure 6.9: Orientation variations of the stably trapped ellipsoidal particles in the CP dual fiber traps as the increase of the one fiber tilted angle. (a1) to (a6) present the spatial orientation of the stably trapped ellipsoidal particles corresponding to one fiber-tilted angle δ from 1.0° to 6.0° in increments of 1.0°, respectively.

spherical particles made the orbital rotation. The range of one fiber tilt angle at this point basically corresponds to the range when the ellipsoid is in the state of the subtrap. In addition, by comparing Fig. 6.10 and Fig. 6.7, we found elliptical particle is more tolerant to radial misalignment than a spherical particle of the same volume, ensuring stable capture in the trap despite larger radial misalignment, while a spherical particle of the same volume exhibits better capture tolerance to greater angular deviation caused by the tilt of the single fiber.

6.3.3.2 Two optical fiber tilt together

In this section, we further investigated the case of two optical fibers tilted together at the same angle δ in the CP dual fiber trap to understand the trapping dynamics of the ellipsoidal particle, and the schematic of this trapping scheme is shown in Fig. 6.11(a).

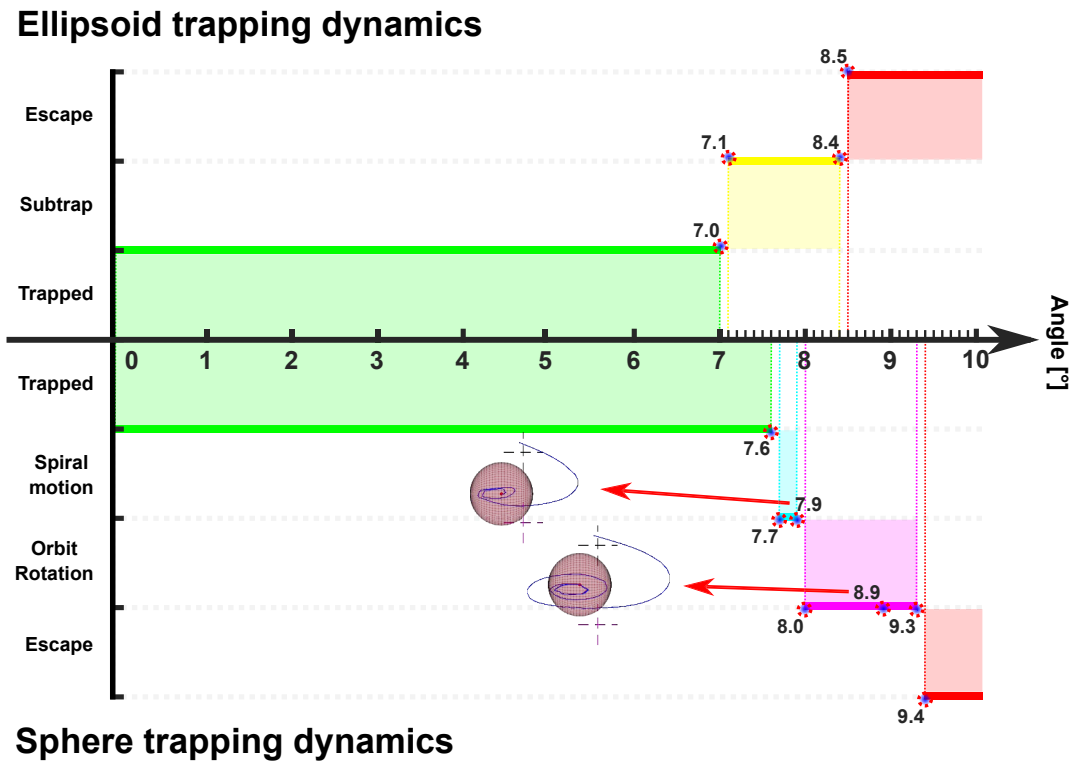

Figure 6.10: Comparison of the variation of dynamics of an ellipsoidal particle and spherical particle with the same volume (65.45μm^3) as the increase of one fiber tilted angle in the CP dual fiber traps.

When we defined the two fiber tilted angle of δ to be 11.0°, Fig. 6.11(b) demonstrated the simulated moving trajectory of the ellipsoidal particle until it was stably captured in the trapping field. We can find that the ellipsoidal particle was trapped in the position directly below the intersection of the optical axis of the two tilted fibers, which is consistent with the trapping position of the spherical particle studied in Chapter 5 under the same trapping conditions. As for the particle's trapping orientation β, it is almost equal to zero (in this study, β is 0.20°), which is similar to the result when trapping under well-aligned conditions. Regarding the spatial orientation of the ellipsoidal particle before it was stably trapped, the particle still maintained the random 3D variations during the trapping process, which can be demonstrated in Fig. 6.11(c).

To quantify the orientation variations of the stably trapped ellipsoidal particle in the CP dual fiber with two fibers tilted together at the same angle, we conducted a series of simulations with the tilt angle δ increasing from 1.0° to 10.0° in increments of 1.0°

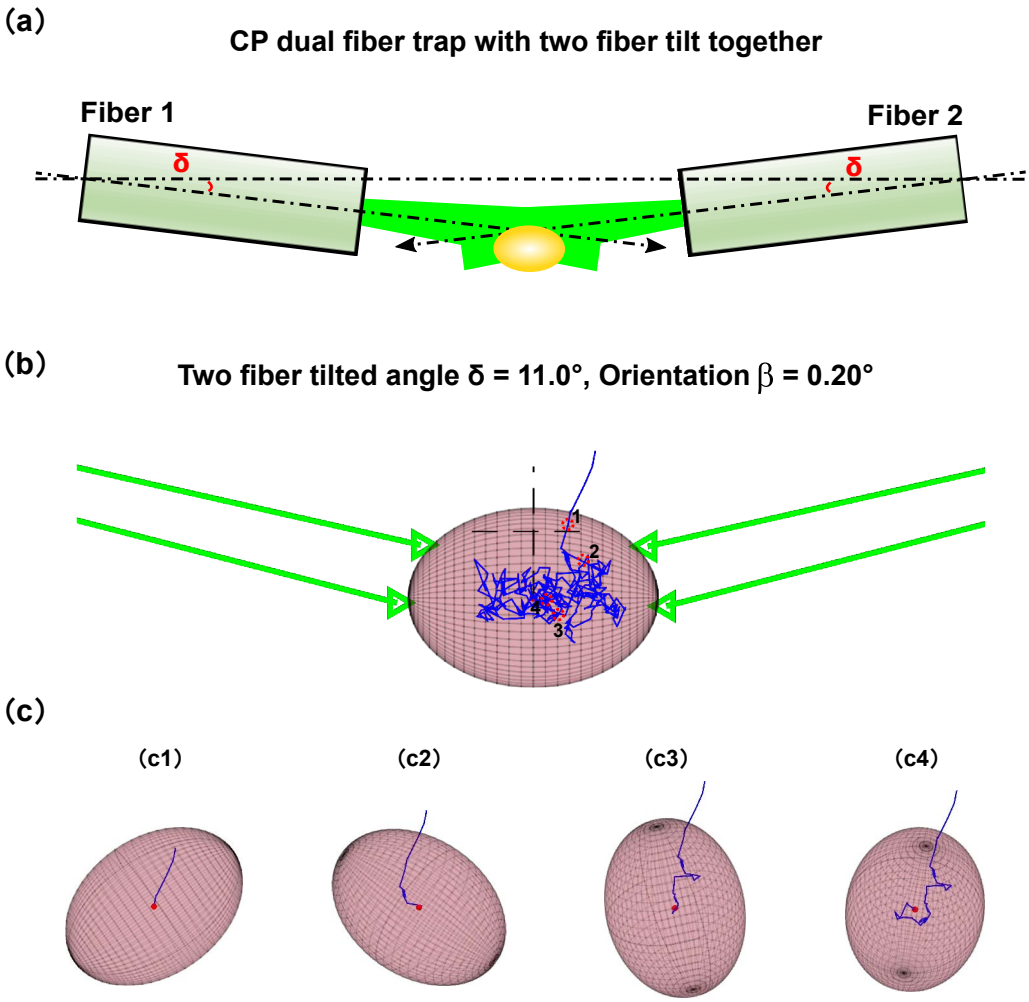

Figure 6.11: (a) Schematic diagram of CP dual fiber trapping micro-sized ellipsoidal particle with two fiber tilt together. (b) Simulated moving trajectory of the ellipsoidal particle in the CP dual fiber trap with the maximum two fiber tilted angle δ of 11.0°. (c) Dynamic snapshots of the ellipsoidal particle during the trapping process, where (c1) to (c4) correspond to the different positions labeled in (b), respectively. The green arrow lines indicate the incoming laser rays, and the blue curves represent the trajectories of the particle.

to clarify whether the two fiber tilted angle does not have an impact on the trapping orientation of particle in this trapping scheme, i.e., the final trapping orientation of the ellipsoidal particles always remain zero with very tiny error. According to Fig. 6.12, we found that the trapping orientations for all the trapped ellipsoidal particles under the trapping condition of different dual fibers' tilted angles are all almost equal to 0°. The fitted curve also aligned with the line of trapping orientation δ = 0°. We argue that the

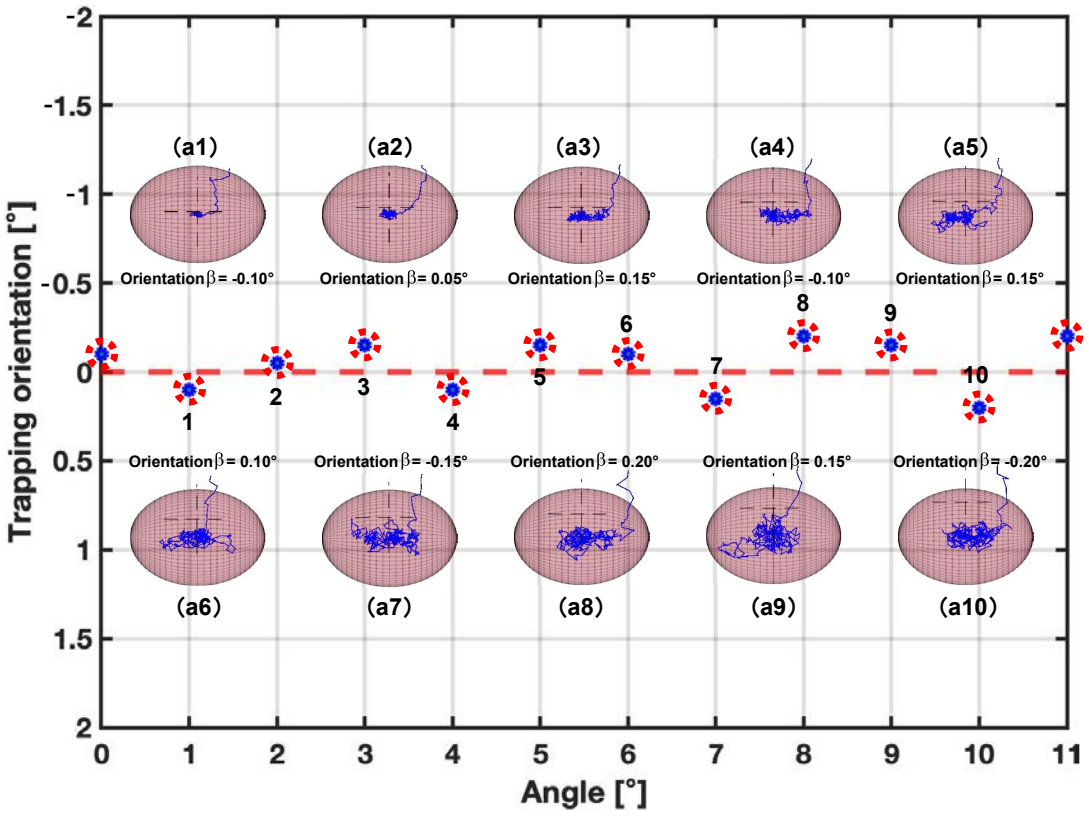

Figure 6.12: Orientation variations of the stably trapped ellipsoidal particles in the CP dual fiber traps as the increase of the two fiber tilted angle. (a1) to (a6) present the spatial orientation of the stably trapped ellipsoidal particles corresponding to two fiber tilted angle δ from 1.0° to 10.0° in increments of 1.0°, respectively.

tiny errors in these simulations should originate from the interference of noises rather than the effect of optical forces.

Finally, we quantified how the dynamics of the ellipsoidal particle will change as the two fiber tilted angle continues to increase (δ > 11.0°). According to Fig. 6.13, we present the simulated results of dynamics of an ellipsoidal particle and spherical particle with the same volume as the increase of two fiber tilted angle in the CP dual fiber traps. It is worth noting that for an ellipsoidal particle and a spherical particle of the same volume, in this trapping scheme (two fibers titled together at the same angle), when the tilt angle exceeds the maximum trapping threshold at which stable trapping can be achieved, both particles will escape the trapping field directly. Unlike the cases when trapping with radial misalignment or angular deviation originating from one fiber tilt, for the

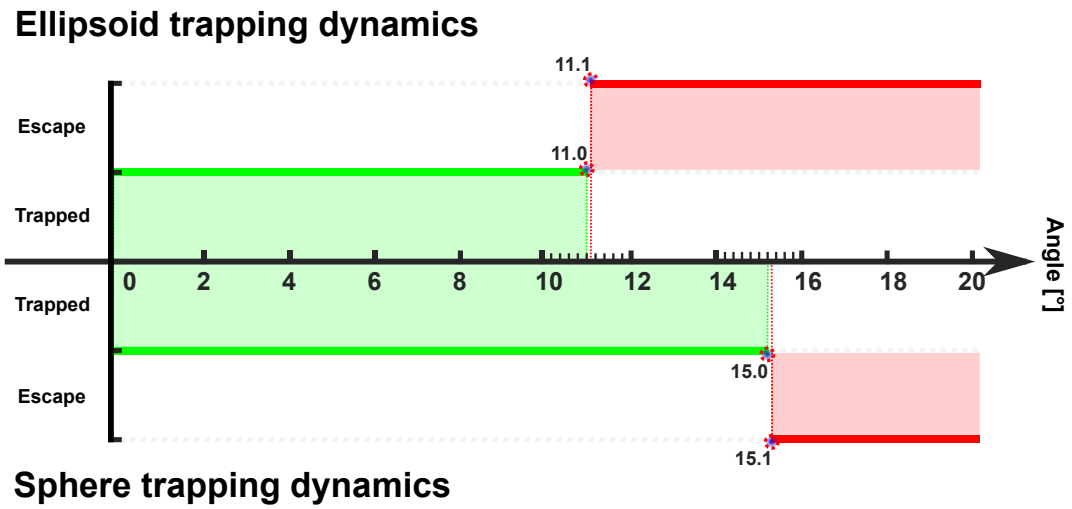

Figure 6.13: Comparison of the variation of dynamics of an ellipsoidal particle and spherical particle with the same volume (65.45μm^3) as the increase of two fiber tilted angle in the CP dual fiber traps.

ellipsoidal particle, there exists dynamics of subtrap, while for the spherical particle, there are two extra dynamics of spiral motion and orbital rotation.

6.4 Conclusion

We quantified the trapping size range, dynamics, and orientation variation of ellipsoidal droplets under three different CP dual fiber trapping schemes by numerical simulations, and compared the results with the case of spherical droplets of the same volume. First, we developed computational models to calculate the optical forces and torques applied to ellipsoidal droplets in the trapping field by vector ray tracing and rotational coordinate transformation, and then simulated the dynamics of single ellipsoidal droplets in the trap by using the OTS toolbox. Next, through quantitative investigations, we found that the ellipsoidal droplets trapped size range showed the same trend as that of spherical droplets when trapped under well-aligned CP dual fiber traps, i.e., the trapping size range increases with the increase of the dual fiber separation, and the spatial orientation of the stably trapped ellipsoidal droplets always satisfied that the particle's long axis is parallel to the optical axis of the trapping fiber and was not affected by its initial spatial orientation. As for traps with radial misalignment, we found that when the radial misalignment is within the threshold that can guarantee the stable capture of ellipsoidal

droplets, the trapped position is still in the middle of dual fibers. But under this trapping scheme, the trapped particle's spatial orientation shows a linear increase with the increase of radial misalignment. As the radial misalignment continues to increase, the ellipsoid will experience a subtrap state in the optical trap before eventually escaping. In this case, the range of radial misalignment when the ellipsoidal droplet is made to be in the subtrap state is almost aligned with the range of radial misalignment when the same volume of the spherical droplet is made to undergo spiral motion as well as orbit rotation.

For traps with angular deviations, in the trapping configuration with one fiber tilt, the trapping dynamics and orientation variation of the ellipsoidal droplets demonstrate the same changing trend compared to the results when trapping only with radial misalignment in the CP dual fiber traps. While in the trapping configuration with two fiber tilted together at the same angle, the spatial orientation of the stably trapped ellipsoidal droplets shows the posture in which their long axis is almost aligned with the optical axis of the fiber without tilt, and their trapping dynamics are simpler, with only two states of trapped and escape. The works in this chapter provide some new insights into how the trapping dynamics of ellipsoidal droplets vary under three different CP dual fiber trapping schemes. It also gives a quantitative analysis that helps to determine the parameters of the current trapping system to guide future experimental validation.

CHAPTER 7

AEROSOL TRAPPING WITH BEAM SHAPING

One very specific challenge faced when trapping single liquid aerosols based on CP dual fiber traps is that for a random sample of aerosols, the surfaces of the trapping chamber and fiber facets will be coated in droplets or possibly absorbing particles. This causes scattering of the light into the chamber and will, at best, diminish trapping efficiency and, at worst, destroy any chance of trapping anything. Here, in Chapter 7, I optimized the trapping field required to manipulate an aerosol within a targeted trapping geometry with the help of beam shaping technique achieved by spatial light modulator (SLM) . Based on this method, the transmission matrix can be calculated for the Multimode fiber (MMF) in our experiments. We demonstrated the momentum transfer from the MMF with individual output modes to a single droplet. This attempt paves the way for beam shaping-assisted CP dual beam traps to capture single aerosols with higher stability in dynamic processes.

7.1 Introduction

In previous studies, we have demonstrated the use of two SMFs as two trapping arms to construct the CP dual beam trapping system to quantitatively investigate the capture and manipulation of individual liquid aerosol particles in air. However, in practical implementation, the SMF-based CP dual beam trap has limitations in terms of the stable trapping location and the number of traps that can be formed, the type of manipulation that can be controlled, and the trapping stability that can be maintained. Specifically,

for the number and trapping position under the SMF-based CP dual beam trap, only one trapping position can be formed at the midpoint of two SMFs in most cases, and if two trapping points located near two SMF facets are to be constructed, they need to be realized by shortening the separation distance between two SMFs. Regarding the manipulation types, there are three main controllable manipulations for the SMF-based CP double beam trap, including guiding, spiral motion, and orbit rotation. Among them, guiding is achieved by tuning the ratio of the relative output power of the two SMFs to move the captured individual aerosol particles along the optical axis. The latter two types of manipulation are performed by quantitatively adjusting the misalignment of the two SMFs to control the spiral motion and orbit rotation of the captured individual particles in the trapping field. In terms of trapping stability, a very specific challenge faced when trapping single liquid aerosols is that for a random sample of aerosols, the surfaces of the trapping chamber and fiber facets will be coated in droplets or possibly absorbing particles. This will lead to scattering or distortion of light, which will reduce the trapping efficiency of the formed trap or even lead directly to the failure of trapping anything.

To overcome the above-mentioned limitations, beam shaping techniques implemented by using SLM to generate targeted trap beam geometries have demonstrated a very promising capability to solve these problems [81, 83, 106, 123, 150]. Currently, in free space, Porfirev et al. have experimentally demonstrated the performance of using SLM to trap the single or multiple absorbing aerosol particles at any defined locations as well as conduct the controlled manipulations of single or multiple aerosol particles in one-dimensional, 2D, and 3D space, respectively [123]. Moreover, Burnham et al. also demonstrated the developed HOTs can capture trap water droplets in air in a matrix fashion, and also showed controlled manipulation along the x, y, and z directions, which ultimately led to the coagulation of the droplets [25]. While, in our experiments, we are more interested in shaping the light through optical fiber, and finally contributing to achieving the stable trapping and arbitrary holographic manipulation of aerosol particles in air. However, to the best of our knowledge, fiber-based optical trapping and manipulation experiments assisted with beam shaping technique so far are all demonstrated in liquid environments [81, 83, 106, 150]. Specifically, Mosk et al. demonstrated 2D optical manipulation of sixteen polystyrene microparticles through an MMF [106]. Subsequently, Leite et al. demonstrated the real-time holographic manipulation of multiple microparticles through a lenless MMF [83]. Except in the case of using a single optical fiber

to form traps, Kreysing et al. demonstrated the adaptive manipulation of living-cells rotation under the CP dual few-mode fiber trap [81]. Furthermore, Sun et al. recently demonstrated arbitrary axes cell-rotation in 3D using one multi-core fiber (MCF) and one SMF as two trap arms to form the CP dual beam trap [150]. As a result, CP dual fiber traps assisted with beam shaping technique will play a significant role in developing a toolbox for controlling optically trapped aerosol particles.

In this chapter, the aim is to optimize the trapping field with the help of beam shaping through an MMF implemented by SLM to manipulate aerosols in the target trapping geometry, so that this attempt would pave the way for beam shaping-assisted CP dual fiber traps (one MMF and one SMF) to capture single aerosols with higher stability in dynamic processes. First, we explain the principle of using an SLM to shape the light passing through the MMF. We then progressed to introduce the optical setup that we developed for our experiments. Subsequently, we show the results of shaping the light passing through the MMF to generate a single output mode and also demonstrate the momentum transfer from the shaped MMF with individual output mode to a single droplet. Finally, we discuss the development plan for future experiments to engineer an aerofluidic chip, which will allow the more powerful and functional *in situ* control and measurement of the optically trapped single aerosol particle.

7.2 Principle

In Fig. 7.1, the input field of the MMF is modulated using the SLM to create an optimized focus at an arbitrary output position. Initially, we sequentially scan the MMF's input facet using a diffraction-limited spot, modulated by a specific SLM grating. Each scanned point generates a distinct speckle pattern at the MMF's output. These output speckle patterns are overlaid with an externally collimated Gaussian beam from an SMF to create an interference pattern. By varying the phase of the scanned point across a 2π range, all interference patterns collected at each phase step are utilized to extract optimal phase and amplitude for the probe's position. This process is repeated for all scanned points, yielding optimal phases and amplitudes for the probe's positions. These values are then employed in generating an optimized hologram through Fast Fourier Transform (FFT) of the MMF's measured transmission matrix (TM). Ultimately, the optimized hologram is sent to the SLM to produce a shaped field at the input side of the MMF, resulting in the creation of the optimized focus at the MMF's output.

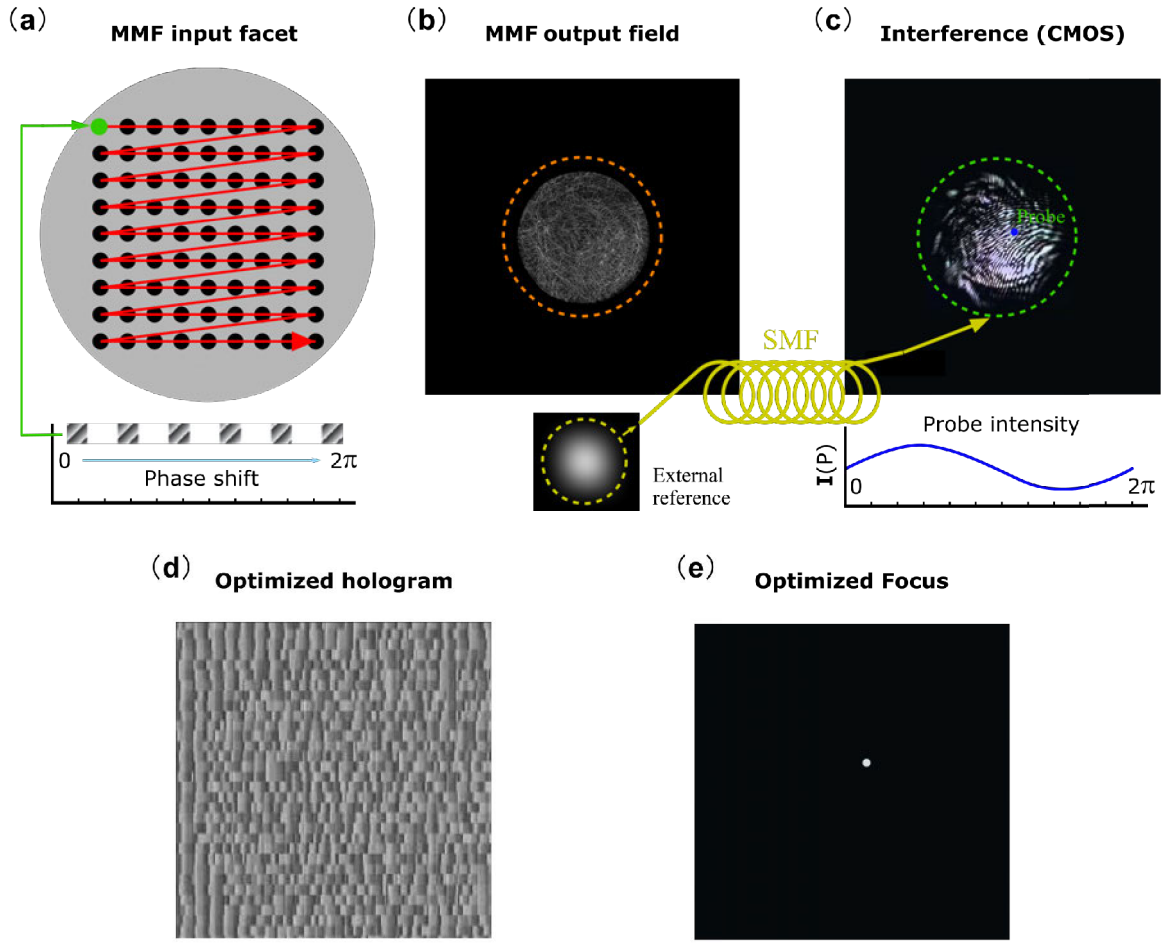

Figure 7.1: The principle of using SLM to shape the light passing through the MMF to produce an optimized focus. (a) The MMF input facet is sequentially scanned by a diffraction-limited spot, which is modulated by using an SLM applied with a specific grating. In addition, in each spot, the phase is also subsequently shifted over 2π range. (b) The MMF output field is a speckle pattern when scanning each spot at the MMF input facet. (c) The interference pattern generated by superimposing the MMF output field with an externally collimated Gaussian beam transmitted through the SMF is captured by a CMOS camera. After phase shift over 2π range, the optimal phase and amplitude at the probe position can be extracted at the current scan spot. (d) When all the scans and the corresponding phase shifts are completed, we can obtain all the optimal phases and amplitudes at the probe position, which are used to generate an optimized hologram. (e) The optimized focus at the MMF output is created by sending the optimized hologram to the SLM to generate the shaped field to the input side of the MMF.

7.3 Experimental setup

Fig. 7.2(a) illustrates the experimental setup for shaping the output field of MMF into an optimized focus, which is based on an off-axis holography configuration. A CW 532nm laser (Torus Laser Quantum 891mW) is used for all experiments. After passing laser beam through an isolator (Thorlabs IO-3-532-LP), the beam is split into two beams by the HWP and the PBS, where two beams' power ratio can be controlled by rotating the HWP. One of the divided beams is coupled into a SMF (Thorlabs P1-460AR-2) as the reference beam, and the other one is utilized as the signal beam. The signal beam is then expanded by a telescope to overfill the short axis of the SLM (Holoeye LCR-2500) with a small incident angle, in which the HWP is used to align the polarization between the SLM and signal beam. Next, the SLM is applied with a series of specific gratings to achieve the sequential scanning of the input facet of the MMF (Thorlabs M92L01) by a diffraction-limited spot. Specifically, the first 4f system (L1 and L2) is used to image the SLM onto the back aperture of the MO1 (Olympus RMS20X), and the second 4f system (L2 and MO1) is used to image the selected diffraction limited spot into the MMF input facet, where the APT (Thorlabs SM1D12D) is used to select the first diffraction order, the CMOS1 (Basler acA1920-150μm) is used to monitor the modulated signal beam, and the QWP1 and QWP2 are used to control the signal beam's polarization state propagated in the MMF [122]. Finally, the speckle pattern from the output side of the MMF interferes with the collimated reference beam, and the resulting image is captured by the CMOS2 (Basler acA2040-120μm), which will finally be used for TM measurement.

In addition, before TM measurement, SLM must be calibrated for phase modulation for a given wavelength to keep SLM working correctly in subsequent experiments. Fig. 7.2(b) shows optical setup to calibrate SLM for phase modulation. The linearly polarized Gaussian beam passes through a pre-designed mask with two holes to generate two coherent beams that finally hit the centers of two independent halves of SLM. Reflected beams will be superposed with each other at the focus and resulting interference fringes will be captured by CMOS camera via a MO. By displaying 256 gray-level patterns sequentially on SLM, we can capture a set of fringe measurements for later analysis. After that, there are two methods available to make the correction for SLM by using captured fringe measurements. One is to generate a Look-Up-Table (LUT), and the other one is to create a compensate hologram. The former method has been carefully detailed in these two references [26, 80], and the latter one can be found in Richard et al. [72].

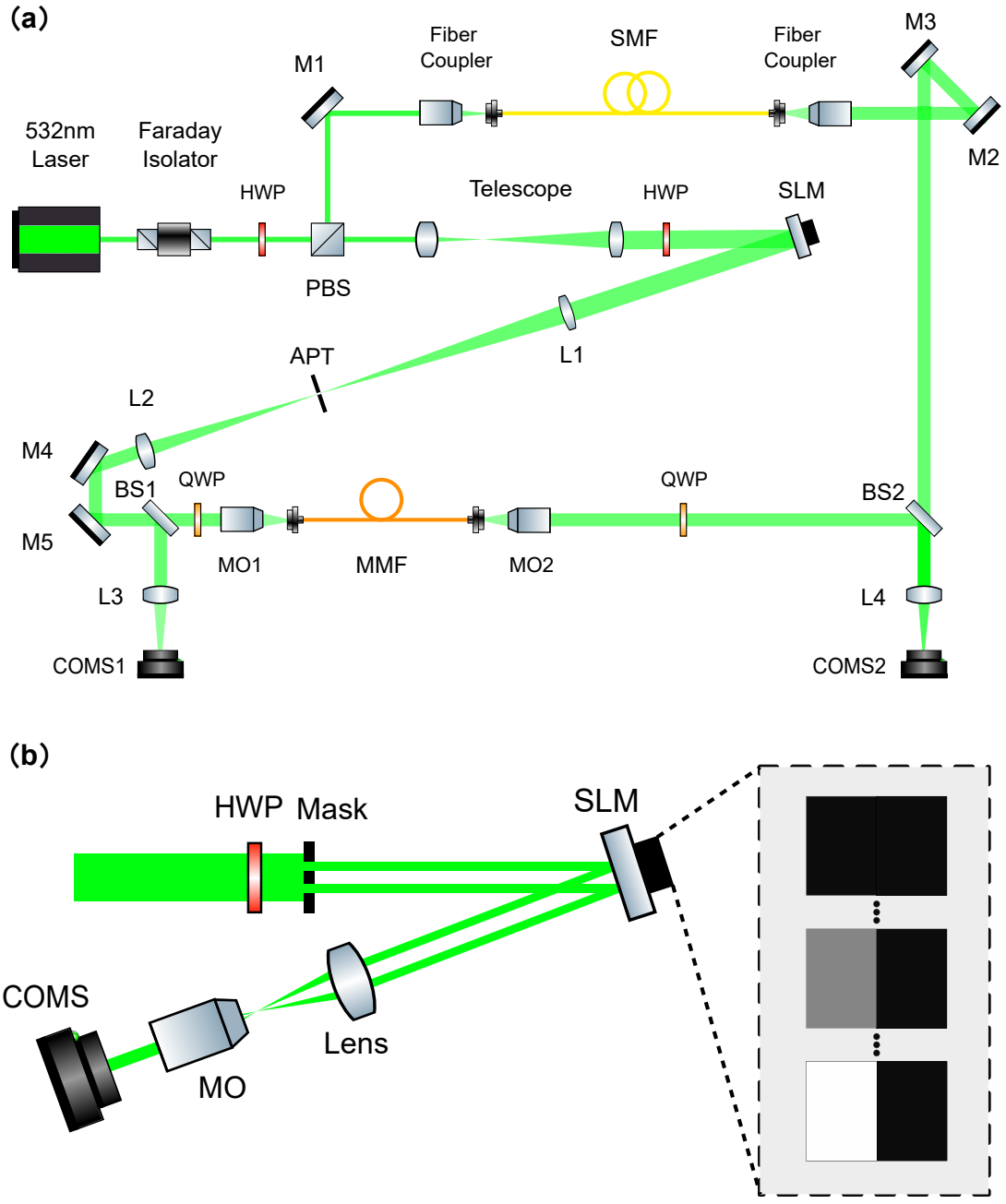

Figure 7.2: (a) Experimental setup for shaping the output field of MMF into an optimized focus through an off-axis holography configuration. M: mirror: L: lens; BS: beam splitter; APT: aperture; MO: microscope objective; PBS: polarizing beam splitter; HWP: half-wave plate; QWP: quarter-wave plate; SMF: single mode fiber; MMF: multi-mode fiber. SLM: spatial light modulator. (b) Optical setup for SLM phase modulation calibration, in which 256 gray-level patterns will be sequentially displayed onto the SLM to modulate the phase, and the COMS camera will capture the resulting interference fringes.

7.4 Preliminary result

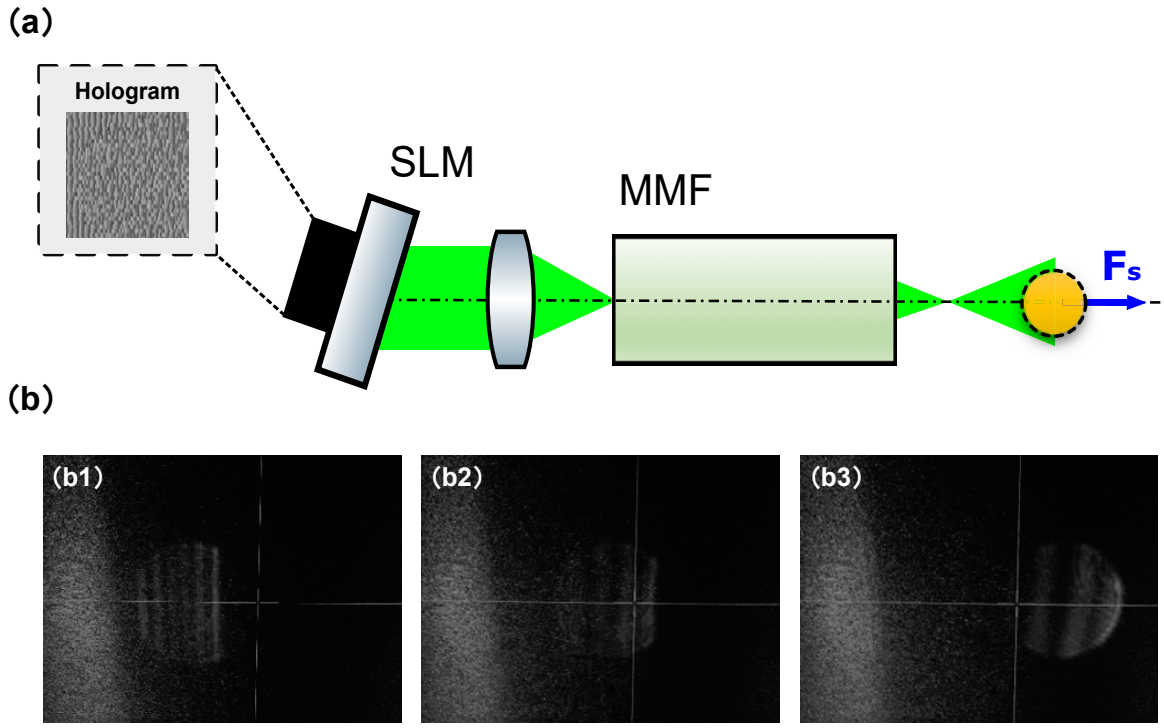

Figure 7.3: (a) The schematic of the momentum transfer from the MMF with individual output modes to a single droplet. (b) The scattering image of a single droplet propelled by the MMF is shaped with an optimized output single focus.

Fig. 7.3(a) shows an experimental schematic of momentum transfer to a single droplet in air by using an optimized MMF to produce a single output mode. What can be seen is that the shaped beam emitted by the MMF converges first and then diverges in space. However, due to the small NA of the MMF itself, the scattering force dominates at this point compared to the gradient force, and it is not possible to form a 3D trapping of a single droplet directly around the focal position. Instead, individual droplets will achieve momentum transfer under the scattering force and be instantaneously pushed away from the outlet surface of the MMF. Fig. 7.3(b1) to (b3) demonstrates the scattering images of a single droplet propelled by the MMF shaped with an optimized output single focus. We should note that the patterns of fringes are visible in the scattering image, which likely stems from the phenomenon termed "Mie scattering." This phenomenon arises due to the interaction between coherent laser light and aerosol particles. Mie scattering takes place when particle dimensions approach the wavelength of the incident light. This interaction gives rise to alternating patterns of constructive and destructive interference,

manifesting as fringes within the scattering image. We also can find that individual water droplet is pushed along the optical axis by the scattering force, which proves that the optimized single focus generated by the shaped MMF can achieve the momentum transfer to the individual droplet particles in the air and thus lead to the corresponding motion generated by the single droplet. In addition, the scattering images serve two functions in the subsequent trapping experiments: firstly, it assists in determining the location of the emitting point of the dual fibers so as not to introduce radial misalignment during the alignment of dual fibers; Second, the scattering images can be used to resolve the size and refractive index of the aerosol particles.

7.5 Future development

In our current findings, we have taken the initial step of employing beam shaping technology to manipulate aerosol particles. However, to effectively address the concern raised by the examiner, our objective is to pioneer innovative iterative feedback solutions. These solutions will utilize beam shaping, achieved through spatial light modulation within the evolving field of complex photonics. This field involves calculating the transmission matrix for specific scattering objects, including delicate diffusers, optical fibers, and in our case, a surface featuring droplets. Detailed technical insights can be accessed in this paper [106].

In addition, we propose a development plan for future experiments as shown in Fig. 7.4. First, Fig. 7.4(a) shows the schematic of beam shaping-assisted CP dual beam traps with one MMF and one SMF to capture single droplet in air. We will use short-length bare fibers to replace the patch cables used in previous experiments, i.e. SMF (Thorlabs P1-460AR-2) and MMF (Thorlabs M92L01) to form two trapping arms. The advantage of this replacement is that the single focused beam produced by the shaped MMF will not be affected by the fiber bending due to the long length, thus making the profile and power of the outgoing focused beam not significantly degraded, which is the key to ensure the successful and robust trapping of the single droplet in this trapping scheme. However, a tricky problem of this capture scheme is the alignment of the two bare fibers. Unlike the use of patch cables, we designed special holders to facilitate the clamping of the two trapping arms, and followed the calibration protocols I described in Chapter 3 to align the two fibers, ultimately ensuring stable trapping of the single droplet in air.

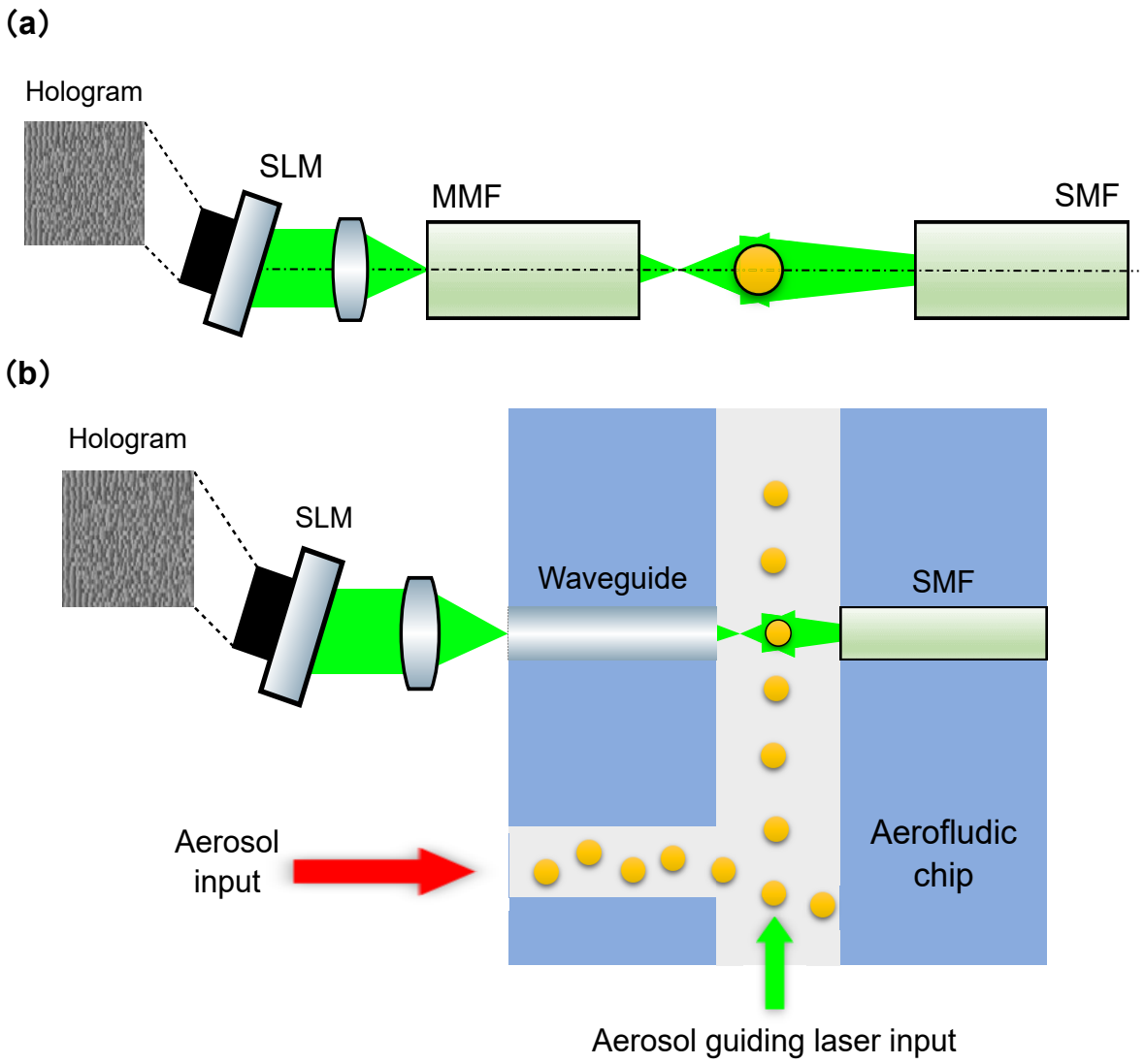

Figure 7.4: (a) The schematic of beam shaping-assisted CP dual beam traps with one MMF and one SMF to capture a single water droplet in air. (b). Beam shaping for on-chip aerosol trapping. By application of an optimized correction hologram, the beam passing through the PDMS waveguide can be shaped to enable a focused beam to form a CP dual beam trap with a divergence beam emitted from an SMF so as to form an aerofludic chip.

To this end, we further propose a beam shaping for the on-chip aerosol trapping scheme as shown in Fig. 7.4(b). By using Polydimethylsiloxane (PDMS) as the substrate material for the chip structure [117], various channels and waveguides used for trapping are created by laser writing [146]. By application of an optimized correction hologram, the beam passing through the PDMS waveguide can be shaped to enable a focused beam to form a CP dual beam trap with a divergence beam emitted from an SMF so as to form an aerofludic chip. By designing and developing such aerofludic chips, no complex alignment is required for aerosol particle capture and on-chip experiments can be implemented easily and flexibly. Moreover, by developing real aberration correction algorithms, it is possible to optimize the capture field for arbitrary aerosol particles in dynamic processes. In addition, we can also integrate spectroscopy measurement, temperature and humidity control, and aerosol launch control. on this aerofluidic chip, which will allow the more powerful and functional *in situ* control and measurement of the optically trapped single aerosol particle.

7.6 Conclusion

In conclusion, we have proposed to use the optimized trapping field with the help of beam shaping through an MMF implemented by SLM to trap and manipulate aerosols in a target trapping geometry. The concept is to shape the output beam profile of the MMF with the help of the measured TM, which can be solved by using an off-axis holographic configuration. We have demonstrated momentum transfer from a shaped MMF with a single focused beam to a single water droplet, where the corresponding individual droplet is pushed away along the optical axis of the shaped MMF. Based on the current experimental results, we further propose two CP dual beam trapping schemes for future practice, which will enable more powerful and functional *in situ* control and measurement of optically trapped individual aerosol particles on the basis of an engineered aerofluidic chip.

CHAPTER 8

CONCLUSION AND OUTLOOK

8.1 Conclusion

The focus of this thesis is to develop an advanced single aerosol trapping and manipulation platform based on fiber-based optical traps. The main contribution and outcomes of my Ph.D. work are summarized as follows:

In Chapter 2, I provide an overview of optical trapping and the use of this technique to study aerosols. I first present the theory and basics of optical trapping so that the novices can have a general understanding of how trapping forces are generated and how the dynamics of trapped aerosols vary. Then, I summarize four types of aerosol optical trapping configurations and point out the characteristics of each of them. Finally, I describe in detail the aerosol trapping considerations involved in the construction of optical aerosol traps.

In Chapter 3, I systematically described the strategies, development, and implementation related to the successful trapping and manipulation of individual aerosol particles based on the CP dual fiber traps. The loading method of the liquid aerosol sample I used in the experiment and the strategy to manage its evaporation was described in detail, and a salt solution with a concentration of 50g/L was chosen as the sample to be used. Next, the design, construction, and calibration of the experimental system are described in detail, pointing out the key technical details of the CP dual fiber trapping system used

to trap and manipulate individual aerosol particles. The basic experimental results are shown to demonstrate the successful trapping and manipulation of a single droplet in air.

In Chapter 4, I present the results of the developed theoretical model of light-matter interaction of optically trapped aerosols to quantify the trapped aerosol size range within the trap under different dual fiber separations. We build the size area plot for stable aerosol trapping through a parameter analysis that allows the tolerance of such traps to trap fluctuations to be understood. The findings contribute to the repeatable quantitative results of aerosol trapping under the CP dual fiber trapping setup.

In Chapter 5, I present results exploring the effect of angular deviations on the dynamics of trapped single aerosol particles, quantifying the trapping viability as the function of misalignment, and how particle dynamics change when interacting with displaced fibers. In addition, I investigated how four main factors (including beam divergence, fiber separation distance, fiber output power, and aerosol radius) affect the single aerosol particle trapping performance and dynamic changes in the tilted CP dual fiber traps. These findings provide insight into the development of optical fiber-based traps as well as a novel approach to managing light-induced rotation in air.

In Chapter 6, I present the results of the trapping size range and kinetic properties of individual ellipsoidal particles under three different CP dual fiber trapping schemes by numerical simulations, and compared the results with the case of spherical droplets of the same volume. The developed new model provides a more accurate understanding of the droplet trapping dynamics in the CP dual fiber traps, and also helps interested parties to explore some parameters that are difficult or impossible to obtain experimentally in the short term, which in turn can provide some insight for future experimental validation.

In Chapter 7, I present the result of optimizing the trapping field required to manipulate an aerosol within a targeted trapping geometry with the help of beam shaping technique achieved by an SLM. The findings pave the way for beam shaping-assisted CP dual beam traps to improve the single aerosol trappings stability for arbitrary aerosol undergoing dynamic processes.

8.2 Outlook

The research works presented in this thesis can be further developed to provide insightful knowledge and additional functionality for the optical trapping and manipulation of single aerosol particles. Here I list the potential research directions:

8.2.1 Beam shaping for multiple aerosols trapping and control

Beam shapes and trapping beam geometries will play a significant role in developing a toolbox for controlling optically trapped aerosols. In Chapter 7, I only demonstrate the capability of this technique to generate one optimized single focus emitted through an MMF. However, in practice, once we get the MMF's TM, we can actually generate multiple optimized focuses while we can design and change their spatial distribution in real-time. On this basis, it will allow holographic 3D trapping and manipulation of aerosol particles by carefully engineered fiber-based optical traps.

8.2.2 Metasurface-based aerosol trapping and manipulations

In recent years, with the rapid development of nanotechnology, the use of ultrathin metasurfaces composed of subwavelength elements to shape the optical field behind the fiber output facet has allowed for more compact and flexible modulation and tailoring of the beam at the interface. One of the particular example is that researcher has demonstrated the design and printing of an ultra-high NA metalens onto the output facet of an SMF, thus enabling the trapping and manipulation of the silica bead and Escherichia coli bacterium in the liquid environment with higher stability [121]. I believe that this kind of Metasurface-based optical fiber trap can also be a powerful and promising tool to trap and manipulate aerosol particles, which will eliminate the need to use the SLM to do the wavefront shaping for the MMF, and make the trapping setup more compact, and the trapping process easier to perform.

8.2.3 On-chip design and optofluidics system

A more ambitious plan is to put the trapping, manipulation, and characterization of aerosol particles all on a single chip. For this chip, as I mentioned in Chapter 7, PDMS will be used as the substrate material for the chip. Laser writing techniques will be employed to fabricate the chip structure. The developed beam shaping algorithms will be applied to optimize the trapping field for arbitrary aerosol particles undergoing dynamic

processes. Integrated spectral measurements, temperature and humidity control, and aerosol loading control will enable the characterization of trapped aerosol particles. That is to say, the developed optofluidics system will benefit for investigating contact, condensation, and immersion freezing mechanisms for model secondary organic aerosol particle types.

BIBLIOGRAPHY

[1] C. ALPMANN, M. ESSELING, P. ROSE, AND C. DENZ, *Holographic optical bottle beams*, Applied Physics Letters, 100 (2012), p. 111101.

[2] S. ANAND, J. NYLK, C. DODDS, J. COOPER, S. NEALE, AND D. MCGLOIN, *Optical manipulation of aerosols using surface acoustic wave nebulisation*, in Optical Trapping and Optical Micromanipulation VIII, vol. 8097, SPIE, 2011, pp. 374–383.

[3] S. ANAND, J. NYLK, S. L. NEALE, C. DODDS, S. GRANT, M. H. ISMAIL, J. REBOUD, J. M. COOPER, AND D. MCGLOIN, *Aerosol droplet optical trap loading using surface acoustic wave nebulization*, Optics Express, 21 (2013), pp. 30148–30155.

[4] L. ANDEREGG, B. L. AUGENBRAUN, Y. BAO, S. BURCHESKY, L. W. CHEUK, W. KETTERLE, AND J. M. DOYLE, *Laser cooling of optically trapped molecules*, Nature Physics, 14 (2018), pp. 890–893.

[5] Y. ARITA, M. MAZILU, AND K. DHOLAKIA, *Laser-induced rotation and cooling of a trapped microgyroscope in vacuum*, Nature Communications, 4 (2013), pp. 1–7.

[6] P. ASENBAUM, S. KUHN, S. NIMMRICHTER, U. SEZER, AND M. ARNDT, *Cavity cooling of free silicon nanoparticles in high vacuum*, Nature Communications, 4 (2013), pp. 1–7.

[7] A. ASHKIN, *Acceleration and trapping of particles by radiation pressure*, Physical Review Letters, 24 (1970), p. 156.

[8] A. ASHKIN, *Forces of a single-beam gradient laser trap on a dielectric sphere in the ray optics regime*, Biophysical Journal, 61 (1992), pp. 569–582.

[9] A. ASHKIN AND J. DZIEDZIC, *Optical levitation by radiation pressure*, Applied Physics Letters, 19 (1971), pp. 283–285.

[10] A. ASHKIN AND J. DZIEDZIC, *Radiation pressure on a free liquid surface*, Physical Review Letters, 30 (1973), p. 139.

[11] A. ASHKIN AND J. DZIEDZIC, *Feedback stabilization of optically levitated particles*, Applied Physics Letters, 30 (1977), pp. 202–204.

[12] A. ASHKIN, J. M. DZIEDZIC, J. E. BJORKHOLM, AND S. CHU, *Observation of a single-beam gradient force optical trap for dielectric particles*, Optics Letters, 11 (1986), pp. 288–290.

[13] D. P. ATHERTON, *Sensitive force measurements with optically trapped microspheres in high vacuum*, University of Nevada, Reno, 2015.

[14] R. BALE, A. IIDA, M. YAMAKAWA, C. LI, AND M. TSUBOKURA, *Quantifying the covid19 infection risk due to droplet/aerosol inhalation*, Scientific Reports, 12 (2022), pp. 1–15.

[15] L. BAN, B. L. YODER, AND R. SIGNORELL, *Size-resolved electron solvation in neutral water clusters*, The Journal of Physical Chemistry A, 125 (2021), pp. 5326–5334.

[16] D. C. BENITO, S. H. SIMPSON, AND S. HANNA, *Fdtd simulations of forces on particles during holographic assembly*, Optics Express, 16 (2008), pp. 2942–2957.

[17] K. BERG-SØRENSEN AND H. FLYVBJERG, *Power spectrum analysis for optical tweezers*, Review of Scientific Instruments, 75 (2004), pp. 594–612.

[18] J. W. BLACK, M. KAMENETSKA, AND Z. GANIM, *An optical tweezers platform for single molecule force spectroscopy in organic solvents*, Nano Letters, 17 (2017), pp. 6598–6605.

[19] J. T. BLAKELY, R. GORDON, AND D. SINTON, *Flow-dependent optofluidic particle trapping and circulation*, Lab on a Chip, 8 (2008), pp. 1350–1356.

[20] C. P. BLAKEMORE, A. D. RIDER, S. ROY, A. FIEGUTH, A. KAWASAKI, N. PRIEL, AND G. GRATTA, *Precision mass and density measurement of individual optically levitated microspheres*, Physical Review Applied, 12 (2019), p. 024037.

[21] R. BOWMAN, D. PREECE, G. GIBSON, AND M. PADGETT, *Stereoscopic particle tracking for 3d touch, vision and closed-loop control in optical tweezers*, Journal of Optics, 13 (2011), p. 044003.

[22] R. W. BOWMAN AND M. J. PADGETT, *Optical trapping and binding*, Reports on Progress in Physics, 76 (2013), p. 026401.

[23] R. BROWN, *Xxvii. a brief account of microscopical observations made in the months of june, july and august 1827, on the particles contained in the pollen of plants; and on the general existence of active molecules in organic and inorganic bodies*, The philosophical magazine, 4 (1828), pp. 161–173.

[24] O. BRZOBOHATÝ, M. ŠILER, AND P. ZEMÁNEK, *Optical manipulation of airborne particles using flexible dual-beam trap*, in Optical Trapping and Optical Micromanipulation IX, vol. 8458, International Society for Optics and Photonics, 2012, p. 84582C.

[25] D. BURNHAM AND D. MCGLOIN, *Holographic optical trapping of aerosol droplets*, Optics Express, 14 (2006), pp. 4175–4181.

[26] D. R. BURNHAM, *Microscopic applications of holographic beam shaping and studies of optically trapped aerosols*, PhD thesis, University of St Andrews, 2009.

[27] C. J. BUSTAMANTE, Y. R. CHEMLA, S. LIU, AND M. D. WANG, *Optical tweezers in single-molecule biophysics*, Nature Reviews Methods Primers, 1 (2021), pp. 1–29.

[28] J. R. BUTLER, J. B. WILLS, L. MITCHEM, D. R. BURNHAM, D. MCGLOIN, AND J. P. REID, *Spectroscopic characterisation and manipulation of arrays of sub-picolitre aerosol droplets*, Lab on a Chip, 9 (2009), pp. 521–528.

[29] M. BY SMOLUCHOWSKI, *On the kinetic theory of brownian motion and suspensions*, Annals of Physics, 326 (1906), pp. 756–780.

[30] A. CALLEGARI, M. MIJALKOV, A. B. GÖKÖZ, AND G. VOLPE, *Computational toolbox for optical tweezers in geometrical optics*, JOSA B, 32 (2015), pp. B11–B19.

[31] A. CARRUTHERS, J. REID, AND A. ORR-EWING, *Longitudinal optical trapping and sizing of aerosol droplets*, Optics Express, 18 (2010), pp. 14238–14244.

[32] A. E. CARRUTHERS, J. S. WALKER, A. CASEY, A. J. ORR-EWING, AND J. P. REID, *Selection and characterization of aerosol particle size using a bessel beam optical trap for single particle analysis*, Physical Chemistry Chemical Physics, 14 (2012), pp. 6741–6748.

[33] S. CHANDRASEKHAR, *Stochastic problems in physics and astronomy*, Reviews of Modern Physics, 15 (1943), p. 1.

[34] Y.-P. CHANG, Y. DEVI, AND C.-H. CHEN, *Micro-droplet trapping and manipulation: Understanding aerosol better for a healthier environment*, Chemistry–An Asian Journal, 16 (2021), pp. 1644–1660.

[35] M. K. CHEEZUM, W. F. WALKER, AND W. H. GUILFORD, *Quantitative comparison of algorithms for tracking single fluorescent particles*, Biophysical Journal, 81 (2001), pp. 2378–2388.

[36] X. CHEN, G. XIAO, X. HAN, W. XIONG, H. LUO, AND B. YAO, *Observation of spin and orbital rotation of red blood cell in dual-beam fibre-optic trap with transverse offset*, Journal of Optics, 19 (2017), p. 055612.

[37] X. CHEN, G. XIAO, H. LUO, W. XIONG, AND K. YANG, *Dynamics analysis of microsphere in a dual-beam fiber-optic trap with transverse offset*, Optics Express, 24 (2016), pp. 7575–7584.

[38] X. CHEN, G. XIAO, K. YANG, W. XIONG, AND H. LUO, *Characteristics of the orbital rotation in dual-beam fiber-optic trap with transverse offset*, Optics Express, 24 (2016), pp. 16952–16960.

[39] S. CHU, *Laser manipulation of atoms and particles*, Science, 253 (1991), pp. 861–866.

[40] S. CHU, L. HOLLBERG, J. E. BJORKHOLM, A. CABLE, AND A. ASHKIN, *Three-dimensional viscous confinement and cooling of atoms by resonance radiation pressure*, Physical Review Letters, 55 (1985), p. 48.

[41] A. L. COLLOPY, S. DING, Y. WU, I. A. FINNERAN, L. ANDEREGG, B. L. AUGENBRAUN, J. M. DOYLE, AND J. YE, *3d magneto-optical trap of yttrium monoxide*, Physical Review Letters, 121 (2018), p. 213201.

[42] A. CONSTABLE, J. KIM, J. MERVIS, F. ZARINETCHI, AND M. PRENTISS, *Demonstration of a fiber-optical light-force trap*, Optics Letters, 18 (1993), pp. 1867–1869.

[43] P. CORRAL ARROYO, G. DAVID, P. A. ALPERT, E. A. PARMENTIER, M. AMMANN, AND R. SIGNORELL, *Amplification of light within aerosol particles accelerates in-particle photochemistry*, Science, 376 (2022), pp. 293–296.

[44] J. C. CROCKER AND D. G. GRIER, *Methods of digital video microscopy for colloidal studies*, Journal of Colloid and Interface Science, 179 (1996), pp. 298–310.

[45] G. DAVID, K. ESAT, S. HARTWEG, J. CREMER, E. CHASOVSKIKH, AND R. SIGNORELL, *Stability of aerosol droplets in bessel beam optical traps under constant and pulsed external forces*, The Journal of Chemical Physics, 142 (2015), p. 154506.

[46] G. DAVID, K. ESAT, I. RITSCH, AND R. SIGNORELL, *Ultraviolet broadband light scattering for optically-trapped submicron-sized aerosol particles*, Physical Chemistry Chemical Physics, 18 (2016), pp. 5477–5485.

[47] G. DAVID, K. ESAT, I. THANOPULOS, AND R. SIGNORELL, *Digital holography of optically-trapped aerosol particles*, Communications Chemistry, 1 (2018), pp. 1–9.

[48] M. E. DIVEKY, M. J. GLEICHWEIT, S. ROY, AND R. SIGNORELL, *Shining new light on the kinetics of water uptake by organic aerosol particles*, The Journal of Physical Chemistry A, 125 (2021), pp. 3528–3548.

[49] M. E. DIVEKY, S. ROY, J. W. CREMER, G. DAVID, AND R. SIGNORELL, *Assessing relative humidity dependent photoacoustics to retrieve mass accommodation coefficients of single optically trapped aerosol particles*, Physical Chemistry Chemical Physics, 21 (2019), pp. 4721–4731.

[50] M. E. DIVEKY, S. ROY, G. DAVID, J. W. CREMER, AND R. SIGNORELL, *Fundamental investigation of photoacoustic signal generation from single aerosol particles at varying relative humidity*, Photoacoustics, 18 (2020), p. 100170.

[51] J. DUPONT-ROC AND G. GRYNBERG, *Photons and atoms: introduction to quantum electrodynamics*, Wiley, 1997.

[52] N. ECKERSKORN, N. ZENG, V. SHVEDOV, W. KROLIKOWSKI, AND A. RODE, *Effect of polarization on transport of particles in air by optical vortex beam*, Journal of Optics, 14 (2012), p. 055302.

[53] A. EINSTEIN, *Theoretische bemerkungen über die brownsche bewegung*, Zeitschrift für Elektrochemie und angewandte physikalische Chemie, 13 (1907), pp. 41–42.

[54] A. EINSTEIN, *Investigations on the Theory of the Brownian Movement*, Courier Corporation, 1956.

[55] K. ESAT, G. DAVID, T. POULKAS, M. SHEIN, AND R. SIGNORELL, *Phase transition dynamics of single optically trapped aqueous potassium carbonate particles*, Physical Chemistry Chemical Physics, 20 (2018), pp. 11598–11607.

[56] R.-J. ESSIAMBRE, *Arthur ashkin: Father of the optical tweezers*, Proceedings of the National Academy of Sciences, 118 (2021).

[57] R. P. FEYNMAN, *The Feynman Lectures on Physics Vol l*, Narosa, 1986.

[58] Z. FU, X. SHE, N. LI, AND H. HU, *Launch and capture of a single particle in a pulse-laser-assisted dual-beam fiber-optic trap*, Optics Communications, 417 (2018), pp. 103–109.

[59] Z. FU, X. SHE, N. LI, W. LI, AND H. HU, *A chip of pulse-laser-assisted dual-beam fiber-optic trap*, in 2018 Progress in Electromagnetics Research Symposium (PIERS-Toyama), IEEE, 2018, pp. 86–91.

[60] R. C. GAUTHIER, *Computation of the optical trapping force using an fdtd based technique*, Optics Express, 13 (2005), pp. 3707–3718.

[61] J. GIESELER, *Dynamics of optically levitated nanoparticles in high vacuum*, (2014).

[62] J. GIESELER, B. DEUTSCH, R. QUIDANT, AND L. NOVOTNY, *Subkelvin parametric feedback cooling of a laser-trapped nanoparticle*, Physical Review Letters, 109 (2012), p. 103603.

[63] F. GITTES AND C. F. SCHMIDT, *Interference model for back-focal-plane displacement detection in optical tweezers*, Optics Letters, 23 (1998), pp. 7–9.

[64] Z. GONG, Y.-L. PAN, G. VIDEEN, AND C. WANG, *Optical trapping and manipulation of single particles in air: Principles, technical details, and applications*, Journal of Quantitative Spectroscopy and Radiative Transfer, 214 (2018), pp. 94–119.

[65] Z. GONG, Y.-L. PAN, G. VIDEEN, AND C. WANG, *Optical trapping and manipulation of single particles in air: Principles, technical details, and applications*, Journal of Quantitative Spectroscopy and Radiative Transfer, 214 (2018), pp. 94–119.

[66] Z. GONG, Y.-L. PAN, G. VIDEEN, AND C. WANG, *Online characterization of single airborne carbon nanotube particles using optical trapping raman spectroscopy*, Applied Spectroscopy, 73 (2019), pp. 910–916.

[67] Z. GONG, Y.-L. PAN, AND C. WANG, *Optical configurations for photophoretic trap of single particles in air*, Review of Scientific Instruments, 87 (2016), p. 103104.

[68] Z. GONG, Y.-L. PAN, AND C. WANG, *Characterization of single airborne particle extinction using the tunable optical trap-cavity ringdown spectroscopy in the ultraviolet*, Optics Express, 25 (2017), pp. 6732–6745.

[69] D. GOSWAMI, *Nobel prize in physics 2018*, Resonance, 23 (2018), pp. 1333–1341.

[70] M. GUILLON, O. MOINE, AND B. STOUT, *Longitudinal optical binding of high optical contrast microdroplets in air*, Physical Review Letters, 96 (2006), p. 143902.

[71] X. HAN, H. LUO, G. XIAO, AND P. H. JONES, *Optically bound colloidal lattices in evanescent optical fields*, Optics Letters, 41 (2016), pp. 4935–4938.

[72] R. D. HANES, M. C. JENKINS, AND S. U. EGELHAAF, *Combined holographic-mechanical optical tweezers: construction, optimization, and calibration*, Review of Scientific Instruments, 80 (2009), p. 083703.

[73] S. HELGADOTTIR, A. ARGUN, AND G. VOLPE, *Digital video microscopy enhanced by deep learning*, Optica, 6 (2019), pp. 506–513.

[74] R. J. HOPKINS, L. MITCHEM, A. D. WARD, AND J. P. REID, *Control and characterisation of a single aerosol droplet in a single-beam gradient-force optical trap*, Physical Chemistry Chemical Physics, 6 (2004), pp. 4924–4927.

[75] M. HORSTMANN, K. PROBST, AND C. FALLNICH, *Towards an integrated optical single aerosol particle lab*, Lab on a Chip, 12 (2012), pp. 295–301.

[76] J. HUISSTEDE, K. VAN DER WERF, M. L. BENNINK, AND V. SUBRAMANIAM, *Force detection in optical tweezers using backscattered light*, Optics Express, 13 (2005), pp. 1113–1123.

[77] P. JONES, O. MARAGÓ, AND G. VOLPE, *Optical tweezers*, Cambridge University Press Cambridge, 2015.

[78] S. JONES, M. KING, AND A. WARD, *Atmospherically relevant core–shell aerosol studied using optical trapping and mie scattering*, Chemical Communications, 51 (2015), pp. 4914–4917.

[79] A. KALUME, C. WANG, AND Y.-L. PAN, *Optical-trapping laser techniques for characterizing airborne aerosol particles and its application in chemical aerosol study*, Micromachines, 12 (2021), p. 466.

[80] C. KOHLER, X. SCHWAB, AND W. OSTEN, *Optimally tuned spatial light modulators for digital holography*, Applied Optics, 45 (2006), pp. 960–967.

[81] M. KREYSING, D. OTT, M. J. SCHMIDBERGER, O. OTTO, M. SCHÜRMANN, E. MARTÍN-BADOSA, G. WHYTE, AND J. GUCK, *Dynamic operation of optical fibres beyond the single-mode regime facilitates the orientation of biological cells*, Nature Communications, 5 (2014), pp. 1–6.

[82] L. D. LANDAU AND E. M. LIFSHITZ, *Fluid Mechanics: Landau and Lifshitz: Course of Theoretical Physics, Volume 6*, vol. 6, Elsevier, 2013.

[83] I. T. LEITE, S. TURTAEV, X. JIANG, M. ŠILER, A. CUSCHIERI, P. S. J. RUSSELL, AND T. ČIŽMÁR, *Three-dimensional holographic optical manipulation through a high-numerical-aperture soft-glass multimode fibre*, Nature Photonics, 12 (2018), pp. 33–39.

[84] D. S. LEMONS AND A. GYTHIEL, *Paul langevin‚Äôs 1908 paper ‚Äúon the theory of brownian motion‚Äù[‚Äúsur la théorie du mouvement brownien,‚Äù cr acad. sci.(paris) 146, 530–533 (1908)]*, American Journal of Physics, 65 (1997), pp. 1079–1081.

[85] I. C. D. LENTON, *Computational tools for simulation and control of optical tweezers*, (2021).

[86] C. Y. LI, M. DING, Y. YANG, P. ZHANG, Y. LI, Y. WANG, L. HUANG, P. YANG, M. WANG, X. SHA, ET AL., *Portrait and classification of individual haze particulates*, Journal of Environmental Protection, 7 (2016).

[87] T. LI, *Fundamental tests of physics with optically trapped microspheres*, Springer Science & Business Media, 2012.

[88] T. LI, *Millikelvin cooling of an optically trapped microsphere in vacuum*, in Fundamental Tests of Physics with Optically Trapped Microspheres, Springer, 2013, pp. 81–110.

[89] W. LI, H. HU, H. SU, Q. ZHU, AND N. LI, *Numerical analysis on the optical force calculation in the rayleigh scattering regime*, Optical Review, 28 (2021), pp. 1–7.

[90] W. LI, N. LI, Y. SHEN, Z. FU, H. SU, AND H. HU, *Dynamic analysis and rotation experiment of an optical-trapped microsphere in air*, Applied Optics, 57 (2018), pp. 823–828.

[91] Y. LI, H. XIN, Y. ZHANG, AND B. LI, *Optical fiber technologies for nanomanipulation and biodetection: a review*, Journal of Lightwave Technology, 39 (2021), pp. 251–262.

[92] L. LING AND Y.-Q. LI, *Measurement of raman spectra of single airborne absorbing particles trapped by a single laser beam*, Optics Letters, 38 (2013), pp. 416–418.

[93] S. LIU AND J.-T. YU, *Comment on longitudinal optical binding of high optical contrast microdroplets in air*, Physical Review Letters, 100 (2008), p. 199403.

[94] Y. LIU AND M. YU, *Investigation of inclined dual-fiber optical tweezers for 3d manipulation and force sensing*, Optics Express, 17 (2009), pp. 13624–13638.

[95] Y. LIU AND M. YU, *Multiple traps created with an inclined dual-fiber system*, Optics Express, 17 (2009), pp. 21680–21690.

[96] V. L. LOKE, T. A. NIEMINEN, N. R. HECKENBERG, AND H. RUBINSZTEIN-DUNLOP, *T-matrix calculation via discrete dipole approximation, point matching and exploiting symmetry*, Journal of Quantitative Spectroscopy and Radiative Transfer, 110 (2009), pp. 1460–1471.

[97] Y. LOU, D. WU, AND Y. PANG, *Optical trapping and manipulation using optical fibers*, Advanced Fiber Materials, 1 (2019), pp. 83–100.

[98] D. LU, L. LABRADOR-PÁEZ, E. ORTIZ-RIVERO, P. FRADES, M. A. ANTONIAK, D. WAWRZYNCZYK, M. NYK, C. D. BRITES, L. D. CARLOS, J. A. GARCIÃÅA SOLEÃÅ, ET AL., *Exploring single-nanoparticle dynamics at high temperature by optical tweezers*, Nano Letters, 20 (2020), pp. 8024–8031.

[99] N. MAGOME, M. I. KOHIRA, E. HAYATA, S. MUKAI, AND K. YOSHIKAWA, *Optical trapping of a growing water droplet in air*, The Journal of Physical Chemistry B, 107 (2003), pp. 3988–3990.

[100] M. MANSURIPUR, *Radiation pressure and the linear momentum of the electromagnetic field*, Optics Express, 12 (2004), pp. 5375–5401.

[101] J. C. MAXWELL, *Viii. a dynamical theory of the electromagnetic field*, Philosophical transactions of the Royal Society of London, (1865), pp. 459–512.

[102] D. MCGLOIN, D. R. BURNHAM, M. D. SUMMERS, D. RUDD, N. DEWAR, AND S. ANAND, *Optical manipulation of airborne particles: techniques and applications*, Faraday Discussions, 137 (2008), pp. 335–350.

[103] M. I. MISHCHENKO, L. D. TRAVIS, AND D. W. MACKOWSKI, *T-matrix computations of light scattering by nonspherical particles: A review*, Journal of Quantitative Spectroscopy and Radiative Transfer, 55 (1996), pp. 535–575.

[104] L. MITCHEM AND J. P. REID, *Optical manipulation and characterisation of aerosol particles using a single-beam gradient force optical trap*, Chemical Society Reviews, 37 (2008), pp. 756–769.

[105] J. MONTEITH AND M. UNSWORTH, *Principles of environmental physics: plants, animals, and the atmosphere*, Academic Press, 2013.

[106] A. P. MOSK, A. LAGENDIJK, G. LEROSEY, AND M. FINK, *Controlling waves in space and time for imaging and focusing in complex media*, Nature Photonics, 6 (2012), pp. 283–292.

[107] V. NATARAJAN AND R. SRINIVASAN, *Nobel prize in physics 1997*, Resonance, 3 (1998), pp. 16–27.

[108] K. C. NEUMAN AND S. M. BLOCK, *Optical trapping*, Review of Scientific Instruments, 75 (2004), pp. 2787–2809.

[109] T. A. NIEMINEN, V. L. LOKE, A. B. STILGOE, G. KNÖNER, A. M. BRAŃCZYK, N. R. HECKENBERG, AND H. RUBINSZTEIN-DUNLOP, *Optical tweezers computational toolbox*, Journal of Optics A: Pure and Applied Optics, 9 (2007), p. S196.

[110] T. A. NIEMINEN, H. RUBINSZTEIN-DUNLOP, N. R. HECKENBERG, AND A. BISHOP, *Numerical modelling of optical trapping*, Computer Physics Communications, 142 (2001), pp. 468–471.

[111] H. M. NUSSENZVEIG, *Cell membrane biophysics with optical tweezers*, European Biophysics Journal, 47 (2018), pp. 499–514.

[112] R. OMORI, T. KOBAYASHI, AND A. SUZUKI, *Observation of a single-beam gradient-force optical trap for dielectric particles in air*, Optics Letters, 22 (1997), pp. 816–818.

[113] OMRON, *Omron microair ne-u100-e nebulizer*, Accompanying datasheet, (2017).

[114] O. OTTO, J. GORNALL, G. STOBER, F. CZERWINSKI, R. SEIDEL, AND U. KEYSER, *High-speed video-based tracking of optically trapped colloids*, Journal of Optics, 13 (2011), p. 044011.

[115] O. OTTO, C. GUTSCHE, F. KREMER, AND U. F. KEYSER, *Optical tweezers with 2.5 khz bandwidth video detection for single-colloid electrophoresis*, Review of Scientific Instruments, 79 (2008), p. 023710.

[116] Y.-L. PAN, S. C. HILL, AND M. COLEMAN, *Photophoretic trapping of absorbing particles in air and measurement of their single-particle raman spectra*, Optics Express, 20 (2012), pp. 5325–5334.

[117] G. PANUSA, Y. PU, J. WANG, C. MOSER, AND D. PSALTIS, *Photoinitiator-free multi-photon fabrication of compact optical waveguides in polydimethylsiloxane*, Optical Materials Express, 9 (2019), pp. 128–138.

[118] H. PARK AND T. W. LEBRUN, *Contact electrification of individual dielectric microparticles measured by optical tweezers in air*, ACS Applied Materials & Interfaces, 8 (2016), pp. 34904–34913.

[119] E. A. PARMENTIER, G. DAVID, P. C. ARROYO, S. BIBAWI, K. ESAT, AND R. SIGNORELL, *Photochemistry of single optically trapped oleic acid droplets*, Journal of Aerosol Science, 151 (2021), p. 105660.

[120] J. PINEDA, B. MIDTVEDT, H. BACHIMANCHI, S. NOÉ, D. MIDTVEDT, G. VOLPE, AND C. MANZO, *Geometric deep learning reveals the spatiotemporal fingerprint of microscopic motion*, arXiv preprint arXiv:2202.06355, (2022).

[121] M. PLIDSCHUN, H. REN, J. KIM, R. FÖRSTER, S. A. MAIER, AND M. A. SCHMIDT, *Ultrahigh numerical aperture meta-fibre for flexible optical trapping*, Light: Science & Applications, 10 (2021), pp. 1–11.

[122] M. PLÖSCHNER, T. TYC, AND T. ČIŽMÁR, *Seeing through chaos in multimode fibres*, Nature Photonics, 9 (2015), pp. 529–535.

[123] A. P. PORFIREV, *Spatial-light-modulator-assisted laser manipulation in air*, Optical Engineering, 59 (2020), p. 055109.

[124] T. C. PRESTON, B. J. MASON, J. P. REID, D. LUCKHAUS, AND R. SIGNORELL, *Size-dependent position of a single aerosol droplet in a bessel beam trap*, Journal of Optics, 16 (2014), p. 025702.

[125] P. PUROHIT, F. J. FORTES, AND J. J. LASERNA, *Optical trapping as a morphologically selective tool for in situ libs elemental characterization of single nanoparticles generated by laser ablation of bulk targets in air*, Analytical Chemistry, 93 (2021), pp. 2635–2643.

[126] G. RANJIT, D. P. ATHERTON, J. H. STUTZ, M. CUNNINGHAM, AND A. A. GERACI, *Attonewton force detection using microspheres in a dual-beam optical trap in high vacuum*, Physical Review A, 91 (2015), p. 051805.

[127] O. REICH, G. DAVID, K. ESAT, AND R. SIGNORELL, *Weighing picogram aerosol droplets with an optical balance*, Communications Physics, 3 (2020), pp. 1–8.

[128] R. S. R. RIBEIRO, O. SOPPERA, A. G. OLIVA, A. GUERREIRO, AND P. A. JORGE, *New trends on optical fiber tweezers*, Journal of Lightwave Technology, 33 (2015), pp. 3394–3405.

[129] H. RISKEN, *Fokker-planck equation*, in The Fokker-Planck Equation, Springer, 1996, pp. 63–95.

[130] A. ROHRBACH AND E. H. STELZER, *Optical trapping of dielectric particles in arbitrary fields*, JOSA A, 18 (2001), pp. 839–853.

[131] A. ROHRBACH AND E. H. STELZER, *Three-dimensional position detection of optically trapped dielectric particles*, Journal of Applied Physics, 91 (2002), pp. 5474–5488.

[132] A. ROHRBACH AND E. H. STELZER, *Trapping forces, force constants, and potential depths for dielectric spheres in the presence of spherical aberrations*, Applied Optics, 41 (2002), pp. 2494–2507.

[133] G. ROOSEN AND C. IMBERT, *Optical levitation by means of two horizontal laser beams: a theoretical and experimental study*, Physics Letters A, 59 (1976), pp. 6–8.

[134] D. RUDD, C. LOPEZ-MARISCAL, M. SUMMERS, A. SHAHVISI, J. GUTIÉRREZ-VEGA, AND D. MCGLOIN, *Fiber based optical trapping of aerosols*, Optics Express, 16 (2008), pp. 14550–14560.

[135] R. SAIJA, P. DENTI, F. BORGHESE, O. M. MARAGO, AND M. A. IATI, *Optical trapping calculations for metal nanoparticles. comparison with experimental data for au and ag spheres.*, Optics Express, 17 (2009), pp. 10231–10241.

[136] K. SCHASCHEK, J. POPP, AND W. KIEFER, *Observation of morphology-dependent input and output resonances in time-dependent raman spectra of optically levitated microdroplets*, Journal of Raman Spectroscopy, 24 (1993), pp. 69–75.

[137] J. H. SEINFELD AND S. N. PANDIS, *From air pollution to climate change*, Atmospheric Chemistry and Physics, 1326 (1998).

[138] X. SHAN, F. WANG, D. WANG, S. WEN, C. CHEN, X. DI, P. NIE, J. LIAO, Y. LIU, L. DING, ET AL., *Optical tweezers beyond refractive index mismatch using highly doped upconversion nanoparticles*, Nature Nanotechnology, 16 (2021), pp. 531–537.

[139] H. H. SHENG HU, YONG ZHAO, *Numerical model of photoinduced dielectrophoresis of ellipsoidal particles*, Journal of Northeastern University (Natural Sciences), 37 (2016), p. 457.

[140] K. SHIMA, R. OMORI, AND A. SUZUKI, *Forces of a single-beam gradient-force optical trap on dielectric spheroidal particles in the geometric-optics regime*, Japanese Journal of Applied Physics, 37 (1998), p. 6012.

[141] V. SHVEDOV, A. S. DESYATNIKOV, A. V. RODE, Y. IZDEBSKAYA, W. KROLIKOWSKI, AND Y. S. KIVSHAR, *Optical vortex beams for trapping and transport of particles in air*, Applied Physics A, 100 (2010), pp. 327–331.

[142] V. G. SHVEDOV, A. S. DESYATNIKOV, A. V. RODE, W. KROLIKOWSKI, AND Y. S. KIVSHAR, *Optical guiding of absorbing nanoclusters in air*, Optics Express, 17 (2009), pp. 5743–5757.

[143] E. SIDICK, S. D. COLLINS, AND A. KNOESEN, *Trapping forces in a multiple-beam fiber-optic trap*, Applied Optics, 36 (1997), pp. 6423–6433.

[144] S. H. SIMPSON AND S. HANNA, *Optical trapping of spheroidal particles in gaussian beams*, JOSA A, 24 (2007), pp. 430–443.

[145] T. F. STOCKER, D. QIN, G.-K. PLATTNER, M. M. TIGNOR, S. K. ALLEN, J. BOSCHUNG, A. NAUELS, Y. XIA, V. BEX, AND P. M. MIDGLEY, *Climate change 2013: The physical science basis. contribution of working group i to the fifth assessment report of ipcc the intergovernmental panel on climate change*, (2014).

[146] K. SUGIOKA, Y. HANADA, AND K. MIDORIKAWA, *Three-dimensional femtosecond laser micromachining of photosensitive glass for biomicrochips*, Laser & Photonics Reviews, 4 (2010), pp. 386–400.

[147] M. SUMMERS, D. BURNHAM, AND D. MCGLOIN, *Trapping solid aerosols with optical tweezers: A comparison between gas and liquid phase optical traps*, Optics Express, 16 (2008), pp. 7739–7747.

[148] M. SUMMERS, J. REID, AND D. MCGLOIN, *Optical guiding of aerosol droplets*, Optics Express, 14 (2006), pp. 6373–6380.

[149] M. D. SUMMERS, *Optical micromanipulation of aerosols*, PhD thesis, University of St Andrews, 2009.

[150] J. SUN, N. KOUKOURAKIS, J. GUCK, AND J. W. CZARSKE, *Rapid computational cell-rotation around arbitrary axes in 3d with multi-core fiber*, Biomedical Optics Express, 12 (2021), pp. 3423–3437.

[151] K. TAGUCHI, K. ATSUTA, T. NAKATA, AND M. IKEDA, *Levitation of a microscopic object using plural optical fibers*, Optics Communications, 176 (2000), pp. 43–47.

[152] K. TAGUCHI, M. TANAKA, AND M. IKEDA, *Theoretical study of an optical levitation using dual beam from optical fibers inserted at an angle*, Optics Communications, 194 (2001), pp. 67–73.

[153] K. TAGUCHI, H. UENO, T. HIRAMATSU, AND M. IKEDA, *Optical trapping of dielectric particle and biological cell using optical fibre*, Electronics Letters, 33 (1997), pp. 413–414.

[154] I. N. TANG, A. TRIDICO, AND K. FUNG, *Thermodynamic and optical properties of sea salt aerosols*, Journal of Geophysical Research: Atmospheres, 102 (1997), pp. 23269–23275.

[155] S. TAURO, A. BAÑAS, D. PALIMA, AND J. GLÜCKSTAD, *Dynamic axial stabilization of counter-propagating beam-traps with feedback control*, Optics Express, 18 (2010), pp. 18217–18222.

[156] R. THURN AND W. KIEFER, *Raman-microsampling technique applying optical levitation by radiation pressure*, Applied Spectroscopy, 38 (1984), pp. 78–83.

[157] A. VAN DER HORST, P. D. VAN OOSTRUM, A. MOROZ, A. VAN BLAADEREN, AND M. DOGTEROM, *High trapping forces for high-refractive index particles trapped in dynamic arrays of counterpropagating optical tweezers*, Applied Optics, 47 (2008), pp. 3196–3202.

[158] I. VERDENY, A. FARRÉ, J. MAS SOLER, C. LÓPEZ-QUESADA, E. MARTÍN BADOSA, AND M. MONTES USATEGUI, *Optical trapping: a review of essential concepts*, Óptica Pura y Aplicada, 2011, vol. 44, num. 3, p. 527-551, (2011).

[159] B. J. WALLACE AND T. C. PRESTON, *Water uptake and loss in viscous aerosol particles with concentration-dependent diffusivities*, The Journal of Physical Chemistry A, 123 (2019), pp. 3374–3382.

[160] C. WANG, Z. GONG, Y.-L. PAN, AND G. VIDEEN, *Optical trap-cavity ringdown spectroscopy as a single-aerosol-particle-scope*, Applied Physics Letters, 107 (2015), p. 241903.

[161] C. WANG, Z. GONG, Y.-L. PAN, AND G. VIDEEN, *Laser pushing or pulling of absorbing airborne particles*, Applied Physics Letters, 109 (2016), p. 011905.

[162] C. WANG, Y.-L. PAN, S. C. HILL, AND B. REDDING, *Photophoretic trapping-raman spectroscopy for single pollens and fungal spores trapped in air*, Journal of Quantitative Spectroscopy and Radiative Transfer, 153 (2015), pp. 4–12.

[163] C. WANG, Y.-L. PAN, AND G. VIDEEN, *Optical trapping and laser-spectroscopy measurements of single particles in air: a review*, Measurement Science and Technology, (2021).

[164] M. C. WANG AND G. E. UHLENBECK, *On the theory of the brownian motion ii*, Reviews of Modern Physics, 17 (1945), p. 323.

[165] G. H. WANNIER, *Statistical physics*, Courier Corporation, 1987.

[166] J. WEBB, *Application of the finite-element method to electromagnetic and electrical topics*, Reports on Progress in Physics, 58 (1995), p. 1673.

[167] W. H. WRIGHT, G. SONEK, AND M. BERNS, *Parametric study of the forces on microspheres held by optical tweezers*, Applied Optics, 33 (1994), pp. 1735–1748.

[168] G. XIAO, T. KUANG, W. XIONG, X. HAN, AND H. LUO, *A pzt-assisted single particle loading method for dual-fiber optical trap in air*, Optics & Laser Technology, 126 (2020), p. 106115.

[169] H. XIN AND B. LI, *Fiber-based optical trapping and manipulation*, Frontiers of Optoelectronics, 12 (2019), pp. 97–110.

[170] W. XIONG, G. XIAO, X. HAN, J. ZHOU, X. CHEN, AND H. LUO, *Back-focal-plane displacement detection using side-scattered light in dual-beam fiber-optic traps*, Optics Express, 25 (2017), pp. 9449–9457.

[171] A. ZAKHARIAN, P. POLYNKIN, M. MANSURIPUR, AND J. MOLONEY, *Single-beam trapping of micro-beads in polarized light: Numerical simulations*, Optics Express, 14 (2006), pp. 3660–3676.

[172] X. ZHANG, S. YANG, AND L. YUAN, *Optical-fiber-based powerful tools for living cell manipulation*, Chinese Optics Letters, 17 (2019), p. 090603.

[173] Z. ZHANG AND C.-H. MENQ, *Three-dimensional particle tracking with subnanometer resolution using off-focus images*, Applied Optics, 47 (2008), pp. 2361–2370.

[174] X. ZHAO, N. ZHAO, Y. SHI, H. XIN, AND B. LI, *Optical fiber tweezers: A versatile tool for optical trapping and manipulation*, Micromachines, 11 (2020), p. 114.

[175] J.-H. ZHOU, M.-C. ZHONG, Z.-Q. WANG, AND Y.-M. LI, *Calculation of optical forces on an ellipsoid using vectorial ray tracing method*, Optics Express, 20 (2012), pp. 14928–14937.

[176] X. ZHU, N. LI, J. YANG, X. CHEN, AND H. HU, *Revolution of a trapped particle in counter-propagating dual-beam optical tweezers under low pressure*, Optics Express, 29 (2021), pp. 11169–11180.

[177] S. ZWICK, T. HAIST, Y. MIYAMOTO, L. HE, M. WARBER, A. HERMERSCHMIDT, AND W. OSTEN, *Holographic twin traps*, Journal of Optics A: Pure and Applied Optics, 11 (2009), p. 034011.